

**DEVELOPMENT OF NANO-STRUCTURED  
SENSORS FOR ELECTRONIC NOSE  
APPLICATIONS**

*Thesis Submitted*

*By*

**SAMIR CHANDRA DAS**

*Doctor of Philosophy (Engineering)*

**Department of Instrumentation & Electronics Engineering  
Faculty Council of Engineering & Technology  
Jadavpur University  
Kolkata, India**

**August, 2015**



**Jadavpur University  
Kolkata – 700 032**

**INDEX NO. 66/ 08/Engg.**

**Title of the Thesis:**                    **DEVELOPMENT OF NANO-STRUCTURED  
SENSORS FOR ELECTRONIC NOSE  
APPLICATIONS**

**Name, Designation &  
Institution of the  
Supervisors:**

**Prof. Rajib Bandyopadhyay** Department of  
Instrumentation and Electronics Engineering  
Jadavpur University  
Salt Lake Campus  
Kolkata-700 098, India

**Prof. Panchanan Pramanik**  
Department of Chemistry  
Indian Institute of Technology, Kharagpur  
Kharagpur-721302,  
West Bengal, India



## **List of Publications:**

### **Papers published in International Journals:**

- [1] S. C. Das, R. Bandyopadhyay, P. Pramanik, Nanostructured ZnO based Gas Sensors to use in Electronic Nose for Biochemical Compounds in Black Tea, International Journal of Advanced Information Science and Technology, 2014, Volume 29, No.29, Pages 124-128.
- [2] S. C. Das, R. Bandyopadhyay, S. Ghosh, P. Pramanik, Fabrication of doped zinc oxide nanostructured sensor array in electronic nose for aroma estimation of CTC black tea and PCA clustering, International Journal of Innovative Science and Applied Engineering Research, Volume 13, Issue 40, 2014, Pages 8-18.
- [3] S. C. Das, K. Sadani, R. Bandyopadhyay, P. Pramanik, Sensing characteristics of Molybdenum doped Zinc Oxide nanoparticles chemoresistor pellets towards black tea-biochemicals, International Journal of Advances in Engineering Science and Technology, Volume 3, Issue 3, 2014, Pages 120-131.
- [4] S. C. Das, R. Bandyopadhyay, P. Pramanik, Development of W doped ZnO nanostructure chemoresistor pellet sensors for black tea aroma monitoring, International Journal of Innovative Science, Engineering and Technology, Volume 2, Issue 3, 2015, Pages 107-113.

### **Publications as Book Proceedings:**

- [1] S. C. Das, B. Tudu, N. Bhattacharyya, R. Bandyopadhyay, P. Pramanik, Nanostructured ZnO sensor in Electronic Nose for Environmental Monitoring on Industrial Premises, Book proceedings, ICLMSC-2011, Pages 165-167, ISBN: 978-93-80813-14-1.
- [2] S. C. Das, B. Tudu, N. Bhattacharyya, R. Bandyopadhyay, P. Pramanik, Development of Nanostructured ZnO based Gas Sensors to use in Electronic Nose towards Hydrogen, Ammonia and LPG, Proceedings book, MDCCT-2012, Pages 204-207, ISBN: 978-93-80663-36-4.

- [3] S. C. Das, R. Bandyopadhyay, P. Pramanik, Developing doped Zinc Oxide nanoparticles chemoresistor pellets and assessing their response to black tea biochemicals, Proceedings book, ICONSEA-2014, Pages 133, ID-085, ISBN: 978-81-924726-2-1.

#### **Publication as Book Chapter:**

- [1] S. C. Das, B. Tudu, N. Bhattacharya, R. Bandyopadhyay, P. Pramanik, Doped ZnO Nanostructured Sensor in Electronic Nose for Detection of Ammonia, Hydrogen and Liquefied Petroleum Gas, Advanced Nanomaterials and Nanotechnology, Springer Publication, Online Springer-Verlag Berlin Heidelberg, Chapter-47, 2013. DOI: 10.1007/978-3-642-34216-5(47) (online).
- [2] S. C. Das, R. Bandyopadhyay, P. Pramanik, Volatile Organic Compounds sensing characteristics of doped Zinc Oxide nanostructured sensors for E-nose applications, NANOSPECTRUM-A Current Scenario, Allied Publishers, 2015, Pages 121-131, ISBN: 978-93-85926-06-8 (Online).

#### **Papers published in International Conference Proceedings:**

- [1] S. C. Das, B. Tudu, N. Bhattacharyya, R. Bandyopadhyay, P. Pramanik, Doped Nanostructured ZnO based Gas Sensors to use in Electronic Nose for Biochemical Compounds in Black Tea Classification, IWoN-2012, Pages 85-87, Jadavpur University, India.
- [2] S. C. Das, S. Ghosh, B. Tudu, N. Bhattacharyya, R. Bandyopadhyay, P. Pramanik, Development of Nanostructured ZnO based Gas Sensors to use in Electronic Nose for Biochemical Compounds in Black Tea, ICST-2012, ID-2591147, Pages 822-826, IEEE (978-1-4673-2248-5/12) (Online).
- [3] S. Ghosh, R. Bandyopadhyay, S. C. Das, Quality estimation of black tea samples using metal doped zinc oxide sensor array, ICNT 2015, ID.PPNMABS537, Haldia Institute of Technology, India, ISBN 978-81-927756-2-3.

### **Papers published in National Conference Proceedings:**

- [1] S. C. Das, B. Tudu, N. Bhattacharyya, R. Bandyopadhyay, P. Pramanik, Development of Nanostructured ZnO based Gas Sensors to use in Electronic Nose towards Hydrogen, Ammonia and LPG, MDCCT-2012, Pages 204-207, University of Burdwan, India, ISBN: 978-93-80663-36-4.
- [2] S. C. Das, B. Tudu, N. Bhattacharyya, R. Bandyopadhyay, P. Pramanik, Nanostructured ZnO based Gas Sensors to use in Electronic Nose for Black Tea Classification, Proceedings book, NSCDST-2012, Pages 62-64, Jadavpur University, W.B., India.

**List of Patents** : Nil

### **List of Presentations in National /International/ Conferences/Workshops**

- [1] 6<sup>th</sup> International Conference on Sensing Technology (ICST-2012), December, 19-21, Hyatt Regency Kolkata, India.
- [2] 2<sup>nd</sup> International Conference on Advance Nanomaterials and Nanotechnology (ICANN-2011), December, 08-10, Dept. of Physics, IIT Guwahati, Assam, India
- [3] India-Australia International Workshop on Nanotechnology in Materials and Energy Application, IAWNT-2011, December, 29-31, Jadavpur University, Kolkata-32, India.
- [4] International Conference on Nano Science & Engineering Applications, ICONSEA-2014, June, 26-28, Jawaharlal Nehru Technology University Hyderabad, India.
- [5] National conference on Sustainable Development through Innovative Research in Science and Technology, NSCDST-2012, September, 28-29, Jadavpur University, W.B., India.






## *Certificate from the Supervisors*

*This is to certify that the thesis titled "DEVELOPMENT OF NANO-STRUCTURED SENSORS FOR ELECTRONIC NOSE APPLICATIONS" submitted by Mr. Samir Chandra Das, who got his name registered on 8<sup>th</sup> August, 2008 for the award of Ph.D. (Engineering) degree of Jadavpur University, is absolutely based upon his own work under joint supervision of the undersigned; and that neither his thesis nor any part of it has been submitted for any degree/diploma or any other academic award anywhere before.*

*Prof. Rajib Bandyopadhyay*  
*Professor*  
*Department of Instrumentation &*  
*Electronics Engineering*  
*Jadavpur University*  
*Salt Lake Campus*  
*Kolkata-700 098, India*  
**Professor**  
**Dept. of Inst. & Electronics Engg.**  
**Jadavpur University**  
**Salt Lake Campus**  
**Kolkata-98**

  
*Prof. Panchanan Pramanik*  
*Former Professor*  
*Department of Chemistry*  
*Indian Institute of Technology, Kharagpur*  
*Kharagpur-721302*  
*West Bengal*  
*India*  
**Former Professor**  
**Department of Chemistry**  
**Indian Institute of Technology, Kharagpur**



*In the Loving Memory*  
*Of*  
*My Father*  
*Late Radheshyam Das*  
*Who has been my Inspiration*



## ***Acknowledgements***

*It is my great privilege to express a deep sense of gratitude and indebtedness to **Prof. Rajib Bandyopadhyay**, Instrumentation & Electronics Engineering (IEE) Department, Jadavpur University, Kolkata and **Prof. Panchanan Pramanik**, Department of Chemistry, Indian Institute of Technology, Kharagpur, W.B. for providing me a very supportive and invaluable guidance in every phase of the program and for giving all possible cooperation throughout the work without which completion of this work could not have been possible.*

*I would like to gratefully acknowledge my colleagues of the Centre for Research in Nanoscience & Nanotechnology, Technology Campus, University of Calcutta for their cooperation and help, and also, for their valuable suggestions in different occasions. I would like to thank all the staff members of Instrumentation & Electronics Engineering Department, Jadavpur University and System Manager office, University of Calcutta for their cooperation and assistance in carrying out this work. Finally, I deeply express gratefulness to my family members for withstanding me and extending their continuous inspiration and support throughout this work.*

*August, 2015*

***Samir Chandra Das***

*Department of Instrumentation &  
Electronics Engineering  
Jadavpur University  
Salt Lake Campus  
Kolkata-700098, India*



## *Contents*

Short Bibliography	ii
List of Publications	iii
Certificate from the Supervisors	vi
Dedication and Acknowledgements	vii-viii
List of Tables	ix-x
List of Figures	xi-xviii
List of Abbreviations	xix
List of Symbols	xxi
<b>Chapter 1: Introduction and scope of the thesis</b>	<b>1-38</b>
1.1. Introduction	3
1.2. Types of sensors in electronic nose	5
1.3. Nanotechnology and nanostructured materials	6
1.3.1. Classification of nanomaterials	8
1.3.2. Nanostructured metal oxides and their importance	9
1.4. Nanostructured Zinc oxide - a unique material	11
1.4.1. Natural sources and production	12
1.4.2. Physical parameters	12
1.4.2.1. Crystal structure and chemical binding	13
1.4.2.2. Mechanical properties	14
1.4.2.3. Thermodynamic properties	14
1.4.2.4. Optical properties	14
1.4.2.5. Electronic band structure	15
1.4.2.6. Physical properties	16
1.4.3. Doped zinc oxide nanostructures	17
1.4.3.1. N-type and P-type doping	17
1.5. Electronic nose	17
1.6. Gas sensors	18
1.6.1. Working principle of metal oxide semiconductor (MOS) gas sensors	19
1.6.2. Role of sensor geometry and contacts	20
1.6.3. Agglomeration	21
1.6.4. Effects of noble and transition metal element doping	22
1.6.5. Effects of particle size	23

1.6.6. Effects of humidity and temperature	23
1.6.7. Basic gas sensing characteristics	24
1.6.7.1. Gas Response	24
1.6.7.2. Response Time	25
1.6.7.3. Recovery Time	25
1.6.7.4. Selectivity	25
1.6.7.5. Detection limit	25
1.6.7.6. Stability and recyclability	26
1.7. Nanostructured metal oxide gas sensors	26
1.7.1. Metal oxide chemo-resistive gas sensors	27
1.7.2. Inversion of type of conduction	28
1.8. Objectives and scope of the thesis	29
References	31
<b>Chapter 2: Synthesis of pure and doped ZnO nanostructures</b>	<b>39-59</b>
2.1. Introduction	41
2.1.1. Chemical vapour deposition (CVD)	43
2.1.2. Chemical bath deposition (CBD)	43
2.1.3. Pulsed laser deposition (PLD)	43
2.1.4. Sol-gel method	44
2.1.5. Hydrothermal method	44
2.1.6. Reported methods for the nanostructure precursor powders	45
2.2. Metal ion-ligand complex based precursor solution method	46
2.3. Synthesis of ZnO nanostructures by chemical method	47
2.3.1. Raw materials used	48
2.3.2. Experiment	49
2.3.3. Synthesis of pure nanostructured ZnO	49
2.3.4. Synthesis procedure	49
2.3.5. Synthesis of metal doped ZnO nanostructures	51
2.4. Metal organic complex decomposition	51
2.4.1. Characterisation techniques of the prepared nanostructured powders	52
2.4.2. Calcination, sintering and pellet formation	53
2.5. Conclusion	55
References	55



<b>Chapter 3: Structural and morphological studies of pure and doped ZnO nanostructures</b>	<b>61-88</b>
3.1. Introduction	63
3.2. Structural parameters of metal oxides controlling gas sensing properties	63
3.3. Structure and morphology of pure ZnO nanostructures	64
3.3.1. X-ray diffraction (XRD) studies	64
3.3.2. Particle size analyser (DLS) results	65
3.3.3. Transmission electron microscopy (TEM) for structural analysis	66
3.4. Morphology of semiconducting metal oxides (SMOX)	67
3.4.1. Atomic force microscopy (AFM)	68
3.4.2. Scanning electron microscope (SEM)	69
3.4.3. Field emission scanning electron microscopy (FESEM)	70
3.5. Chemical composition of ZnO nanostructures	72
3.5.1. Fourier transform infrared spectroscopy (FTIR)	72
3.5.2. Energy dispersive X-ray spectroscopy (EDAX)	73
3.6. Structure and morphology of doped ZnO nanostructures	73
3.6.1. XRD analysis	73
3.6.1.1. Pure ZnO and Co-doped ZnO nanostructures	76
3.6.2. TEM analysis	77
3.6.3. AFM analysis	79
3.6.4. SEM analysis	80
3.6.5. FESEM analysis	82
3.7. Chemical composition of doped ZnO nanostructures	83
3.7.1. FTIR analysis	83
3.7.2. EDAX analysis	84
3.8. Conclusion	84
References	85
<b>Chapter 4: Optical, Electrical and Magnetic properties of pure and metal doped ZnO nanostructures</b>	<b>89-118</b>
4.1. Introduction	91
4.2. Optical properties of ZnO nanostructures	92
4.2.1. UV-Visible spectroscopy studies	92
4.2.2. Photoluminescence (PL) studies	93

4.3. Optical properties of doped ZnO nanostructures	94
4.3.1. UV-Visible spectroscopy analysis	94
4.3.2. Photoluminescence (PL) analysis	96
4.3.3. Cathodoluminescence (CL) analysis	100
4.4. Study of Electrical properties	101
4.4.1. Current-voltage (I–V) characteristics	101
4.4.2. Switching characteristics	103
4.4.3. X-ray photoelectron spectroscopy (XPS) analysis	105
4.5. Study of Magnetic properties	106
4.5.1. Vibrating sample magnetometer (VSM) analysis	106
4.5.2. Magnetic force microscope (MFM) analysis	109
4.6. Conclusion	112
References	112
<b>Chapter 5: Experimental setup and related instrumentation</b>	<b>119-132</b>
5.1. Introduction	121
5.2. Preparation of chemo-resistive pellet	121
5.2.1. Porosity of the pellet	121
5.3. Measurement procedure with nanostructured ZnO pellet sensors	122
5.3.1. Fabricated measurement set-up	123
5.3.2. Heating assembly and sensor measurement circuit	124
5.3.3. Purging assembly	125
5.3.4. Lab-View based data acquisition system (DAS)	125
5.3.5. Interface circuits	126
5.3.6. Measurement procedure with volatile gases	126
5.4. Experimental studies of developed sensors	128
5.5. Conclusion	131
References	131

<b>Chapter 6: Nanostructured ZnO for VOC and Gas-Sensor Applications</b>	<b>133-171</b>
6.1. Introduction	135
6.2. Electrical measurements and gas sensing studies	138
6.3. Results and discussions	139
6.3.1. Performance of pure and 3 wt % (Ni, Co, Pt, Pd)-doped ZnO in black tea bio-chemicals	139
6.3.2. Performance of pure and 3 wt % (Ni, Co, Pt)-doped ZnO at optimum temperature	142
6.3.3. Performance of (Zn <sub>0.97</sub> Pd <sub>0.03</sub> O) sensors in ammonia, hydrogen, liquefied petroleum gas	148
6.3.4. Performance of pure and (1,2,3) wt % Mo-doped ZnO in black tea bio-chemicals	150
6.3.5. Performance of (5,10,15) wt % W-doped ZnO in black tea bio-chemicals and ethanol, methanol and propanol VOC gases	155
6.3.6. Performance of (1, 2, 3) wt % Cd-doped ZnO in ethanol, methanol and propanol	159
6.4. Conclusion	167
References	168
<b>Chapter 7: Conclusion and Future scope</b>	<b>173-180</b>
7.1. Summary of work	175
7.2. Concluding remarks	177
7.2. Future scope	180



## *List of Tables*

<i>Tables</i>	<i>Page No.</i>
<b>Chapter 1: Introduction and scope of the thesis</b>	
<b>Table 1.1.</b> Summary of changes observed in some of the physical properties of nanostructured materials	7
<b>Table 1.2.</b> Physical parameters of zinc oxide	12
<b>Table 1.3.</b> Physical properties for the main precursor material and the dopants used	16
<b>Table 1.4.</b> Types, working principle and applications of gas sensors	18
<b>Chapter 2: Synthesis of pure and doped ZnO nanostructures</b>	
<b>Table 2.1.</b> 1D-Nanostructured ZnO: morphology, methods of preparation, size and other growth parameters	45
<b>Table 2.2.</b> Raw materials used for the preparation of pure and metal doped nanostructured ZnO	48
<b>Table 2.3.</b> Crystallite size of synthesized pure ZnO nanostructure in different compositions	50
<b>Table 2.4.</b> Chemical and structural properties of doped metals	52
<b>Chapter 3: Structural and morphological studies of pure and doped ZnO nanostructures</b>	
<b>Table 3.1.</b> Peaks of XRD analysis (h k l) values	65
<b>Table 3.2.</b> ZnO nanostructure particle size obtained from XRD, DLS, AFM and FESEM	72
<b>Table 3.3.</b> FESEM image elemental analysis	73
<b>Table 3.4.</b> Structural properties of pure and doped ZnO nanostructures	75
<b>Table 3.5.</b> Crystallite size and activation energy of pure and doped ZnO nanostructures	76
<b>Table 3.6.</b> Structural, crystallite size and band-gap energy properties of pure and Co-doped ZnO nanostructures	77
<b>Chapter 4: Optical, Electrical and Magnetic properties of pure and metal doped ZnO nanostructures</b>	
<b>Table 4.1.</b> Absorption peak and band-gap for pure and doped ZnO nanostructures	95
<b>Table 4.2.</b> The peak positions of individual emission bands obtained from multiple Gaussian curve fitting of the PL data for ZnO, (Zn <sub>0.97</sub> Co <sub>0.3</sub> O), (Zn <sub>0.97</sub> Ni <sub>0.3</sub> O) and (Zn <sub>0.97</sub> W <sub>0.3</sub> O) nanostructures	96

<i>Tables</i>	<b>Page No.</b>
<b>Table 4.3.</b> UV and visible emission peaks in the CL spectra of the (Zn <sub>0.97</sub> Ni <sub>0.03</sub> O) and (Zn <sub>0.97</sub> Co <sub>0.03</sub> O) at room temperatures	101
<b>Table 4.4.</b> ON/OFF ratios and response times for ZnO, (Zn <sub>0.97</sub> Co <sub>0.03</sub> O), (Zn <sub>0.97</sub> Ni <sub>0.03</sub> O) and (Zn <sub>0.97</sub> W <sub>0.03</sub> O) nanostructured device	104
<b>Table 4.5.</b> Dark current and photocurrent densities of ZnO, (Zn <sub>0.97</sub> Co <sub>0.03</sub> O), (Zn <sub>0.97</sub> Ni <sub>0.03</sub> O) and (Zn <sub>0.97</sub> W <sub>0.03</sub> O) nanostructured devices along with the values obtained from the literature	105
<b>Table 4.6.</b> Coercive Field and Saturation Magnetization of nanostructured doped ZnO	107
<b>Table 4.7.</b> Particle analysis and surface roughness of 3 wt % (Ni, Co, W)-doped nanostructured materials	111
<b>Chapter 6: Nanostructured ZnO for VOC and Gas-Sensor Applications</b>	<b>133-171</b>
<b>Table 6.1.</b> Aroma chemicals responsible for black tea flavour	136
<b>Table 6.2.</b> Chemical structure and properties of used volatile organic compounds and gases	137
<b>Table 6.3.</b> Summary of the performances of doped ZnO nanostructured sensors at optimum temperature of 350°C	147
<b>Table 6.4.</b> Performance of Noble metal doped ZnO nanostructure chemo-resistive pellet for sensor applications	150
<b>Table 6.5.</b> Performance of ZnO: Mo nanostructure sensors at optimum temperature 350°C	154
<b>Table 6.6.</b> Performance of (Zn <sub>0.98</sub> Cd <sub>0.02</sub> O) nanostructured sensors	163
<b>Chapter 7: Conclusion and Future scope</b>	<b>173-180</b>
<b>Table 7.1.</b> Prepared ZnO nanostructures and their properties	176
<b>Table 7.2.</b> Noble metal 3 wt % (Pd, Pt)-doped ZnO nanostructures chemo-resistive pellet for sensor applications	177
<b>Table 7.3.</b> Transition metal 3 at. % (Ni, Co)-doped ZnO nanostructure powders for absorption band colour	178
<b>Table 7.4.</b> ON/OFF ratios and response times for ZnO, (Zn <sub>0.97</sub> Co <sub>0.03</sub> O), (Zn <sub>0.97</sub> Ni <sub>0.03</sub> O) and absorption band colour	179
<b>Table 7.5.</b> Coercive field (H <sub>C</sub> ), Saturation magnetization (M <sub>S</sub> ), and Remanence-magnetization (M <sub>R</sub> ) of doped ZnO nanostructures	179

## *List of Figures*

---

<i>Figures</i>	<i>Page No.</i>
<b>Chapter 1: Introduction and scope of the thesis</b>	
<b>1-38</b>	
<b>Fig. 1.1.</b> Types of sensors commonly employed in electronic nose	5
<b>Fig. 1.2.</b> Images demonstrating nanomaterial classifications	9
<b>Fig. 1.3. (a)</b> The hexagonal wurtzite structure model of ZnO, <b>(b)</b> The tetrahedral coordination of ZnO	13
<b>Fig. 1.4. (a)</b> Band diagram and <b>(b)</b> Hysteresis loop or M–H curve	15
<b>Fig. 1.5.</b> Block diagram of electronic nose	18
<b>Fig. 1.6. (a)</b> Construction of solid-state metal oxide sensors and topologies of measurement contacts, <b>(b)</b> Spillover effect at the ZnO nanostructure surface at 180-210°C.	21
<b>Fig. 1.7. (a)</b> FESEM image of Ni-Mo doped ZnO nanostructure (100nm) by chemical synthesis and diagrams illustrating peculiarities of electro-conductivity, <b>(b)</b> gas sensing reactions in chemo-resistive pellet sensor	22
<b>Fig. 1.8. (a)</b> Variation in sensitivity with average particle size, <b>(b)</b> Gas sensing mechanism of doped ZnO nanostructure in the atmosphere of injected gas	23
<b>Fig.1.9.(a)</b> Receptor and transducer function of a semiconductor gas sensor. Parameters influencing sensor performance: Inset <b>Fig.(i)</b> ZnO:Ni sensor response as a function of crystal size and <b>(b)</b> The conductance of n-type ZnO sensor as a function of the band bending change determined by simultaneous work function and conductivity measurements at $\approx 320^\circ\text{C}$	28
<b>Chapter 2: Synthesis of pure and doped ZnO nanostructures</b>	
<b>39-59</b>	
<b>Fig. 2.1.</b> Schematic illustration for Bottom-up and Top-down approach	41
<b>Fig. 2.2.</b> SEM images of ZnO nanostructures grown by <b>(a)</b> PLD on Si (111) and <b>(b)</b> PVT on Si(111)	44
<b>Fig. 2.3.</b> Schematic representation of the preparation of pure ZnO nanostructure powders	46
<b>Fig. 2.4.</b> Black carbonaceous fluffy mass	47
<b>Fig. 2.5.</b> Schematic representation of the preparation of metal doped ZnO nanostructure powders	51
<b>Fig. 2.6. (a)</b> Flow chart of sensor development and measurement process <b>(b)</b> Formation of ZnO nanostructures during calcination	53
<b>Fig. 2.7.</b> Flow chart of complete synthesis process, prepared nanostructured powder sample before and after calcination for characterization of crystal structure, average particle size, shape, elemental compositions, morphology, optical, electrical and magnetic properties studied	54

---

<i>Figures</i>	<b>Page No.</b>
<b>Chapter 3: Structural and morphological studies of pure and doped ZnO nanostructures</b>	<b>61-88</b>
<b>Fig. 3.1.</b> (a) Structural parameters of MOS which control gas sensing properties, (b) Diagram of band bending after chemisorption of charged species	64
<b>Fig. 3.2.</b> (a) XRD pattern of nanostructured ZnO powder obtained through chemical synthesis, (b) X-ray diffractometer (Bruker D8 Advance) at IUC, UGC, Salt Lake	65
<b>Fig. 3.3.</b> (a) Particle size analysis of ZnO solid solution, (b) Particle size analyser (DLS) instrument image at CRNN, CU	66
<b>Fig. 3.4.</b> (a) Particle size, (b) HRTEM and (c) SAED pattern of TEM images of ZnO nanostructures	66
<b>Fig. 3.5.</b> (a) Block diagram of TEM, (b) TEM instrument ( JEOL, JEM 2100, Japan) PC controlled 200 KV (HR version) at CRNN, CU	67
<b>Fig. 3.6.</b> Doped nanostructured ZnO surface morphology by (a) SEM and (b)TEM image	68
<b>Fig. 3.7.</b> (a) Schematic diagram of AFM and (b) AFM Instrument (Brukar, Veeco-Innova) at IPLS, CU	68
<b>Fig. 3.8.</b> AFM images (1 $\mu$ m x 1 $\mu$ m) of ZnO nanostructure after calcined at 600 $^{\circ}$ C for 5 hours (a) 2D image, (b) 3D image, (c) depth histogram and (d) bearing area plot from 2D tapping amplitude image	69
<b>Fig. 3.9.</b> SEM image of ZnO nanostructure, (a) before calcination and (b) after calcined at 500 $^{\circ}$ C for 4 hours	70
<b>Fig. 3.10.</b> FESEM micrograph of ZnO nanostructures calcined at (a) 500 $^{\circ}$ C for 4 hours, (b) 600 $^{\circ}$ C for 5 hours	71
<b>Fig. 3.11.</b> (a) SEM instrument with INCA Energy 250 Microanalysis System (EDS), ZEISS EVO-MA 10, (b) FESEM instrument (JEOL, JSM-7600F) PC controlled microscope with INCA Energy 250 EDS at CRNN, CU	71
<b>Fig. 3.12.</b> (a) FT-IR spectrum of the nanostructured ZnO powder calcinated at 600 $^{\circ}$ C for 5 hours, (b) FT-IR instrument at CRNN, CU	72
<b>Fig. 3.13.</b> (a) EDAX analysis of ZnO calcined at 600 $^{\circ}$ C for 5 hours, Inset: FESEM image (b)	73
<b>Fig. 3.14.</b> XRD pattern of (Zn <sub>1-x</sub> M <sub>x</sub> O) nanostructures powder obtained through chemical synthesis for (a) (Co, Ni, Pt, Pd)-doped, (b) Mo doped, (c) Cd doped, (d) W doped ZnO nanostructures	74
<b>Fig. 3.15.</b> XRD spectra of (Co, Ni, Pt, Pd)-doped nanostructured ZnO powder (a) (31.0 $^{\circ}$ – 32.5 $^{\circ}$ ), (b) (33.6 $^{\circ}$ – 34.8 $^{\circ}$ ), (c) (35.4 $^{\circ}$ – 36.6 $^{\circ}$ ) and (d) (67.5 $^{\circ}$ – 69.3 $^{\circ}$ )	75



<i>Figures</i>	<i>Page No.</i>
<b>Fig.3.16.(a)</b> X-ray diffraction (XRD) spectra of pure and Co-doped ZnO nanostructures prepared at room temperature range of (30–40°). The inset shows a magnified view of the XRD spectra within the range of (40–60°), <b>(b)</b> Crystallite size and lattice parameter of Co-doping as a function of the atomic percentage	77
<b>Fig.3.17.</b> Particle size and SAED pattern of TEM images of <b>(a-b)</b> (Zn <sub>0.97</sub> Ni <sub>0.03</sub> O) and <b>(c-d)</b> (Zn <sub>0.94</sub> Ni <sub>0.06</sub> O) nanostructures respectively, <b>(e-g)</b> HRTEM images for 20,10 and 5 nm respectively	78
<b>Fig. 3.18.</b> Particle size and SAED pattern of TEM images of <b>(a)</b> (Zn <sub>0.97</sub> Co <sub>0.03</sub> O), <b>(b)</b> (Zn <sub>0.97</sub> Pt <sub>0.03</sub> O) and <b>(c)</b> (Zn <sub>0.97</sub> Pd <sub>0.03</sub> O) nanostructures, HRTEM images for 5 nm <b>(d)</b> ZnO:Co, <b>(e)</b> ZnO:Pt and <b>(f)</b> ZnO:Pd	78
<b>Fig. 3.19.</b> AFM images of doped ZnO nanostructures <b>2D</b> (10 μm x10 μm): <b>(a)</b> ZnO:Ni, <b>(b)</b> ZnO:Co, and <b>(c)</b> ZnO:W; <b>3D</b> (10 μm x10 μm): <b>(d)</b> ZnO:Ni, <b>(e)</b> ZnO:Co, and <b>(f)</b> ZnO:W	79
<b>Fig. 3.20.</b> AFM images of doped ZnO nanostructures <b>2D</b> (1 μm x1 μm): <b>(a)</b> ZnO:Pt, <b>(b)</b> ZnO:Pt, and <b>(c)</b> ZnO:Cd; <b>3D</b> (10 μm x10 μm): <b>(d)</b> ZnO:Pt, <b>(e)</b> ZnO:Pt, and <b>(f)</b> ZnO:Cd	80
<b>Fig. 3.21.(a)</b> SEM micrographs of (Zn <sub>0.97</sub> Ni <sub>0.03</sub> O) nanostructures <b>(b)</b> EDAX analysis of ZnO:Ni nanoparticles	80
<b>Fig. 3.22.</b> SEM images <b>(a)</b> (Zn <sub>0.97</sub> Ni <sub>0.03</sub> O), <b>(b)</b> (Zn <sub>0.97</sub> Co <sub>0.03</sub> O), <b>(c)</b> (Zn <sub>0.97</sub> Pd <sub>0.03</sub> O), and <b>(d)</b> (Zn <sub>0.97</sub> Pt <sub>0.03</sub> O) nanostructured powders sintered at 400°C for 3 hours	81
<b>Fig. 3.23.</b> SEM images <b>(a)</b> (Zn <sub>0.97</sub> Ni <sub>0.03</sub> O), <b>(b)</b> (Zn <sub>0.97</sub> Co <sub>0.03</sub> O), <b>(c)</b> (Zn <sub>0.97</sub> Pd <sub>0.03</sub> O), and <b>(d)</b> (Zn <sub>0.97</sub> Pt <sub>0.03</sub> O) nanostructured powders sintered at 600°C for 5 hours	81
<b>Fig. 3.24.</b> FESEM image of <b>(a)</b> (Zn <sub>0.98</sub> Cd <sub>0.02</sub> O), and <b>(b)</b> (Zn <sub>0.97</sub> Cd <sub>0.03</sub> O) nanostructures; EDAX spectra of <b>(c)</b> (Zn <sub>0.98</sub> Cd <sub>0.02</sub> O), and <b>(d)</b> (Zn <sub>0.97</sub> Cd <sub>0.03</sub> O) nanostructures	82
<b>Fig. 3.25.</b> <b>(a)</b> FESEM image of (Zn <sub>0.97</sub> Mo <sub>0.03</sub> O), and <b>(b)</b> EDAX spectra (Zn <sub>0.97</sub> Mo <sub>0.03</sub> O)	82
<b>Fig. 3.26.</b> <b>(a)</b> FESEM image of (Zn <sub>0.97</sub> W <sub>0.03</sub> O), and <b>(b)</b> EDAX spectra (Zn <sub>0.97</sub> W <sub>0.03</sub> O)	83
<b>Fig.3.27.</b> FTIR spectra of pure ZnO, (Zn <sub>0.97</sub> Co <sub>0.03</sub> O) and (Zn <sub>0.97</sub> Pd <sub>0.03</sub> O) nanostructures	83
<b>Fig.3.28.</b> FTIR spectra of (Zn <sub>0.97</sub> Pt <sub>0.03</sub> O), (Zn <sub>0.97</sub> Ni <sub>0.03</sub> O), (Zn <sub>0.97</sub> Mo <sub>0.03</sub> O) and (Zn <sub>0.97</sub> W <sub>0.03</sub> O) nanostructures	84
<b>Chapter 4: Optical, Electrical and Magnetic properties of pure and metal doped ZnO nanostructures</b>	<b>89-118</b>
<b>Fig. 4.1.</b> <b>(a)</b> The Electromagnetic spectrum, <b>(b)</b> Absorption of ultraviolet and visible radiation	92

<i>Figures</i>	<i>Page No.</i>
<b>Fig. 4.2.</b> (a) UV absorption spectrum for pure nanostructured ZnO calcined at 500°C for 4 hours, (b) UV-vis spectrophotometer (Perkin Elmer, Lambda-1050 UV/Vis/NIR) at CRNN, CU	93
<b>Fig. 4.3.</b> (a) Room temperature PL spectra of nanostructured ZnO calcined at 500°C for 4 hours, (b) Photoluminescence (PL) spectrometer (Perkin Elmer LS-55) at IUC, UGC, Salt Lake	93
<b>Fig. 4.4.</b> UV-vis spectra (a) Absorbance vs. wavelength (b) Intensity vs. energy of 3 wt % ( $Zn_{1-x}M_xO$ ), where M = Ni, Pt, Pd, Co, Cd and W	94
<b>Fig. 4.5.</b> (a) Visible region colour wheel, (b) PL spectra of ZnO, ( $Zn_{0.97}Co_{0.3}O$ ), ( $Zn_{0.97}Ni_{0.3}O$ ) and ( $Zn_{0.97}W_{0.3}O$ ) calcined at 600°C for 5 hours (Indicating luminescence emission in visible range)	96
<b>Fig. 4.6.</b> PL spectra fitted to multiple Gaussian curves for (a) ZnO, (b) ( $Zn_{0.97}Co_{0.3}O$ ), (c) ( $Zn_{0.97}Ni_{0.3}O$ ) and (d) ( $Zn_{0.97}W_{0.3}O$ ) sintered at 600°C for 5 hours	97
<b>Fig. 4.7.</b> (a) Schematic band diagram of the defect levels of ZnO obtained from PL spectra and (b) Schematic energy levels of defects in ZnO	98
<b>Fig. 4.8.</b> (a) PL intensity vs. wavelength, (b) PL intensity vs. energy of doped ZnO nanostructures sintered at 400°C for 3 hours	99
<b>Fig. 4.9.</b> CL spectra of (a, c) ( $Zn_{0.97}Ni_{0.3}O$ ) and (b, d) ( $Zn_{0.97}Co_{0.3}O$ ) nanostructures, (c, d) visible emission parts of spectra (a) and (b)	100
<b>Fig. 4.10.</b> (a,b) Schematic diagram of the fabricated MSM (Ag/ZnO/Ag) or (Ag/doped ZnO/Ag) Schottky diode	102
<b>Fig. 4.11.</b> I-V characteristics of (a) ZnO, (b) ZnO:Co, (c) ZnO:Ni, (d) ZnO:W nanostructures with and without light illumination	103
<b>Fig. 4.12.</b> ON/OFF light switching behaviour at a bias of 1V for (a) ZnO, (b) ( $Zn_{0.97}Co_{0.03}O$ ), (c) ( $Zn_{0.97}Ni_{0.03}O$ ) and (d) ( $Zn_{0.97}W_{0.03}O$ ) nanostructures device	104
<b>Fig. 4.13.</b> XPS data for Ni doped ZnO nanostructures showing peaks corresponding to Zn 2p <sub>3/2</sub> , Zn 2p <sub>1/2</sub> , O1s and Ni 2p <sub>3/2</sub> lines	105
<b>Fig. 4.14.</b> M-H curves of (a) ( $Zn_{0.97}Ni_{0.03}O$ ), (b) ( $Zn_{0.97}Co_{0.03}O$ ) and (c) ( $Zn_{0.97}W_{0.03}O$ ) at room temperature (T=300K)	107
<b>Fig. 4.15.</b> M-H curves of (a) ( $Zn_{0.95}Ni_{0.05}O$ ), (b) ( $Zn_{0.95}Co_{0.05}O$ ), (c) ( $Zn_{0.95}W_{0.05}O$ ), and (d) ( $Zn_{0.95}Mo_{0.05}O$ ) at room temperature (T=300K)	108
<b>Fig. 4.16.</b> (a) Theoretical M-H curve (b) Variation of the coercivity (H <sub>c</sub> ) of magnetic nanoparticles with size, (c) View of the MPMS SQUID VSM, at CRNN, CU	108

<i>Figures</i>	<i>Page No.</i>
<b>Fig. 4.17.</b> MFM images of (Zn <sub>0.97</sub> Ni <sub>0.03</sub> O) nanostructures, 2D (10 μm x 12.8 μm) for depth histogram ( <b>a, d</b> ), 3 section ( <b>b, e</b> ) and 3D (10 μm x 10μm) for bearing area ( <b>c, f</b> )	109
<b>Fig. 4.18.</b> MFM images of (Zn <sub>0.97</sub> Co <sub>0.03</sub> O) nanostructures, 2D (10 μm x 12.8 μm) for depth histogram ( <b>a, d</b> ), 3 section ( <b>b, e</b> ) and 3D (10 μm x 10μm) for bearing area ( <b>c, f</b> )	110
<b>Fig. 4.19.</b> MFM images of (Zn <sub>0.97</sub> W <sub>0.03</sub> O) nanostructures, 2D (10 μm x 12.8 μm) for depth histogram ( <b>a, d</b> ), 3 section ( <b>b, e</b> ) and 3D (10 μm x 10μm) for bearing area ( <b>c, f</b> )	111
<b>Chapter 5: Experimental setup and related instrumentation</b>	<b>119-132</b>
<b>Fig. 5.1.</b> Pellet making instrument ( <b>a</b> ) Pellet press ( <b>b</b> ) Dies and ( <b>c</b> ) Pressure gauge	122
<b>Fig.5.2.</b> Schematic representation of the various steps involved for fabrication of pelletized nanostructured ZnO sensors	122
<b>Fig. 5.3.</b> Sensor assembly inside the quartz tube along with allied fittings viz. thermocouple, silica gel tube, inlets for vapours and connecting leads: ( <b>a</b> ) Customized sensing measurement set-up	123
( <b>b</b> ) Schematic diagram of instrument setup	124
( <b>c</b> ) Equipment setup of in-situ resistance measurements	124
<b>Fig. 5.4.</b> ( <b>a</b> ) Pellet sensor in a quartz tube (left) and schematic diagram (right)	125
( <b>b</b> ) Sensor holding in ceramic base of brass holder (left) and schematic diagram of silver plate use as anode and cathode (right)	125
<b>Fig. 5.5.</b> ( <b>a</b> ) Schematic diagram of data acquisition system (DAS)	126
( <b>b</b> ) Connection of analog to digital converter (amplifier, buffer, attenuator) AD 620	127
( <b>c</b> ) Temperature control loop	127
( <b>d</b> ) Electrical circuit for measuring the chemo-resistive pellet gas sensor	127
( <b>e</b> ) Data acquisition system block diagram	127
( <b>f</b> ) Voltage divider network showing connection of sensor with 100 KΩ series resistance	128
<b>Fig. 5.6.</b> ( <b>a</b> ) Screen shot of DAS software using Labview and ( <b>b</b> ) the sample response of nanostructured sensor to bio-chemical compounds of black tea	129
<b>Fig. 5.7.</b> Response of (Zn <sub>0.98</sub> Ni <sub>0.02</sub> O) nanostructured sensors at 350°C towards ( <b>a</b> ) Geraniol ( <b>b</b> ) Trans-2-Hexenal ( <b>c</b> ) Linalool Oxide ( <b>d</b> ) Linalool	130
<b>Fig. 5.8.</b> Response of (Zn <sub>0.98</sub> Cd <sub>0.02</sub> O) nanostructures sensors at 300°C towards ( <b>a</b> ) Ethanol, ( <b>b</b> ) Methanol, and ( <b>c</b> ) Propanol to increasing injected ppm	130

<i>Figures</i>	<i>Page No.</i>
<b>Chapter 6: Nanostructured ZnO for VOC and Gas-Sensor Applications</b>	<b>133-171</b>
<b>Fig. 6.1.</b> Performance of pure and 3 wt % (Ni, Co, Pt, Pd)-doped nanostructured ZnO sensors towards VOCs of black tea aroma (Linalool, Linalool oxide, Geraniol, Trans-2-hexenal)	
<b>(a)</b> at 200°C	140
<b>(b)</b> at 250°C	140
<b>(c)</b> at 300°C	141
<b>(d)</b> at 350°C	141
<b>(e)</b> at 400°C	142
<b>Fig. 6.2.</b> Performance of nanostructured ZnO sensors towards VOCs of black tea aroma (Linalool, Linalool oxide, Geraniol, Trans-2-hexenal) at optimum temperature 350°C for	
<b>(a)</b> pure ZnO	142
<b>(b)</b> 3 at % Ni-doped	143
<b>(c)</b> 3 at % Co-doped	143
<b>(d)</b> 3 at % Pt-doped	144
<b>(e)</b> 3 at % Pd-doped	144
<b>Fig. 6.3.</b> Performance of pure and 3 wt % (Ni, Co, Pt, Pd)-doped nanostructured ZnO sensors towards VOCs of black tea aroma at optimum temperature 350°C for	
<b>(a)</b> Trans-2-hexenal	145
<b>(b)</b> Geraniol	146
<b>(c)</b> Linalool oxide	146
<b>(d)</b> Linalool	147
<b>Fig. 6.4.</b> Performance of (Zn <sub>0.97</sub> Pd <sub>0.03</sub> O) nanostructured chemo-resistive sensor in alternating environment of air at 500 ppm for	
<b>(a)</b> Response vs. operating temperature of H <sub>2</sub> , LPG and NH <sub>3</sub>	148
<b>(b)</b> Electrical resistance vs. time of at 300°C	148
<b>(c)</b> Response and recovery time vs. operating temperature of H <sub>2</sub> , LPG and NH <sub>3</sub>	149
<b>(d)</b> Response vs. time of NH <sub>3</sub> in air at different temperatures	149
<b>Fig. 6.5.</b> Sensitivity vs. Temperature to 900 ppm of pure and (1, 2) wt % Mo-doped ZnO chemo-resistive pellets sintered at 500°C for 3 hours with	
<b>(a)</b> Linalool	150
<b>(b)</b> Linalool oxide	151
<b>(c)</b> Geraniol	151
<b>(d)</b> Trans-2-hexenal	152

<i>Figures</i>	<i>Page No.</i>
<b>Fig. 6.6.</b> Sensitivity vs. Temperature to 900 ppm of pure and (1, 2, 3) at % Mo-doped ZnO chemo-resistive pellets sintered at 350°C for 6 hours with	
<b>(a)</b> Linalool	153
<b>(b)</b> Linalool oxide	153
<b>(c)</b> Geraniol	154
<b>(d)</b> Trans-2-hexenal	154
<b>Fig. 6.7. (a-f)</b> Performance of (5,10,15) at % W-doped nanostructured ZnO sensors with 500 ppm towards VOCs of black tea aroma (Linalool, Linalool oxide, Geraniol, Trans-2-hexenal) vapour, <b>(a, c, e)</b> Sensitivity vs. Temperature and <b>(b, d, f)</b> Rate of Response vs. Temperature. Figures <b>(a, b)</b> are 5 at %, <b>(c, d)</b> are 10 at % and <b>(e, f)</b> 15 at % at 250°C - 450°C	
<b>(a)</b> 5 at % ZnO:W (500 ppm) Sensitivity vs. Temperature	155
<b>(b)</b> 5 at % ZnO:W (500 ppm) Rate of Response vs. Temperature	156
<b>(c)</b> 10 at % ZnO:W (500 ppm) Sensitivity vs. Temperature	156
<b>(d)</b> 10 at % ZnO:W (500 ppm) Rate of Response vs. Temperature	156
<b>(e)</b> 15 at % ZnO:W (500 ppm) Sensitivity vs. Temperature	157
<b>(f)</b> 15 at % ZnO:W (500 ppm) Rate of Response vs. Temperature	157
<b>Fig. 6.8. (a-d)</b> Performance of (5,10) at % W-doped nanostructured ZnO sensors with 500 ppm towards VOCs (Methanol, Ethanol, Propanol) <b>(a, c)</b> Sensitivity vs. temperature and <b>(b, d)</b> Rate of Response vs. temperature. Figures <b>(a, b)</b> are 5 at %, <b>(c, d)</b> are 10 at % at 300°C - 400°C	
<b>(a)</b> 5 at % ZnO:W (500 ppm) Sensitivity vs. Temperature	158
<b>(b)</b> 5 at % ZnO:W (500 ppm) Rate of Response vs. Temperature	158
<b>(c)</b> 10 at % ZnO:W (500 ppm) Sensitivity vs. Temperature	158
<b>(d)</b> 10 at % ZnO:W (500 ppm) Rate of Response vs. Temperature	159
<b>Fig. 6.9. (a-f)</b> Performance of (1, 2, 3) at % Cd-doped nanostructured ZnO sensors with 300 ppm towards VOCs (Methanol, Ethanol, Propanol) <b>(a, c, e)</b> Sensitivity vs. operating temperature and <b>(b, d, f)</b> Rate of Response vs. operating temperature. Figures <b>(a, b)</b> are 1 at %, <b>(c, d)</b> are 2 at % and <b>(e, f)</b> 3 at % at 250°C - 400°C	
<b>(a)</b> 1 at % ZnO:Cd (300 ppm) Sensitivity vs. Operating temperature	159
<b>(b)</b> 1 at % ZnO:Cd (300 ppm) Rate of Response vs. Operating temperature	159
<b>(c)</b> 2 at % ZnO:Cd (300 ppm) Sensitivity vs. Operating temperature	160
<b>(d)</b> 2 at % ZnO:Cd (300 ppm) Rate of Response vs. Operating temperature	160
<b>(e)</b> 3 at % ZnO:Cd (300 ppm) Sensitivity vs. Operating temperature	160
<b>(f)</b> 3 at % ZnO:Cd (300 ppm) Rate of Response vs. Operating temperature	161

<i>Figures</i>	<i>Page No.</i>
<b>Fig. 6.10.</b> Performance of the 1at % Cd-doped nanostructured ZnO chemo-resistive sensors Rate of response vs. concentrations (ppm) of methanol, ethanol, propanol at 350°C	
<b>(a)</b> 1 at % Cd-doped nanostructured ZnO chemo-resistive sensors	161
<b>(b)</b> 2 at % Cd-doped nanostructured ZnO chemo-resistive sensors	162
<b>(c)</b> 3 at % Cd-doped nanostructured ZnO chemo-resistive sensors	162
<b>Fig. 6.11.</b> Response (%) vs. concentration of (Zn <sub>0.98</sub> Cd <sub>0.02</sub> O) nanostructured chemo-resistive sensors to methanol, ethanol, propanol for better performance analysis using sensor array at 350°C	163
<b>Fig. 6.12. (a)</b> Response of (Zn <sub>0.85</sub> W <sub>0.15</sub> O) nanostructured chemo-resistive sensors as a function of time with different concentrations of VOCs at 350°C	164
<b>(b)</b> Response of (Zn <sub>0.85</sub> W <sub>0.15</sub> O) nanostructured sensors as a function of the operation temperature at 350°C with different ppm of VOCs	165
<b>(c)</b> Response vs. recovery time of the gas sensors based on Co-doped nanostructured ZnO chemo-resistive pellet to 900 ppm of trans-2-hexenal and linalool	165
<b>Fig. 6.13.</b> Response of (Zn <sub>0.85</sub> W <sub>0.15</sub> O) nanostructured chemo-resistive sensors with 500 ppm different VOC (propanol, ethanol, methanol, trans-2-hexenal, linalool oxide, geraniol, linalool), gases (NH <sub>3</sub> , H <sub>2</sub> , LPG) and H <sub>2</sub> O (95% RH) at 350°C	166

## *List of Abbreviations*

---

<b>MOS</b>	Metal oxide semiconductor	<b>CTC</b>	Cut–Tear–Curl
<b>ZnO</b>	Zinc Oxide	<b>FTD</b>	First time derivative
<b>DMS</b>	Dilute magnetic semiconductor	<b>FTIR</b>	Fourier transform Infrared spectroscopy
<b>BP</b>	Back propagation	<b>AI</b>	Analog input
<b>CB</b>	Conduction band	<b>NDMLG</b>	Nitrogen doped multilayer graphene
<b>VB</b>	Valance band	<b>EDTA</b>	Ethylene-diamine-tetra-acetic acid
<b>VOC</b>	Volatile organic compounds	<b>DEA</b>	Diethanolamine
<b>IMC</b>	Ion mobility spectrometry	<b>EDAX</b>	Energy dispersive X-ray analysis
<b>GC</b>	Gas chromatography	<b>MIM</b>	Metal-insulator-metal
<b>MC</b>	Mass spectrometry	<b>MSM</b>	Metal-semiconductor-metal
<b>STM</b>	Scanning tunnelling microscope	<b>PXRD</b>	Powder X-ray diffractometry
<b>AFM</b>	Atomic force microscope	<b>I-V</b>	Current-voltage
<b>0D</b>	Zero dimensional	<b>XPS</b>	X-ray photoelectron spectroscopy
<b>3D</b>	Three dimensional	<b>MFM</b>	Magnetic force microscope voltammetry
<b>CFCOM</b>	Catalyst free combust-oxidized mesh	<b>M–H</b>	Magnetization curves
<b>PES</b>	Photoelectron spectroscopy	<b>SMOX</b>	Semiconducting metal oxide
<b>PL</b>	Photoluminescence	<b>RTFM</b>	Room temperature ferromagnetic
<b>CL</b>	Cathodoluminescence	<b>PVA</b>	Poly-vinyl alcohol
<b>UV-Vis</b>	UV-Vis spectrometry	<b>MCB</b>	Miniature Circuit Breaker
<b>XRD</b>	X-ray diffractometry	<b>LPG</b>	Liquefied petroleum gas
<b>SEM</b>	Scanning electron microscopy	<b>MLFFN</b>	Multilayer feed-forward network
<b>EDS</b>	Energy-dispersive spectroscopy	<b>RSE</b>	Referenced single-ended
<b>PSA</b>	Particle size analyzer	<b>MPPA</b>	Mean percentage prediction
<b>SCS</b>	Semiconductor characterization system	<b>TC</b>	Thermocouple
<b>HRTEM</b>	High resolution transmission electron microscopy	<b>DAS</b>	Data acquisition system
<b>FESEM</b>	Field emission scanning electron microscopy	<b>NI</b>	National Instruments
<b>E-Nose</b>	Electronic Nose	<b>NIDAQ</b>	National Instruments data acquisition card
<b>SAED</b>	Selected area electron diffraction	<b>NIR</b>	Near infrared spectroscopy
<b>SQUID</b>	Superconducting quantum interferences device	<b>OD</b>	Optical density
<b>VSM</b>	Vibrating sample magnetometer	<b>PCA</b>	Principal component analysis
<b>DEA</b>	Diethalamine	<b>OP</b>	Operational amplifier
<b>NBE</b>	Near-band edge emissions	<b>MEMS</b>	Micro-electro mechanical systems
<b>ET</b>	Electronic tongue	<b>ARPES</b>	Angle-resolved photoelectron spectroscopy

---





## *List of Symbols*

---

$\theta$	angle of diffraction (degree)	$k_B$	boltzmann constant
$\lambda$	wavelength (nm)	$\alpha$	magnetoelectric coupling coefficient
$\omega$	angular frequency	$M_S$	saturation magnetization
$M$	magnetization	$M_R$	remnant magnetization
$H$	magnetic field	$H_C$	coercivity
$q$	electron charge	$\tau_{rec}$	recovery time
$Q$	electric charge	$\tau_{res}$	response time
$C$	capacitance (Farad)	$R_b$	bulk resistance
$C_0$	capacitance of vacuum	$R_{agl}$	resistance of the agglomerate
$V$	voltage	$I_T/I_0$	transmittance
$P$	polarization ( $\mu C/cm^2$ )	$I_R/I_0$	reflectance
$F$	farads	$eV$	electron volt
$Z$	impedance	$I_{VS}/I_{UV}$	visible-to-UV intensity ratio
$\epsilon$	dielectric permittivity	$V_o$	oxygen vacancy
$k$	absorption index	$O_i$	oxygen interstitials
$n$	refractive index	$\Omega cm$	resistivity
$X$	necks width	$E_{BG}$	band-gap energy
$L_D$	Debye length	$Zn_i$	zinc interstitial
$d$	grains size	$V_{Zn}$	zinc vacancy
$h$	planck's constant	$V_o^\bullet$	oxygen vacancy states
$c$	velocity of light	$T_D$	theoretical density
$D$	crystallite size	$A_D$	apparent density
$c$	lattice parameter	$R_0$	external resistor
$m$	mass of the pellet	$R_a$	resistance in air
$d$	diameter of the pellet	$R_g$	resistance in target gas
$\tan\delta$	loss factor	$R$	response
$\phi_b$	barrier height	$S$	sensitivity
$J$	current density	$(V_0)_{air}$	voltage in air
$T_B$	Blocking temperature	$(V_0)_{gas}$	voltage in target gas

---



# Chapter 1

## Introduction and scope of the thesis

---

**The introductory chapter starts with a brief discussion on different types of sensors which are used in electronic-nose system. It is followed by a brief introduction to nanotechnology. Then a brief description of electronic nose, its applications and a detailed discussion on MOS sensors used in electronic nose are presented. It is concluded with the objective of the thesis work and a chapter wise description.**

---

### *List of sections*

- 1.1. Introduction
  - 1.2. Types of sensors in electronic nose
  - 1.3. Nanotechnology and nanostructured materials
    - 1.3.1. Classification of nanomaterials
    - 1.3.2. Nanostructured metal oxides and their importance
  - 1.4. Nanostructured Zinc oxide - a unique material
    - 1.4.1. Natural sources and production
    - 1.4.2. Physical parameters
      - 1.4.2.1. Crystal structure and chemical binding
      - 1.4.2.2. Mechanical properties
      - 1.4.2.3. Thermodynamic properties
      - 1.4.2.4. Optical properties
      - 1.4.2.5. Electronic band structure
      - 1.4.2.6. Physical properties
    - 1.4.3. Doped zinc oxide nanostructures
      - 1.4.3.1. N-type and P-type doping
  - 1.5. Electronic nose
  - 1.6. Gas sensors
    - 1.6.1. Working principle of metal oxide semiconductor (MOS) gas sensors
    - 1.6.2. Role of sensor geometry and contacts
    - 1.6.3. Agglomeration
    - 1.6.4. Effects of noble and transition metal element doping
    - 1.6.5. Effects of particle size
    - 1.6.6. Effects of humidity and temperature
    - 1.6.7. Basic gas sensing characteristics
      - 1.6.7.1. Gas Response
      - 1.6.7.2. Response Time
      - 1.6.7.3. Recovery Time
      - 1.6.7.4. Selectivity
      - 1.6.7.5. Detection limit
      - 1.6.7.6. Stability and recyclability
  - 1.7. Nanostructured metal oxide gas sensors
    - 1.7.1. Metal oxide chemo-resistive gas sensors
    - 1.7.2. Inversion of type of conduction
  - 1.8. Objectives and scope of the thesis
- References



# Chapter 1

## Introduction and scope of the thesis

### 1.1. Introduction

Electronic Noses (e-Noses) are systems that detect and identify odours and vapours by linking chemical sensing devices with signal processing and pattern recognition sub-systems. This electronic nose technology has been successfully employed for recognition and quality analysis of various food and agro products, viz., wine [1-2], cola [3], meat [4], fish [5], coffee [6], tobacco etc. Electronic nose has shown promise to be used for continuous and real time monitoring of aroma of in-process as well as finished tea as has been reported by other researchers. But these instruments employ metal oxide semiconductor (MOS) based gas sensors which are broadly tuned and non-specific in nature. Chemo-resistive MOS gas sensors rely on changes of electrical conductivity due to a change in the surrounding atmosphere and is related to the reactions between ion absorbed surface oxygen and target analyte gas [7]. As a result, the sensitivity is poor and the accuracy of quality evaluation is not very high. But sensors, specifically tuned to the aroma determining chemicals in tea, can greatly improve the performance of such instruments.

Buck and Axel in the year 2004 [8] received Nobel Prize for their revolutionary contribution in explaining olfactory transduction mechanism in mammals. However complex the olfaction mechanism may be; the scientists have not kept themselves diffident in mimicking the mammalian olfactory system with electronic means and in the year 1982, Persaud and Dodd [9] proposed an artificial electronic olfactory system with various sensors and intelligent pattern classifiers. Since then, worldwide extensive research and development work have been carried out in the field of electronic nose and associated sensors.

Nanotechnology enables us to create functional materials, devices, and systems by controlling matter at the atomic and molecular scales, and to exploit novel properties and phenomena. Most chemical and biological sensors, as well as many physical sensors, depend on the interactions occurring at these levels and nanotechnology is expected to have a tremendous impact on the sensor world. Nanotechnology enables us to design sensors that are much smaller, less power hungry, and more sensitive than current nano or micro

sensors. Sensing applications will thus enjoy benefits far beyond those offered by MEMS and other sensors. In semiconductor material, the electron follows from the valance band (VB) to conduction band (CB). The change of carrier concentration due to the presence of chemical vapour is monitored by many of the solid state chemical sensors, e.g. ZnO, WO<sub>3</sub> etc. However, most of them are active at higher temperature because, at higher temperature the chemical reactions are facilitated on the surface which add or deplete electron on the surface causing the change of conductivity. The most important aspect of the ZnO material is that it is completely an environment-friendly direct band gap material with wide band-gap energy of 3.37 eV and high excitation binding energy of ~ 60 meV. Another attractive feature of ZnO is that its band-gap energy can be engineered by changing dopant materials [10]. Very recently, nanostructured ZnO gas sensors have attracted more interest due to their better properties of detecting pollutants, toxic gases, alcohols and food freshness, especially fish freshness [11], or as gas-sensing films integrated on one chip to make an 'electronic nose' [12]. The sensitivities of gas sensors can be greatly improved by doping MnO<sub>2</sub>, TiO<sub>2</sub> and Co<sub>2</sub>O<sub>3</sub>. In a recent paper, identification of flavour components through pattern recognition analysis of Chinese liquors was carried out using doped nanostructured ZnO gas sensor array and different statistical techniques were compared for their classification ability [13].

This thesis presents a few methodologies for the development of pure and metal doped nanostructured ZnO chemo-resistor sensors for black tea aroma as well as aromatic black tea biochemical compounds like Linalool, Linalool Oxide, Geraniol and, Trans-2-hexenal. Also the results of Volatile Organic Compounds (VOC) like methanol, ethanol, propanol, and ammonia, hydrogen, liquefied petroleum gas detection are presented.

This introductory chapter is organized as follows: first, the different types of sensors and preparation of zinc oxide nanostructures are discussed. Different properties of ZnO nanostructures (like crystal structure and chemical binding, thermodynamics, mechanical, optical, electrical and magnetic properties) and applications in rubber manufacturing, medical uses, food additives, anti corrosive coatings and electronic appliances are described in literature review. Then a brief description of electronic nose, its applications and different types of MOS sensors used in electronic nose are presented. Different applications of ZnO semiconductors in areas such as laser diodes, solar cells, gas sensors, optoelectronic devices are described. It is focused on ZnO nanostructures prepared by chemical synthesis route using ionic liquids. The ZnO nanostructures have been characterized for crystal

structure, average particle size, shape, elemental compositions and morphology. Optical, electrical and magnetic properties have been investigated by different sophisticated scientific instruments at different laboratories. The synthesized pure and metal (M=Ni, Co, Pd, Pt, Mo, W, Cd)-doped nanostructured ZnO material is shaped into pellet form of diameter 13 mm and thickness 2 mm with the help of a pellet making instrument for studying their sensing characteristics. Finally, there is a description about the customized electronic nose used for pure and doped ZnO chemo-resistive pellet sensors, for which the target vapours are volatile organic compounds like methanol, ethanol, propanol, ammonia, hydrogen, liquefied petroleum gas etc.

## 1.2. Types of sensors in electronic nose

The detection system of an electronic nose consists of an array of MOS gas sensors. An array of chemical sensors like chemo-resistors are mostly used in present day electronic nose systems, even though bio-sensors have shown a lot of promise and may even replace the chemical sensors in future.

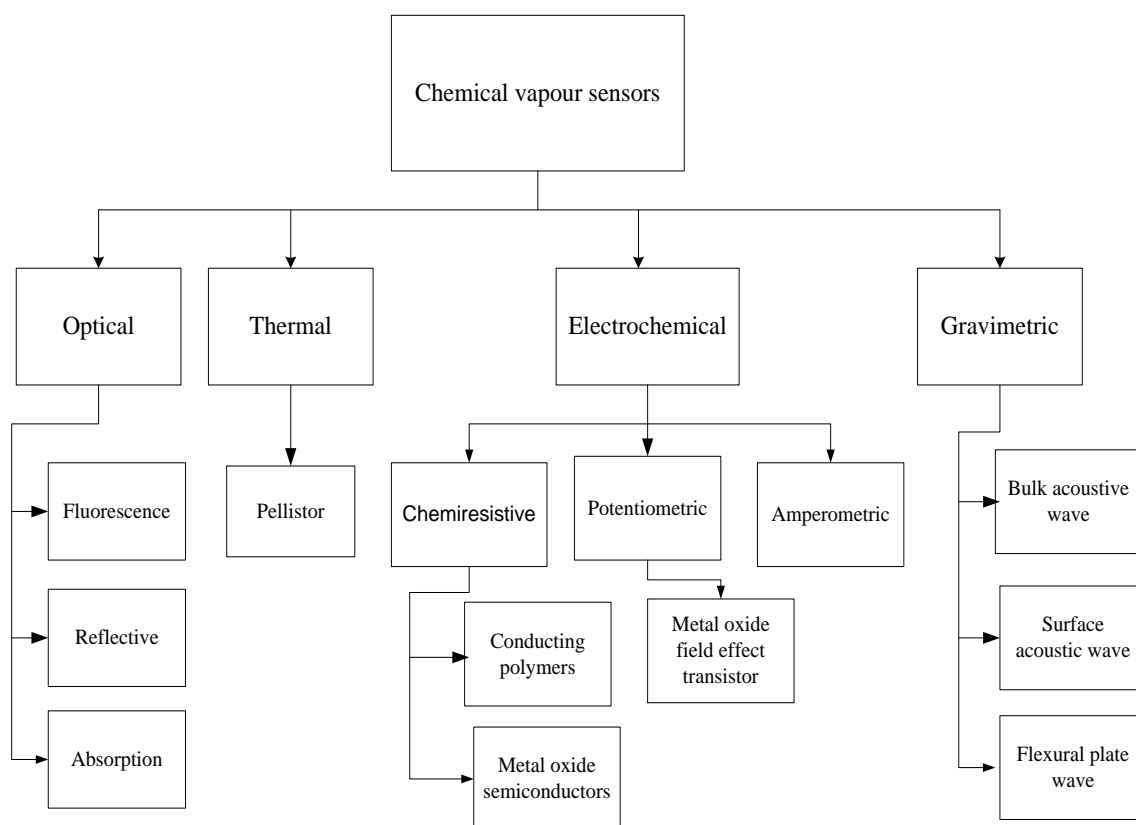


*Fig.1.1. Types of sensors commonly employed in electronic nose*

The chemical sensors used in the array convert a chemical quantity into an electrical signal. The concentration of specific particles such as atoms, molecules, ions in gases, etc. can then be related to that electrical signal [14]. The types of MOS sensors that can be used in an electronic nose need to respond to molecules in the gas phase, which are typically VOC and other gases with different relative molar masses [15]. Apart from gas sensors, some new technologies like gas chromatography (GC), mass spectrometry (MS), ion mobility spectrometry (IMS), etc. also have been recently employed as detectors. Detailed descriptions about the types of sensors have been elaborated in references [16–19]. The commonly used types of sensors and their principles of detection are summarized in Fig.1.1.

### **1.3. Nanotechnology and nanostructured materials**

Today's widespread activity in the field of 'nanoscience' and 'nanotechnology' is actually rooted in the ideas of some leading scientists of the last century. Among them, the foremost name was Nobel Prize-winner physicist, Richard P. Feynman, way back in 1959 [20], but it was only in 1974 that the terminology was actually conceived by Norio Taniguchi [21] and defined as the processes of separation, consolidation and deformation of materials in the molecular scale. The term was later explored and popularized by K. Eric Drexler through his journal articles [22] and the book 'Engines of Creation: The Coming Era of Nanotechnology' [23]. The word 'nanotechnology', is derived from the Greek word 'nānos' meaning 'dwarf', and is appropriately used to underline its fundamental theme of miniaturization. It can be broadly defined as the technology that deals with structures and processes in the spatial dimensions of less than 100 nanometers (1 nanometer =  $1 \times 10^{-9}$  meter). Some of these technologies despite having only limited control of structure at the nanometer scale are already in use, producing useful products, in which the structure of matter is more precisely controlled. Nanotechnology received its greatest momentum when scientists acquired new sophisticated tools such as, the scanning tunnelling microscope (STM) and the atomic force microscope (AFM) to obtain pictures of single atoms with unprecedented clarity. STM, invented in 1982 by Binnig and Rohrer, allows imaging of solid surfaces of conducting samples with the atomic scale resolution. AFM, developed in 1986 by Binnig, Quate and Gerber, enables scientists to study non-conducting surfaces as it scans Van Der Waals forces with its 'atomic' tips. Since the early 1990s, the term 'nanostructured material' and synonymous terminologies such as, nanoscaled material / nanophase material / nanosized material / nanomaterial, have emerged to encompass the



structure of matter, controlled at the nanometer scale, that can be used to produce novel materials and devices with useful and unique properties. Nanostructured material may be broadly identified as those which have dimensions larger than that of a molecular cluster but smaller than that of a bulk material, more importantly they show selected properties/phenomena that are different from either and can be uniquely assigned to them. Accordingly, it is nanotechnology through which we attempt to harness these phenomena of the nanostructured materials for the application at the macroscopic scale such as, for device application. ‘Nanomaterial’ is now a generic term used to designate materials that have structures within 100 nm in at least one of the spatial dimensions.

**Table 1.1.** Summary of changes observed in some of the physical properties of nanostructured materials

<b>Properties</b>	<b>Change observed in nanostructured materials</b>
<i>Mechanical</i>	<ul style="list-style-type: none"> <li>• Increase in hardness and strength of metals and alloys</li> <li>• Enhanced ductility and toughness in metals and alloys</li> </ul>
<i>Electrical</i>	<ul style="list-style-type: none"> <li>• Higher electrical conductivity in ceramics and magnetic nanostructures</li> <li>• Higher electrical resistivity in metals</li> </ul>
<i>Magnetic</i>	<ul style="list-style-type: none"> <li>• Increase in coercivity down to a critical grain size</li> <li>• Decrease in coercivity leading to super paramagnetic behaviour in magnetic material below critical grain size</li> </ul>
<i>Catalytic</i>	<ul style="list-style-type: none"> <li>• Increased catalytic activity due to enhanced surface area, large interface volume and modified coordination number of the surface atoms in metal/alloys/ceramics</li> </ul>
<i>Optical</i>	<ul style="list-style-type: none"> <li>• Blue-shift of optical spectra of quantum-confined crystallites</li> <li>• Increase in luminescence efficiency of semiconductors</li> </ul>
<i>Temperature</i>	<ul style="list-style-type: none"> <li>• Decrease of sintering and melting temperature and increase of plasticity in pure and composite metals and ceramics</li> </ul>

Materials with particle sizes (i.e., diameters) in the nano-size regime have experienced a rapid development in last two decades due to their exciting and potential applications in a wide variety of technological areas. With particle sizes diminishing to nanometer scale, the

materials exhibit unique and interesting properties compared to their conventional coarse/bulk counterparts. A list of the physical properties which undergo change with diminishing grain sizes in a nanostructured material is summarized in Table 1.1.

The unique properties of nanostructured materials can be attributed due to their high surface areas and dominance of quantum effects. The nanomaterials possess high surface-to-volume ratio and are therefore characterized by (i) large fraction of surface atoms and large number of grain boundaries (ii) high surface energy, and (iii) spatial confinement, which do not exist in their corresponding coarse-grained polycrystalline counterparts [24]. Thus, in nanomaterials a large fraction of atoms are boundary atoms and as the grain size is reduced from 10 nm, 5 nm to 1 nm, the fraction of their atoms at the surfaces or, at the grain boundaries increase by 30%, 40% to 98% respectively [25]. These surface atoms are characterized by a (a) lower coordination number, (b) lower coordination symmetry, and (c) lower atomic density [26]. Therefore, the interface structure plays an important role in determining the physical and mechanical properties of nanomaterials, and the entire material would be affected by the surface properties of nanosized materials [27]. As the size is reduced to tens of nanometers or less, quantum effects come into play, and these can significantly change the materials' physico-chemical properties, such as optical, magnetic or electrical properties etc [28]. Therefore, high surface areas and thus, large fractions of surface atoms together with small particle sizes provides scope for distinctly new and different properties in the nanocrystalline materials.

### **1.3.1. Classification of nanomaterials**

According to their dimensionalities, nanomaterials are commonly classified as zero dimensional (0D) (quantum dots or mostly spherical nanoparticles), one dimensional (1D) (nanowires, nanotubes, and nanobelts), two-dimensional (2D) (thin films and quantum wells) and three-dimensional (3D) (plates and flower-like) as shown in Fig. 1.2. The classification is based on the number of dimensions in which the material is outside the nano-regime. A thin film, for example, consists of large expanses of material in both in-plane directions, and is nanosized only in its thickness; therefore it is termed a two-dimensional (2D) nanomaterial. Due to the effects of size discussed in the previous section, the dimensionality of nanomaterials can alter their properties. A thin film may behave very differently from a nanowire with the same chemistry. These distinctions therefore are not arbitrary, but important in distinguishing these materials according to their unique characteristics.

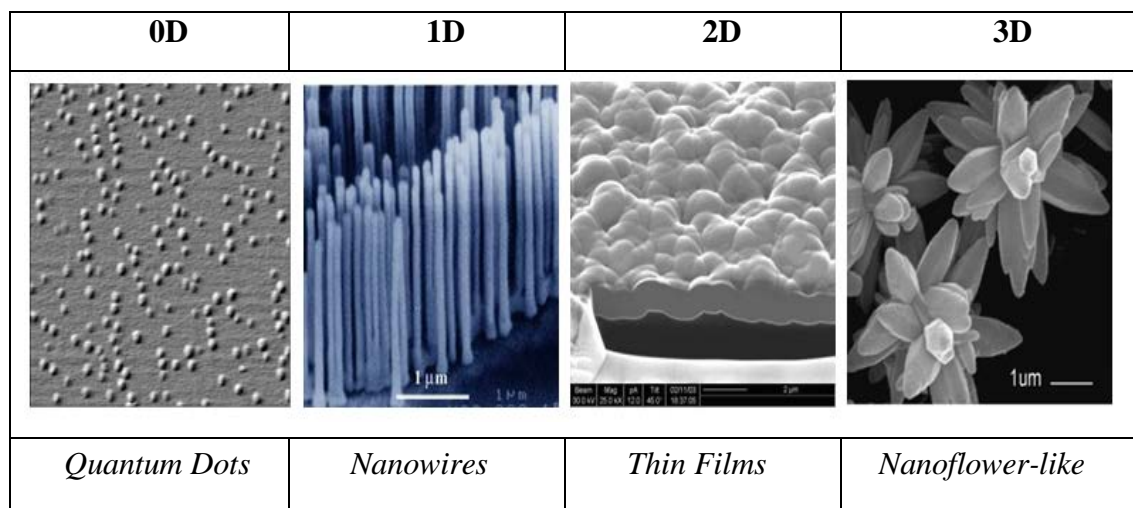


*Fig.1.2. Images demonstrating nanomaterial classifications*

### 1.3.2. Nanostructured metal oxides and their importance

Metals form a large variety of oxide compounds that can exist in a number of structural geometries and depending on their electronic structure they can show insulating, semiconducting, metallic and even superconducting behaviour. Metal oxides specially, transition metals, play a significant role in many areas of chemistry, physics and material science [29, 30] due to their wide ranging physico-chemical properties originating from the multiple valence states of the metal ions. In technological applications, metal oxides are used in the fabrication of microelectronic circuits, chemical sensors, piezoelectric devices, in coatings for corrosion protection or thermal isolation, in heterogeneous and environmental catalysis, etc [31]. The major proportions of the catalysts used in industrial applications involve metal oxides either as an active phase, or/and a promoter, or/and as “support”. The chemical and petrochemical industries predominantly use metal and metal oxide catalysts [32]. For monitoring environmental pollution, metal oxide based catalysts or sorbents are employed to remove the oxides of carbon, nitrogen and sulphur species generated during the combustion of fossil-derived fuels. Additionally, metal oxides are vastly used in the semiconductor industry. Most of the chips used in computers today contain a metal oxide component. In the emerging field of nanotechnology, an objective is to formulate nanostructured metal oxide materials with unique properties which are much improved with respect to those of bulk materials with unique properties [33, 34]. Nanostructured oxides can exhibit unique chemical properties either owing to the limited size of their grains and a high density of low-coordinated surface sites or, can provide new extended systems with unprecedented structure, morphology and/or composition. Very

unreactive oxides in the form of massive crystals become highly reactive when prepared in high surface area form [35]. Similarly, unique structures and /or, chemical compositions of nanocrystalline oxides can bring about revolutionary properties in the materials. Nanostructured metal oxides have found technological applications in electronic, magnetic, optical, ceramics, catalytic and porous materials etc. A brief account of their varied applications is documented below.

- Nanostructured oxides are used as heterogeneous catalysts and their catalytic activity is due to their enhanced surface area, large interface volume and modified coordination number of the surface atoms. Heterogeneous catalysis plays an important role in the production of fine chemicals, petroleum refinery, environmental protection and remediation and processing of consumer products and advanced materials.
- Nanostructured oxides have great technological and industrial importance for their photo-activity. There are many applications of pure, functionalized or doped oxide films or oxide nanoparticles (e.g., Titania) for the photo-catalytic activity in our everyday life, such as, in solar cells, as self-cleaning surface film on glass windows.
- Thin films of nanostructured metal oxides with high dielectric constants, also called high-K dielectrics, are important in microelectronics industry as a substitute for silicon as an insulating component in metal oxide field effect transistors.
- Recent years have witnessed a tremendous growth of research in the field of magneto-electronics, in view of its obvious potential for novel devices with entirely new capabilities. The oxides of transition metals and their interfaces with metals and semiconductors represent one of the most exciting areas currently studied in magnetism.
- Nanostructured semiconducting metal oxides with controlled composition are indeed of increasing interest in gas sensing and also constitute a new and exciting subject in fundamental research.
- Nanostructured metal oxide based pigments are commercially important because of their good chemical and thermal stability, high refractive indices, insolubility (bleed resistance), high surface coverage, easy dispersability in dispersing medium for paint formulation.

## 1.4. Nanostructured Zinc oxide - a unique material

Zinc oxide (ZnO), a representative of II–VI semiconductor compounds, is a very versatile and important material. ZnO has a unique position among semiconducting oxides due to its piezoelectric and transparent conducting properties. It has a high electrical conductivity and optical transmittance in the visible region. These properties make it an ideal candidate for applications like transparent conducting electrodes in flat panel displays and window layers in solar cells. ZnO has a wide band gap (3.37eV) and a large exciton binding energy (60 meV) and exhibits many potential applications in areas such as laser diodes, solar cells, gas sensors, optoelectronic devices. A wide band gap has many benefits like enabling high temperature and power operations, reducing electrical noise, sustaining in large electric fields and raising breakdown voltages. By proper alloying with MgO or CdO, the band gap can be tuned in the range of 3-4 eV. ZnO nanostructures have an active role to play in nano devices like nano gas sensors because the huge surface area enhances the gas sensing properties of the sensors. Apart from this, bio-safe characteristics of ZnO make it very attractive for biomedical applications. A method for economical mass production of ZnO nanostructures would therefore be very useful. This is why the ZnO nanostructures are of great interest. Physically, ZnO has the appearance of a white powder and is referred to as Zinc white or Zincite. As far as solubility is concerned, it is almost insoluble in water and alcohol but it is readily soluble in acids like HCl even though it is tarnished in their presence. The mineral form of ZnO takes up a red or yellow colour instead of the usual white due to the presence of impurities like manganese and other elements. Crystalline form of ZnO is thermo-chromic in nature and due to this; it changes from white to yellow on heating and vice-versa on cooling. ZnO displays amphoteric properties and it is also referred to as an II-VI semiconductor because Zinc belongs to the second group and oxygen belongs to the sixth group of the periodic table. ZnO has three crystal forms: the hexagonal wurtzite, the cubic zinc blende and the cubic rock salt which is rarely observed. The wurtzite structure is most commonly used as it has the highest stability under normal working conditions. Hexagonal and zinc blende structures do not display inversion symmetry and these properties are responsible for the piezoelectricity and pyroelectricity of ZnO. ZnO is considered to be a soft material with a reading of 4.5 on the Mohs hardness scale. Its elastic constants are not that impressive but ZnO does not possess very good thermal properties like high melting point, high thermal capacity and conductivity and a low coefficient of thermal expansion which makes it suitable for use as a ceramic. Zinc oxide has attracted significant attention as a material for ultraviolet (UV)

light-emitters, varistors, transparent high power electronics, surface acoustic wave devices, piezoelectric transducers and gas sensors and also as a window material for displays and solar cells. As a wide band gap semiconductor ( $E_g = 3.37$  eV), zinc oxide is a candidate host for solid state blue to UV optoelectronics, including lasers. The applications include high density data storage systems, solid state lighting, secure communications and bio-detection.

### 1.4.1. Natural sources and production

The most important zinc ore is zinc sulfide, found as the mineral sphalerite. The majority of zinc oxide is produced by the so called ‘French Process’, which has been utilized since 1844. For this metallic zinc is melted at  $419.5^\circ\text{C}$  in a graphite crucible and vapourized above  $907^\circ\text{C}$ . The zinc vapour then reacts with oxygen in the air to form zinc oxide, which normally consists of agglomerated zinc oxide particles with sizes ranging from  $0.1\mu\text{m}$  to a few microns, and a purity of up to 99%. A modification of French process, known as the catalyst free combust-oxidized mesh (CFCOM) process, yields acicular ZnO nanostructures (rods, wires, tripods, tetrapods, plates) [36].

### 1.4.2. Physical parameters

Few important physical parameters [36-38] are given in Table 1.2.

*Table 1.2. Physical parameters of zinc oxide*

<i>Properties</i>	<i>Values</i>
Molecular formula	ZnO
Molar mass	81.4084 g/mol
Appearance	Amorphous white or yellowish white powder
Odour	Odourless
Density	$5.606\text{ g/cm}^3$
Melting point	$1975^\circ\text{C}$
Boiling point	$2360^\circ\text{C}$
Solubility in water	0.16 mg/100 mL
Refractive index	2.0041
Lattice Constants	$a_0 = 0.32469\text{ \AA}$ $c_0 = 0.52069\text{ \AA}$
Relative Dielectric Constant	8.66
Energy Gap	3.4 eV Direct
Intrinsic Carrier Concentration	$< 10^6 /\text{cc}$

Exciton Binding Energy	60 meV
Electron effective mass	0.24
Electron mobility (at 300 K)	200 cm <sup>2</sup> /V.sec
Hole Effective mass	0.59
Hole mobility (at 300 K)	5-50 cm <sup>2</sup> /V.sec

### 1.4.2.1. Crystal structure and chemical binding

Zinc oxide is a semiconducting compound of the group-II<sup>b</sup> element  $_{30}\text{Zn}$  and the group VI element  $_{8}\text{O}$ . Zinc has five stable isotopes, the prevalent ones are  $^{64}\text{Zn}$  (48.89%),  $^{66}\text{Zn}$  (27.81%), and  $^{68}\text{Zn}$  (18.57%), while oxygen consists primarily of  $^{16}\text{O}$  (99.76%). Zinc has the electron configuration  $(1s)^2 (2s)^2 (2p)^6 (3s)^2 (3p)^6 (3d)^{10} (4s)^2$ ; the oxygen configuration is  $(1s)^2 (2s)^2 (2p)^4$ .

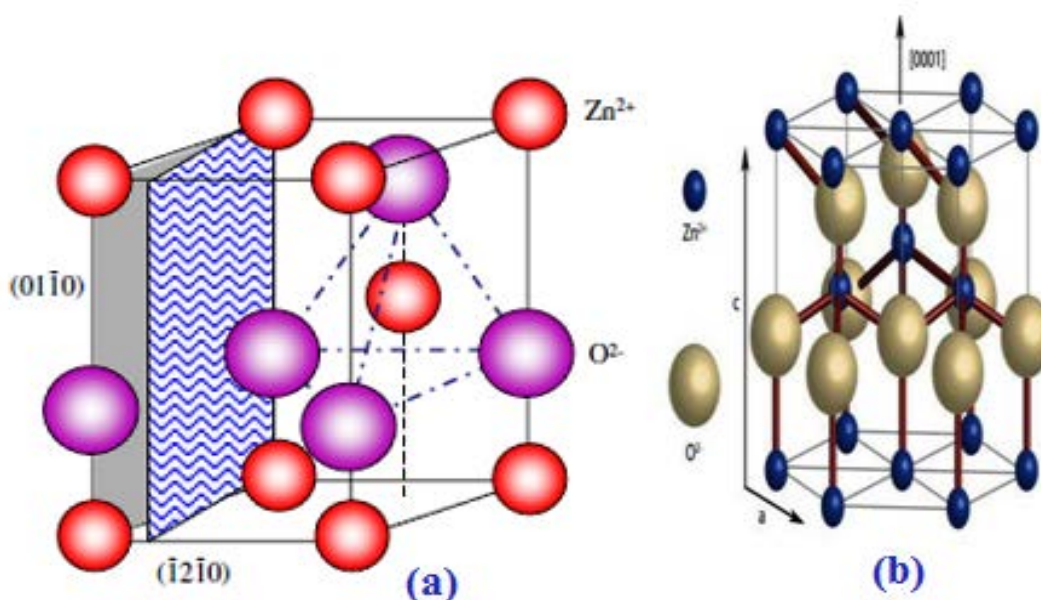


**Fig.1.3** (a) The hexagonal wurtzite structure model of ZnO, (b) The tetrahedral coordination of ZnO

The ZnO binding in its crystal lattice involves a  $sp^3$  hybridization of the electron states, leading to four equivalent orbitals, directed in tetrahedral geometry. In the resulting semiconducting crystal, the bonding  $sp^3$  state constitutes the valence band, while the conduction band originates from its anti-bonding counterpart. The resulting energy gap is 3.4 eV, i.e. in the UV spectral range, which has triggered interest in ZnO as a material for transparent electronics. The cohesive energy per bond is as high as 7.52 eV, which also leads to a very high thermal stability: The melting temperature  $T_m$  of ZnO is 2,242K. For

comparison, the melting temperature of ZnSe is considerably lower:  $T_m = 1,799\text{K}$  [36]. Zinc oxide normally has the hexagonal wurtzite (Fig 1.3) crystal structure. ZnO prepared via the flash evaporation method has the cubical crystal structure [39].

#### **1.4.2.2. Mechanical properties**

The mechanical properties of polycrystalline ZnO are of special importance for their applications as varistors. When a varistor experiences a high-current pulse, the electrical energy is quickly converted to heat. The inertia of the material, which resists its thermal expansion, and the resonances of the resultant elastic waves in the block, may lead to microcracks and finally to mechanical failure [40]. Characteristic values of mechanical properties of ZnO ceramics are 1.2-1.4 MPa for fracture toughness, and 100-125 MPa for flexural strength [36, 40].

#### **1.4.2.3. Thermodynamic properties**

Intrinsic point defects are deviations from the ideal structure caused by displacement or removal of lattice atoms. Possible intrinsic defects are vacancies, interstitials, and antisites. In ZnO, these are denoted as  $V_{zn}$  and  $V_o$ ,  $Zn_i$  and  $O_i$  and as  $Zn_o$  and  $O_{zn}$  respectively. There are also combinations of defects like neutral schotty (cation and anion vacancy) and Frenkel pairs (cation vacancy and interstitial), which are abundant in ionic compounds like alkali halides. As a rule of thumb, the energy to create a defect depends on the difference in charge between the defect and the lattice site occupied by the defect, e.g., in ZnO vacancy or an interstitial can carry a charge of  $\pm 2$  while an antisite can have a charge of  $\pm 4$ . This makes vacancies and interstitials more likely in polar compounds and antisite defects less important [36, 41].

#### **1.4.2.4. Optical properties**

Intrinsic optical properties of ZnO nanostructures are the focus of studies right now as they can be used for implementing photonic devices. As a part of these studies, Photoluminescence (PL) spectra of ZnO nanostructures have been widely reported. Excitonic emissions have been observed from the PL spectra of ZnO nanorods. It is shown that if we confine the quantum size then it can greatly enhance the exciton binding energy but an interesting observation is that the green emission intensity increases with a decrease in the diameter of the nanowires. This is because of the larger surface-to-volume ratio of thinner nanowires which favours a higher level of defects and surface recombination. Red



luminescence band has also been reported for which doubly ionized oxygen vacancies are considered responsible [41].

### 1.4.2.5. Electronic band structure

The band structure of a given semiconductor is pivotal in determining its potential utility. Consequently, an accurate knowledge of the band structure is critical if a particular semiconductor material is considered for device applications. Several theoretical approaches of varying degrees of complexity have been employed to calculate the band structure of ZnO for its wurtzite, zinc-blende, and rocksalt polytypes. Besides, a number of experimental data have been published regarding the band structure of the electronic states of wurtzite ZnO. X-ray or UV reflection / absorption or emission techniques have conventionally been used to measure the electronic core levels in solids. These methods basically measure the energy difference by inducing transitions between electronic levels (for example, transitions from the upper valence-band states to the upper conduction-band states, and from the lower valence-band states) or by exciting collective modes (for example, the upper core states to the lower edge of the conduction band and to excitations of plasmons). Another important method for the investigation of the energy region is based on the photoelectric effect extended to the x-ray region, namely, photoelectron spectroscopy (PES). The peaks in emission spectrum correspond to electron emission from a core level without inelastic scattering, which is usually accompanied by a far-less-intense tail region in the spectrum.

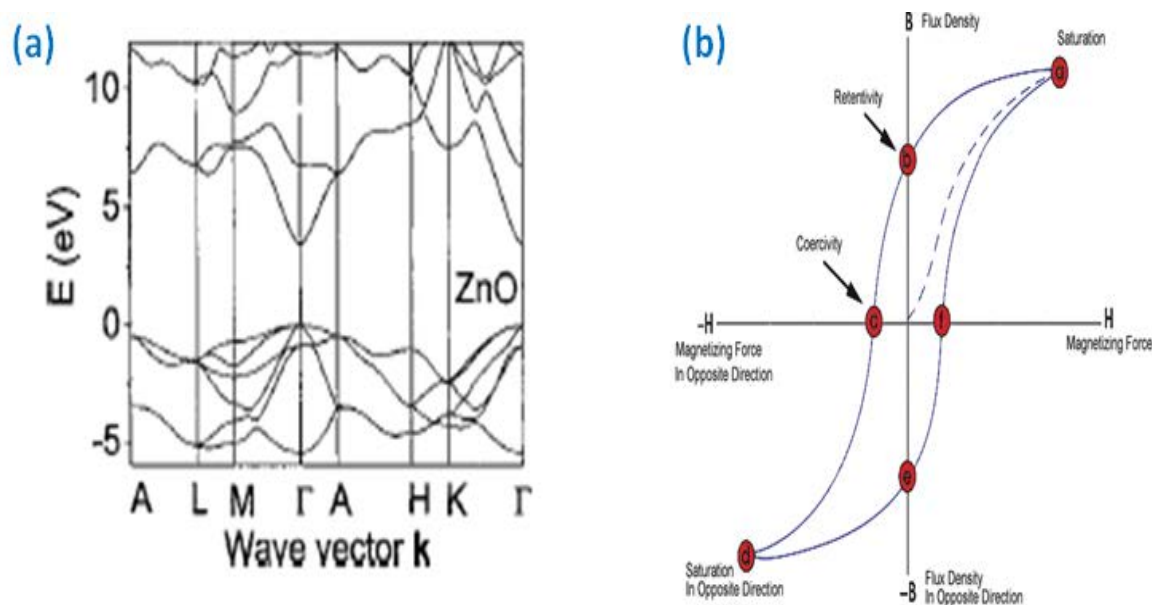


*Fig.1.4. (a) Band diagram and (b) Hysteresis loop or  $M$ - $H$  curve*

More recently, angle-resolved photoelectron spectroscopy (ARPES) technique has started to be used. This technique together with synchrotron radiation excitation has been recognized as a powerful tool that enables experimental bulk and surface electronic band structure determinations under the assumptions of k conservation and single nearly-free electron-like final band. Since ZnO is a direct gap semiconductor with the global extreme of the uppermost valence and the lowest conduction bands (VB and CB, respectively) at the same point in the Brillouin zone, namely at  $k = 0$ , i.e. at the  $\Gamma$ -point, we are mainly interested in this region. The lowest CB is formed from the empty 4s states of  $Zn^{2+}$  or the anti-bonding  $sp^3$  hybrid states. A typical representation of the band structure looks as in Fig 1.4(a) [42].

### 1.4.2.6. Physical properties

Physical properties for the main precursor material and the dopants used in this work are given in Table 2.2 [43].

**Table 1.3.** Physical properties for the main precursor material and the dopants used

Material	Crystal Structure	Atomic number Electron Configuration	Lattice Parameter 'a' Å	Lattice Parameter 'c' Å	Melting point in K	Ionic Radii Å
Zinc (Zn)	hcp	30 - $(1s)^2(2s)^2(2p)^6$ $(3s)^2(3p)^6(3d)^{10} (4s)^2$	2.66	4.95	692.7	0.74
Oxygen (O)	complex	8 - $(1s)^2(2s)^2(2p)^4$	-	-	54.36	1.4
Aluminium (Al)	fcc	13 - $(1s)^2(2s)^2(2p)^6$ $(3s)^2(3p)^1$	4.05	-	933.5	0.50
Cadmium (Cd)	hcp	48 - $(1s)^2(2s)^2(2p)^6$ $(3s)^2(3p)^6(3d)^{10}$ $(4s)^2(4p)^6(4d)^{10}(5s)^2$	2.98	5.62	594.3	0.97
Manganese (Mn)	cubic	25 - $(1s)^2(2s)^2(2p)^6$ $(3s)^2(3p)^6(3s)^2(3d)^5$	complex	-	1520	
Cobalt (Co)	hcp	27 - $(1s)^2(2s)^2(2p)^6$ $(3s)^2(3p)^6(3s)^2(3d)^7$	2.51	4.07	1770	0.78
Nickel (Ni)	fcc	28 - $(1s)^2(2s)^2(2p)^6$ $(3s)^2(3p)^6(3s)^2(3d)^8$	3.52	-	1728	0.55

### 1.4.3. Doped zinc oxide nanostructures

#### 1.4.3.1. N-type and P-type doping

When, ZnO nanostructures are grown, they are n-type due to structural defects from the growth process, such as oxygen vacancies, zinc interstitials and antisites. An antisite occurs when a nucleus of one species occupies a lattice site that is typically occupied by another species, such as a zinc atom on an oxygen site. A vacancy is an unoccupied lattice site, resulting in unsatisfied bonds within the lattice. An interstitial defect is formed by an interstitial atom that does not occupy a lattice site. Photoluminescence and temperature dependent Hall studies of electron irradiated ZnO have shown that Zn is the most likely candidate for purely lattice-related dominant shallow donor, with an activation energy about 30-50 meV [44]. The *p*-type doping in ZnO may be possible by substituting either group-I elements (Li, Na, and K) for Zn sites or group-V elements (N, P, and As) on O sites. It was found that group-I elements could be better *p*-type dopants than group-V elements in terms of shallowness of acceptor levels [45]. However, group-I elements tend to occupy the interstitial sites, due to their small atomic radii, rather than substitutional sites, and therefore, they act as donors instead of acceptors. Moreover, larger bond length for Na and K than ideal Zn–O bond length (1.93Å) induces lattice strain, increasingly forming native defects such as vacancies which compensate the shallow dopants.

### 1.5. Electronic nose

An electronic nose is a machine that is designed to detect and discriminate complex odors using sensor arrays. The sensor array consists of broadly tuned (non-specific) sensors that are treated with a variety of odor-sensitive biological or chemical materials. An odor stimulus generates a smellprint from the sensory array. Patterns or smellprints from known odors are used to construct a database and train a pattern recognition system so that unknown odors can subsequently be classified and identified. Electronic nose, as a complete instrument, would, therefore, consist of a few specific modules as shown in Fig.1.5 [46]. From the block diagram, it can be seen that an electronic nose system primarily consists of six functional blocks, viz., odour handling and delivery system, sensor array, the signal conditioning unit, data acquisition module, signal processing block and intelligent pattern analysis and recognition. The array of sensors is exposed to volatile odor vapours through suitable odour handling and delivery system, which ensures constant exposure rate to the sensors. The response signals of sensor array are conditioned and

processed through suitable circuitry and fed to the intelligent pattern recognition engine for classification, analysis and declaration of odour [47].

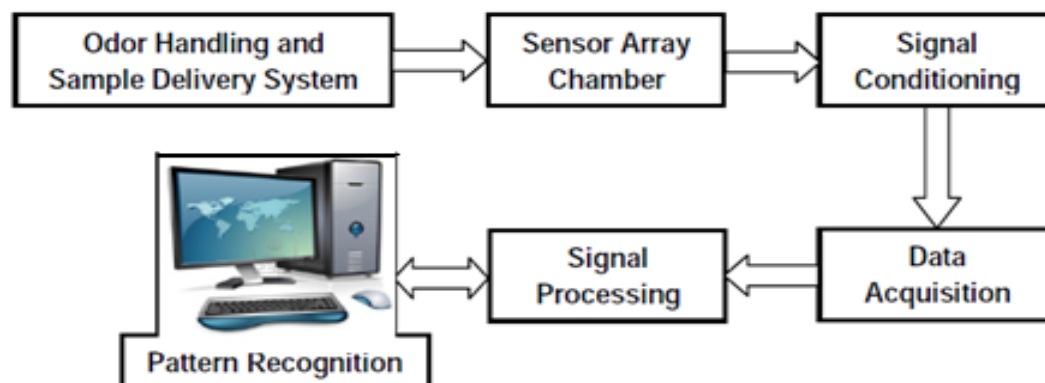


Fig.1.5. Block diagram of electronic nose

## 1.6. Gas sensors

A gas sensor is a transducer that detects gas molecules and which produces an electrical signal with a magnitude proportional to the concentration of the gas. Unlike other types of measurement, types that are relatively straightforward and deal with voltage, temperature, and humidity, the measurement of concentration of gases is much more complicated.

Table 1.2. Types, working principle and applications of gas sensors

Based on	Working principle	Applications
Metal oxide (chemo-resistors)	Detection principle of resistive sensors is based on change of the resistance of a semiconductor upon adsorption of the gas molecules on the surface.	<b>Automobiles</b> Car ventilation control, Gasoline vapour detection
Capacitance	Change in dielectric constant of nanostructure between the electrodes as a function of the gas concentration.	<b>Pollution control</b> SO <sub>x</sub> , NO <sub>x</sub> , CO, CO <sub>2</sub> etc. Halocarbons like CFC
Acoustic wave (sound based)	Uses piezoelectric material either in the nanostructure / bulk form which has one or more transducers on its surface.	<b>Food</b> Food quality control (Fruits, fishes freshness)
Calorimetric	Change in temperature at catalytic surfaces.	<b>Industrial production</b> Fermentation control Process control
Optical (speed of light)	Absorbance and fluorescence properties (analyte molecules or a chemo-optical transducing element).	<b>Medicine</b> Breath analysis, Disease detection
Electro-chemical	Oxidizing the target gas at an electrode and measurement of the resulting current.	<b>Defence sector</b> Chemical and biological warfare

Because there are literally hundreds of different gases, and there is a wide array of diverse applications in which these gases are present, each application must implement a unique set of requirements. For example, some applications may require the detection of one specific gas, while eliminating readings from other background gases. The necessity for new gas sensors, which can respond sensitively, selectively and quickly to a target gas, has accelerated research in this field and several research groups all over the world are working towards the development of gas sensors with new technologies and also for different applications. At present, there is a great deal of interest in the development of gas sensors for applications of air pollution monitoring, detection of harmful gases in mines, grading of agro-products like tea, coffee and spices, home safety, exhaust gas monitoring, hand held breath analyzers etc [48].

### 1.6.1. Working principle of metal oxide semiconductor (MOS) gas sensors

Metal oxide semiconductor (MOS) sensors use metal oxide based sensing thick films or nanostructure deposited on to a Si-micro-machined substrate. The electrodes attached with the sensor measure the resistance of the sensing layer. When oxygen in the atmosphere is adsorbed on the surface of the n-type semiconductor [49], the free electrons are trapped from the semiconductor and consequently a high resistive layer is formed in the vicinity of the surface. The reaction between reducing gas and oxygen generates electrons and thus increases the conductivity of the resistive layer as a result of increase in carrier concentration. This mechanism follows the reaction is written below:



where  $e$  is an electron,  $R(g)$  is reducible gas,  $s$  and  $g$  imply surface and gas respectively. MOS sensors are responsive to many reducible gases in the sensing environment and undergo change in resistance upon redox reaction between the gas and oxygen [50]. The sensor resistance value depends on the concentration of the reducible gases and their adsorption and desorption of gas to the sensor surface. The temperature of the sensor decides the level, type and rate of adsorption and desorption of the gas. At moderate concentrations, above the sensors' noise floor and below the saturation level of the sensor, resistance is related to the gas concentration as follows:

$$R_s = \frac{1}{AC^\alpha} \quad (1.3)$$

where,  $R_s$  is the resistance of the metal oxide sensors,  $C$  is the concentration of the gas,  $A$  and  $\alpha$  are the constants. The constants  $A$  and  $\alpha$  depend on the type of the reducing gas and the sensor temperature. The noise in the sensor heaters and the surface chemistry variation put limitations on this relationship at the lower end. At the upper end, increase in sensor surface temperature induced by exothermic reactions between the gas and the sensor surface produces changes in the above relationship. In a controlled environment, this relationship fits well to the gas concentrations between these high and low limits, although effects of diffusion, turbulent air flow and similar other factors are not considered in equations (1.1) to (1.3). The nature of sensor response significantly depends on operating temperature, amount of oxygen available on the sensor surface to be desorbed in the presence of reducible gases. Sometimes, the presence of impurities and catalytic metals like platinum or palladium increases the sensitivity and selectivity. Most commonly used semiconductor material as a gas sensor is pure and doped ZnO or SnO<sub>2</sub> with small amount of impurities and catalytic metal additives changes the selectivity of the sensors [51]. Operating temperature of the sensor is application specific and varies from 200°C to 400°C with satisfactory responses.

### 1.6.2. Role of sensor geometry and contacts

The sensor geometric parameters of length ( $L$ ) and width ( $W$ ) do not influence sensor response in most cases. The  $L/W$  ratio influences only sheet conductivity of the gas sensor (GS). As a rule, one needs to use inter-digital geometry of contacts as shown in Fig.1.6 (a) with small distance between contacts ( $L$ ) in order to get small sheet conductivity. Appropriate adjustment of these design parameters can achieve acceptable value of gas sensor resistance suitable for further electronic processing. Spill-over is a very important term in catalysis. It is used as a shorthand description of the diffusion of adsorbed species from an active adsorbent to an otherwise inactive support. In the area close to the contacts (spill-over zones), electrode materials act as catalysts to increase activity of gas-sensing metal oxide [52] shown in Fig.1.6 (b). The width of spill-over zone depends on the material and the nature of the detected gas. The influence of the contacts on sensor response with decreased length of the sensitive layer could become stronger because of another

reason as well. At some distance the resistance of the contact could be comparable in magnitude or more than the resistance of the gas sensitive layer, especially in the atmosphere of reducing gases (for  $n$ -type semiconductors) [53]. The potential barrier between the metal of the electrode and the gas-sensing oxide could be comparable to the potential barriers between the metal oxide grains. Under these circumstances, the chemical reactions between gas and metal–metal oxide interface could affect the total conductance of the sensor, even without the influence of the spill-over effect.

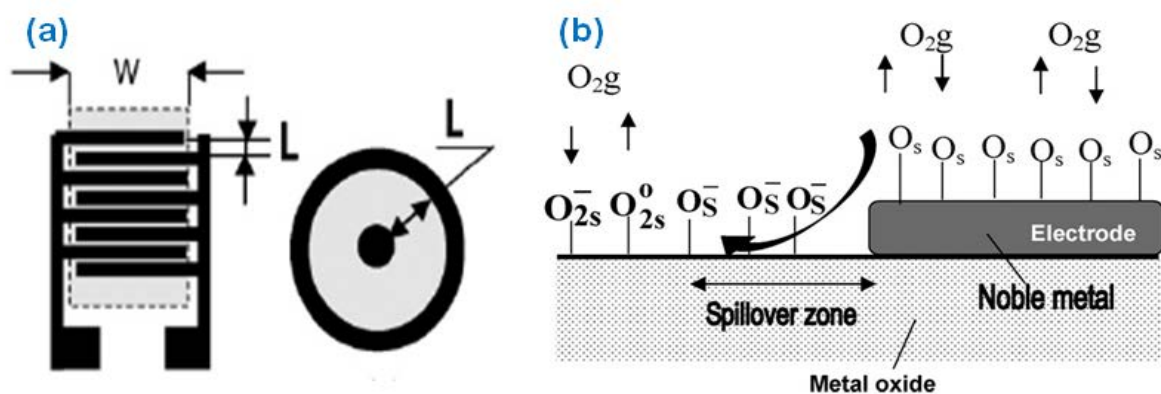


**Fig.1.6.** (a) Construction of solid-state metal oxide sensors and topologies of measurement contacts, (b) Spillover effect at the ZnO nanostructure surface at 180-210°C

### 1.6.3. Agglomeration

The agglomeration and aggregation of matter are ubiquitous phenomena expected to occur almost everywhere in nature. Their appearance ranges from metallic poly-crystals to colloidal aggregates and clusters, as well as lipid-protein visco-elastic matrices often called bio-membranes. In most cases the metal oxide films are agglomerated as well. One example of a ZnO nanostructured agglomerated sample is shown in Fig. 1.7. However, it is necessary to note that the role of agglomeration in gas-sensing has not been studied in detail yet. Mostly, an agglomeration problem exists either for thin films, or for ceramic and thick films sensors. It was established that in many cases synthesized powders agglomerate into big particles. FESEM images indicate that as a rule, the agglomerates formed during ceramic synthesis are more porous and have larger size than those formed by the methods of thin film technology. It is found that the agglomerate size of doped ZnO nanostructures, prepared by using the hydrothermal method does not exceed 50-100 nm. The gas-sensing matrix of agglomerated nanostructure chemo-resistive pellet can be schematically presented in Fig. 1.7. The gas-sensing matrix, we consider is a 3-D network of crystallites (grains) forming a gas-sensing film. Here  $R_{(a-a)}$  represents the resistance of inter-agglomerate

contacts,  $R_c$  is the resistance of inter-crystallite (inter-grain) contacts,  $R_b$  is the bulk resistance of the crystallites (grains), and  $R_{agl}$  is the resistance of the agglomerate. From this scheme, we observe that in gas-sensing matrix, we have four gas sensitive elements, which can affect the sensor response [51-53]. They are as follows:

- inter-grain (inter-crystallite) contacts;
- inter-agglomerate contacts;
- agglomerates; and
- grains.

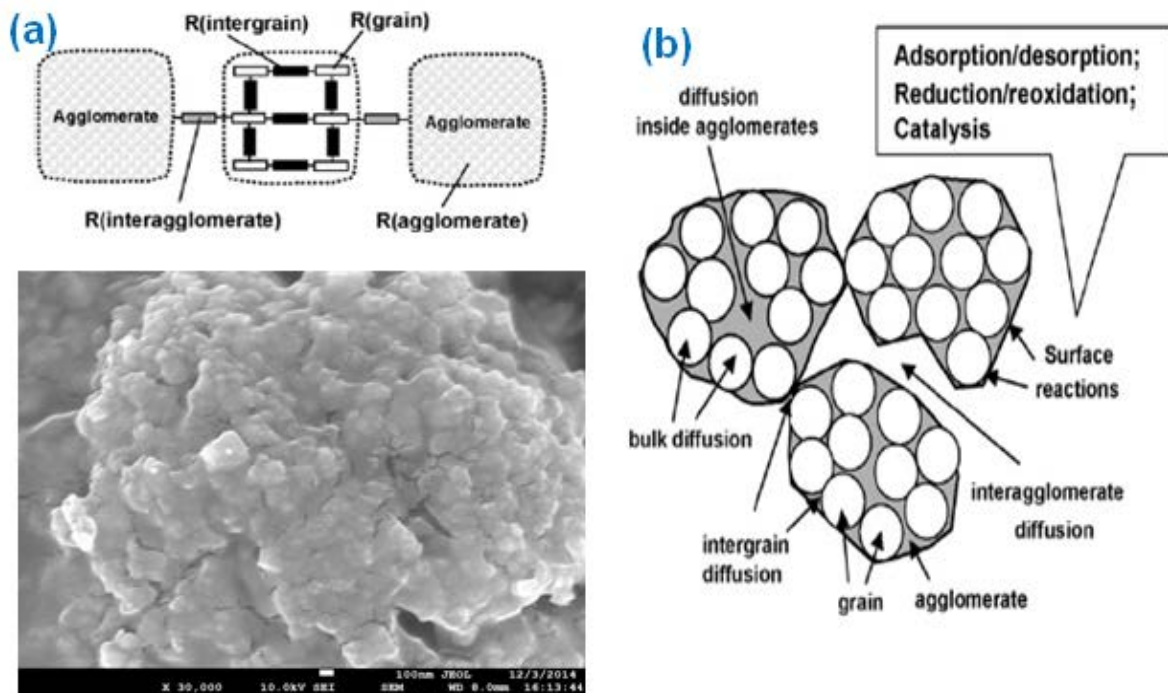


**Fig.1.7.** (a) FESEM image of Ni-Mo doped ZnO nanostructure (100nm) by chemical synthesis and diagrams illustrating peculiarities of electro-conductivity, (b) gas sensing reactions in chemo-resistive pellet sensor

Here, the agglomerate resistance is an integral resistance, representing a three-dimension grain network. Thus, it is seen that if there are alterations of the porosity of either agglomerates or the gas-sensing matrix, the role of above-mentioned gas-sensing elements on sensor response changes. For example, a decrease of grain size increases the role of grains in gas-sensing effects. A low gas-permeability of agglomerates promotes an increase in the influence of inter-agglomerate contact on sensor response.

#### 1.6.4. Effects of noble and transition metal element doping

In many gas sensors, the conductivity response is determined by the efficiency of catalytic reactions with detected gas participation, taking place at the surface of gas-sensing



material. Therefore, control of catalytic activity of gas sensor material is one of the most commonly used means to enhance the performances of gas sensors. Noble metals are very effective as oxidation catalysts and also increase the base resistance. Recently, research has shifted into transitional metals like (Fe, Co, Ni, Mn)-doped ZnO.  $[\text{Zn}_{(1-x)}\text{M}_x\text{O}]$  is one of the most promising dilute magnetic semiconductors (DMSs), which are envisioned as being promising building blocks for spintronic devices. Nevertheless, the chemical synthesis of  $(\text{Zn}_{1-x}\text{M}_x\text{O})$  nanomaterials is rather difficult as compared to that of pure ZnO. The properties of nanostructure are strongly dependent on their shapes and sizes. Therefore, the morphology-controlled synthesis of  $(\text{Zn}_{1-x}\text{M}_x\text{O})$  is very important for exploring the applications of these materials in spintronics, optics, catalysis, and so on [54, 55].

### 1.6.5. Effects of particle size

A sensor's sensitivity can be significantly increased by using materials with very small grain sizes. Sensitivity generally increases drastically if the particle diameter becomes smaller than 20 nm as shown in Fig.1.8 (a). For small grains and narrow necks, when the grain size is less than twice the thickness of surface charge layers, the grain is fully involved in the space-charge layer.

### 1.6.6. Effects of humidity and temperature

Environmental humidity is an important factor influencing the performance of metal oxide gas sensors. The reaction between the surface oxygen and the water molecules conduces to a decrease in baseline resistance of the gas sensor, and results in a decrease of the sensitivity.

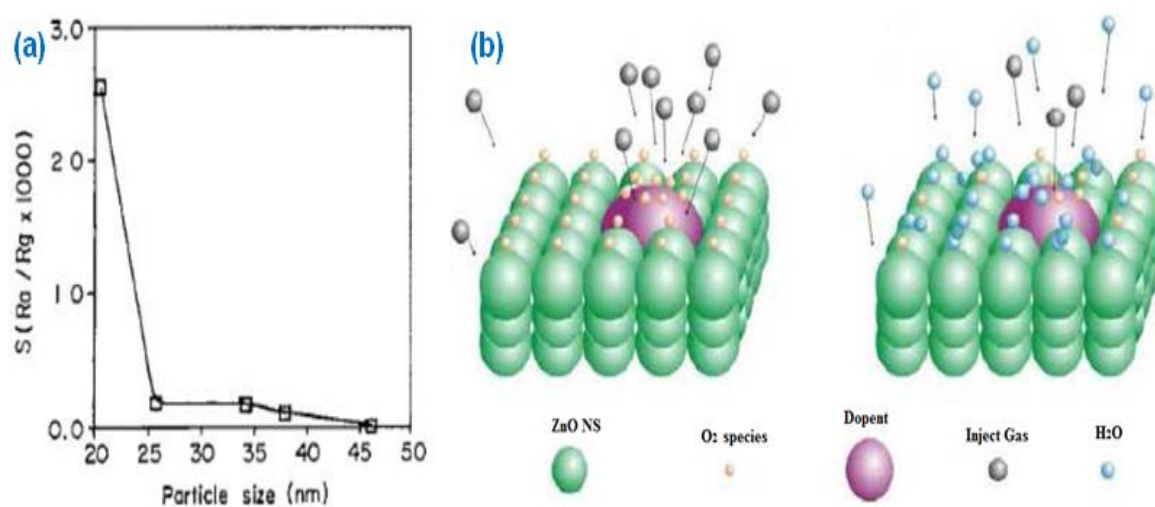


**Fig.1.8.** (a) Variation in sensitivity with average particle size, (b) Gas sensing mechanism of doped ZnO nanostructures in the atmosphere of injected gas

Secondly, the adsorption of water molecules leads to less chemisorption of oxygen species on the sensor surface due to the decrease of the surface area that is responsible for the sensor response. Fig. 1.8(b), it is shown that water adsorption will significantly lower the sensitivity of metal oxide gas sensors. Furthermore, prolonged exposure to humid environments leads to the gradual formation of stable chemisorbed OH<sup>-</sup> on the surface, causing a progressive deterioration of the sensitivity of gas sensors. However, surface hydroxyls start to desorb at about 400°C and the hydroxyl ions can be removed by heating to temperatures higher than 400°C. However, subsequent heating up the sensor to a temperature of 450°C for several minutes leads to a full recovery of the signal. Temperature is also an important factor for the metal oxide gas sensors. The responses increase and reach their maximums at a certain temperature, and then decrease rapidly with increasing the temperature and this property is commonly observed in many reports [56-58].

### 1.6.7. Basic gas sensing characteristics

In the literature, a number of gas sensing parameters such as gas response ( $R$ ), response time ( $\tau_{res}$ ), recovery time ( $\tau_{rec}$ ), analyte concentration, operating temperature, and detection limit for ZnO-based gas sensors are reported. These parameters are elaborated in this section.

#### 1.6.7.1. Gas Response

Gas response of a gas sensor is generally defined as the ratio of the resistance change on the surface of the gas sensor before and after being exposed to the gas analyte. It is mathematically expressed in different forms by different group of researchers as shown in the following equations:

$$R = \frac{R_g}{R_a} \quad (1.4)$$

$$R = \frac{R_g - R_a}{R_a} = \frac{\Delta R}{R_a} \quad (1.5)$$

$$R = \frac{R_g - R_a}{R_a} \times 100 = \frac{\Delta R}{R_a} \times 100 \quad (1.6)$$

$$R = \frac{I_0 - I_g}{I_g} = \frac{\Delta I}{I_g} \quad (1.7)$$

where,  $R_a$  is the sensor resistance in presence of ambient dry air and  $R_g$  the sensor resistance in the presence of target gas;  $I_0$  the reference value (baseline) of the ZnO nanostructures in dry air ambient and  $I_g$  the current of the ZnO nanostructures in the presence of target gas.

### 1.6.7.2. Response Time

Response time is the time taken by a gas sensor upon exposure to a target gas from the first reaction to the stable end value when the signal reaches a particular percent-age level (in general taken as 90% in many reports and is usually represented as  $T_{90}$ ). Further, lower the response time better are the sensing properties of the sensor. The response time is short for higher concentrations of target gases. Therefore, care should be taken for monitoring toxic gases at low concentrations as they may take a longer response time. In ZnO-based gas sensor, typical response time may be of the order of a minute or less. Other parameters which may affect the response time are flow rate, temperature, and pressure of the analyte gas.

### 1.6.7.3. Recovery Time

Recovery time is the time required by a sensor so as to return to 90% of the original baseline signal when the target gas is removed and the sensor is subsequently cleaned with dry air. For good sensor applications, sensor recovery time should be small so that the sensor can be used over and over again.

### 1.6.7.4. Selectivity

In general, the selectivity of a gas sensor material means the preferential chemiresistive sensing for a particular gas in the presence of another gas under similar operating conditions. The selectivity of ZnO-based nanostructures can be expressed as in equation (1.8).

$$\text{Selectivity} = \left[ \frac{\text{Sensitivity of the sensor toward interface gas}(S_i)}{\text{Sensitivity of the sensor toward target gas}(S_g)} \right] \quad (1.8)$$

### 1.6.7.5. Detection Limit

For high-performance sensor applications, sensor should be capable to detect even very low concentrations of the gases. The minimum concentration of analyte gas which can be detected by a sensor under operative conditions is called its lower detection limit. For nanostructured ZnO based gas sensors, reports of the lowest detection limit of  $\text{NO}_2$  gas are 50 ppb at 300 °C, 10 ppb at 250°C, and 100 ppb at 250°C [59, 60].

### 1.6.7.6. Stability and Recyclability

Stability of the sensor material refers to its ability to maintain its sensing properties repeatedly and even for long durations. ZnO nanostructures sensor exhibits relatively high response which drops with time due to interface modification during operation to a steady state. All these parameters depend on the nature, particle size and morphology of the sensing material, the type of interactions and reactions occurring between the gas and the sensor material, the sensor operating conditions, etc.

## 1.7. Nanostructured metal oxide gas sensors

The idea of using metal oxide semiconductors as gas responsive devices was instigated in 1952, while first reported the gas sensitivity of Germanium [61] and they observed that metal oxides were gas sensitive and they went ahead to demonstrate that ZnO could be used for the detection of inflammable and toxic gases. Unrelated but concurrent work was carried out by Taguchi and they introduced SnO<sub>2</sub> as the first commercially available metal oxide gas sensor in 1968 [62]. Since then, gas sensors using simple binary metal oxides, such as ZnO, SnO<sub>2</sub>, TiO<sub>2</sub>, WO<sub>3</sub>, Fe<sub>2</sub>O<sub>3</sub> and In<sub>2</sub>O<sub>3</sub> have been extensively investigated. Amongst them, SnO<sub>2</sub> is by far the most popular gas sensitive oxide. These metal oxides are n-type semiconductors; they possess an electron depleted surface under normal atmospheric conditions and in the typical operational temperatures range of 200-400°C. Thus complex multi component metal oxide based materials emerged as the next contender for sensor fabrication. When metal oxides are scaled down to nano-scale, surface properties like energy of adsorption and desorption, sticking coefficients, surface potential and crystallite barrier are expected to be significantly affected by new boundaries between grains and different chemical compositions. Now we know sensitivity of any sensor material is related to its grain size, surface morphology, surface area and internal porosity. Nanostructures have high surface to volume ratio, small particle size and low coordinated surface sites. Combined with gas sensing properties of thick or thin film metal oxides, nanostructured metal oxides make an excellent choice for sensor material. Xu et. al. proposed a model to relate the depletion layer of a metal oxide formed due to adsorption of oxygen [63] with the Debye length,  $L_D$ . The relation between  $L_D$  and sensitivity of the sensing material is given by Equation 1.9. Usually it is displayed through the so-called “dimension” effect e.g., a comparison of the grains size ( $d$ ) or necks width ( $X$ ) with the Debye length ( $L_D$ ).

$$L_D = \sqrt{\frac{\epsilon kT}{2\pi e^2 N}} \quad (1.9)$$

where,  $k$  is the Boltzmann constant,  $T$  is the absolute temperature in °K,  $\epsilon$  is the static dielectric constant of the material, and  $N$  is the concentration of charge carriers. The distribution of the potential along polycrystalline oxides for different  $d$ ,  $X$  and  $L_D$  is presented. It is clear that the width of the necks determines the height of the potential barrier for current carriers, while the length of the necks determines the depletion-layer width of the potential barrier. It has been found out that the sensor material shows maximum sensitivity when grain size is half of Debye length of the material which causes the depletion layer to spread through the grain [63, 64]. This causes depletion of mobile charge carriers leading to increase in resistance of sensor material. Such a condition will favour better gas sensitivity since any contact of the chemisorbed  $O_2^-$  with a reducing gas will result in a higher release of conduction electrons. Thus doped nanostructured ZnO metal oxide gas sensors which combine the gas sensing mechanism of metal oxides with the enhanced catalytic properties endowed by nanotechnology gives the opportunity to create excellent gas sensors [64, 65].

### 1.7.1. Metal oxide chemo-resistive gas sensors

Chemo-resistive gas sensors based on metal oxides have been used quite extensively for several applications. In comparison to other methods, e.g. gas chromatography (GC) and mass spectrometry (MS), such sensors offer several advantages such as simplicity, high miniaturization potential [65], low power and low cost production that make them extremely attractive. These sensors are based on the electrical properties of metal oxide semiconductors. Such chemo-resistive gas sensor films can be produced by a variety of techniques [64, 65] that may affect their sensing performance with respect to sensitivity, selectivity, reproducibility and long term stability [66]. For example, when a reducing gas like CO or H<sub>2</sub> comes in contact with the sensor's surface (Fig.1.9, receptor function), it changes the density of the ionosorbed oxygen. This is detected as a change in the sensor's conductance. Typically the sensing layer consists of single crystalline grains that are loosely connected (Fig.1.9 transducer function) so the target gas can diffuse through the porous sensing layer. The usual operating temperature of metal oxide gas sensors is from 200 to 500°C [67]. To avoid long term changes, metal oxide based gas sensors, should be operated at temperatures low enough so that significant bulk variations are prevented [68], and high enough so that gas reactions occur within the desired response time [69].

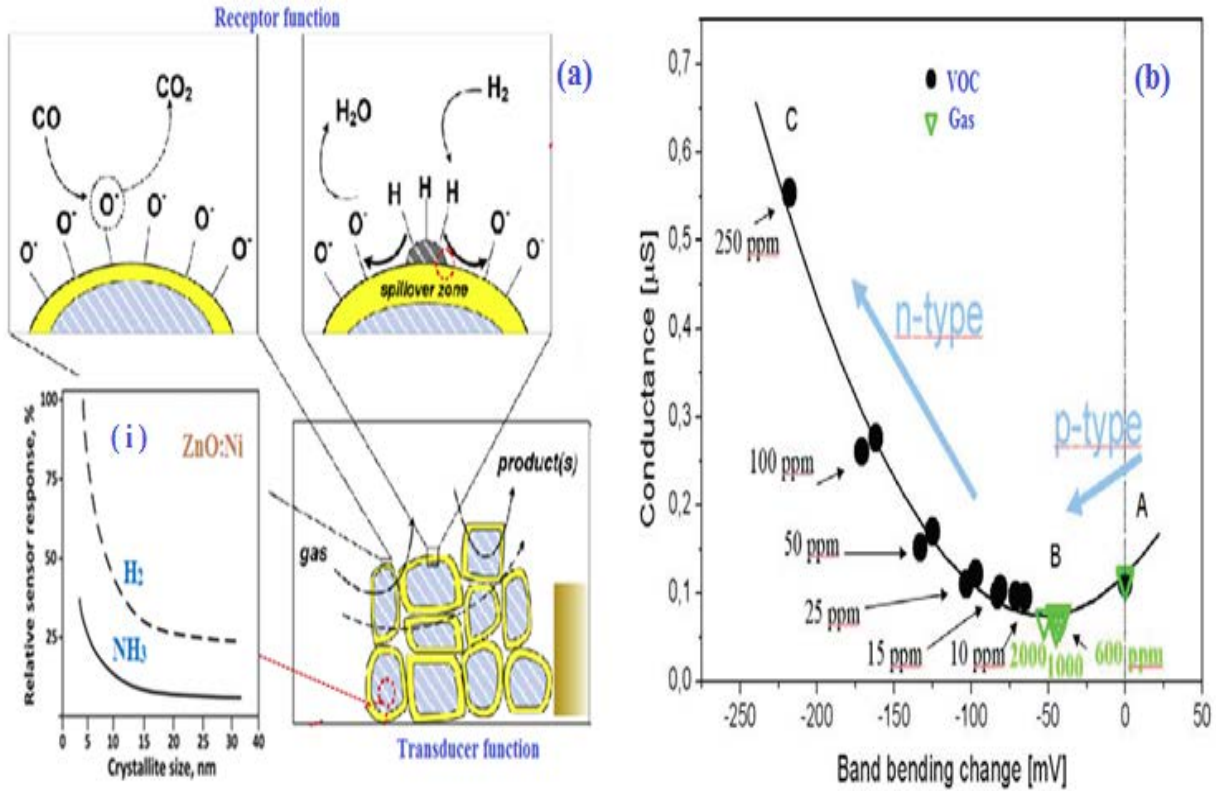


**Fig.1.9.** (a) Receptor and transducer function of a semiconductor gas sensor : Inset **Fig. (i)** ZnO:Ni sensor response as a function of crystal size and (b) The conductance of n-type ZnO sensor as a function of the band bending change determined by simultaneous work function and conductivity measurements at  $\approx 320^\circ\text{C}$

### 1.7.2. Inversion of type of conduction

For a n-type semiconductor, one records a change of conduction type at the surface because of the oxygen ionosorption [69]. This phenomenon brings about an inverted type of sensor response: the resistance increases during exposure to low concentrations of reducing gases and decreases when the concentrations are further increased. Fig. 1.9(b) shows the results of simultaneous measurements of DC electrical resistance and work function changes. We observe that there is a transition between dominant *p*-type conduction (AB region) to dominant *n*-type conduction (BC region). It is clear from that even if the effect of the reaction with the reducing gases could be kept same all the time, reducing the surface negative charge demonstrated by the decrease of the surface band bending, the electronic effect of change of conduction type determines different sensor signals. The presentation is clearly showing the importance of the conduction mechanism for the magnitude and, in special cases, even the direction of the sensor signal [70].

## 1.8. Objectives and scope of the thesis

The first version of electronic nose developed for tea quality estimation has many shortcomings, even though considerably good results have been reported due to the intelligent pattern recognition programs. The limitations of the Figaro, Japan make sensors; primarily the poor sensitivity and selectivity to tea aroma chemicals have inspired us to take up research work to make new sensors which will specifically respond more with the tea aroma bio-chemicals and tea samples. The first version electronic nose uses Figaro, Japan TGS gas sensors, for which the target vapours are VOCs like methanol, ethanol, propanol, and detection of ammonia, hydrogen, liquefied petroleum gas. None of them are tuned for the tea aroma bio-chemicals like Linalool, Linalool oxide, Trans-2-hexenal and Geraniol, etc.

In this thesis work, we have considered the nanostructured zinc oxide based gas sensors to be used in an electronic nose to have far better discrimination ability between the different varieties of tea. The advantages of nano-sensors are due to their particle size which is less than 100 nm and these nanostructures possess some unique properties compared to other bulk materials as already mentioned. Further, to improve the selectivity of the nanostructure sensors, it is doped with various noble and transition metals. The gas sensing performance of doped nanostructure sensor increases due to the catalytic activity of the doped metals at the sensor surface during reaction with reducing gases. An array of sensors, synthesized from different nanocrystalline materials having better affinity towards tea aroma chemicals have been used for this purpose. The result of the response of the sensor array is then used for the quality estimation of black tea aroma. Though gas sensor synthesized from nanocrystalline materials does not overcome all the limitations of MOS gas sensors, but they still provide a considerable improvement for gas detection. Further research regarding synthesis of specific nanostructured gas sensor towards detection of tea aroma chemical can boost the electronic sensing technology to a greater extent.

The objective of the present investigation is to establish the proposed chemical synthesis technique through preparation of various metal doped ZnO nanostructure samples that are listed below, followed by characterization of the powder and pellet samples including their respective properties. The objective may be summarized as follows:

Prepared nanostructure	Properties studied
<ul style="list-style-type: none"> <li>▪ Pure ZnO nanostructures calcined at 400°C and 600°C in 3 and 5 hours, respectively.</li> <li>▪ Transition metals (Co, Ni )-doped ZnO nanostructures</li> <li>▪ Noble metals (Pt, Pd, Mo, W, Cd )-doped ZnO nanostructures</li> <li>▪ Developed chemo-resistive pellet with the help of pellet making instrument for study their sensing characteristics.</li> </ul>	<ul style="list-style-type: none"> <li>▪ Synthesis and characterization</li> <li>▪ Structural and morphological properties</li> <li>▪ Optical, electrical and magnetic properties</li> <li>▪ Sensing characteristics in black tea biochemicals, linalool, linalool oxide, geraniol and, trans-2-hexenal, methanol, ethanol, propanol, and detection of ammonia, hydrogen, liquefied petroleum gas, etc.</li> </ul>

A brief chapter-wise organization of the thesis is presented below.

**Chapter 1** of the thesis makes a brief description about nanotechnology, nanostructures and their physical properties and characteristics. Brief description of electronic nose, gas sensor and nanostructured ZnO based pure and metal doped gas sensors, their applications and how the gas sensors have been used in electronic nose are presented. Metal oxide semiconductor based nanostructured gas sensors and their gas sensing mechanism are also illustrated in this chapter. The problem statement is defined and justified based on a short literature survey. A detailed literature survey on pure and metal doped ZnO nanostructure chemo-resistive sensors, chemical synthesis techniques, characteristics including their respective properties are also presented.

**Chapter 2** of this thesis is focused on ZnO nanostructures prepared by chemical synthesis route using ionic liquids. Chemical synthesis route is very simple, provides high ionic conductivity, high heat capacity, low toxicity and high dissolving capability.

**Chapter 3** portrays the characterization studies of the ZnO nanostructures by X-ray diffractometer (XRD), particle size analyzer (PSA), field emission scanning electron microscopy (FESEM), energy dispersive X-ray spectroscopy (EDAX), high resolution transmission electron microscopy (HRTEM), fourier transform infrared (FTIR)



spectroscopy and atomic force microscopy (AFM) for crystal structure, average particle size, shape, elemental compositions and morphology.

In **chapter 4**, investigation for the optical properties through UV-Vis spectrometry, photoluminescence (PL) emission, cathodoluminescence (CL), etc are presented. The characterization details of their electrical (current-voltage I-V and switching measurement) using semiconductor characterization system (SCS), superconducting quantum interferences device (SQUID), vibrating sample magnetometer (VSM) for magnetic (M-H curve, coercivity, saturation magnetization and remanence magnetization measurement at room temperature), magnetic force microscopy (MFM) for inside domain structures and configuration have been described with results and discussions.

**Chapter 5** deals with the experimental setup developed for the purpose of evaluating the sensor response towards the individual aromatic compounds of black tea aroma bio-compounds.

**Chapter 6** of the thesis makes a brief development of pure and metal doped ZnO nanostructure chemo-resistor pellet sensors for black tea aroma monitoring. The results and discussions with black tea biochemical compounds like linalool, linalool oxide, geraniol and, trans-2-hexenal. Also the results with volatile organic compounds like methanol, ethanol, propanol, and ammonia, hydrogen, liquefied petroleum gas are presented.

Finally, **chapter 7** sums up the major and important findings of the thesis work and concludes with the future direction of research scopes in the field of nanostructured sensors for electronic nose applications.

## References

- [1] J. Lozano, J. P. Santos, M. Aleixandre, I. Sayago, J. Gutierrez, M. C. Horrillo, Identification of typical wine aromas by means of an electronic nose, *IEEE Sensors Journal*, Volume 6, 2006, Pages 173-178.
- [2] C. D. Nucci, A. Fort, S. Rocchi, L. Tondi, V. Vignoli, F. D. Francesco, M. B. S. Santos, A measurement system for odor classification based on the dynamic response of QCM sensors, *IEEE Transactions on Instrumentation and Measurement*, Volume 52, 2003, Pages 1079-1086.

- [3] B. G. Kermani, S. S. Schiffman, H. T. Nagle, Performance of the Levenberg-Marquardt neural network training method in electronic nose applications, *Sensors and Actuators B: Chemical*, Volume 110, 2005, Pages 13-22.
- [4] D. D. H. Boothe, J. W. Arnold, Electronic nose analysis of volatile compounds from poultry meat samples, fresh and after refrigerated storage, *Journal of the Science of Food and Agriculture*, Volume 82, 2002, Pages 315-322.
- [5] M. O'Connell, G. Valdora, G. Peltzer, R. Martin Negri, A practical approach for fish freshness determinations using a portable electronic nose, *Sensors and Actuators B: Chemical*, Volume 80, 2001, Pages 149-154.
- [6] M. Pardo, G. Sberveglieri, Coffee analysis with an electronic nose, *IEEE Transactions on Instrumentation and Measurement*, Volume 51, 2002, Pages 1334-1339.
- [7] N. Barsan, M. Schweizer-Berberich, W. Göpel, Machine Olfaction: Electronic Nose Technology, *Fresenius Journal of Analytical Chemistry-Springer*, Volume 365, Issue 4, 1999, Pages 287- 304.
- [8] L. Buck, R. Axel, A novel multigene family may encode odorant receptors: a molecular basis for odor recognition, *Cell*, Volume 65, 1991, Pages 175-187.
- [9] K. Persaud, G. Dodd, Analysis of discrimination mechanisms in the mammalian olfactory system using a model nose, *Nature*, Volume 299, 1982, Pages 352 - 355.
- [10] I. B. Karki, J. J. Nakarmi, P. K. Mandal , S. Chatterjee, Study of Tea Aroma Based on ZnO Nanorod Sensing Element, *The Himalayan Physics*, Volume 3, 2012, Pages 1-5.
- [11] Ü. Özgür, A comprehensive review of ZnO materials and devices, *Journal of Applied Physics*, Volume 98, 2005, Pages 1-103.
- [12] H. Tang, M. Yan, X. Ma, H. Zhang, M. Wang, D. Yang, Ethanol sensing properties of PVP electrospun membranes studied by quartz crystal microbalance, *Sensors and Actuators B: Chemical*, Volume 113, Issue 1, 2006, Pages 324-328.
- [13] W. Shen, Y. Zhao, C. Zhang, The preparation of ZnO based gas-sensing thin films by ink-jet printing method, *Thin Solid Films*, Volume 483, 2005, Pages 382-387.
- [14] J. W. Gardner, P. N. Bartlett, A brief history of electronic noses, *Sensors and Actuators B: Chemical*, Volume 18, 1994, Pages 211-220.

- [15] R. W. Cattrall, *Chemical Sensors*, Oxford University Press, Oxford, 1997, Pages 1-2.
- [16] E. A. H. Hall, *Biosensors*, Open University Press, Milton Keynes, Buckingham, 1990, Pages 1-10.
- [17] K. C. Persaud, P. J. Travers, *Arrays of broad specificity films for sensing volatile chemicals*, CRC Press, Boca Raton, 1997, Pages 563–589.
- [18] D. L. Garcia-Gonzalez, R. Aparicio, *Sensors: From Biosensors to the Electronic Nose*, *Grasas y Aceites*, Volume 53, 2002, Pages 96-114.
- [19] D. James, S. M. Scott, Z. Ali, W. T. O'Hare, *Chemical sensors for electronic nose systems*, *Microchimica Acta-Springer*, Volume 149, 2005, Pages 1-17.
- [20] R. P. Feynman, *There's plenty of Room at the Bottom*, *Engineering and Science*, Volume 23, 1960, Pages 22-26.
- [21] N. Taniguchi, *On the basic concept of 'Nano-Technology'*, *Proceeding of International Conferences on Nano Technology*, London, Part II, British Society of Precision Engineering, 1974.
- [22] K. E. Drexler, *Molecular engineering: An Approach to the Development of General capabilities for Molecular Manipulation*, *Proceedings of the National Academy of Sciences*, Volume 78, Issue 9, 1981, Pages 5275-5278.
- [23] K. E. Drexler, *Engines of Creation: The Coming Era of Nanotechnology*, Anchor Press, New York, Volume 4, 1986.
- [24] G. Cao, *Nanostructures and Nanomaterials: Synthesis, Properties and Applications*, Imperial College Press, London, 2004.
- [25] A. Pathak, P. Pramanik, *Nano-Particles of Oxides through Chemical Methods*, *Proceeding of the Indian National Science Academy*, Volume 67, Issue 1, 2001, Pages 47-70.
- [26] H. Gleiter, *Nanocrystalline Materials*, *Progress in Materials Science-Elsevier*, Volume 33, 1989, Pages 223-315.
- [27] H. Lüth, *Surfaces and Interfaces of Solid Materials*, Springer-Verlag Berlin Heidelberg, Third Edition, 1995.

- [28] T. F. Barker, L. Fatehi, M. T. Lesnick, T. J. Mealey, R. R. Raimond, *Nanotechnology and the Poor: Opportunities and Risks for Developing Countries*, Nanotechnology and Society, Springer, Netherlands, 2008, Pages 243-263.
- [29] M. F. Garcia, A. M. Arias, J. C. Hanson, J. A. Rodriguez, *Nanostructured Oxides in Chemistry: Characterisation and Properties*, Chemical Review, Volume 104, 2004, Pages 4063-4104.
- [30] D. G. Rickerby, M. Morrison, *Nanotechnology and the Environment: A European Perspective*, Science and Technology of Advanced Materials, Volume 8, 2007, Pages 19-24.
- [31] H. A. Al-Abadleh, V. H. Grassian, *Oxide Surfaces as Environmental Interfaces*, Surface Science Reports, Volume 52, Issue 3-4, 2003, Pages 63-161.
- [32] G. Ertl, H. Knözinger, J. Weitkamp, *Hand book of Heterogenous Catalysis*, Weinheim, Wiley-VHC, Volume 5, 1997.
- [33] M. Bäumer, H. J. Freund, *Metal Deposits on well-ordered oxide films*, Progress in Surface Science, Volume 61, Issue 7-8, 1999, Pages 127-198.
- [34] M. L. Trudeau, J. Y. Ying, *Nanocrystalline Materials in Catalysis and Electrolysis: Structure Tailoring and Surface*, Nanostructured Materials, Volume 7, Issue 1-2, 1996, Pages 245-458.
- [35] M. Valden, X. Lai, D. W. Goodman, *Onset of Catalytic Activity of Gold Clusters on Titania with the Appearance of Nanometallic Properties*, Science, Volume 17, 1998, Pages 5501-5505.
- [36] R. Riedel, I. W. Chen, *Ceramics Science and Technology, Synthesis and Processing, Materials and Properties*, Heimann Sensor, Volume 2, 2010.
- [37] J. Han, P. Mantas, A. M. R. Senos, *Structural and electronic characteristics of pure and doped ZnO varistors*, Journal of the European Ceramic Society, Volume 22, 2002, Pages 49-54.
- [38] E. Klaus, A. Klein, *Transparent Conductive Zinc Oxide: Basics and Applications in Thin Films*, Materials Science-Springer, 2008.

- [39] T. Tanigaki, S. Komara, N. Tamura, C. Kaito, A comprehensive review of ZnO materials and devices, *Japanese Journal of Applied Physics*, Volume 41, 2002, Pages 041301-103.
- [40] L. Yaodong, L. Jianshe, Optical and electrical properties of aluminum-doped ZnO thin films grown by pulsed laser deposition, *Applied Surface Science*, Volume 253, Issue 7, 2007, Pages 3727-3730.
- [41] A. Vojta, D. R. Clarke, Mechanical Properties and Microstructure of Zinc Oxide nanostructures, *Journal of the American Ceramic Society*, Volume 80, 1997, Pages 2086-2092 .
- [42] H. K. Yadav, K. Sreenivas, V. Gupta, Influence of postdeposition annealing on the structural and optical properties of cosputtered Mn doped ZnO thin films, *Journal of Applied Physics*, Volume 99, 2006, Pages 083507-8.
- [43] B. B. Straumal, S. G. Protasova, A. A. Mazilkin, A. A. Myatiev, P. B. Straumal, G. Schütz, E. Goering, Ferromagnetic properties of the Mn-doped nanograined ZnO films, *Journal of Applied Physics*, Volume 108, 2010, Pages 073923-6.
- [44] A. A. M. Farag, M. Cavas, F. Yakuphanoglu, F. M. Amanullah, Area-Selective ZnO Thin Film Deposition on Variable Microgap Electrodes and Their Impact on UV Sensing, *Journal of Alloys and Compounds*, Volume 509, Issue 30, 2011, Pages 7900–7908.
- [45] R. Elilarassi, G. Chandrasekaran, Microstructural and photoluminescence properties of Co-doped ZnO films fabricated using a simple solution growth method, *Materials Science in Semiconductor Processing*, Volume 14, 2011, Pages 179-183.
- [46] S. C. Das, R. Bandyopadhyay, S. Ghosh, P. Pramanik, Fabrication of doped zinc oxide nanostructured sensor array in electronic nose for aroma estimation of CTC black tea and PCA clustering, *International Journal of Innovative Science and Applied Engineering Research*, Volume 13, Issue 40, 2014, Pages 8-18.
- [47] N. Bhattacharyya, R. Bandyopadhyay, M. Bhuyan, B. Tudu, D. Ghosh, A. Jana, Electronic Nose for Black Tea Classification and Correlation of Measurements with Tea Tester Marks, *IEEE Transactions on Instrumentation and Measurement*, Volume 57, Issue 7, 2008, Pages 1313-1321.

- [48] N. Barsan, D. Koziej, U. Weimar, Metal oxide based gas sensor research: how to?, *Sensors and Actuators B:Chemical*, Volume 121, 2007, Pages 18-35.
- [49] S. Pokhrel, C. E. Simion, V. Quemener, N. Bârsan, U. Weimar, Transduction in Semiconducting Metal Oxide Based Gas Sensors, *Sensors and Actuators B: Chemical*, Volume 133, 2008, Pages 1-78.
- [50] M. A. Cougule, S. Sen, V. B. Patil, Fabrication of nanostructured ZnO thin film sensor for NO<sub>2</sub> monitoring, *Ceramics International*, Volume 38, 2012, Pages 2685-2692.
- [51] N. V. Duy, N. V. Hieu, P. H. Huy, N. D. Chien, M. Thamilselvan, J. Yi, Mixed SnO<sub>2</sub>/TiO<sub>2</sub> Included with Carbon Nanotubes for Gas-Sensing Application, *Physica E*, Volume 41, 2008, Pages 258-263.
- [52] A. Gurlo, M. Sahn, A. Oprea, N. Barsan, U. Weimar, A p to n transition on  $\alpha$ -Fe<sub>2</sub>O<sub>3</sub>-based thick film sensors studied by conductance and work function change measurements, *Sensors and Actuators B: Chemical*, Volume 102, 2004, Pages 2-291.
- [53] M. Hübner, C. E. Simion, A. Tomescu-Stănoiu, S. Pokhrel, N. Bârsan, U. Weimar, Influence of humidity on CO sensing with p-type CuO thick film gas sensors, *Sensors Actuators B: Chemical*, Volume 153, 2011, Pages 2-347.
- [54] S. Gemming, R. Janisch, M. Schreiber, N. A. Spaldin, Density-functional investigation of the twin grain boundary in Co-doped anatase TiO<sub>2</sub> and its influence on magnetism in dilute magnetic semiconductors, *Physical Review B*, Volume 76, 2007, Pages 045204-10.
- [55] J. M. D. Coey, J. T. Mlack, M. Venkatesan, P. Stamenov, Magnetization Process in Dilute Magnetic Oxides, *IEEE Transactions on Magnetics*, Volume 46, Issue 6, 2010, Pages 2501-2503.
- [56] C. Wang, L. Yin, L. Zhang, D. Xiang, R. Gao, Metal Oxide Gas Sensors: Sensitivity and Influencing Factors, *Sensors*, Volume 10, 2010, Pages 2088-2106.
- [57] G. S. Devi, T. Hyodo, Y. Shimizu, M. Egashira, Synthesis of Mesoporous TiO<sub>2</sub>-Based Powders and Their Gas-Sensing Properties, *Sensors and Actuators B*, Volume 87, 2002, Pages 122-129.

- [58] A. Cabot, J. Arbiol, A. Cornet, J. R. Morante, F. Chen, M. Liu, Mesoporous Catalytic Filters for Semiconductor Gas Sensors, *Thin Solid Films*, Volume 436, 2003, Pages 64-69.
- [59] A. Mitra, R. K. Thareja, V. Ganesan, A. Gupta, P. K. Sahoo, V. N. Kulkarni, Pulsed laser deposited Al-doped ZnO thin films for optical applications, *Applied Surface Science*, Volume 174, Issue 3, 2001, Pages 232-239.
- [60] M. A. Chougule, S. Sen, V. B. Patil, Fabrication of nanostructured ZnO thin film sensor for NO<sub>2</sub> monitoring, *Ceramics International*, Volume 38, 2012, Pages 2685-2692.
- [61] T. Seiyama, A. Kato, K. Fujiishi, M. Nagatani, A New Detector for Gaseous Components Using Semiconductive Thin Films, *Analytical Chemistry*, Volume 34, Issue 11, 1962, Pages 1502-1523.
- [62] N. Taguchi, A Metal Oxide Gas Sensor, Japanese Patent 45-38200, 1970.
- [63] C. Xu, J. Tamaki, N. Miura, N. Yamazoe, Correlation between Gas Sensitivity and Crystallite Size in porous SnO<sub>2</sub>-Based Sensors, *Chemistry Letters*, Volume 19, Issue 3, 1991, Pages 441-444.
- [64] D. E. Williams, Semiconducting oxides as gas-sensitive resistors, *Sensors and Actuators B: Chemical*, Volume 57, 1999, Pages 1-16.
- [65] N. Barsan, U. Weimar, Conduction Model of Metal Oxide Gas Sensors, *Journal of Electroceram*, Volume 7, 2001, Pages 3-143.
- [66] M. Hübner, C. E. Simion, A. T. Stănoiu, S. Pokhrel, N. Bârsan, U. Weimar, Influence of humidity on CO sensing with p-type CuO thick film gas sensors, *Sensors and Actuators B: Chemical*, Volume 153, 2011, Pages 347-353.
- [67] J. C. Kim, H. K. Jun, J. S. Huh, D. D. Lee, Tin Oxide-Based Methane Gas Sensor Promoted by Alumina-Supported Pd Catalyst, *Sensors and Actuators B*, Volume 45, 1997, Pages 271-277.
- [68] E. Traversa, Ceramic Sensors for Humidity Detection: The State of the art and Future Developments, *Sensors and Actuators B*, Volume 23, 1995, Pages 135-156.

- [69] H. Ogawa, M. Nishikawa, A. Abe, Hall Measurement Studies and an Electrical Conduction Model of Tin Oxide Ultrafine Particle Films, *Journal of Applied Physics*, Volume 53, 1982, Pages 4448-4455.
- [70] C. Xu, J. Tamaki, N. Miura, N. Yamazoe, Grain Size Effects on Gas Sensitivity of Porous SnO<sub>2</sub> Based Elements, *Sensors and Actuators B*, Volume 3, 1991, Pages 147-155.



# Chapter 2

## Synthesis of pure and doped ZnO nanostructures

In this work, we have prepared pure and metal doped zinc oxide nanostructures by chemical synthesis route from pyrolysis of zinc acetate dihydrate  $[\text{Zn}(\text{CH}_3\text{CO}_2)_2 \cdot 2\text{H}_2\text{O}]$  solution with diethanolamine (DEA) with adequate dopant. After complete dehydration of the precursor solution, a black, carbonaceous, mesoporous fluffy mass is obtained, which after calcinations produces the desired nanostructured materials. The sources of dopants are Cobalt nitrate hexa-hydrate, Nickel nitrate hexahydrate, Manganese acetate, Platinum tetrachloride, Palladium tetrachloride, Ammonium heptamolybdate tetrahydrate, Ammonium para tungstate and Cadmium acetate. The amount of dopants is about 1 wt % to 10 wt % or higher based on ZnO for gas sensing materials or catalyst coatings.

### *List of sections*

- 2.1. Introduction
  - 2.1.1. Chemical vapour deposition (CVD)
  - 2.1.2. Chemical bath deposition (CBD)
  - 2.1.3. Pulsed laser deposition (PLD)
  - 2.1.4. Sol-gel method
  - 2.1.5. Hydrothermal method
  - 2.1.6. Reported methods for the nanostructured precursor powders
- 2.2. Metal ion-ligand complex based precursor solution method
- 2.3. Synthesis of ZnO nanostructures by chemical method
  - 2.3.1. Raw materials used
  - 2.3.2. Experiment
  - 2.3.3. Synthesis of pure nanostructured ZnO
  - 2.3.4. Synthesis procedure
  - 2.3.5. Synthesis of metal doped ZnO nanostructures
- 2.4. Metal organic complex decomposition
  - 2.4.1. Characterisation techniques of the prepared nanostructured powders
  - 2.4.2. Calcination, sintering and pellet formation
- 2.5. Conclusion
- References

### *Contents of this chapter are based on following publications:*

1. S. C. Das, R. Bandyopadhyay, S. Ghosh, P. Pramanik, Fabrication of doped zinc oxide nanostructured sensor array in electronic nose for aroma estimation of CTC black tea and PCA clustering, *International Journal of Innovative Science and Applied Engineering Research*, Volume 13, Issue 40, 2014, Pages 8-18.
2. S. C. Das, B. Tudu, N. Bhattacharya, R. Bandyopadhyay, P. Pramanik, Doped ZnO Nanostructured Sensor in Electronic Nose for Detection of Ammonia, Hydrogen and Liquefied Petroleum Gas, *Advanced Nanomaterials and Nanotechnology*, Springer-Verlag Berlin Heidelberg, Chapter 47, 2013, Pages 473-482, DOI: 10.1007/978-3-642-34216-5(47) (Online).
3. S. C. Das, S. Ghosh, B. Tudu, N. Bhattacharyya, R. Bandyopadhyay, P. Pramanik, Development of Nanostructured ZnO based Gas Sensors to use in Electronic Nose for Biochemical Compounds in Black Tea, ICST-2012, IEEE, ID-2591147, Pages 93-94, DOI: 10.1007/978-1-4673-2248-5/12 (Online).



# Chapter 2

## Synthesis of pure and doped ZnO nanostructures

### 2.1. Introduction

Zinc oxide (ZnO) is a semiconducting material having direct wide band gap of 3.37 eV and high excitonic binding energy of 60meV at room temperature. These features make it a promising material for transparent electronics, solar cells and other optoelectronic devices [1]. Growth of ZnO nanostructures such as one-dimensional rods, wires, tubes etc., has received increasing attention for its specific properties and for the fabrication of nanoscale devices. Many different techniques were employed for the growth of nanostructure; these include vapour-liquid-solid (VLS) epitaxy [2], chemical vapour deposition (CVD)[3], pulse laser deposition (PLD), thermal decomposition, hydrothermal synthesis [4], etc. There are two basic approaches involved in the synthesis of metal oxide nanoparticles or nanostructure; i.e., bottom-up and top-down approaches [5]. Both approaches are schematically represented in Fig. 2.1. All the solution based chemical methods for syntheses of oxides belong to the bottom-up approach. It involves building up of nanostructure through stacking of the fundamental building-blocks which can be atom-by-atom, or molecule-by-molecule, or cluster-by-cluster.

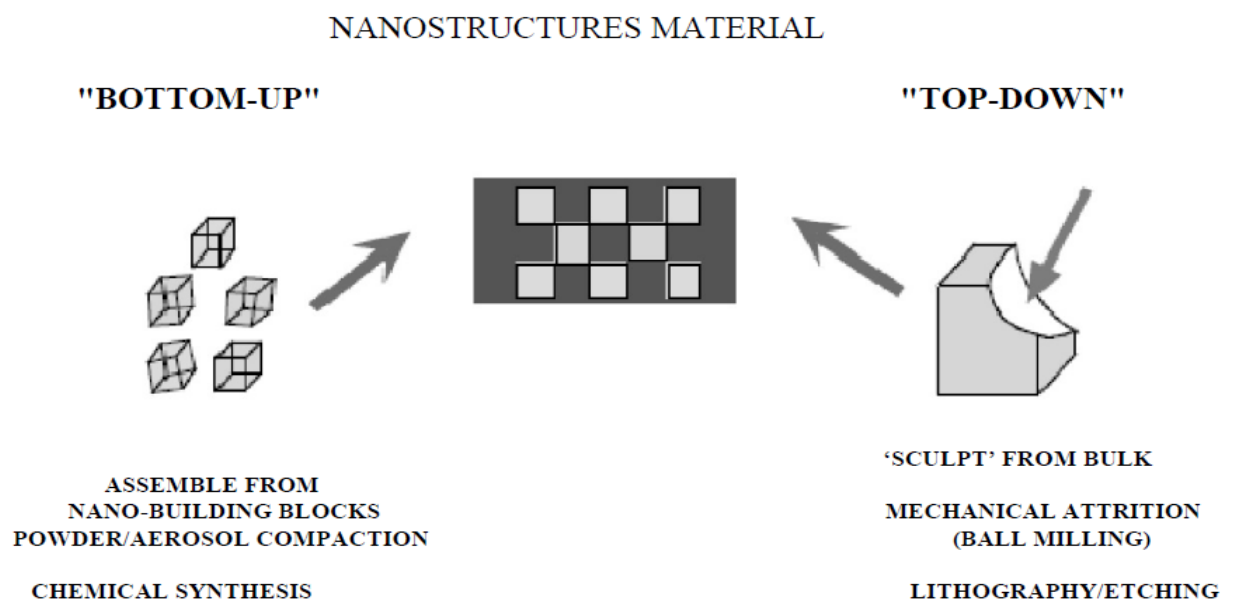


*Fig.2.1. Schematic illustration for Bottom-up and Top-down approach*

However, top-down approach leads to the formation of nanostructure by breaking down bulk materials gradually into smaller sizes until the grains in the nanometric dimension are obtained. Thermal or mechanical attrition or millings of the bulk material are typical examples of this approach [6]. Although, the top-down approach of synthesis of oxides offers reliability and is suitable for fabrication of complex device components, they are constrained by higher energy usages, and greater waste generation compared to the bottom-up approach. Moreover, the conventional top-down approach such as, lithography results in imperfection in the surface structure and introduces additional defects at the etching step. Despite of these disadvantages, the top-down strategy till date remains as a significant approach for the synthesis of oxide nanoparticles. Bottom-up approach is the most common approach for synthesis of nanomaterials. It can be classified into three major heads, depending upon the techniques of processing; they are chemical synthesis, self-assembly, and positional assembly.

- Chemical synthesis is a method which essentially involves production of raw materials, such as, molecules or particles, which can either be used directly in products with their bulk disordered form, or as the building blocks of more advanced ordered materials, produced using the self assembly, and positional assembly techniques.
- Self assembly is a bottom-up synthesis technique in which atoms or molecules arrange themselves spontaneously under equilibrium conditions into ordered and stable nano-scaled structures by physical or chemical interactions between the units.
- In the final bottom-up technique, atoms, molecules or clusters are deliberately manipulated and positioned one-by-one.

Bottom-up approach promises a better chance to obtain nanostructure with less defects, high chemical homogeneity and long range ordering. Bottom-up approach is driven mainly by the reduction of Gibbs free energy, so that the produced nanoparticles are closer to thermodynamic equilibrium. Solution based chemical synthesis techniques are among the most common and crucial bottom-up synthesis strategies available for the synthesis of nanostructured powders, especially for the multi-component oxide systems. Most popularly known chemical synthesis routes [7] available for the preparation of nanostructured mixed oxides include: co-precipitation, solvo-thermal / hydrothermal, sol-gel, micro-emulsion and solvent evaporation methods. A few research reports on common chemical synthesis

techniques for the preparation of nanostructures mixed with oxide powders are summarized below.

### 2.1.1. Chemical vapour deposition (CVD)

In this method, films are deposited at 150-350°C at a rate of typically 0.70 nm/s. They exhibit low resistivity ( $<10^{-3}$   $\Omega$ -cm), high transmittance in the visible wavelength region ( $>80\%$ ) and a rough surface texture. The crystallite size and surface roughness increase with increasing deposition temperature and flow of argon gas [8].

### 2.1.2. Chemical bath deposition (CBD)

ZnO thin films are fabricated using six different complexing agents, namely ammonia, hydrazine, ethanolamine, methylamine, triethanolamine and dimethylamine by chemical bath deposition (CVD) method. The developed films were mainly ZnO<sub>2</sub> with a band gap around 4.3 eV. Films annealed at 400°C were identified as ZnO with a band gap around 3.3 eV. X-ray diffraction and micro-Raman spectroscopy revealed that the films consist mainly of cubic zinc peroxide that was transformed into hexagonal ZnO after annealing. High-resolution transmission electron microscopy (HRTEM) showed small variations of the order of 10 nm in film thickness which corresponds to the average grain size. A high carrier density ( $2.24 \times 10^{19}$ )  $\text{cm}^{-3}$  and a low resistivity ( $6.48 \times 10^{-1}$ )  $\Omega$ -cm were obtained for the films annealed at 500°C in argon ambient [9].

### 2.1.3. Pulsed laser deposition (PLD)

In this method the forms and properties of ZnO nanostructures can be grown on Si (111) surface and *c*-plane sapphire (*c*-Al<sub>2</sub>O<sub>3</sub>) substrates using three different growth processes: metal organic chemical vapor deposition (MOCVD), pulsed laser deposition (PLD), and physical vapor transport (PVT). Wide variety ZnO nanostructures can be observed, including nanorods, nanoneedles, nanocombs as shown in Fig 2.2(a-b) and some novel structures resembling 'bevelled' nanowires. PVT gave the widest family of nanostructure. PLD gave dense regular arrays of nanorods with a preferred orientation perpendicular to the substrate plane on both Si and *c*-Al<sub>2</sub>O<sub>3</sub> substrates, without the use of a catalyst [10].

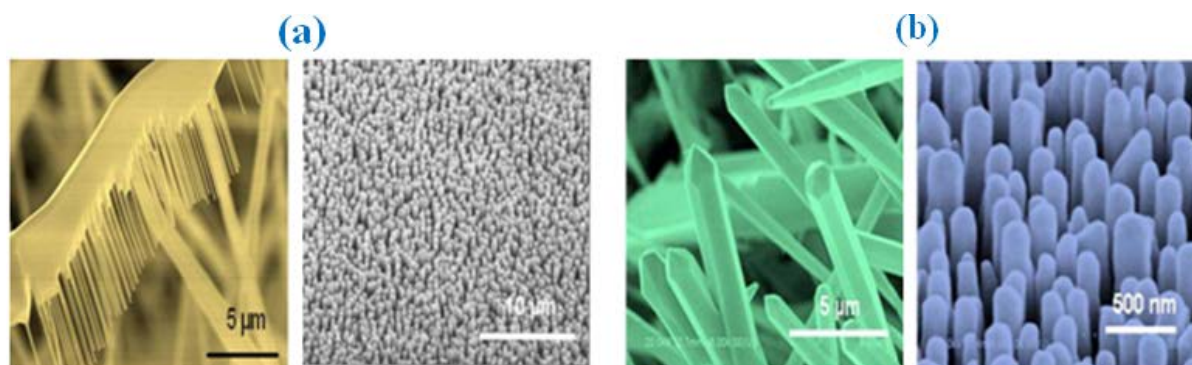


**Fig.2.2.** SEM images of ZnO nanostructures grown by (a) PLD on Si (111) and (b) PVT on Si (111)

#### 2.1.4. Sol-gel method

The fabrication of ZnO thin films are done by sol-gel method using  $\text{Zn}(\text{CH}_3\text{COO})_2 \cdot 2\text{H}_2\text{O}$  as starting material in order to prepare an acetone gas sensor. A homogeneous and stable solution was prepared by dissolving the zinc acetate in a solution of ethanol and ethanolamine. The sol-gel solution was coated on alumina substrates with various thicknesses by spin coating technique. The effect of thickness on physical and electrical properties of deposited ZnO thin films has been studied. The deposited ZnO thin films were characterized by X-ray diffraction spectroscopy, field emission scanning electron microscopy and atomic force microscopy. The root mean square surface roughness values are increased with increasing thickness of the films. The activation energies of the films were calculated from the resistance temperature characteristics. The sensitivities of the ZnO films towards the acetone gas were determined at an operating temperature of  $200^\circ\text{C}$ . The sensitivity towards acetone vapour strongly depends on the surface morphology of the ZnO thin films [11].

#### 2.1.5. Hydrothermal method

Syntheses of aligned ZnO nanorods are carried out by a simple hydrothermal method without calcination. A seed layer of zinc acetate ( $\text{ZnAc}_2$ )/sodium dodecyle sulfate (SDS) nanocomposite was used for the nucleation of ZnO nanorods. First, a  $\text{ZnAc}_2$ /SDS composite was deposited on a Si substrate by spin-coating. And then, ZnO nanorods were grown under hydrothermal conditions at  $90^\circ\text{C}$ . ZnO crystals were grown in the direction of c-axis perpendicular to the surface of the Si substrate. However, nucleation did not occur on the substrate of a  $\text{ZnAc}_2$  seed layer without SDS, indicating that the presence of the  $\text{ZnAc}_2$ /SDS seed enhanced the nucleation of ZnO crystals. These results show that high

dispersion of  $\text{ZnAc}_2$  in the nanocomposite effectively assists a nucleation of ZnO crystals [12].

### 2.1.6. Reported methods for the nanostructure precursors powders

It has been reported a chemical synthetic route for the preparation of various nanosized metal doped tungstate powders starting from a polymer based metal-complex precursor solution [13]. Also the novel chemical route for the preparation of nano crystalline (average particle size around  $\sim 20$  nm), single phase  $\alpha\text{-Al}_2\text{O}_3$  powder are synthesized [14]. However, due to high temperature and pressure of the reaction process, the direct formation of pure and metal doped ZnO nanostructures via hydrothermal process has not been commercially exploited.

*Table 2.1.1D-Nanostructured ZnO: morphology, methods of preparation, size and other growth parameters,[16-24]*

Morphology	Synthetic method	Growth reagents	Substrate	Anne. Temp. ( $^{\circ}\text{C}$ )	Anne. Time (in h)	Particle size (in nm)	
						Diameter	Length
<i>Nanorods</i>	Hydrothermal	$\text{Zn}(\text{NO}_3)_2 \cdot 6\text{H}_2\text{O}$ , HMTA	Glass	500	2	30-120	250
<i>Nanorods</i>	Hydrothermal	$\text{Zn}(\text{NO}_3)_2 \cdot 6\text{H}_2\text{O}$ , HMTA	Alumina	–	–	100	1.62 $\mu\text{m}$
<i>Nanosheets</i>	Electrochemical deposition	$\text{ZnCl}_2$ , KCl	Porous silicon	–	–	200	700
<i>Flower-like nanorods</i>	PEG-assisted hydrothermal	$\text{Zn}(\text{CH}_3\text{COO})_2$ , PEG	–	600	4	52	3 $\mu\text{m}$
<i>Nanowires</i>	Carbothermal reduction	ZnO/C	$\text{SiO}_2/\text{Si}$	–	–	80-120	10 $\mu\text{m}$
<i>Nanolines</i>	Sol-gel method	$\text{Zn}(\text{CH}_3\text{CO}_2)_2$ , $2\text{H}_2\text{O}$ , DEA	–	700	1	Nanoline gap between 100 and 400 nm	
<i>Nanobelt</i>	RF sputtering	ZnO	Sapphire	–	–	10	50
<i>Nanoneedles</i>	Low-temp. hydrothermal process	$\text{Zn}(\text{CH}_3\text{CO}_2)_2 \cdot 2\text{H}_2\text{O}$ , HMTA	Glass	–	–	15	300
<i>Nanoprisms</i>	Sol-gel method	$\text{Zn}(\text{CH}_3\text{CO}_2)_2 \cdot 2\text{H}_2\text{O}$ , PVA	$\text{Al}_2\text{O}_3$	700	–	25	100–500
<i>Nanofibers</i>	Electrospinning methods	$\text{Zn}(\text{CH}_3\text{CO}_2)_2 \cdot 2\text{H}_2\text{O}$ , PVA	–	400, 700	–	–	–
<i>Nanotubes</i>	Hydrothermal method	$\text{ZnCl}_2$ , methenamine	Silicon (100) wafer	400	6	200	–

The synthesis of nitrogen doped multilayer graphene (NDMLG) by chemical process using simple precursors is carried out and its electro catalytic activities for the determination of ascorbic acid, uric acid and dopamine in a mixture are analyzed [15]. Pure and metal doped ZnO has been prepared and investigated by a number of groups where the reported structure for the system predominantly is wurtzite. The reported methods for the synthesis of ZnO nanoparticles are combustion method, simply known as thermal decompositions. Some of the reported methods for the synthesis of ZnO nanoparticles are summarized below. The materials are very appropriate for various applications. Varieties of morphologies for ZnO have been synthesized using various physical and chemical methods explained in this section. A number of methods are reported in literature for the fabrication of 1-D ZnO nanostructures for gas sensors. For the growth of 1-D ZnO nanostructures, processing details are summarized in Table 2.1.

## 2.2. Metal ion-ligand complex based precursor solution method

The synthesis method involves pyrolysis of aqueous based precursor solution that comprises of water-soluble, metal ion-ligand complexes of the desired metal ions in the requisite molar ratios. The complexing /chelating agents generally used for obtaining the water-soluble, metal ion-ligand complexes are triethanolamine (TEA), oxalic acid, ethylene-diamine-tetra-acetic acid (EDTA) and tartaric acid.

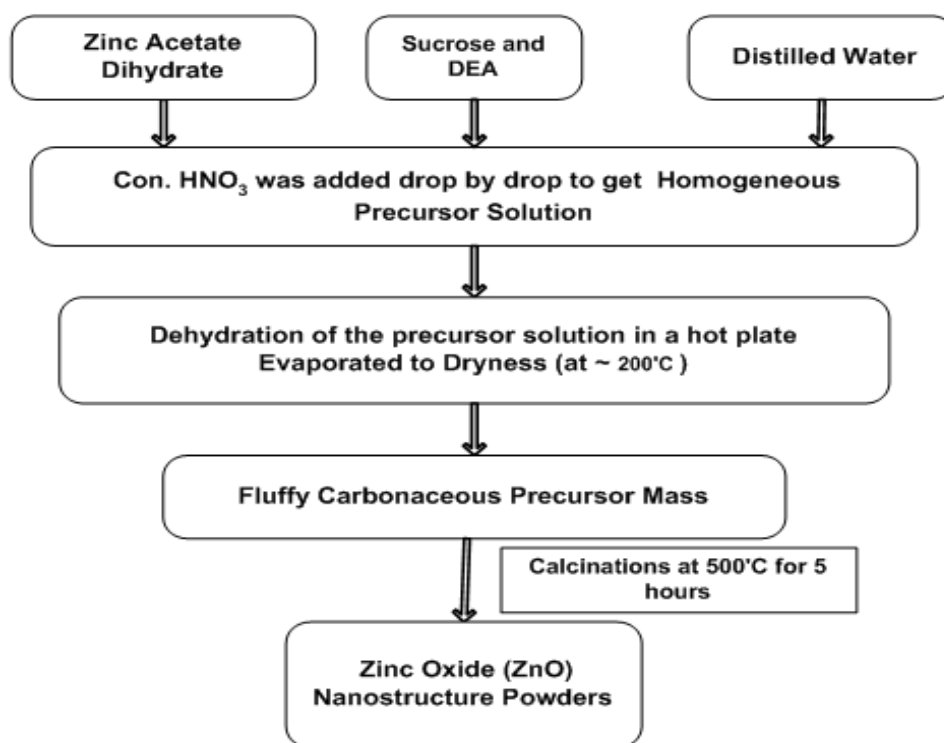


**Fig.2.3.** Schematic representation of the preparation of pure ZnO nanostructured powders



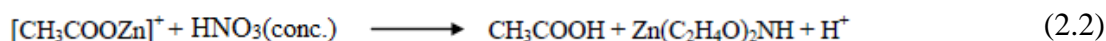
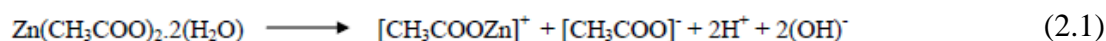
The complexing/chelating agents are used to keep the metal ions in homogeneous solution throughout the reaction without undergoing precipitation. To ensure this, the moles of the complexing/chelating agent per unit mole of the metal ion in the starting solution are always kept in excess. The choice of the appropriate organic acid as the complexing agent is based on the solubility of the resulting complex in water. The synthesis method involves the complete dehydration of the metal complexes. The decomposition results in a voluminous, organic based black fluffy mass. This organic mass is easily crushed to fine powders to get the precursor powders [25]. A generalized process for the preparation of the nanostructured mixed oxides through the metal ion-ligand complex based precursor solution method by flow diagram is shown in Fig. 2.3. A photograph of a voluminous, organic based, black, fluffy mass [26], obtained through the process is depicted in Fig. 2.4.



*Fig. 2.4. Black carbonaceous fluffy mass*

### **2.3. Synthesis of ZnO nanostructures by chemical method**

In our work, we have used the simple process for the preparation of nanostructured ZnO preparation; Water soluble zinc acetate dihydrate as a starting material, diethanolamine (DEA) as stabilizer, and (70%) conc.  $\text{HNO}_3$  were used. The thermal decomposition of Zinc acetate dihydrate takes place at  $300^\circ\text{C}$ . It is simple and cost effective process for the preparation of ZnO nanostructure materials. In this process  $[\text{CH}_3\text{COOZn}]^+$  ion,  $[\text{CH}_3\text{COO}]^-$  ion,  $\text{H}^+$  ion, and  $(\text{OH})^-$  ion are produced from hydrolysis of zinc acetate dihydrate and presented in equation (2.1). The reaction process of  $\text{HNO}_3$  (conc.) with the  $[\text{CH}_3\text{COOZn}]^+$  complex is given in equation (2.2). The ZnO nanostructure is synthesized from the decomposition of  $\text{Zn}(\text{C}_2\text{H}_4\text{O})_2\text{NH}$  after heat treatment.



ZnO nanoparticles are produced from the reaction between zinc acetate dihydrate and sucrose by using diethanolamine (DEA) as a stabiliser [27]. It is a catalyst free process and applicable for the uniform growth of nanostructured ZnO. The structural, optical, electrical and magnetic properties of the synthesized ZnO show strong dependency on reaction conditions, such as choice and concentration of surfactant used and reaction time. Powder X-ray diffraction (PXRD) of the sample showed that the average particle size of the crystal was ~ 40 to 56 nm. The chemical composition of the synthesized pure and metal doped ZnO nanostructures have been characterized through energy dispersive X-ray analysis (EDAX) and Fourier transform infrared (FTIR) spectroscopy was used for determination of the chemical structure of materials by revealing the characteristics frequencies of functional group.

### 2.3.1. Raw materials used

**Table 2.2.** Raw materials used for the preparation of pure and metal doped nanostructured ZnO

Chemicals	Formula	Molar mass (g/mol)	Density (g/cm <sup>3</sup> )	Soluble in water	Physical state
Zinc acetate di-hydrate	Zn(CH <sub>3</sub> COO) <sub>2</sub> ·2H <sub>2</sub> O	219.50	1.735 at (20°C)	soluble	solid
Zinc nitrate hexa-hydrate	Zn(NO <sub>3</sub> ) <sub>2</sub> ·6H <sub>2</sub> O	297.49	2.065 at (20°C)	soluble	solid
Cobalt nitrate hexa-hydrate	Co(NO <sub>3</sub> ) <sub>2</sub> ·6H <sub>2</sub> O	291.04	1.87 at (20°C)	soluble	solid
Nickel nitrate hexa-hydrate	Ni(NO <sub>3</sub> ) <sub>2</sub> ·6H <sub>2</sub> O	290.79	2.05 at (25°C)	soluble	solid
Manganese acetate	(CH <sub>3</sub> COO) <sub>2</sub> Mn·4H <sub>2</sub> O	245.087	1.59 at (25°C)	soluble	solid
Platinum tetrachloride	PtCl <sub>4</sub>	336.89	2.43 at (25°C)	soluble	solid
Palladium tetrachloride	PdCl <sub>4</sub>	177.33	4.0 at (25°C)	soluble	solid
Ammonium hepta-molybdate tetra-hydrate	(NH <sub>4</sub> ) <sub>6</sub> Mo <sub>7</sub> O <sub>24</sub> ·4H <sub>2</sub> O	1235.86	2.49 at (20°C)	soluble	solid
Ammonium para tungstate	(NH <sub>4</sub> ) <sub>6</sub> W <sub>7</sub> O <sub>24</sub>	3132.20	3.3 at (25°C)	Soluble	solid
Cadmium acetate dihydrate	(CH <sub>3</sub> COO) <sub>2</sub> Cd·2H <sub>2</sub> O	266.52	2.01 at (20°C)	soluble	solid
Diethanolamine (DEA)	C <sub>4</sub> H <sub>11</sub> NO <sub>2</sub>	105.14	1.097 at (20°C)	soluble	liquid

Triethanolamine (TEA)	$C_6H_{15}NO_3$	149.19	1.124 at (20°C)	soluble	liquid
Sucrose	$C_{12}H_{22}O_{11}$	342.29	1.59	soluble	solid
Nitric acid (70%)	$HNO_3$	63.02	1.42 at (20°C)	soluble	liquid
Polyvinyl alcohol	PVA	44.05	1.26 at (25°C)	soluble	solid

All the chemicals of analytical grade were purchased from Merck Specialties Pvt. Ltd., India, and used without further purification. All the required aqueous solutions were prepared using de-ionised (millipore) water ( $<16M\Omega cm^{-1}$ ) received from Merck Millipore system.

### 2.3.2. Experiment

In this work, we have prepared pure and metal doped nanostructured zinc oxide by chemical synthesis route from pyrolysis of zinc acetate dihydrate [ $Zn(CH_3CO_2)_2 \cdot 2H_2O$ ] solution with diethanolamine (DEA) with adequate dopant. After complete dehydration of the precursor solution, a black, carbonaceous, mesoporous fluffy mass is obtained shown in Fig.2.4, which after calcination produces the desired nanostructured material. The compound sources of dopants are Cobalt nitrate hexa-hydrate, Nickel nitrate hexahydrate, Manganese acetate, Platinum tetrachloride, Palladium tetrachloride, Ammonium heptamolybdate tetrahydrate, Sodium tungstate dehydrate and Cadmium acetate. The amount of dopants is about 1-15wt % or higher based on ZnO for gas sensing materials or catalyst coatings. The experiments were carried out at room temperature ( $25 \pm 2^\circ C$ ).

### 2.3.3. Synthesis of pure nanostructured ZnO

The present study describes the chemical synthesis of ZnO nanomaterials through a metal ion ligand complex based precursor route, using water soluble zinc acetate dehydrate, diethanolamine (DEA) and sugar. In this process, the aqueous metal ion ligand complex precursor solution is obtained by mixing aqueous solution of zinc acetate dehydrate, diethanolamine and sucrose in the required amount. The precursor solution is then pyrolysed to voluminous carbonaceous mass through oxidative decomposition of the metalo-organic complexes. This solid precursor is calcined to obtain the nanostructured powders of ZnO.

### 2.3.4. Synthesis procedure

First 200 ml of 0.25 (M) Zinc acetate dihydrate which is the precursor is prepared. The amount of solute, i.e., Zinc acetate dihydrate required is calculated from the formula as given below.

$$X = M * M.W.*V \quad (2.3)$$

where,  $X$  = weight in grams of solute required,  $M$  = required molarity of solution,  $M.W.$  = molar weight in g/mol,  $V$  = volume of solvent required.

Using this formula the calculated amount of solute is 10.5 g in 200 ml of solvent. 200 ml of 0.25 (M) precursor solutions is prepared and DEA is added to it with constant stirring, and the metal ion to DEA molar ratio is maintained at 1:4. Addition of DEA to the solution causes precipitation. Then (70%) conc.  $\text{HNO}_3$  as oxidising agent is added drop wise and the pH of the solution is maintained between 3-4 for mild acidic. After the addition of required amount of nitric acid, a clear homogeneous precursor solution is obtained. Another set of a clear solution of zinc acetate dihydrate is prepared by dissolving 10.5g of zinc acetate dehydrate in 200 ml di-ionised water [28]. We have prepared four different set of samples by varying the amount of DEA and sugar in each sample as shown in Table 2.3.

**Table 2.3.** Crystallite size of synthesized pure ZnO nanostructure in different compositions

Zinc acetate dihydrate	Sucrose and DEA	Calcinations	Crystallite size
10.5 g in 200 ml de-ionised water	9g sucrose and 1ml DEA	500°C for 4 hours	64.2 nm
10.5 g in 200 ml de-ionised water	9g sucrose and 1ml DEA	600°C for 4 hours	62.8 nm.
10.5 g in 200 ml de-ionised water	7g sucrose and 3ml DEA	500°C for 4 hours	60.2 nm
10.5 g in 200 ml de-ionised water	7g sucrose and 3ml DEA	600°C for 5 hours	56.4 nm

The resulting solution is the DEA complex of Zn ion which is completely dehydrated at 110°C using a hot plate. On complete dehydration the precursor decomposes to form a black, fluffy mass as shown in Fig. 2.4. The black fluffy mass is then crushed into powders. Calcinations of these carbonaceous precursor powders at 500°C for 4h produce carbon free white coloured nanostructured powders of ZnO in the wurtzite form. The method for preparation of nanostructured powders of ZnO is schematically depicted in Fig. 2.3. In this work we have prepared pure and metal doped zinc oxide nanostructures by chemical synthesis route from pyrolysis of zinc acetate dihydrate [ $\text{Zn}(\text{CH}_3\text{CO}_2)_2 \cdot 2\text{H}_2\text{O}$ ] solution with diethanolamine (DEA) with appropriate dopant [29]. The compound sources of dopants were cobalt nitrate hexa-hydrate, nickel nitrate hexahydrate, manganese acetate, platinum

tetrachloride, palladium tetrachloride, ammonium hepta-molybdate tetrahydrate, ammonium para tungstate and cadmium acetate. The amount of dopants was about 1 wt % to 10 wt % or higher based on ZnO for gas sensing materials or catalyst coatings.

### 2.3.5. Synthesis of metal doped ZnO nanostructures

According to equation (2.3), the required solute, molarity of solution and volume of solvent for preparing the precursor solution are calculated. The method for preparation of metal doped ZnO nanostructure powders in (general formula:  $Zn_{1-x}M_xO$ ), where (M= Ni, Co, Mn, Pt, Pd, Mo, W and Cd) is schematically depicted in Fig. 2.5. The chemical and structural properties of the doped metals are presented in Table 2.4.

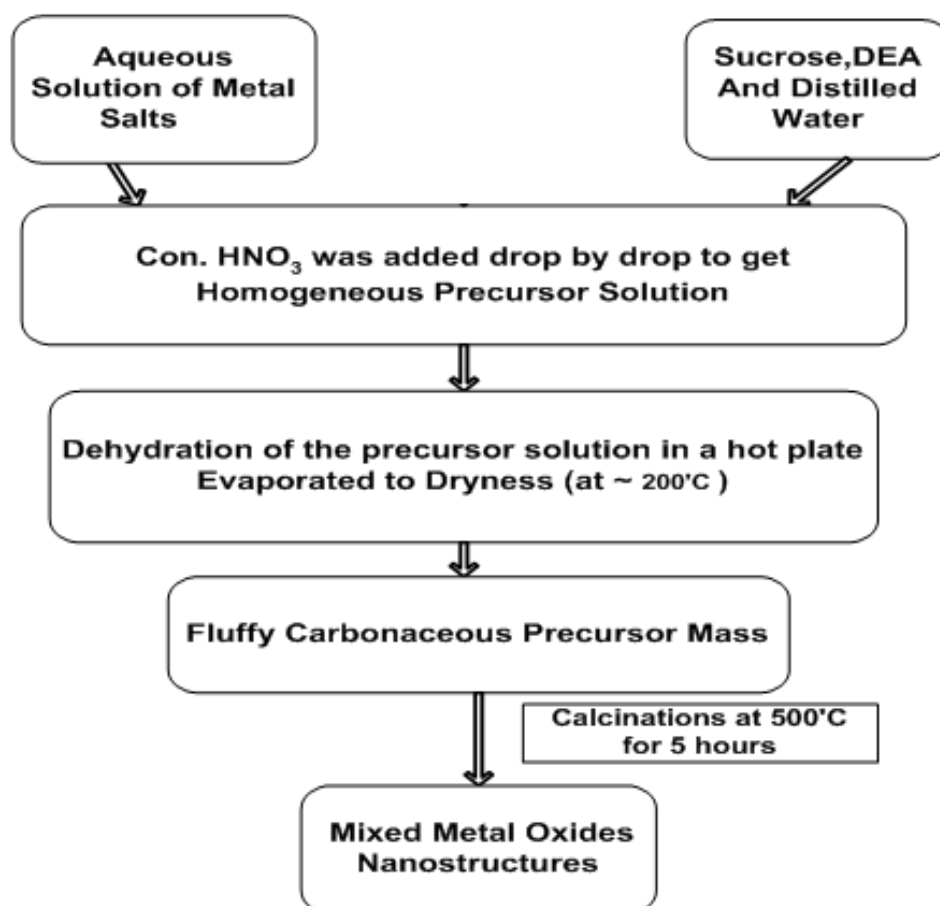


*Fig.2.5. Schematic representation of the preparation of metal doped ZnO nanostructure powders*

## 2.4 Metal organic complex decomposition

For the synthesis of  $(Zn_{1-x}W_xO)$  nanostructures, an aqueous solution of 10g of zinc acetate dihydrate and 10g of sucrose was prepared initially. Then 4ml of diethanolamine was added under constant stirring to obtain white, highly viscous solution. Concentrated Nitric acid was then added drop wise to obtain a clear solution with pH value close to 3-4

for mild acidic. For tungsten (W) doping, we have added calculated mass of sodium tungstate dihydrate (calculated such that molar ratios are W: Zn = 0.05:1, 0.1:1, 0.15:1 and 0.2:1 for 5, 10, 15 and 20 percent doping respectively) to excess conc. nitric acid to obtain bright yellow precipitate of zinc tungsten oxide ( $ZnWO_4$ ). After that the precipitate was thoroughly washed and dissolved overnight in 7ml of triethanolamine at 70°C. This clear solution was mixed with the solution of zinc acetate and di-ethanolamine and pH close to 3-4 was again obtained by adding a few drops of conc.(70%)  $HNO_3$ . Now the solution was transferred into a beaker and kept on a hotplate at 110°C. In approximately half an hour, dense black fumes emerging from the solution burns into a black fluffy mass. This is known as metal-organic complex decomposition [30].

**Table 2.4.** Chemical and structural properties of doped metals

Properties	Metals name							
	Cobalt (Co)	Nickel (Ni)	Manganese (Mn)	Platinum (Pt)	Palladium (Pd)	Molybdenum (Mo)	Tungsten (W)	Cadmium (Cd)
Density (g/cm <sup>3</sup> )	8.9	8.90	7.43	21.4	12.0	10.2	19.3	8.65
Atomic number	27	28	25	78	46	42	74	48
Atomic weight	58.93	58.71	54.93	195.1	106.4	95.94	183.85	112.41
Melting point(°C)	1495	1453	1245	1772	1552	2617	3410±20	320.9
Boiling point (°C)	2870	2732	1962	3827	2927	4612	5660	765
Oxidation state	+3,+2	+3,+2	+7,+6,+4 ,+3,+2	+4,+2	+4,+2	+6,+5,+4,+ 3, +2	+6,+5,+4, +3,+2	+2
Ionisation potential(volts)	7.86	7.63	7.435	9.0	8.34	7.099	7.98	8.993
BondRadius(Å)	1.16	1.15	1.17	1.3	1.28	1.3	1.3	1.48
Electronegativity	1.88	1.91	1.55	2.28	2.2	2.16	2.36	1.69
Stable isotope No.	1	5		5	6	7	5	7
Electronic configuration	[Ar]3d 7 4s2	[Ar]3d 8 4s2	[Ar]3d5 4s2	[Xe]4f1 4 5d9 6s1	[Kr]4d10	[Kr]4d5 5s1	[Xe]4f14 5d4 6s2	[Kr]4d10 5s2

### 2.4.1. Characterisation techniques of the prepared nanostructured powders

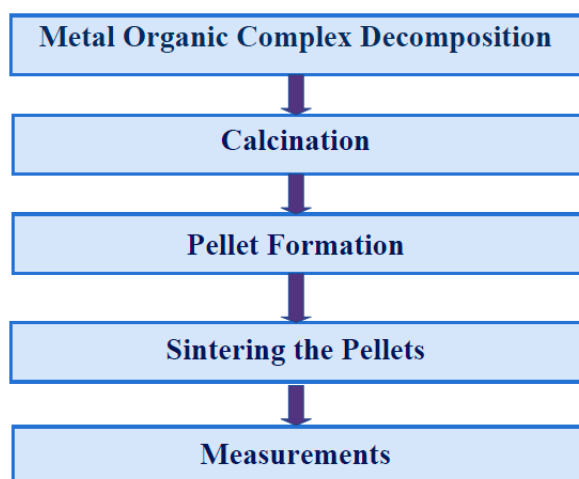
The prepared nanostructured powders have been characterized through powder XRD and FESEM to understand their particle size, porosity and surface morphology. The surface

morphology of the nanostructure is studied by Scanning electron microscopy (SEM) and Field emission scanning electron microscopy (FESEM). The surface of the ZnO powder showed hexagonal wurtzite structure [31]. The diameter of the nanostructure are of the order of 40-70nm. The optical properties of the samples are studied by UV-Vis spectrophotometer. The reflectance of the nanostructure showed an absorption edge at the band gap of ZnO. The photoluminescence of nanostructure showed UV emission at room temperature. PVA is used as a binder for the formation of pellets of ZnO nanomaterial as well as metal doped ZnO nanomaterials.

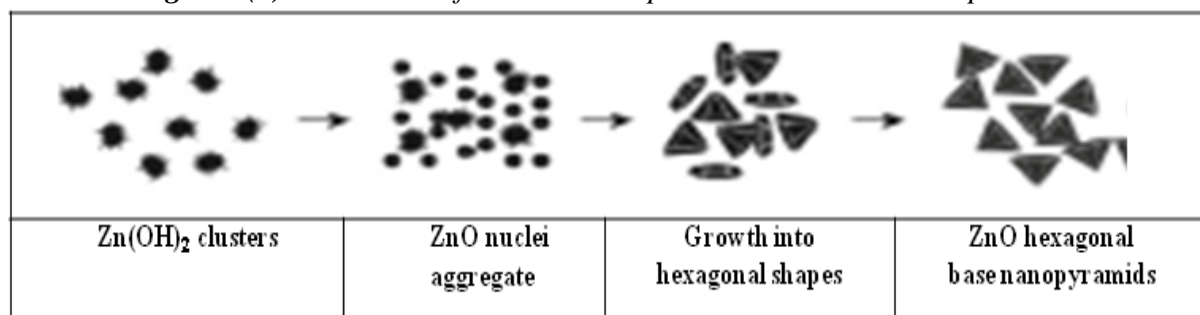
#### 2.4.2. Calcination, sintering and pellet formation

Fig. 2.6(a) illustrates the four basic steps before finally the pellets are used for measurements. The pellets are sintered at (i) 500°C for 3 h and (ii) 350°C for 6 h to complete the sintering stage. By this process the PVA volatilizes off lending some porosity to the pellet as well. A pellet is broken and sent for material characterizations. Each pellet is contacted with colloidal silver and clamped to a brass holder for measurements [30, 33].

**Calcination:** The fluffy mass obtained from the above step is calcined at 500°C for 5 hrs in a furnace. On cooling, white powders of doped ZnO nanostructure are obtained. This completes the calcination stage [32].



*Fig. 2.6.(a) Flow chart of sensor development and measurement process*



*Fig. 2.6.(b) Formation of ZnO nanostructures during calcination*

**Pellet Formation:** In the pellet formation stage, 0.7g of the calcined powder and a drop of poly-vinyl alcohol (PVA) solution are thoroughly mixed in a crucible. The mass is then pressed with 8 tons of pressure using KBr pelletiser for approximately 5 minutes to obtain the sensor pellets.

**Sintering:** The pellets are sintered at 500°C for 5 hours, by this process, the PVA volatilizes off lending some porosity to the pellet as well.

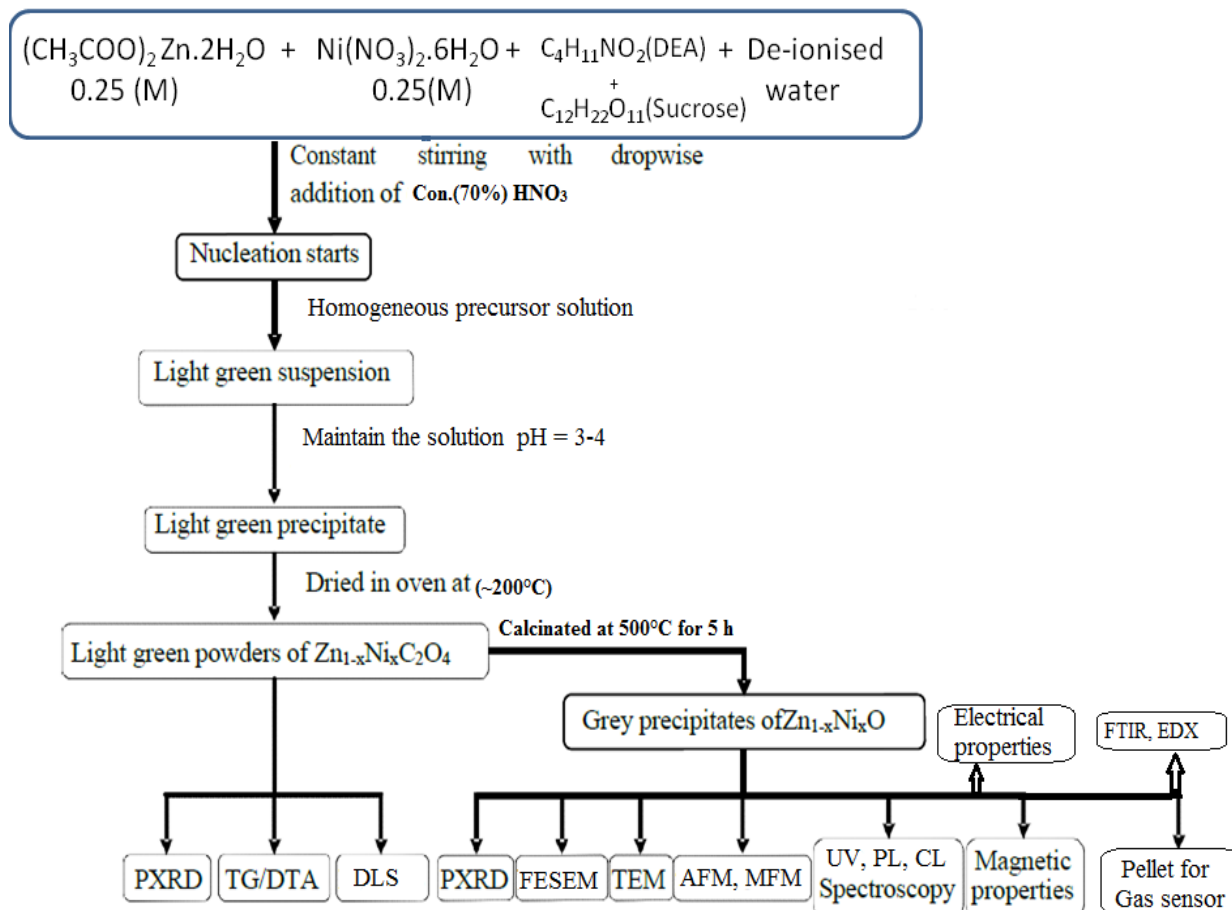


**Fig. 2.7.** Flow chart of complete synthesis process, prepared nanostructured powder sample before and after calcination for characterization of crystal structure, average particle size, shape, elemental compositions, morphology, optical, electrical and magnetic properties

**Measurements:** Each pellet is contacted with silver paste and is used to complete the circuit and clamped to a brass holder inside the quartz tube along with allied fittings viz. thermocouple, silica gel tube, inlets for vapours and connecting leads as anode and cathode for measurements. Chapter 5 explains the measurement setup and techniques used for the quality estimation of black tea bio-chemicals and other VOCs like ethanol, methanol and propanol, and Chapter 6 explains



the results and discussions of the experimental work and the analysis of the data obtained from the fabricated sensors. Fig. 2.7 shows the complete synthesis process step wise including preparation of nanostructured powder sample before and after calcination and the different characterisation. The prepared chemo-resistive pellets are used for sensing the black tea bio-chemicals and different other toxic gases [33].

## 2.5. Conclusions

In this chapter, we have described the synthesis of nanostructured ZnO material by chemical method. In this chemical synthesis route, DEA is used for the formation of a metal-DEA complex and sucrose is used as a fuel and to keep the metal-DEA complex in a polymeric network. The route involves the dehydration of the solution of a metal ion-DEA complex, followed by pyrolysis of the sucrose imbedded metal ion-DEA complex. To ensure this, the amount of sucrose in the starting solution has been optimized. Complete dehydration of the resulting solution to dryness produces a voluminous, organic based black, fluffy mass. The dried carbonaceous mass is grounded to a fine powder to produce the precursor material. Heat treatment of the precursor material results in the nanostructured pure and doped ZnO powder. Pure and doped nanostructured ZnO powder also have been formed using only DEA (in the absence of sucrose), but the agglomerations are very frequent in the process. To avoid this situation sucrose is used in this process. Another important point, that a mesoporous structure of carbonaceous material has been formed easily in the presence of sucrose, which controls agglomeration and particle size of the nanomaterials. Zinc acetate dehydrate is used as a precursor material and diethanolamine and sucrose are used as fuel for combustion in addition to 70% concentrated nitric acid as oxidizing agent and calcined at 600°C for 5 hours PVA is used as a binder to prepare the pellets of pure ZnO nanomaterials and metal doped ZnO nanomaterials.

## References

- [1] R. A. Smith, Semiconductors, Oxford University Press, Second Edition, 1978, Pages 237-240.
- [2] K. Vanheusden, C. H. Seager, W. L. Warren, D. R. Tallant, J. A. Voigt, Correlation between photoluminescence and oxygen vacancies in ZnO phosphors, Applied Physics Letters, Volume 68, Issue 3, 1996, Pages 403-405.

- [3] D. C. Wei, Y. Q. Liu, Y. Wang, H. L. Zhang, L. P. Huang, G. Yu, Synthesis of N-Doped Graphene by Chemical Vapor Deposition and Its Electrical Properties, *Nano Letters*, Volume 9, Issue 5, 2009, Pages 1752 -1758.
- [4] D. Deng, X. Pan, L. Yu, Y. Cui, Y. Jang, J. Oi, W. X. Li, Q. Fu, X. Ma, Q. Ceu, G. Sui, X. Bao, Toward N-Doped Graphene via Solvothermal Synthesis, *Chemistry of Materials*, Volume 23, Issue 5, 2011, Pages 1188-1193.
- [5] R. W. Siegel, E. Hu, M. C. Roco, Synthesis and Assembly in Nanostructure Science and Technology R&D Status and Trends in Nanoparticles, Nanostructured Materials and Nanodevices, Chapter 2, 1999, Pages 15-33.
- [6] C. C. Koch, Materials Synthesis by Mechanical Alloying, *Annual Review of Materials Science*, Volume 19, 1989, Pages 121-143.
- [7] B. L. Cushing, V. L. Kolesnichenko, C. J. Connor, Recent Advances in the Liquid-Phase Synthesis of Inorganic Nanoparticles, *Chemical Review*, Volume 104, Issue 9, 2004, Pages 409-414.
- [8] R. Groenena, J. Löfflerb, P. M. Sommelingc, J. L. Lindend, E. A. G. Hamersa, R. E. I. Schroppb, M. C. M. Sandena, *Thin Solid Films*, Volume 392, 2001, Pages 226-230.
- [9] H. Khallaf, G. Chai, O. Lupan, H. Heinrich, S. Park, A. Schulte, L. Chow, Investigation of chemical bath deposition of ZnO thin films using six different complexing agents, *Journal of Physics D: Applied Physics*, Volume 42, 2009, Pages 135304-8.
- [10] S. Ilican, Y. Caglar, M. Caglar, M. Kundakci, A. Ates, Photovoltaic solar cell properties of  $Cd_xZn_{1-x}O$  films prepared by sol-gel method, *International Journal of hydrogen energy*, Volume 34, Issue 12, 2009, Pages 5201-5207.
- [11] N. Kakati, S. H. Jee, S. H. Kim, J. Y. Oh, Y. S. Yoon, Thickness dependency of sol-gel derived ZnO thin films on gas sensing behaviors, *Thin Solid Films*, Volume 519, 2010, Pages 494-498.
- [12] N. Ueno, T. Maruo, N. Nishiyama, Y. Egashira, K. Ueyama, Low-temperature synthesis of ZnO nanorods using a seed layer of zinc acetate/sodium dodecyle sulfate nanocomposite, *Materials Letters*, Volume 64, 2010, Pages 513-515.

- [13] A. Sen, P. Pramanik, A chemical synthesis route for the preparation of fine-grained metal tungstate powders (M = Ca, Co, Ni, Cu, Zn), *Journal of the European Ceramic Society*, Volume 21, 2001, Pages 745-750.
- [14] A. Janbey, R. K. Pati, S. Tahir, P. Pramanik, A new chemical route for the synthesis of nano-crystalline  $\alpha$ -Al<sub>2</sub>O<sub>3</sub> powder, *Journal of the European Ceramic Society*, Volume 21, 2001, Pages 2285-2289.
- [15] S. Biswas, R. Das, D. Chakraborty, R. Bandhyopadhyay, P. Pramanik, Synthesis of Nitrogen Doped Multilayered Graphene Flakes: Selective Non-enzymatic Electrochemical Determination of Dopamine and Uric Acid in presence of Ascorbic Acid, *Electroanalysis*, Wiley-VCH, Volume 27, 2014, Pages 1053-1059.
- [16] S. Öztürk, N. Kılınc, Z. Z.Öztürk, Fabrication of ZnO nanorods for NO<sub>2</sub> sensor applications: effect of dimensions and electrode position, *Journal of Alloys Compounds*, Volume 581, 2013, Pages 196–201.
- [17] Y. Sahin, S. Öztürk, N. Kılınc, A. Kösemen, M. Erkovane, Z. Z. Öztürk, Electrical conduction and NO<sub>2</sub> gas sensing properties of ZnO nanorods, *Applied Surface Sciences*, Volume 303, 2014, Pages 90–96.
- [18] D. Yan, M. Hu, S. Li, J. Liang, Y. Wu, S. Ma, Electrochemical deposition of ZnO nanostructures onto porous silicon and their enhanced gas sensing to NO<sub>2</sub> at room temperature, *Electrochemical Acta*, Volume 115, 2014, Pages 297-305.
- [19] M. W. Ahn, K. S. Park, J. H. Heo, D. W. Kim, K. J. Choi, J. G. Park, On-chip fabrication of ZnO-nanowire gas sensor with high gas sensitivity, *Sensors and Actuators B: Chemical*, Volume 138, Issue 1, 2009, Pages 168-173.
- [20] S. W. Fan, A. K. Srivastava, V. P. Dravid, Nanopatterned polycrystalline ZnO for room temperature gas sensing, *Sensors and Actuators B: Chemical*, Volume 144, Issue 1, 2010, Pages 159–163.
- [21] A. Z. Sadek, W. Wlodarski, K. K. Zadeh, S. Choopun, ZnO nanobelt based conductometric H<sub>2</sub> and NO<sub>2</sub> gas sensors, *Proceedings of Sensors IEEE*, 2005, Pages 1326-1329.
- [22] R. C. Pawar, J. W. Lee, V. B. Patil, C. S. Lee, Synthesis of multi-dimensional ZnO nanostructures in aqueous medium for the application of gas sensor, *Sensors and*

- Actuators B: Chemical, Volume 187, 2013, Pages 323-330.
- [23] M. Hjiri, L. E. Mir, S. G. Leonardi, N. Donato, G. Neri, CO and NO<sub>2</sub> selective monitoring by ZnO-based sensors, *Nanomaterials*, Volume 3, Issue 3, 2013, Pages 357-369.
- [24] J. X. Wang, X. W. Sun, Y. Yang, C. M. L. Wu, N-P transition sensing behaviors of ZnO nanotubes exposed to NO<sub>2</sub> gas, *Nanotechnology*, Volume 20, Issue 46, 2009, Pages 465501-4.
- [25] S. C. Das, B. Tudu, N. Bhattacharya, R. Bandyopadhyay, P. Pramanik, Doped ZnO Nanostructured Sensor in Electronic Nose for Detection of Ammonia, Hydrogen and Liquefied Petroleum Gas, *Advanced Nanomaterials and Nanotechnology: Springer-Verlag Berlin Heidelberg*, Chapter 47, 2013, Pages 473-482.
- [26] S. K. Biswas, P. Pramanik, Studies on the gas sensing behaviour of nanosized CuNb<sub>2</sub>O<sub>6</sub> towards ammonia, hydrogen and liquid petroleum gas, *Sensors and Actuators B: Chemical*, Volume 133, 2008, Pages 449-455.
- [27] M. Wang, J. Wang, W. Chen, Y. Cui, L. Wang, Effect of preheating and annealing temperatures on quality characteristics of ZnO thin film prepared by sol-gel method, *Materials Chemistry and Physics*, Volume 97, 2006, Pages 219-225.
- [28] S. C. Das, S. Ghosh, B. Tudu, N. Bhattacharyya, R. Bandyopadhyay, P. Pramanik, Development of Nanostructured ZnO based Gas Sensors to use in Electronic Nose for Biochemical Compounds in Black Tea, ICST-2012, ID-2591147, Online IEEE, Pages 93-94.
- [29] P. Pramanik, Synthesis of nano particles of inorganic oxides by polymer matrix, *Bulletin of Materials Science*, Volume 18, Issue 6, 1995, Pages 819-829.
- [30] S. C. Das, R. Bandyopadhyay, P. Pramanik, Development of W doped ZnO nanostructure chemoresistor pellet sensors for black tea aroma monitoring, *International Journal of Innovative Science, Engineering and Technology*, Volume 2, Issue 3, 2015 Pages 107-113.
- [31] P. Pramanik, Chemical synthesis of nanosized oxides, *Bulletin of Materials Science*, Volume 19, Issue 6, 1996, Pages 957-961.

- [32] D. E. Williams, Semiconducting oxides as gas-sensitive resistors, *Sensors and Actuators B: Chemical*, Volume 57, 1999, Pages 1-16.
- [33] S. C. Das, R. Bandyopadhyay, S. Ghosh, P. Pramanik, Fabrication of doped zinc oxide nanostructured sensor array in electronic nose for aroma estimation of CTC black tea and PCA clustering, *International Journal of Innovative Science and Applied Engineering Research*, Volume 13, Issue 40, 2014, Pages 8-18.



## Chapter 3

# Structural and morphological studies of pure and doped ZnO nanostructures

This chapter is focused on structural and morphological studies of ZnO nanostructures by chemical synthesis route using thermal decomposition of zinc acetate. Chemical synthesis route is very simple, has low toxicity and high dissolving capability. The obtained ZnO nanostructures have been characterized by X-ray diffractometer (XRD), particle size analyzer (PSA), field emission scanning electron microscopy (FESEM), energy dispersive X-ray spectroscopy (EDAX), high resolution transmission electron microscopy (HRTEM), fourier transform infrared (FTIR) spectroscopy and atomic force microscopy (AFM) for crystal structure, average particle size, shape, elemental compositions, chemical composition group and surface roughness morphology study respectively.

### *List of sections*

- 3.1. Introduction
- 3.2. Structural parameters of metal oxides controlling gas sensing properties
- 3.3. Structure and morphology of pure ZnO nanostructures
  - 3.3.1. X-ray diffraction (XRD) studies
  - 3.3.2. Particle size analyser (DLS) results
  - 3.3.3. Transmission electron microscopy (TEM) for structural analysis
- 3.4. Morphology of semiconducting metal oxides (SMOX)
  - 3.4.1. Atomic force microscopy (AFM)
  - 3.4.2. Scanning electron microscope (SEM)
  - 3.4.3. Field emission scanning electron microscopy (FESEM)
- 3.5. Chemical composition of ZnO nanostructures
  - 3.5.1. Fourier transform infrared spectroscopy (FTIR)
  - 3.5.2. Energy dispersive X-ray spectroscopy (EDAX)
- 3.6. Structure and morphology of doped ZnO nanostructures
  - 3.6.1. XRD analysis
    - 3.6.1.1. Pure ZnO and Co-doped ZnO nanostructures
  - 3.6.2. TEM analysis
  - 3.6.3. AFM analysis
  - 3.6.4. SEM analysis
  - 3.6.5. FESEM analysis
- 3.7. Chemical composition of doped ZnO nanostructures
  - 3.7.1. FTIR analysis
  - 3.7.2. EDAX analysis
- 3.8. Conclusion
- References

*Contents of this chapter are based on following publication:*

1. S. C. Das, K. Sadani, R. Bandyopadhyay, P. Pramanik, Sensing characteristics of Molybdenum doped Zinc Oxide nanoparticles chemoresistor pellets towards black tea-biochemicals, International Journal of Advances in Engineering Science and Technology, Volume 3, Issue 3, 2014, Pages 120-131.





# Chapter 3

## Structural and morphological studies of pure and doped ZnO nanostructures

### 3.1. Introduction

Metal oxides exhibit extraordinary properties in the nano-scale level. ZnO nanostructures have high refractive index, thermal, conductivity, binding, antibacterial, UV-properties etc. Due to these properties ZnO nanostructures are used in many industrial applications such as ceramics, glass, cement, rubber, lubricants, paints, ointments, sealants, pigments, foods, batteries, ferrites and fire retardants [1-5]. Generally many synthesis methods exist to synthesize ZnO nanostructures. This thesis is focused on ZnO nanostructures by chemical synthesis route using thermal decomposition of zinc acetate [6]. Chemical synthesis route is very simple, low toxicity nature and high dissolving capability. The obtained ZnO nanostructures have been characterized by X-ray diffractometer (XRD), particle size analyzer (PSA), field emission scanning electron microscopy (FESEM), energy dispersive X-ray spectroscopy (EDAX), high resolution transmission electron microscopy (HRTEM), fourier transform infrared (FTIR) spectroscopy and atomic force microscopy (AFM) for crystal structure, average particle size, shape, elemental compositions, chemical composition group and surface roughness morphology study respectively.

### 3.2. Structural parameters of metal oxides controlling gas sensing properties

The fundamentals of resistive type sensor operation are based on the changes in resistance (or conductance) of the gas-sensing material as induced by the surrounding gas. The changes are caused by various processes, which can take place both at the surface and in the bulk of gas sensing material. The control of gas sensing properties depends upon adsorption/desorption, catalysis, reduction/re-oxidation, and diffusion in gas sensors and influenced by structural parameters of the sensor material [7]. This affirms that gas-sensing effects are structurally sensitive as well. Taking into account the complexity of the gas-sensing mechanism and its dependence on numerous factors, it becomes clear that we have to consider the influence of a great number of various structural parameters of metal oxide matrix on gas sensors' parameters in Fig.3.1(a).The parameters on gas-sensing characteristics

takes place through the changes in the effective area of inter-grain and inter-agglomerate contacts, energetic parameters of adsorption/desorption, number of surface sites, concentration of charge carriers, initial surface band bending, coordination number of metal atoms on the surface, etc [8].

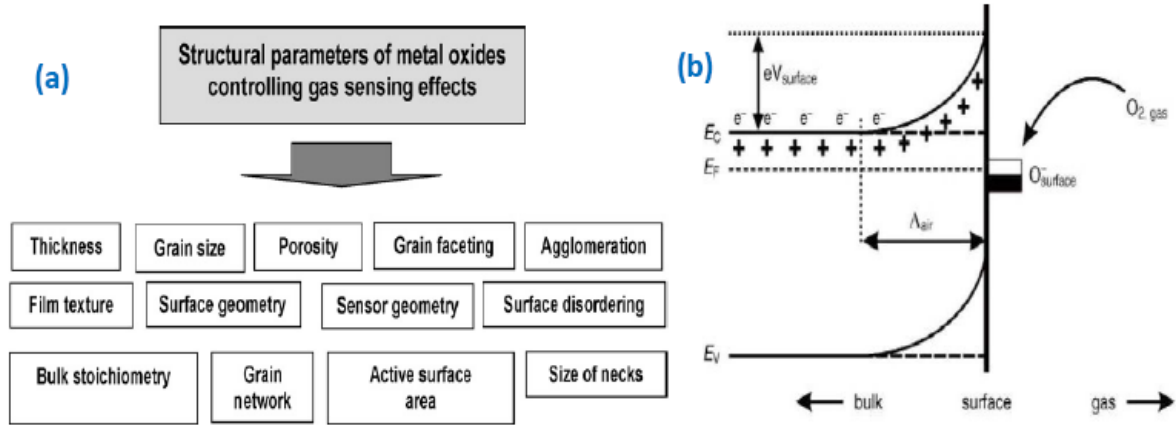


**Fig.3.1.** (a) Structural parameters of MOS which control gas sensing properties (b) Diagram of band bending after chemisorption of charged species

In the schematic diagram of band bending after chemisorptions of charged species (here the ionosorption of oxygen) as shown in Fig. 3.1(b),  $E_C$ ,  $E_V$ , and  $E_F$  denote the energy of the conduction band, valence band, and the Fermi level, respectively, while  $\lambda_{\text{air}}$  denotes the thickness of the space-charge layer, and  $eV_{\text{surface}}$  denotes the potential barrier. The conducting electrons are represented by  $e^-$  and  $+$  represents the donor sites. However this sensing mechanism is suitable only for n-type semiconducting metal oxides of which depletion regions are smaller than grain size [9].

### 3.3. Structure and morphology of pure ZnO nanostructures

#### 3.3.1. X-ray diffraction (XRD) studies

The X-ray diffraction (XRD) analysis of the synthesized ZnO nanomaterial is done using Bruker 8 Advance powder XRD which is operated at 40kV and 30mA with Cu radiation and K- $\beta$  filter. The data is collected over  $2\theta$  angle range of  $20^\circ \leq 2\theta \leq 80^\circ$  with step size of  $0.02^\circ$ . The phase identification is done using [JCPDS card No.80-0075] data base [10] and presence of synthesized material is identified. The obtained XRD graph is shown in Fig. 3.2(a). The prepared Zinc Oxide nanostructures confirmed that the Hexagonal structure was formed. The peaks were observed and the corresponding (h k l) values are shown in Table 3.1.

Table 3.1. Peaks of XRD analysis (h k l) values

2 $\theta$ degree	31°	34°	36°	47°	56°	62°	66°	68°	69°	77°
(h k l)	(100)	(002)	(101)	(102)	(110)	(103)	(200)	(112)	(201)	(202)

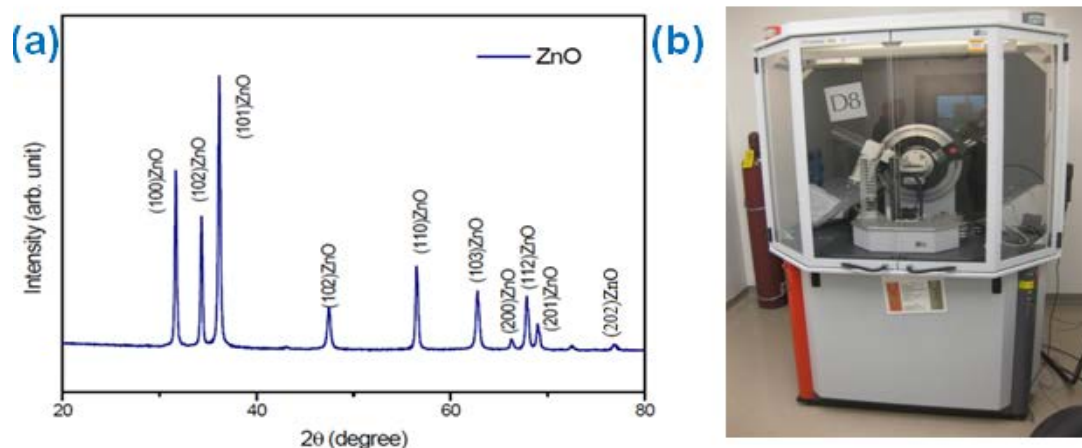


Fig.3.2.(a) XRD pattern of nanostructured ZnO powder obtained through chemical synthesis, (b) X-ray diffractometer (Bruker D8 Advance) at IUC, UGC, Salt Lake

### Particle size analysis from XRD

When the particle size of the individual crystal is less than  $100 \text{ \AA}^3$ , the term particle size is used. The average crystallite size can be calculated by using Debye Scherer equation,

$$D = \frac{0.9\lambda}{\beta \cos\theta} \quad (3.1)$$

where,  $D$  is the average crystallite size of the particle,  $\lambda$  is the wavelength of radiation of  $\text{CuK}\alpha$  X-rays,  $\beta$  is the full width half maximum (FWHM) of the peak,  $\theta$  = the Bragg's angle. In our experiment, the lattice parameters were  $a = b = 0.3249 \text{ nm}$  and  $c = 0.5206 \text{ nm}$ . The average crystallite size can be calculated by using equation (3.1). The crystallite size for ZnO nanostructures are found about  $\sim 60.2 \text{ nm}$  (calcined at  $500^\circ\text{C}$  for 4 hours) and  $\sim 56.2 \text{ nm}$  (calcined at  $600^\circ\text{C}$  for 5 hours) obtained [11].

### 3.3.2. Particle size analyser (DLS) results

The particle size of the nanostructure powder is obtained by particle size analyzer (DLS). Ethanol was used as dispersion medium for ZnO nanostructures and sonicated using ultrasonicator. The particle distribution was observed in the form of histogram Fig 3.3 (a). The mean value of the histogram was taken as the average particle size. The average particle size is found to be about  $\sim 61.2 \text{ nm}$  (calcined at  $500^\circ\text{C}$  for 4h) and  $\sim 57 \text{ nm}$  (calcined at  $600^\circ\text{C}$  for

5 hours) respectively. This value is comparable to the data obtained from XRD [12]. Dynamic light scattering (also known as photon correlation spectroscopy) is an analytical technique to determine the size distribution of macromolecular solutions. The technique relies on determination of rate of fluctuations of laser light intensity that is scattered by particles. This is performed by measuring the second order autocorrelation function of the intensity trace. The particle size of the material is studied by particle size analyser (DLS) (Delsa Nano C, Beckman Coulter) shown in Fig. 3.3(b).

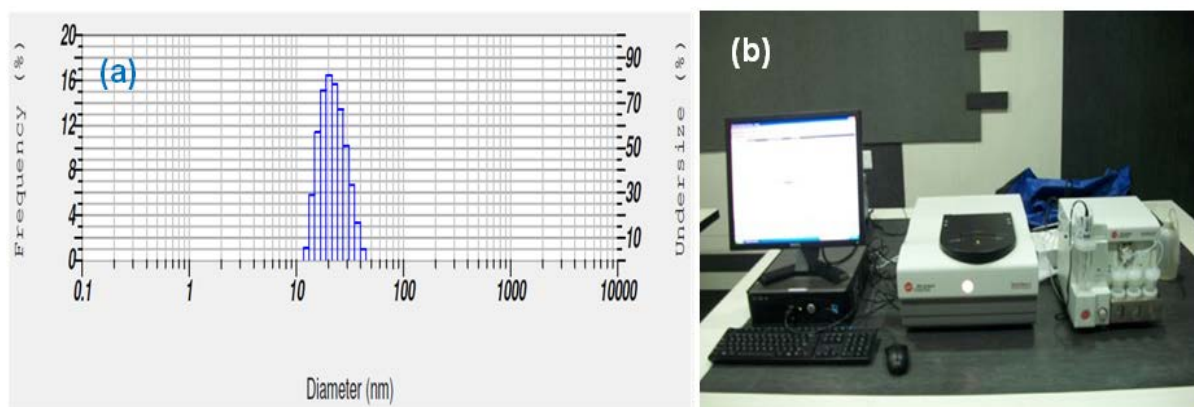


**Fig.3.3.** (a) Particle size analysis of ZnO solid solution, (b) Particle size analyser (DLS) instrument image at CRNN, Technology Campus, CU

### 3.3.3. Transmission electron microscopy (TEM) for structural analysis

The morphology of the ZnO nanostructures was observed in TEM image. The following TEM image infers that the spherically agglomerated nanoparticles were formed and also observed that uneven distribution of the nanoparticles. The selected area electron diffraction infers that the ZnO nanostructures prepared by chemical synthesis method exhibit hexagonal structure. The SAED pattern supports the XRD crystal structure analysis.

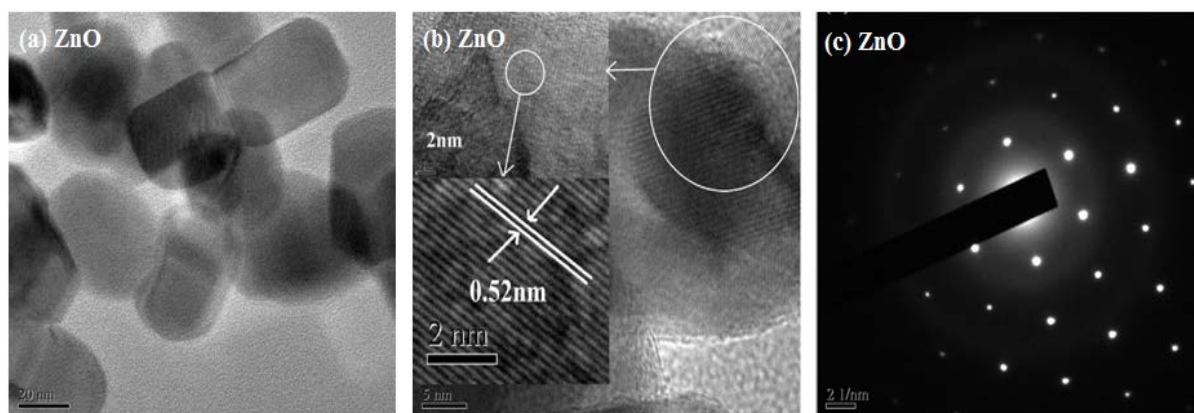


**Fig.3.4.** (a) Particle size, (b) HRTEM and (c) SAED pattern of TEM images of ZnO nanostructures

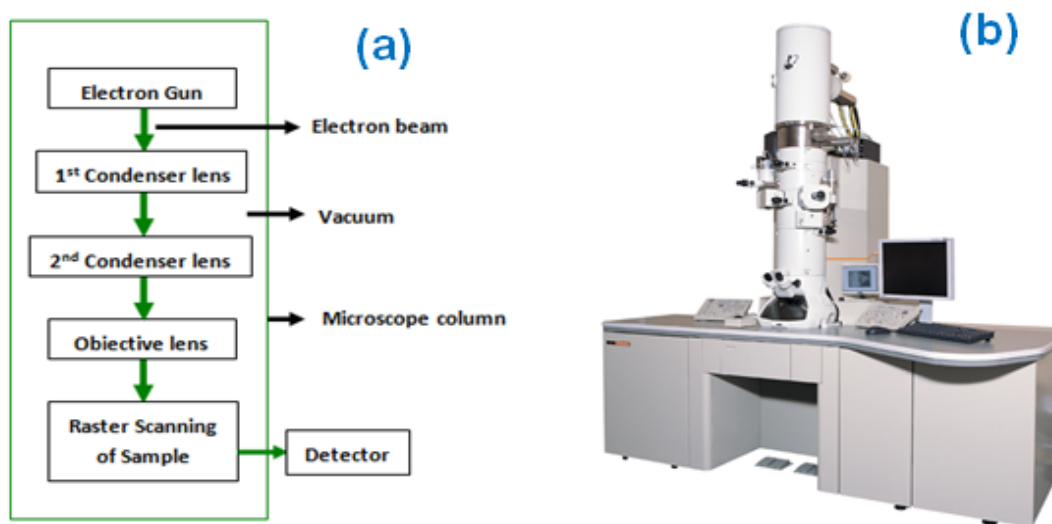


**Fig.3.5.(a)** Block diagram of TEM **(b)** TEM instrument (JEOL, JEM 2100, Japan) PC controlled 200 KV (HR version) at CRNN, Technology Campus, CU

TEM was employed to examine the morphology and distribution of particle size of the synthesized pure and doped nanostructures. It has been traditionally applied to characterizing the interior structure of nanomaterials. With the help of this instrument, atomic planes of nanoparticles can be observed in Fig. 3.4(a-c), and was used to observe the internal structure of sample. TEM (JEOL, JEM 2100, Japan) is a PC controlled 200 KV (HR version) shown in Fig. 3.5(a-b).

### 3.4. Morphology of semiconducting metal oxides (SMOX)

Chemo-resistive gas sensors based on Semiconducting Metal Oxides (SMOX) are widely used in applications spanning from natural gas leak alarms to automotive (in-cabin air quality control) to complex chemical sensor systems [7]. The most successful materials are ZnO, SnO<sub>2</sub> and WO<sub>3</sub>, which are both n-type semiconductors and currently used in commercial devices. For the state of the art sensors, using porous and thick sensing films realized by screen printing or drop coating looks like being the approach of choice. The reason, as explained in [8], is the fact that such a morphology has the advantage of providing easy access to the whole of the sensitive material; ensuring the largest impact of the surface phenomena onto the resistance of the sensing layer; minimizing the electrical effect of the electrodes. For *p*-type materials, it was shown recently that such a morphology is not the most appropriate to translate their considerable surface reactivity into large sensor signals [13]. These facts points out the essential role played by the conduction in the sensing layer in gas sensing with SMOX based devices [14-15]. Fig.3.6 (a-b) shows the doped nanostructured ZnO surface morphology by SEM and TEM image.

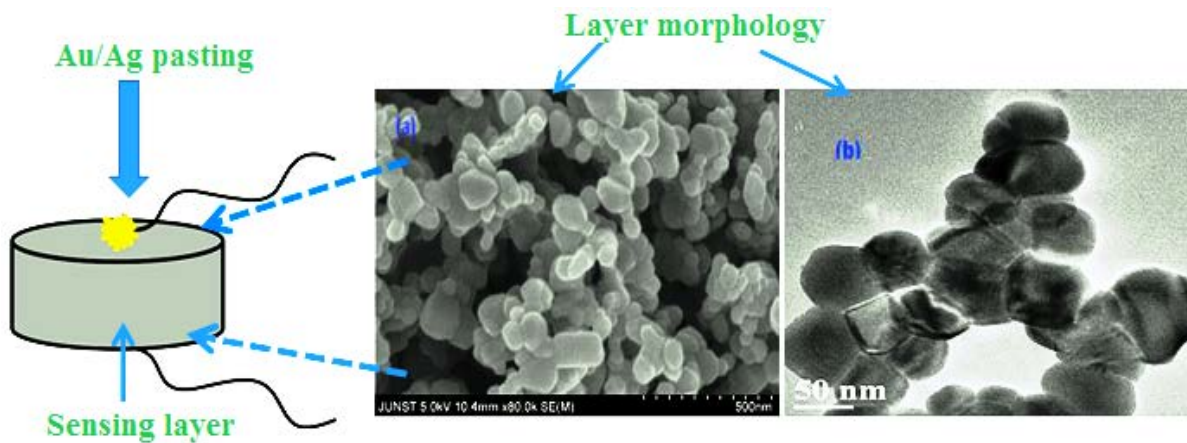


*Fig.3.6. Doped nanostructured ZnO surface morphology by (a) SEM and (b) TEM image*

### 3.4.1. Atomic force microscopy (AFM)

AFM is a powerful tool in manipulating and characterizing the properties of nanostructures. It has been demonstrated to be an invaluable technique for the surface morphological characterization of nanostructures. This technique provides 2-D and 3-D images of the nanostructure surfaces for evaluation. The microscopy uses a tiny cantilever beam with an attached tip to interact with the surface. The deflection of the cantilever due to repulsive electronic interactions between the atoms of the tip end and the specimen is measured to provide an image of the surface structure. Both contact and tapping mode AFM is possible, the latter employed in case of soft surfaces avoiding contact of the tip with the surface. The Schematic diagram and Instrument setup of AFM are shown in Fig. 3.7(a-b).

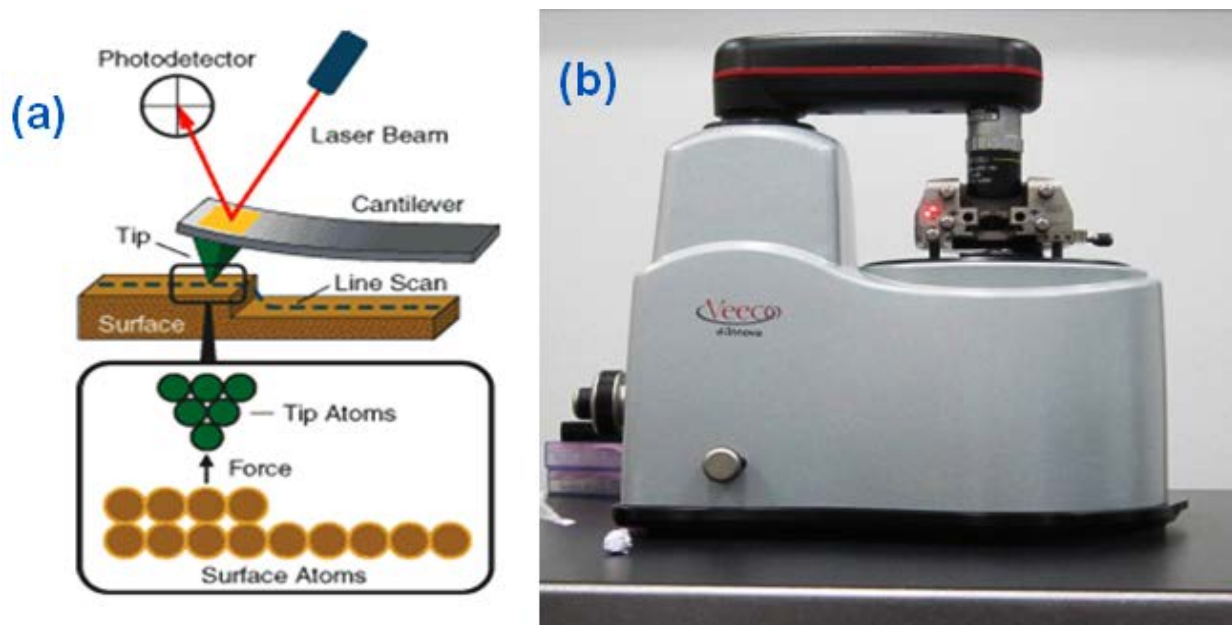


*Fig.3.7. (a) Schematic diagram of AFM and (b) AFM Instrument (Bruker, Veeco-Innova) at IPLS, CU*

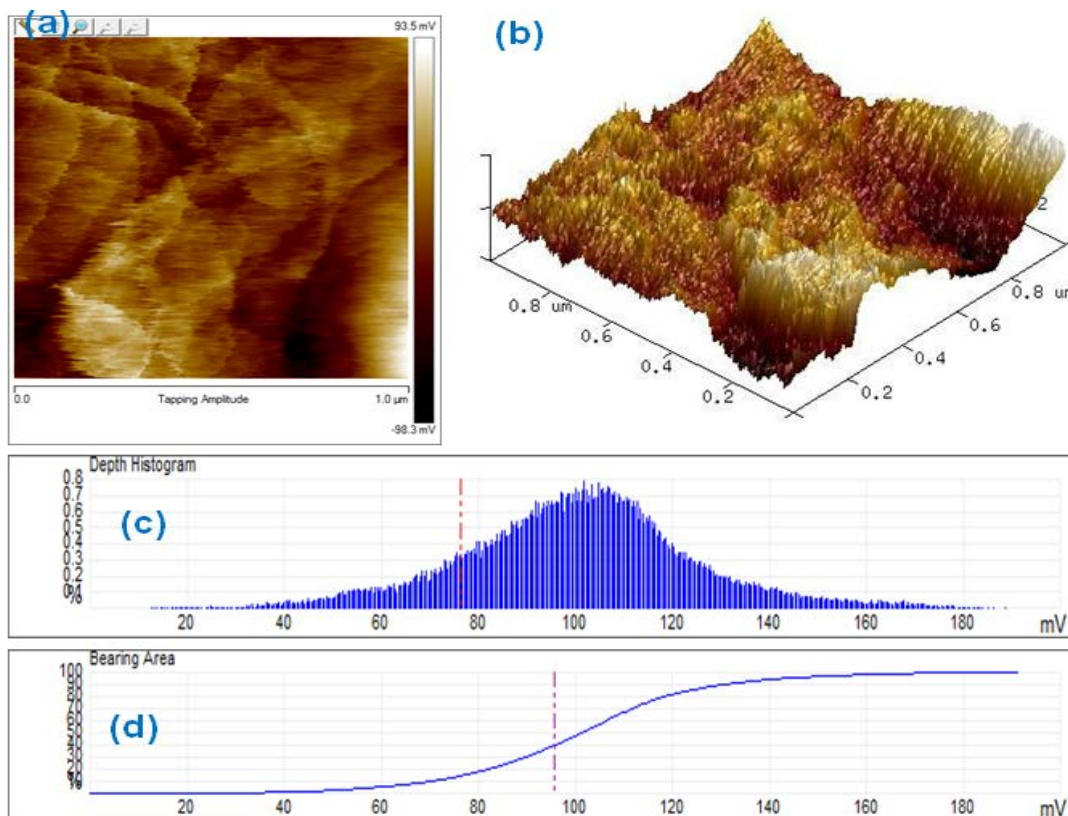


**Fig.3.8.** AFM images ( $1\mu\text{m} \times 1\mu\text{m}$ ) of nanostructured ZnO after calcined at  $600^\circ\text{C}$  for 5h (a) 2D image, (b) 3D image, (c) depth histogram and (d) bearing area plot from 2D tapping amplitude image

This imaging technique has proved to be effective in our study of the morphology and physical parameters of the resultant doped nanostructured ZnO powder samples. Due to nanoparticles surface, we used tapping mode atomic force microscopy (AFM) at a scan rate of 1.5 Hz using a Bruker (Veeco-Innova) scanning probe microscope shown in Fig.3.7 (b). Two-dimensional (2D) and three-dimensional (3D) AFM images of ZnO nanostructures are shown in Fig. 3.8(a-b). In order to analyze the surface morphology and grain size, Nanoscope analysis imaging software was used that covered ( $1\mu\text{m} \times 1\mu\text{m}$ ) area. The result of roughness averages of 10.86 nm shows ZnO nanostructures has a smooth and dense surface morphology [16]. The particle size of about  $\sim 61.2$  nm (calcined at  $500^\circ\text{C}$  for 4 hours) and  $\sim 56.8$  nm (calcined at  $600^\circ\text{C}$  for 5h ) were found by direct measurement using the Nanoscope analysis dimension-edge-tapping image-processing software (version 1.40). Fig.3.8 (c) show the depth histogram and (d) show the bearing area plot from 2D tapping amplitude image.

### 3.4.2. Scanning Electron Microscope (SEM)

The surface morphology of ZnO nanostructures has been investigated by SEM and results are shown in Fig. 3.9 (a) and (b) with different magnifications. The Scanning Electron

Micrograph shows that, the clusters of nano-particles look like cauliflowers. It was observed that nanostructures resulting from the combustion reaction have porous morphology forming fuzzy network of nano-crystalline ZnO, and this may be due to the rapid release of gaseous by products during the combustion process.

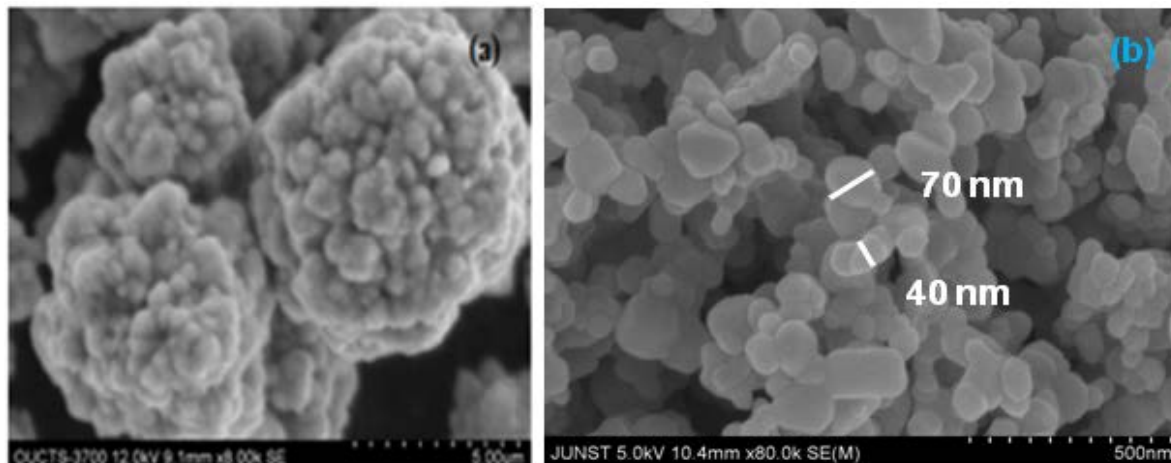


**Fig.3.9.** SEM image of ZnO nanostructure, (a) before calcination and (b) after calcined at 500°C for 4 hours

At a higher magnification shown in Fig. 3.9 (b) at (9.1mm x 32.0 k SE), the agglomerated ZnO nano-particles consisting of tiny nano-particles. The size range is 40 nm to 70 nm [13, 15]. SEM was performed using a ZEISS, EVO-MA 10 with INCA Energy 250 Microanalysis System (EDS) at CRNN, CU shown in Fig. 3.11(a) consists of an electron gun and electromagnetic lens system to study the surface structure and morphology of solids. It is a type of electron microscope capable of producing high-resolution images of a sample surface. The nanostructure of hexagonal wurtzite-type structure was examined using a SEM. Unlike Optical microscopy, SEM requires the vacuum environment and specimen surface to be electrically conductive. The depth of focus is much larger than the optical microscope image even at lowest magnifications and it is one of the major advantages of SEM.

### 3.4.3. Field emission scanning electron microscopy (FESEM)

The FESEM micrograph of the prepared ZnO nanostructure powder is presented in Fig. 3.10 (a) and (b). The slightly agglomerated particles exhibit spherical morphology. Each particle represents the aggregate of smaller grains, integrated in an open circular or grape cluster structure. Loosely sintered particles are evident inside agglomerates of spherical or rod-like grains, indicating that the powder obtained through the chemical synthesis method is very reactive. Statistical review of the FESEM microphotographs implies uniformity of particle size and shapes with the mean particle size. Nanoparticles of ZnO were distributed



uniformly over the surface. Average sizes of nanoparticles of ZnO are found about  $\sim 60.5$  nm (calcined at  $500^{\circ}\text{C}$  for 4 hours) and  $\sim 56.4$  nm (calcined at  $600^{\circ}\text{C}$  for 5 hours) obtained by direct measurement from FESEM Images.

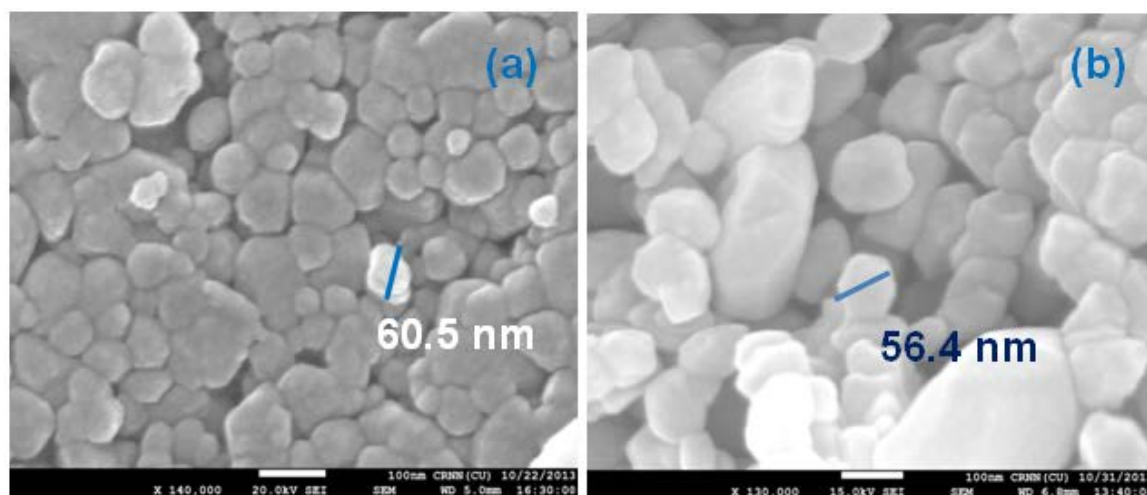


**Fig.3.10.** FESEM micrograph of ZnO nanostructures calcined at (a)  $500^{\circ}\text{C}$  for 4 hours, (b)  $600^{\circ}\text{C}$  for 5 hours

FESEM was performed using a JEOL, JSM-7600F PC controlled microscope with (INCA Energy 250 EDS) an energy dispersive X-ray spectroscopy (EDAX) system and (MonoCL-4, Gatan) a cathodoluminescence system accessories to the FESEM instrument at CRNN, CU shown in Fig. 3.11(b).



**Fig.3.11.**(a) SEM instrument with INCA Energy 250 Microanalysis System (EDS), ZEISS EVO-MA 10, (b) FESEM instrument (JEOL, JSM-7600F) PC controlled microscope with INCA Energy 250 EDS at CRNN, CU

Using these facilities we get the elemental mapping and crystallographic information. Luminescence from semiconductor nanoparticles can be obtained at a wide range of colour ranging from the UV to the IR using these facilities. In addition, the sample under investigation can be cooled down to cryogenic temperatures in order to study the temperature

dependence of the luminescence properties. So, the particle sizes measured are almost same as those obtained from XRD, DLS, AFM, and FESEM images and the results are shown in Table 3.2. It is believed that the ZnO nanoparticles are a product of reaction between zinc acetate dihydrate and sucrose which is stabilized by diethanolamine (DEA). FESEM results confirm smaller particle size in larger specific surface area.

**Table 3.2.** ZnO nanostructure particle size obtained from XRD, DLS, AFM and FESEM

ZnO nanostructures	Particle size			
	XRD	DLS	AFM	FESEM
500 <sup>o</sup> C for 4 hours	60.2 nm	61.2 nm	61.2 nm	60.5 nm
600 <sup>o</sup> C for 5 hours	56.2 nm	57.0 nm	56.8 nm	56.4 nm

### 3.5. Chemical Composition of ZnO nanostructures

#### 3.5.1. Fourier transform infrared spectroscopy (FTIR)

An infrared spectrum of a solid, liquid or gas can be obtained by FTIR technique. This is primarily used for determining the chemical structure of materials by revealing the characteristics frequencies of a chemical functional group. FTIR has unique advantages over the dispersive spectrometer (collection of signal over the entire spectral range simultaneously resulting in a faster data acquisition, better signal to noise ratio owing to lesser loss from optics, use of laser as an internal standard for precise measurements by wavelength calibration).

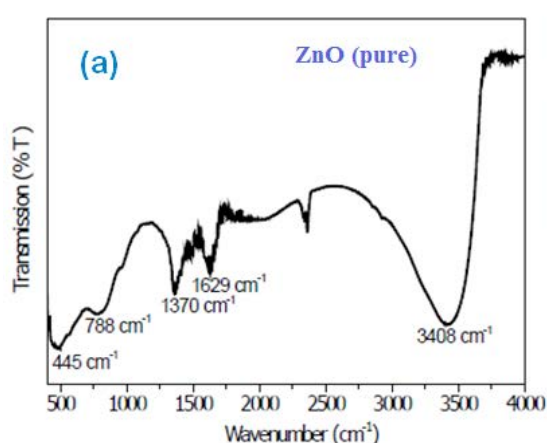


**Fig.3.12.** (a) FT-IR spectrum of the nanostructured ZnO powder calcinated at 600<sup>o</sup>C for 5 hours, (b) FT-IR instrument at CRNN, CU

Sample under interest absorbs at some portions of the spectral range, and the transmitted part reaches the detector. The detector collects the signal from the entire spectral range simultaneously. The detector signal is Fourier transformed to obtain the corresponding

transmittance and hence the absorption spectrum. FT-IR (Jasco FT/IR-6300 with Jasco IRT-7000) is shown in Fig. 3.12(b). The FTIR spectrum of ZnO is shown in Fig 3.12 (a). There is a broad band with very low intensity at  $3408\text{ cm}^{-1}$  corresponding to the vibration mode of water OH group indicating the presence of small amount of water adsorbed on the ZnO nanocrystal surface. The band at  $1629\text{ cm}^{-1}$  is due to the presence OH bending of water. A strong band at  $445\text{ cm}^{-1}$  is attributed to the Zn-O stretching band [15].

### 3.5.2. Energy Dispersive X-ray Spectroscopy (EDAX)

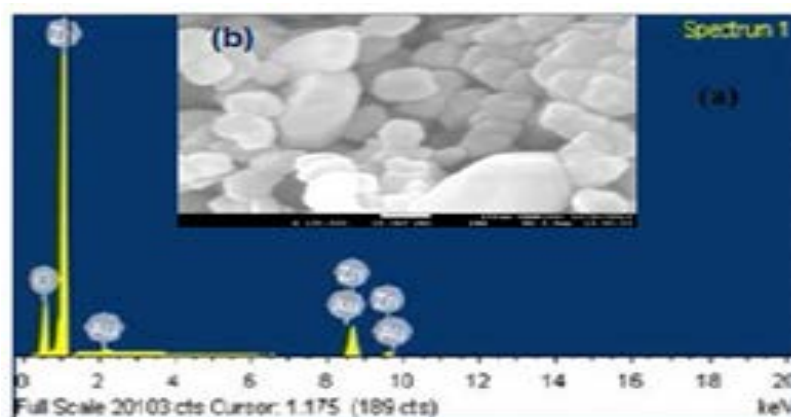


**Fig.3.13.** (a) EDAX analysis of ZnO calcined at  $600^{\circ}\text{C}$  for 5h, Inset: FESEM image (b)

The composition of the synthesized product was investigated using EDAX. Fig. 3.13 shows a representative EDAX pattern, which indicates that the ZnO structures are composed of only Zn and O almost with 1:1 atomic percentage, confirming the formation of stoichiometric ZnO as shown in Table 3.3. This has been attributed to the synthesis of pure hexagonal-phase ZnO structures. No characteristic peaks from impurities are detected except Au (this is attributed to the gold coating), which indicates purity of the product.

**Table 3.3.** FESEM image elemental analysis

Element	Weight %	Atomic%
OK	18.81	49.10
Zn L	78.89	50.41
Au M	2.30	0.49
<b>Total</b>	<b>100.00</b>	<b>100.00</b>

## 3.6. Structure and morphology of metal doped ZnO nanostructures

### 3.6.1. XRD analysis

The XRD data for the crystalline and the preferred crystal orientation of doped nanostructured ZnO as  $(\text{Zn}_{1-x}\text{M}_x\text{O})$ , where  $(\text{M} = \text{Ni}, \text{Co}, \text{Pt}, \text{Pd}, \text{Mo}, \text{W}$  and  $\text{Cd})$  in Fig.3.14 show the characteristic peaks at  $2\theta$  values of  $31.52^{\circ}$ ,  $34.25^{\circ}$  and  $36.16^{\circ}$  indexed to (100),

(002) and (101) planes using the equation (3.1), which confirms the formation of well crystallized ZnO hexagonal wurtzite phase belonging to a  $P6_3mc$  space group. The lattice parameters of the nanostructures, calculated using equation 3.4 and Rigaku, PDXL2 software, are given in Table 3.4. The XRD peaks and lattice parameters are matching well with the JCPDS data of ZnO (No. 36-1451).

$$TC(hkl) = \frac{I(hkl)/I_o(hkl)}{N^{-1} \sum_n I(hkl)/I_o(hkl)} \quad (3.4)$$

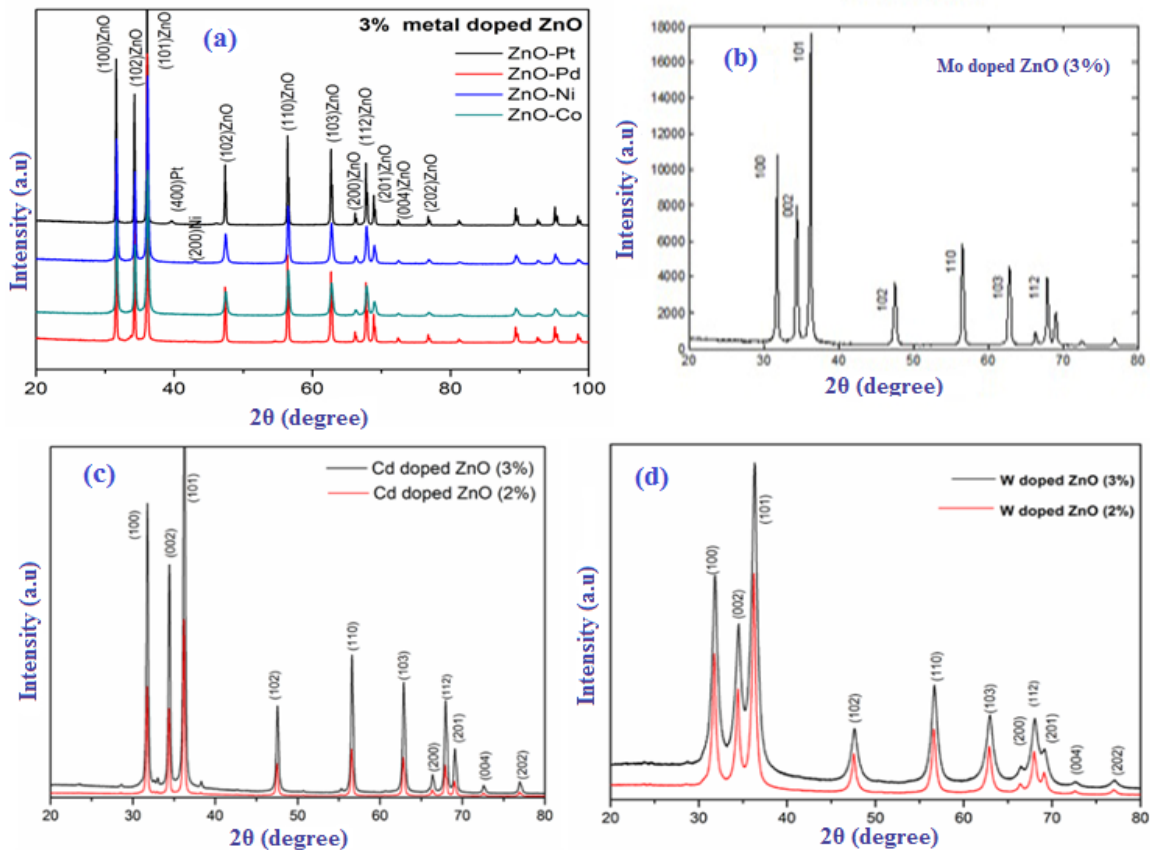


**Fig.3.14.** XRD pattern of  $(Zn_{1-x}M_xO)$  nanostructures powder obtained through chemical synthesis for (a) (Co, Ni, Pt, Pd)-doped, (b) Mo doped, (c) Cd doped, (d) W doped ZnO nanostructures

For the doped samples, no significant shift in peaks is observed. The expected shift in lattice constants could be beyond the resolution of the XRD. The ionic radii of  $Zn^{2+}$  ( $\sim 0.60\text{\AA}$ ) and the doping elements  $Co^{2+}$ ,  $Ni^{2+}$ ,  $Pt^{2+}$ ,  $Pd^{2+}$ ,  $Mo^{2+}$ ,  $W^{2+}$ ,  $Cd^{2+}$  are very similar ionic radii to raddi of  $Zn^{2+}$  from ( $0.56\text{\AA}$ -  $0.74\text{\AA}$ ) [15]. Notably, in Fig.3.14, we found that the intensity of (002) peak is smaller than (100) and (101) peaks for doped ZnO nanostructures, unlike pure ZnO nanostructures where (101) peak intensity is larger than (100) and (002) peaks. Thus, it indicates that the  $c$ -axis oriented growth is favoured in our  $(Zn_{1-x}M_xO)$  nanostructures [17].

According to the Miller's formula in equation (3.4), the phases identified along with  $(hkl)$  indices of the reflections for nanostructures are presented in Table 3.4.

**Table 3.4.** Structural properties of pure and doped ZnO nanostructures [21, 29-31]

Sample	Peaks at $2\theta$ (degree)			peak $(hkl)$		
	31.52	34.25	36.16	(100)	(002)	(101)
ZnO and (Co, Ni, Pt, Pd, Mo, W, Cd)-doped ZnO						

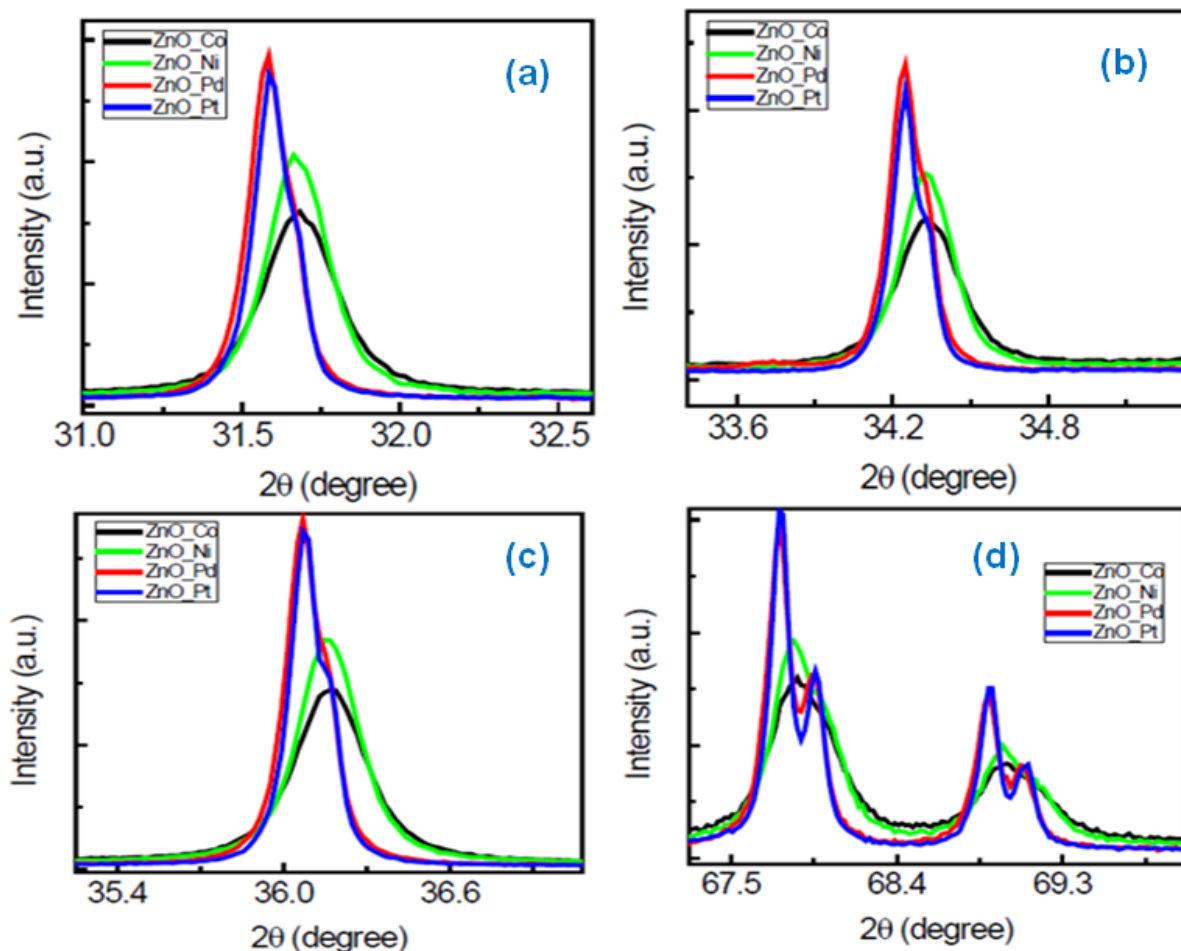


**Fig.3.15.** XRD spectra of (Co, Ni, Pt, Pd)-doped nanostructured ZnO powder  
(a)  $(31.0^\circ - 32.5^\circ)$ , (b)  $(33.6^\circ - 34.8^\circ)$ , (c)  $(35.4^\circ - 36.6^\circ)$ , (d)  $(67.5^\circ - 69.3^\circ)$

According to Table 3.4 XRD spectra of (Co, Ni, Pt, Pd)-doped ZnO nanostructures are shown in Fig. 3.15 (a-d). By referring to JCPDS data of ZnO (No. 36-1451), three peaks of  $31.52^\circ$ ,  $34.25^\circ$ , and  $36.16^\circ$  correspond to (100), (002), and (101) plane [18-20]. The high intensity of these three peaks might be due to the thickness of nanostructured ZnO powder and it shows that crystalline sharply oriented [18] due to the intensity of (101) peak is larger than (100) and (002) peaks. Besides, intensity of (002) peak is smaller than (100) and (101) peaks for doped ZnO nanostructures, unlike pure ZnO nanostructures. Thus, this confirms

that the *c*-axis oriented growth is favoured in our (Co, Ni, Pt, Pd)-doped ZnO nanostructures and crystalline structure is hexagonal-wurtzite, same as pure ZnO nanostructures.

**Table 3.5.** Crystallite size and activation energy of pure and doped ZnO nanostructures [21]

Nanostructures doping type	Crystallite size (nm)	Activation energy (eV)
ZnO (pure)	40	0.60
(Zn <sub>0.97</sub> Ni <sub>0.03</sub> O)	45	0.60
(Zn <sub>0.97</sub> Co <sub>0.03</sub> O)	52	0.65
(Zn <sub>0.97</sub> Pd <sub>0.03</sub> O)	50	0.58
(Zn <sub>0.97</sub> Pt <sub>0.03</sub> O)	42	0.55

### 3.6.1.1. Pure ZnO and Co-doped ZnO nanostructures

We have studied the XRD patterns of the pure and (Zn<sub>1-x</sub>Co<sub>x</sub>O) where (X= 1 to 4) and are shown in Fig. 3.15. All the samples exhibited a hexagonal phase with a wurtzite structure (JCPDS No. 36-1451). The sharp peaks in these structures indicated that all the samples were highly crystalline. The strongest peak, which corresponds to (002) crystallographic direction, represents the preferred orientation. Co-related impurity phases such as those of metallic Co, cobalt oxides, and other compounds are not detected in the doped samples, indicating that Co<sup>2+</sup> replaces Zn<sup>2+</sup> in the ZnO lattice without changing the wurtzite structure [22, 23]. The lattice parameter (*c*) and average crystallite size (*D*) of the ZnO nanostructure are calculated using the XRD data according to the following equations (3.1), (3.4) [24, 25] respectively.

$$\sin^2 \theta = \frac{\lambda^2}{4} \left[ \frac{4}{3} \left( \frac{h^2 + hk + k^2}{a^2} \right) + \frac{l^2}{c^2} \right] \quad (3.4)$$

where  $\lambda$  (1.541 Å) is the wavelength of Cu K $\alpha$  radiation;  $\theta$  is the Bragg angle; *h*, *k*, and *l* are the Miller's indices; and  $\beta$  is the full-width at half maximum (FWHM) of the 002 peak. The calculated values are listed in Table 3.6. Fig.3.16 and Table 3.6 show that the lattice parameter *c* increases with increase in Co concentration. However, Zn<sup>2+</sup> possesses tetrahedral coordination with an ionic radius of 0.60 Å compared with Co<sup>2+</sup> in high spin state having ionic radius of 0.58 Å. Thus, the substitution of Co<sup>2+</sup> with Zn<sup>2+</sup> ions leads to a decrease in lattice parameters [25].

In the present study, the XRD peak is slightly, shifted towards a lower angle with increased Co-concentration, which results in an increase in the lattice parameter *c*. This result indicates that the Co<sup>2+</sup> ions in octahedral coordination with an ionic radius between 0.65 Å (low spin) and 0.745 Å (high spin) caused the unit cell to expand and consequently

the lattice parameter  $c$  is increased [27]. The crystallite size of the pure ZnO nanostructure is increased from 19.82 to 56.35 nm in the Co-doped ZnO (3 wt. %) nanostructure. Then the maximum value of (3%) Co-doped is (56.35 nm) is decreased with further increase in Co concentration to reach 33.83 nm for (4 wt. %) Co-doped. However, the crystallite size of the Co-doped ZnO nanostructures is larger than that of the pure ZnO one. This finding indicated that Co doping enhanced the crystal quality of the ZnO nanostructure. This result is consistent with those of previous studies [5, 28].

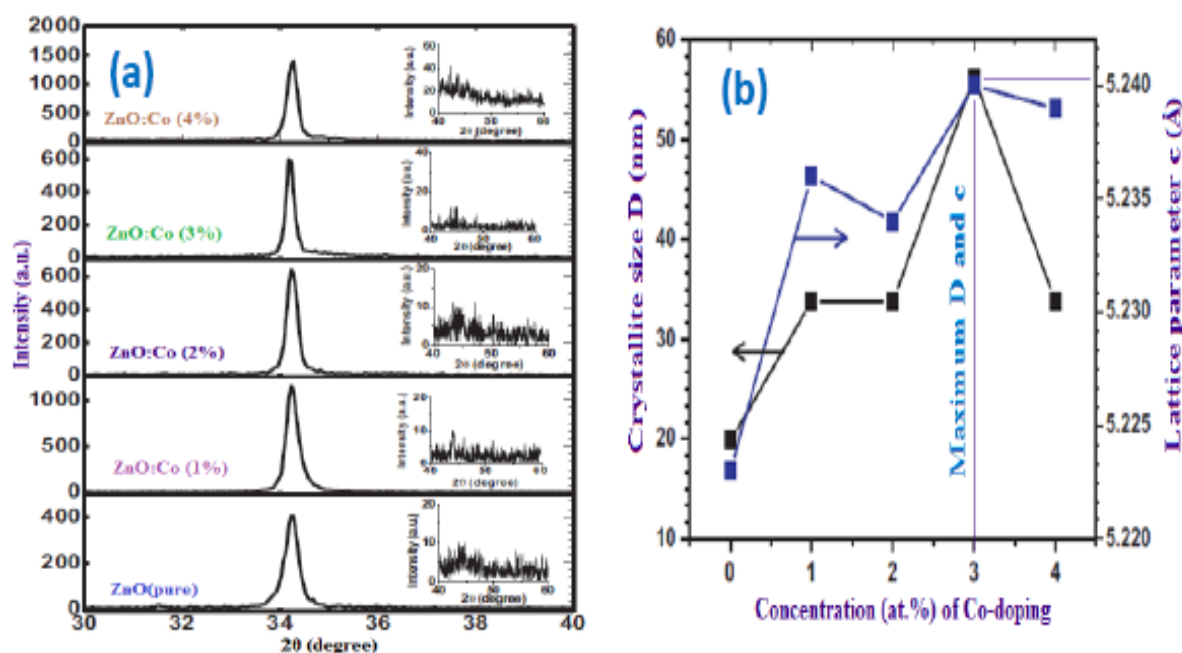


**Fig.3.16.** (a) X-ray diffraction (XRD) spectra of pure and Co-doped ZnO nanostructures prepared at room temperature range of (30–40°). The inset shows a magnified view of the XRD spectra within the range of (40–60°), (b) Crystallite size and lattice parameter of Co-doping as a function of the atomic percentage

**Table.3.6.** Structural, crystallite size and band-gap energy properties of pure and Co-doped ZnO nanostructures

Sample	$2\theta$ (°)	$c$ (Å)	FWHM (°)	D (nm)	$E_g$ (eV)
ZnO (pure)	34.3198	5.224	0.423	19.7	3.26
(Zn <sub>0.99</sub> Co <sub>0.01</sub> O)	34.2263	5.228	0.245	33.5	3.24
(Zn <sub>0.98</sub> Co <sub>0.02</sub> O)	34.2433	5.232	0.247	33.4	3.27
(Zn <sub>0.97</sub> Co <sub>0.03</sub> O)	34.2049	5.238	0.148	56.0	3.28
(Zn <sub>0.96</sub> Co <sub>0.04</sub> O)	34.2084	5.236	0.245	33.5	3.30

### 3.6.2. TEM analysis

Particle size and SAED pattern of TEM images of (a-b) (Zn<sub>0.97</sub>Ni<sub>0.03</sub>O) and (c-d) (Zn<sub>0.94</sub>Ni<sub>0.06</sub>O) nanostructures respectively are shown in Fig.3.17. The images clearly indicate that the average crystallite size is decreasing with an increase in Ni concentrations.

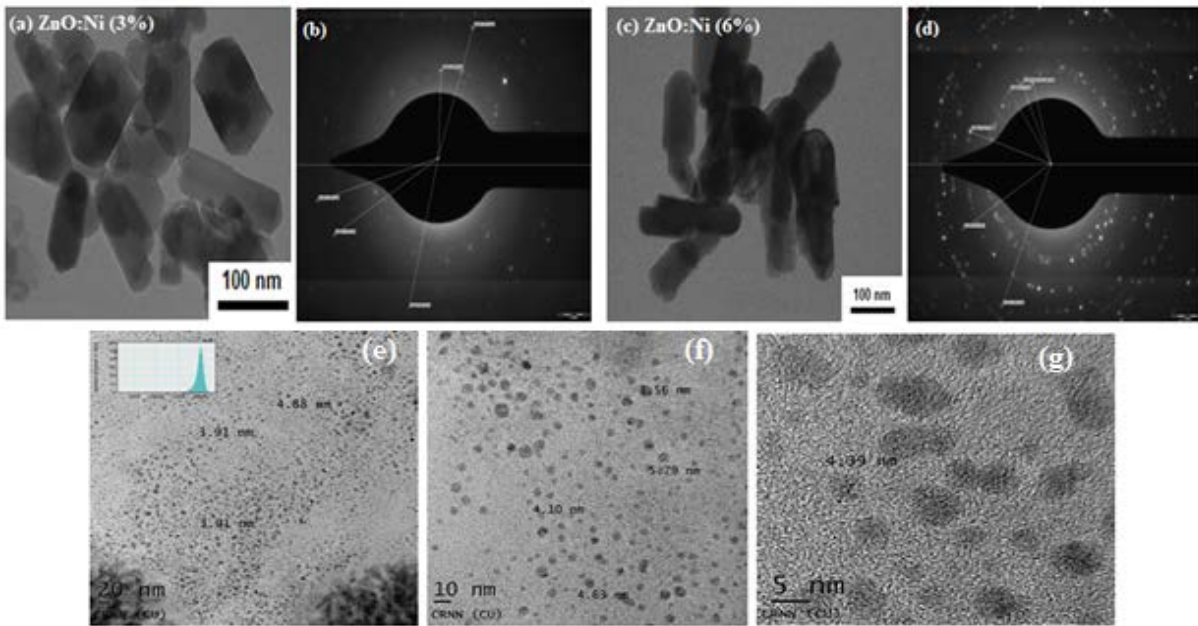


**Fig.3.17.** Particle size and SAED pattern of TEM images of (a-b) ( $Zn_{0.97}Ni_{0.03}O$ ) and (c-d) ( $Zn_{0.94}Ni_{0.06}O$ ) nanostructures respectively, (e-g) HRTEM images for 20,10 and 5 nm respectively [21]

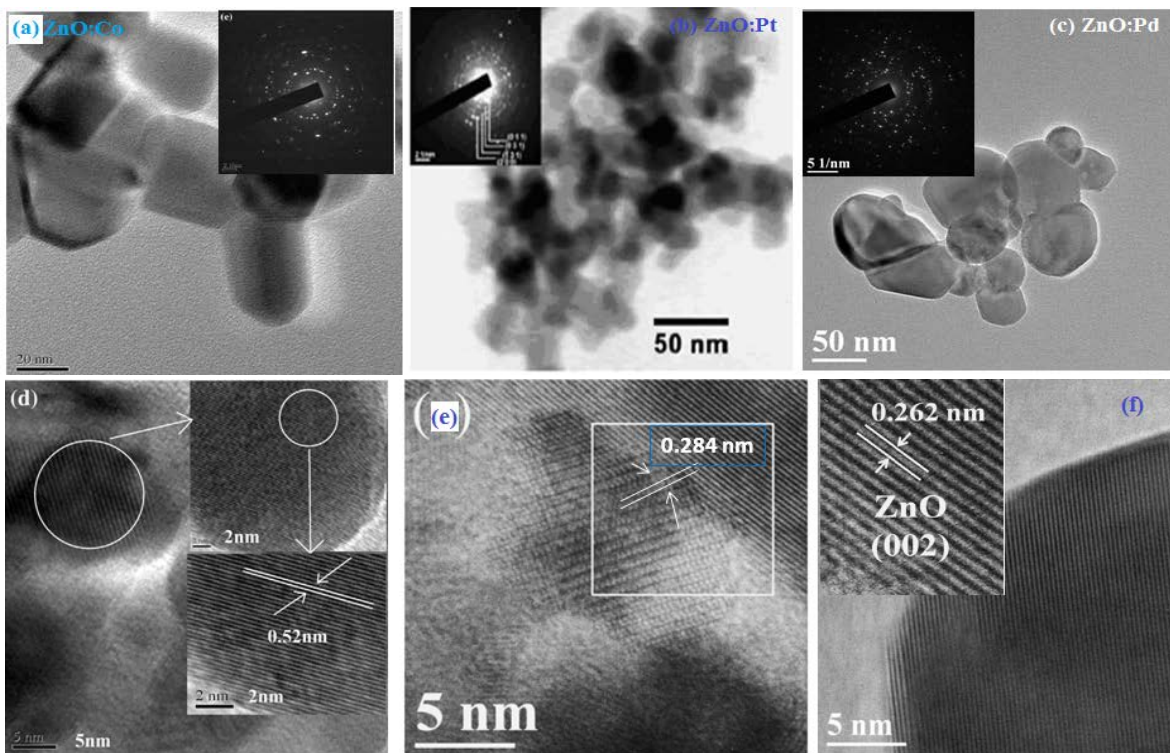


**Fig.3.18.** Particle size and SAED pattern of TEM images of (a) ( $Zn_{0.97}Co_{0.03}O$ ), (b) ( $Zn_{0.97}Pt_{0.03}O$ ) and (c) ( $Zn_{0.97}Pd_{0.03}O$ ) nanostructures, HRTEM images for 5 nm (d) ZnO:Co, (e) ZnO:Pt) and (f) ZnO:Pd [29]

The clarity of the rings in the selected area electron diffraction (SAED) pattern goes on decreasing with Ni-doped concentration which reveals that the particle sizes of Ni-doped



ZnO particles are decreasing. The  $(\text{Zn}_{0.94}\text{Ni}_{0.06}\text{O})$  powder show the diffuse ring pattern which indicates the more decrease in particle size as compared with  $(\text{Zn}_{0.97}\text{Ni}_{0.03}\text{O})$ . The particle size of pure ZnO nanostructures range from 40 nm to 70 nm and show crystalline nature in Fig. 3.4(a), while the crystal size for  $(\text{Zn}_{0.97}\text{Ni}_{0.03}\text{O})$  changes slightly as shown in Fig. 3.17(a-b). The remarkable decrease in the size of the particles is observed in  $(\text{Zn}_{0.96}\text{Ni}_{0.04}\text{O})$  nanostructured powders and is presented in Fig. 3.17 (c-d). The size of the particle for  $(\text{Zn}_{0.97}\text{Ni}_{0.03}\text{O})$  is about 30 nm to 50 nm and that of  $(\text{Zn}_{0.96}\text{Ni}_{0.04}\text{O})$  is about 5 nm to 20 nm, with some agglomeration, which might be the reason for decrease in surface area of these nanostructures and which is confirmed by HRTEM images shown in Fig.3.17(e-g).

### 3.6.3. AFM analysis

AFM is used to measure the surface morphology and grain size of the doped ZnO nanostructures over a Nano-scope analysis imaging software was used that covered  $(10\ \mu\text{m} \times 10\ \mu\text{m})$  area in contact mode. The two-dimensional (2D) and three-dimensional (3D) images of AFM micrographs are shown in Fig.3.19 (a, b, c) and (d, e, f), respectively.  $(10\ \mu\text{m} \times 10\ \mu\text{m})$  bi-dimensional AFM images of  $(\text{Zn}_{1-x}\text{M}_x\text{O})$ , where  $(\text{M} = \text{Ni}, \text{Co}, \text{W})$  nanostructures are shown in Fig.3.19 (a, b, c), respectively.

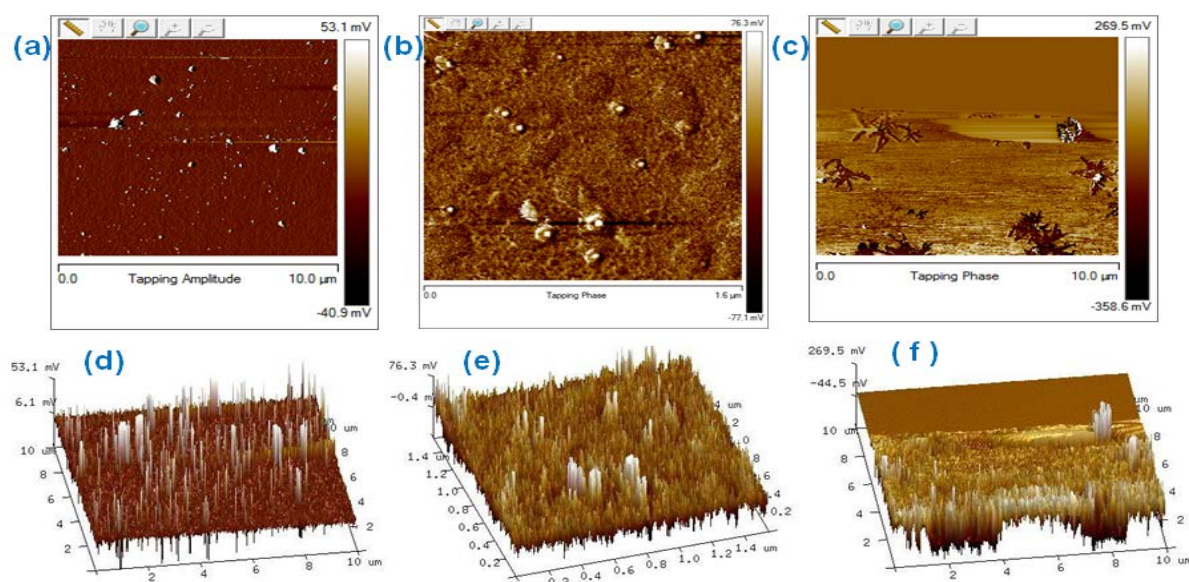


**Fig.3.19.** AFM images of doped ZnO nanostructures **2D** ( $10\ \mu\text{m} \times 10\ \mu\text{m}$ ): (a) ZnO:Ni, (b) ZnO:Co, and (c) ZnO:W; **3D** ( $10\ \mu\text{m} \times 10\ \mu\text{m}$ ): (d) ZnO:Ni, (e) ZnO:Co, and (f) ZnO:W [30]

It can be seen that all the samples have uniform and dense ZnO grains. The grains have a mixture of granular and columnar microstructures and they are in agreement with the result of SEM images. For scanning area  $(2 \times 2)\ \mu\text{m}^2$ , the root-mean squares (RMS) of average

surface roughness are determined as 7.82 nm, 9.38 nm, 10.36 nm for pure ZnO:Ni, ZnO:Co and ZnO:W nanostructures, respectively. As expected, the surface roughness increases as a result of increase in gains caused by the Ni, Co and W doping. The three-dimensional (3D) AFM images of all the samples are shown in Fig. 3.19 (d, e, f ). They have similar morphology to that in SEM measurement. In addition, it is apparent that the increase of surface roughness results from an increase in the average crystallite size in the ZnO nanostructures after Ni, Co and W doping.

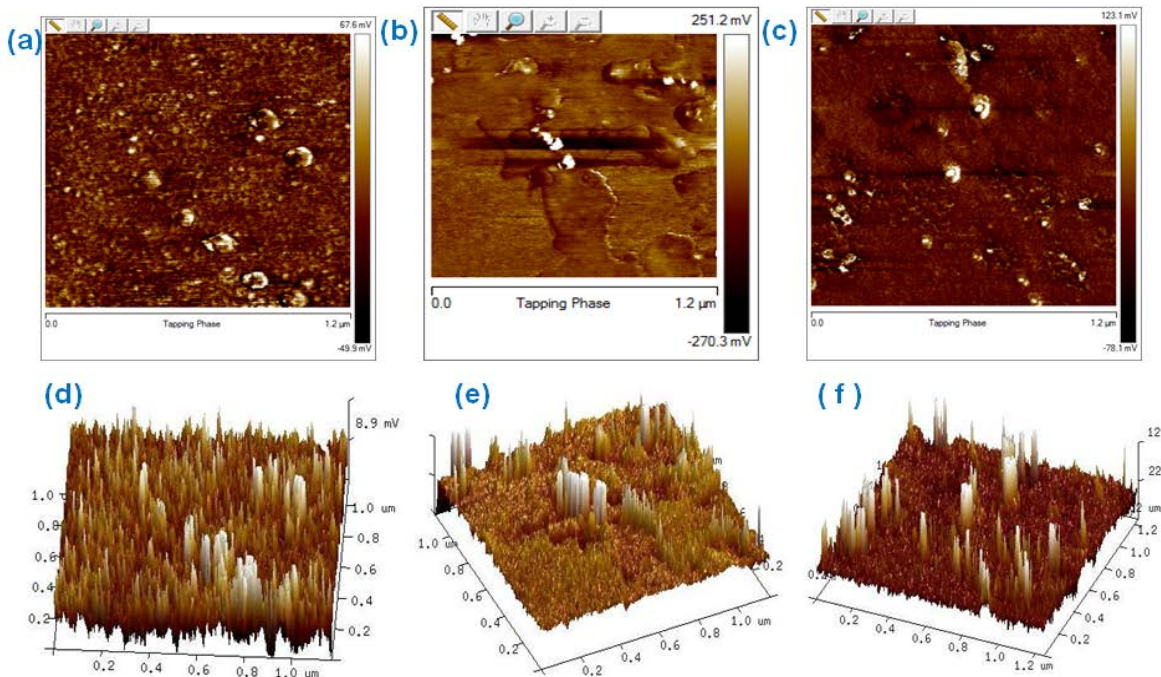


**Fig.3.20.** AFM images of doped ZnO nanostructures **2D** ( $1\ \mu\text{m} \times 1\ \mu\text{m}$ ): (a) ZnO:Pd, (b) ZnO:Pt, and (c) ZnO:Cd; **3D** ( $10\ \mu\text{m} \times 10\ \mu\text{m}$ ): (d) ZnO:Pd, (e) ZnO:Pt, and (f) ZnO:Cd

### 3.6.4. SEM analysis

The morphology of  $(\text{Zn}_{0.97}\text{Ni}_{0.03}\text{O})$  nanostructures are carried out using SEM with EDAX and is shown in Fig. 3.21. A glance at the SEM images of the samples shows a group of dark and bright regions.

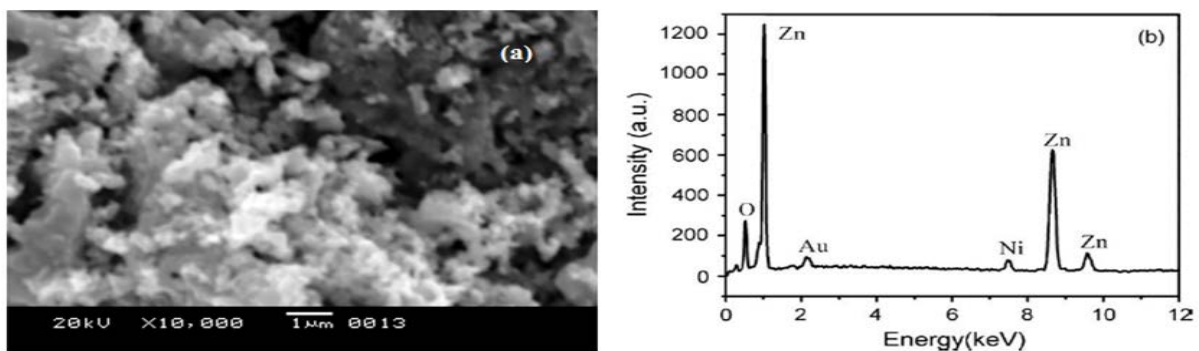


**Fig.3.21.** (a) SEM micrographs of  $(\text{Zn}_{0.97}\text{Ni}_{0.03}\text{O})$  nanostructures (b) EDAX analysis of ZnO:Ni nanoparticles [21]

Fig. 3.21(a) is taken in a resolution of 500 nm; a comparison of least count of particle in this SEM micrograph reveals the presence of the cluster formations surrounded by the pores. It is clearly observed that the cluster comprises of some tiny needle shaped particles. The SEM images shown in Fig. 3.21 (a) reveals that the particles are in nanometer range.

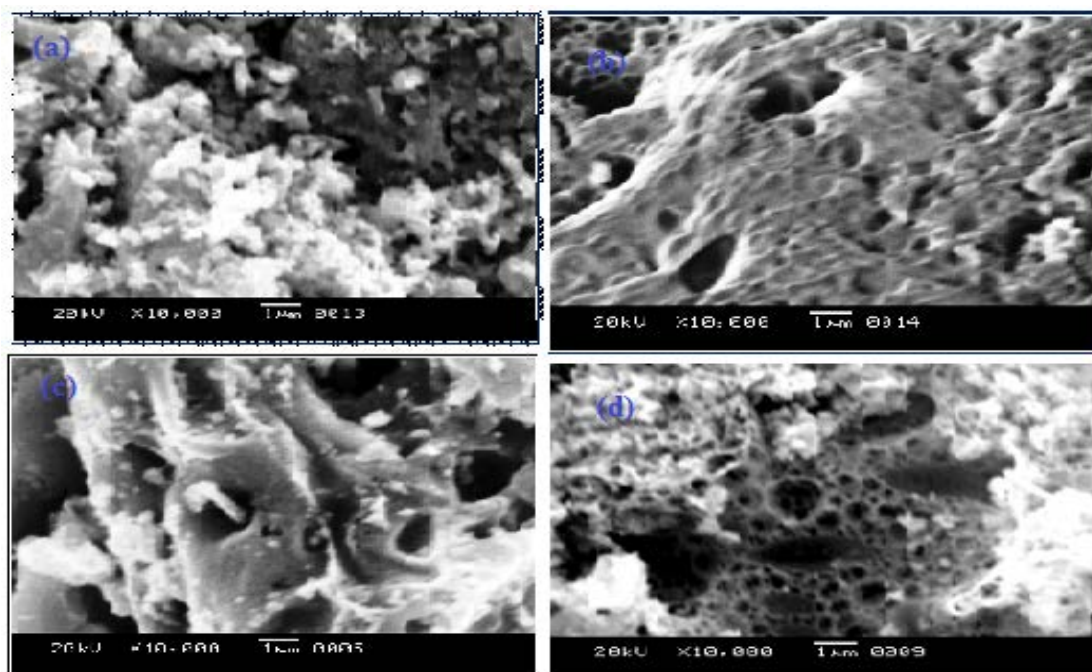


**Fig.3.22.** SEM images (a) ( $Zn_{0.97}Ni_{0.03}O$ ), (b) ( $Zn_{0.97}Co_{0.03}O$ ), (c) ( $Zn_{0.97}Pd_{0.03}O$ ), and (d) ( $Zn_{0.97}Pt_{0.03}O$ ) nanostructured powders sintered at  $400^{\circ}C$  for 3 hours [29]

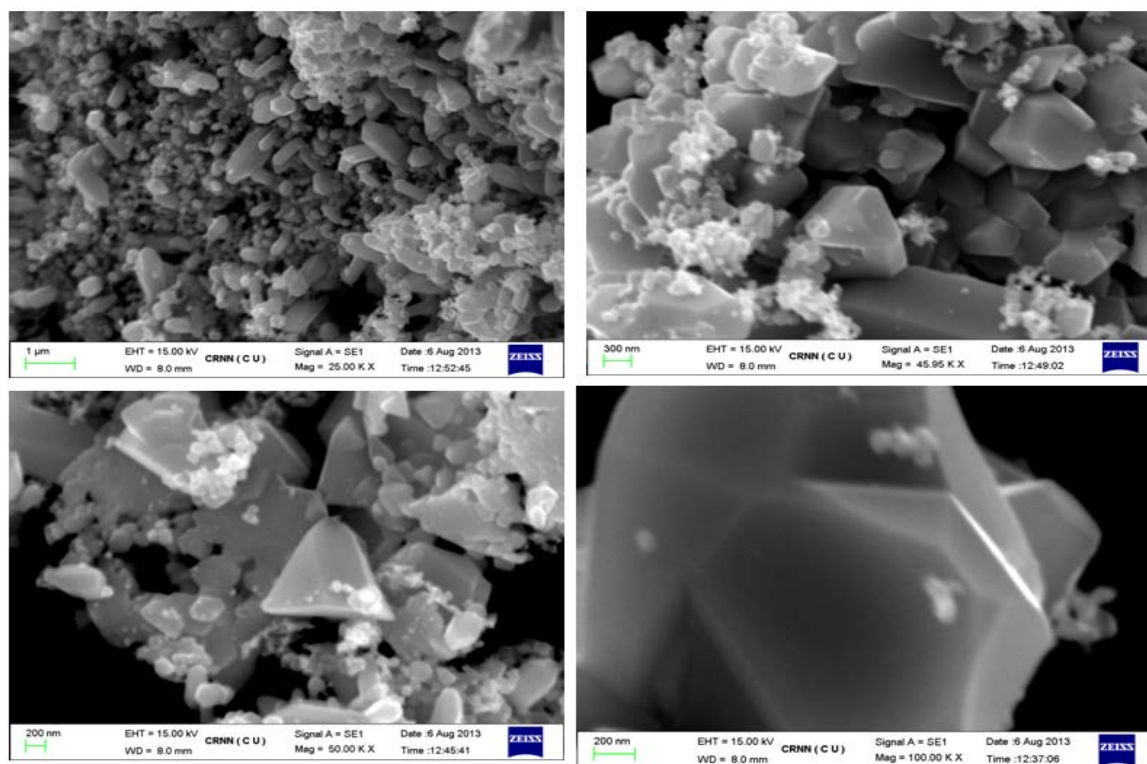


**Fig.3.23.** SEM images (a) ( $Zn_{0.97}Ni_{0.03}O$ ), (b) ( $Zn_{0.97}Co_{0.03}O$ ), (c) ( $Zn_{0.97}Pd_{0.03}O$ ), and (d) ( $Zn_{0.97}Pt_{0.03}O$ ) nanostructured powders sintered at  $600^{\circ}C$  for 5 hours [29]

### 3.6.5. FESEM analysis

The surface morphology of the nanostructures is studied by FESEM. Fig. 3.24(a-b) shows FESEM images of the metal doped ZnO nanostructures. It is seen that the surface morphologies of the nanostructures are almost homogeneous.

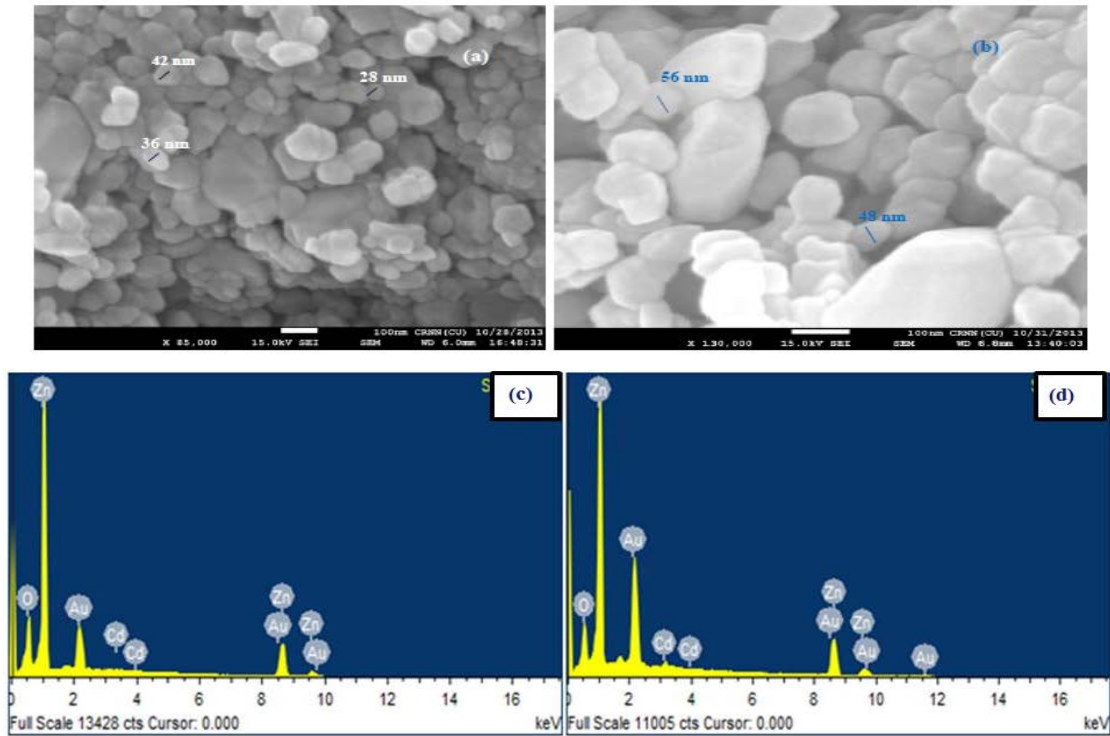


**Fig.3.24.** FESEM image of (a)  $(Zn_{0.98}Cd_{0.02}O)$ , and (b)  $(Zn_{0.97}Cd_{0.03}O)$  nanostructures; EDAX spectra of (c)  $(Zn_{0.98}Cd_{0.02}O)$ , and (d)  $(Zn_{0.97}Cd_{0.03}O)$  nanostructures

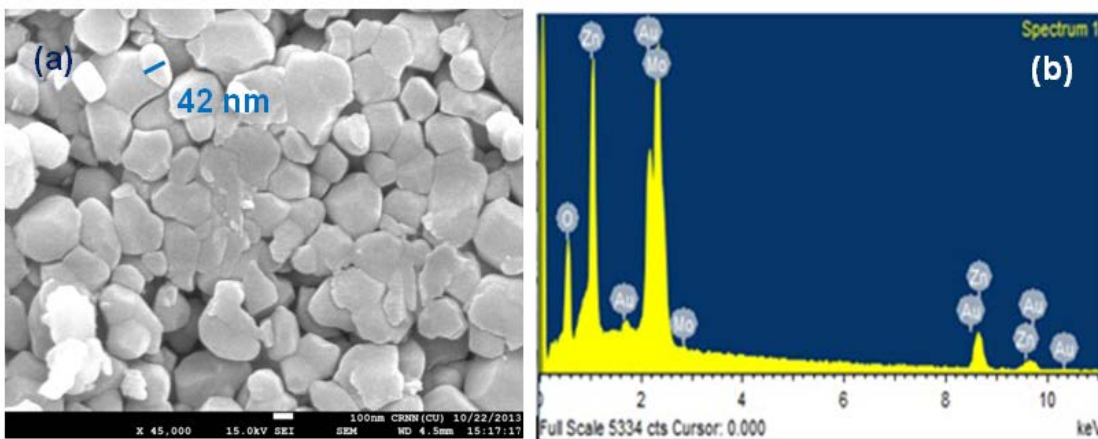


**Fig.3.25.** (a) FESEM image of  $(Zn_{0.97}Mo_{0.03}O)$ , and (b) EDAX spectra  $(Zn_{0.97}Mo_{0.03}O)$  [31]

The connective and partially cylindrical structures may originate from the formation of sintering necks between former possible spherical particles. Furthermore, the FESEM (100nm x 85,000 zoom) for  $(Zn_{0.98}Cd_{0.02}O)$  and (100nm x 130,000 zoom) for  $(Zn_{0.97}Cd_{0.03}O)$  images indicate that all the nanostructures have a wrinkle network with uniform size

distributions. The neck widths are influenced by the Cd content and they are measured in between 28 to 56 nm. The compositional analysis of the nanostructures is confirmed by EDAX analysis.

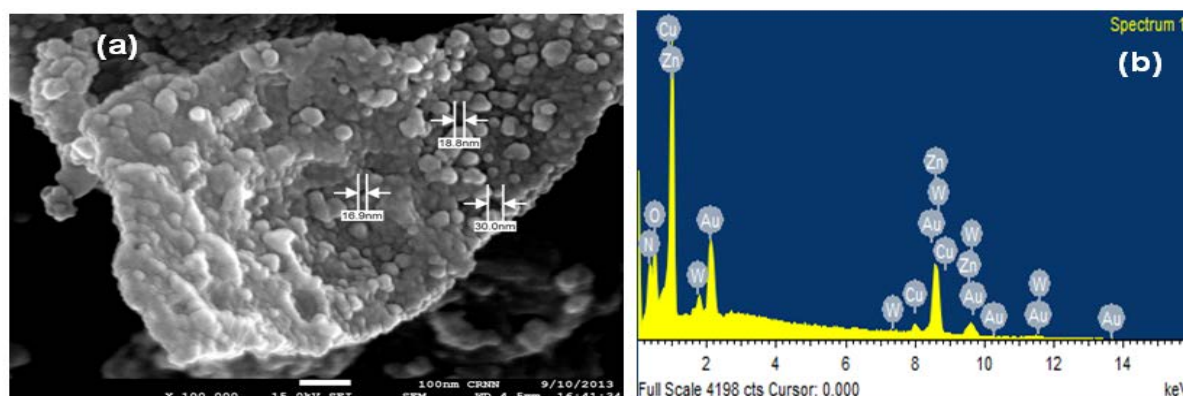


**Fig.3.26.** (a) FESEM image of  $(Zn_{0.97}W_{0.03}O)$ , and (b) EDAX spectra  $(Zn_{0.97}W_{0.03}O)$  [30]

### 3.7. Chemical Composition of doped ZnO nanostructures

#### 3.7.1. FTIR analysis

FTIR spectra of the samples are displayed in Fig. 3.27. A prominent absorption band at  $560\text{ cm}^{-1}$  is observed in the  $(Zn_{0.97}Co_{0.03}O)$  nanostructures that correspond to the stretching vibration of Co–O bond. The pure ZnO shows a prominent absorption band at  $430\text{ cm}^{-1}$ .  $(Zn_{0.97}Pd_{0.03}O)$  nanostructures show wide absorption band at around  $500\text{ cm}^{-1}$ . The presence of Zn–O vibration mode at  $430\text{ cm}^{-1}$  in ZnO and Co–O vibration mode at  $560\text{ cm}^{-1}$  in  $(Zn_{0.97}Co_{0.03}O)$  are confirmed [32].

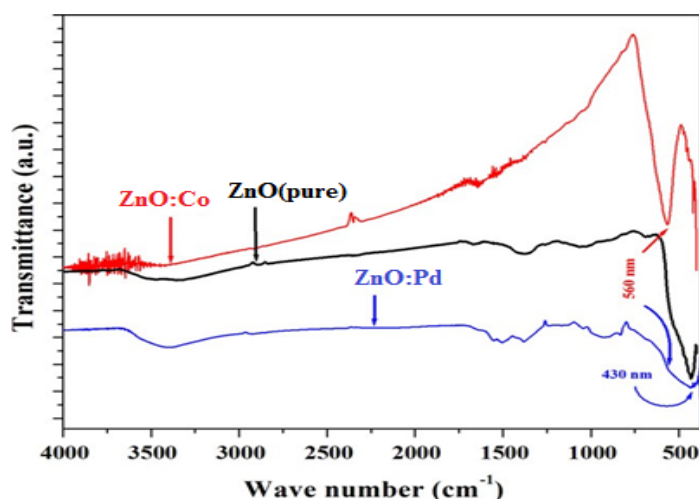


**Fig.3.27.** FTIR spectra of pure ZnO,  $(Zn_{0.97}Co_{0.03}O)$  and  $(Zn_{0.97}Pd_{0.03}O)$  nanostructures

Therefore, FTIR studies also confirm the formation of both ZnO and  $(Zn_{0.97}Co_{0.03}O)$  structures in the synthesized nanostructures. In addition to these absorption bands, the  $(Zn_{0.97}Co_{0.03}O)$  as well as  $(Zn_{0.97}Pd_{0.03}O)$  nanostructures have shown other absorption bands

at 1637, 1379 and 3400  $\text{cm}^{-1}$  that correspond to vibration modes of  $-\text{CO}-$ ,  $-\text{CH}-$  and  $\text{O}-\text{H}$  respectively. This shows the presence of trace amount of PVA on the surface of the prepared nanoparticles.

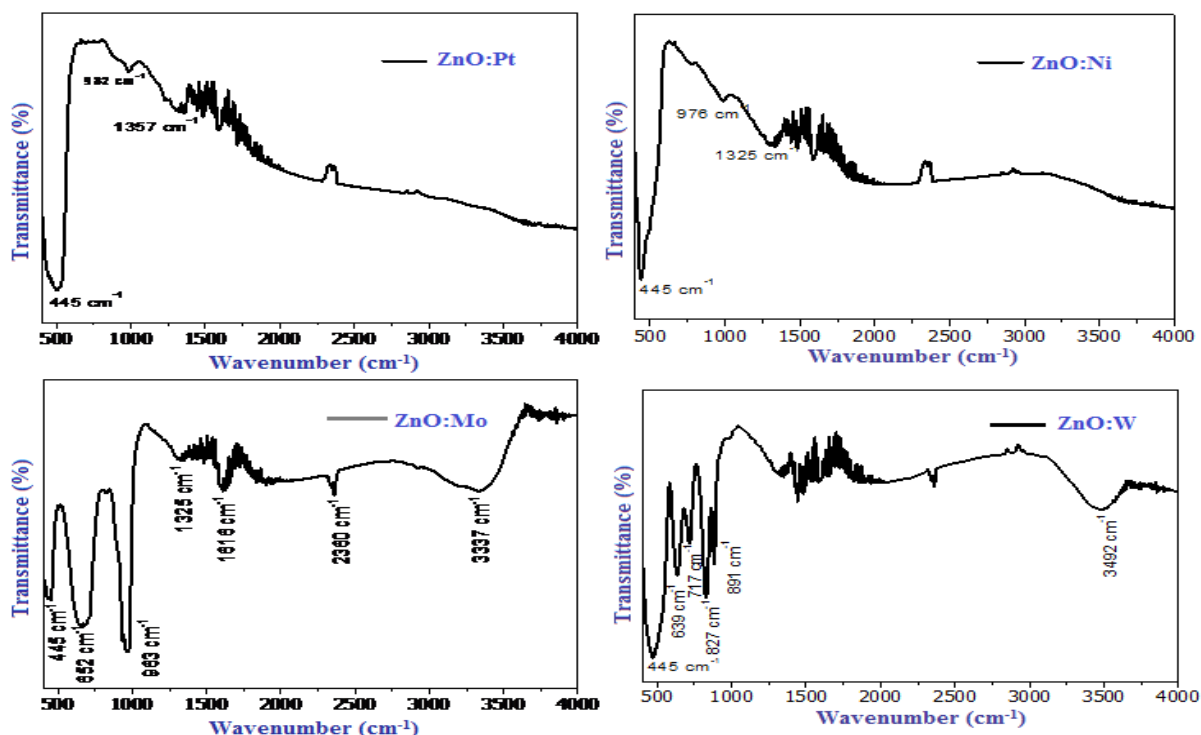


Fig.3.28. FTIR spectra of  $(\text{Zn}_{0.97}\text{Pt}_{0.03}\text{O})$ ,  $(\text{Zn}_{0.97}\text{Ni}_{0.03}\text{O})$ ,  $(\text{Zn}_{0.97}\text{Mo}_{0.03}\text{O})$  and  $(\text{Zn}_{0.97}\text{W}_{0.03}\text{O})$  nanostructures

### 3.7.2. EDAX analysis

The EDAX analysis of ZnO:Ni nanoparticles is carried out to establish purity of the samples and confirm presence of Ni. The observed EDAX patterns are shown in Fig. 3.21(b). It is noticed that the prepared samples contain only Zn, Ni and O. Thus the nanocrystallites are found to contain no spurious contamination. The ratio of the atomic percentage of the elements present in the samples complies with the quantity taken for their preparation. The EDAX spectra of the nanostructures are shown in Fig.3.24(c-d). The Au observed in the spectra may probably come from the gold coating on the nanostructures samples. The elemental weights (wt %) of Zn, O and Cd in the ZnO and Cd doped ZnO nanostructures are listed in Fig.3.24(c-d). The amount of Cd in ZnO structure is approximately the same as the both doping ratio (2% and 3%). These spectra show that the expected elements exist in the deposited nanostructures.

### 3.8. Conclusion

This chapter presents the structural and morphological properties of pure and doped ZnO nanostructures developed through chemical synthesis process. The ZnO nanostructures are

successfully synthesized by chemical synthesis method. The crystal structure and average crystallite size is measured using XRD, i.e., the structure is hexagonal wurtzite-type and average crystallite size is 56.4 nm. So, the measured particle sizes are almost same as obtained from XRD, DLS, AFM, and FESEM images. The spherically agglomerated bunches like structures are observed in SEM and FESEM images. The EDAX analysis concludes that the obtained particles are Zinc and Oxygen for pure ZnO nanostructures. AFM was used to evaluate the grain size, surface roughness and density of ZnO nanoparticles in 2D and 3D configurations of nanostructures. The uneven distributed nanostructures are observed in TEM and the selected area electron diffraction (SAED) supports the hexagonal structure. The doping ion successfully occupied ZnO lattice site and there are no secondary phases or precipitates in the samples. The size of ZnO decreases with the doping-concentrations in ZnO and is confirmed by XRD, TEM and EDAX analysis. FTIR spectra analysis confirmed the presence of traces of PVA on the surface of the prepared nanostructures.

## References

- [1] S. Wang, P. Li, H. Liu, J. Li, Y. Wei, The structure and optical properties of ZnO nanocrystals dependence on Co-doping levels, *Journal of Alloys and Compounds*, Volume 505, 2010, Pages 362-366.
- [2] M. H. Mamat, N. I. Ishak, Z. Khusaimi, M. M. Zahidi, M. H. Abdullah, S. Muhamad, N. D. M. Sin, M. R. Mahmood, Thickness-Dependent Characteristics of Aluminium-Doped Zinc Oxide Nanorod-Array-Based, Ultraviolet Photoconductive Sensors, *Japanese Journal of Applied Physics*, Volume 51, Issue 6s, 2012, Pages 06FF03.
- [3] A. Kasis, M. Saad, Fill factor losses in ZnO/CdS/CuGaSe<sub>2</sub> single-crystal solar cells, *Solar Energy Materials and Solar Cells*, Volume 80, 2003, Pages 491-499.
- [4] R. Kumar, N. Khare, Temperature dependence of conduction mechanism of ZnO and Co-doped ZnO thin films, *Journal of Thin Solid Films*, Volume 516, 2008, Pages 1302–1307.
- [5] E. V. Gritskova, D. M. Mukhamedshina, K. A. Mit, N. A. Dolya, K. A. Abdullin, The structure, photoluminescence, optical and magnetic properties of ZnO films doped with ferromagnetic impurities, *Physica B*, Volume 404, 2009, Pages 4816-4819.

- [6] S. K. Biswas, A. Sarkar, A. Pathak, P. Pramanik, Studies on the sensing behaviour of nanocrystalline  $\text{CuGa}_2\text{O}_4$  towards hydrogen, liquid petroleum gas and ammonia, *Talanta*, Volume 81, 2010, Pages 1607-1612.
- [7] N. Barsan, D. Koziej, U. Weimar, Metal oxide based gas sensor research: how to?, *Sensors and Actuators B: Chemical*, Volume 121, 2007, Pages 18-35.
- [8] N. Barsan, U. Weimar, Conduction Model of Metal Oxide Gas Sensors, *Journal of Electroceram*, Volume 7, 2001, Pages 3-143.
- [9] S. Pokhrel, C. E. Simion, V. Quemener, N. Bârsan, U. Weimar, Transduction in Semiconducting Metal Oxide Based Gas Sensors, *Sensors and Actuators B: Chemical*, Volume 133, 2008, Pages 1-78.
- [10] JCPDS-MDI's Mineral Database is included with JADE 7, [www.materialsdata.com](http://www.materialsdata.com).
- [11] F. M. Moghaddam, H. Saeidian, Controlled microwave-assisted synthesis of ZnO nanopowder and its catalytic activity for O-acylation of alcohol and phenol, *Materials Science and Engineering B*, Volume 139, 2007, Pages 265-269.
- [12] C. H. Ashok, K. R. Venkateswara, ZnO/TiO<sub>2</sub> nanocomposite rods synthesized by microwave-assisted method for humidity sensor application, *Superlattices and Microstructures*, Volume 76, 2014, Pages 46-54.
- [13] S. Pokhrel, C. E. Simion, V. Quemener, N. Barsan, U. Weimar, Chemical sensors measured gas sensitive resistance of the oxide's surface, *Sensors and Actuators B*, Volume 133, Issue 1, 2008, Pages 78-83.
- [14] Z. A. Khorsand, R. Razali, W. H. A. Majid, D. Majid, Synthesis and characterization of a narrow size distribution of zinc oxide nanoparticles, *International Journal of Nanomedicine*, Volume 6, 2011, Pages 1399-1403.
- [15] D. Rajesh, B. VaraLakshmi, C. S. Sunandana, Two-step synthesis and characterization of ZnO nanoparticles, *Physica B*, Volume 407, 2012, Pages 4537- 4539.
- [16] M. Wang, J. Wang, W. Chen, Y. Cui, L. Wang, Zinc Oxide Nanostructures: Growth, Properties and Characteristics, *Materials Chemistry and Physics*, Volume 97, 2006, Pages 219-225.



- [17] R. Elilarassi, G. Chandrasekaran, Structural, optical and magnetic properties of nanoparticles of ZnO:Ni-DMS prepared by sol-gel method, *Materials Chemistry and Physics*, Volume 123, 2010, Pages 450-455.
- [18] S. S. Shariffudin, M. Salina, S. H. Herman, M. Rusop, Effect of Film Thickness on Structural, Electrical, and Optical Properties of Sol-Gel Deposited Layer-by-layer ZnO Nanoparticles, *Transactions on Electrical and Electronic Materials*, Volume 13, Issue 2, 2012, Pages 102-105.
- [19] X. D. Yang, S. C. Su, Y. Xu, T. Mei, Effect of Thickness on the Structural, Electrical and Optical Properties of ZnO Films Deposited by MBE, *Advanced Materials Research*, Volume 311, 2011, Pages 1271-1276.
- [20] S. K. Min, G. Y. Kwang, L. J. Young, K. Soaram, N. Giwoong, L. D. Yul, S. K. Jin, S. K. Jong, Post annealing effect on thin film composed ZnO nano-particles on Thin films, *Journal of the Korean Physical Society*, Volume 59, 2011, Pages 2354 -2359.
- [21] S. C. Das, R. Bandyopadhyay, P. Pramanik, Nanostructured ZnO based Gas Sensors to use in Electronic Nose for Biochemical Compounds in Black Tea, *International Journal of Advanced Information Science and Technology*, Volume 29, Issue 29, 2014, Pages 124-128.
- [22] A. Wang, Z. Zhong, C. Lu, L. Lv, X. Wang, B. Zhang, Study on field-emission characteristics of electrodeposited Co-doped ZnO thin films, *Physica B*, Volume 406, 2011, Pages 1049–1052.
- [23] J. J. Hassan, Z. Hassan, H. A. Hassan, High-quality vertically aligned ZnO nanorods synthesized by microwave-assisted CBD with ZnO-PVA complex seed layer on Si substrates, *Journal of Alloys and Compounds*, Volume 509, 2011, Pages 6711–6719.
- [24] P. Li, S. Wang, J. Li, Y. Wei, Structural and optical properties of Co-doped ZnO nanocrystallites prepared by a one-step solution route, *Journal of Luminescence*, Volume 132, 2012, Pages 220-225.
- [25] H. Yang, S. Nie, Preparation and characterization of Co-doped ZnO nanomaterials, *Materials Chemistry and Physics*, Volume 114, 2009, Pages 279-282.
- [26] D. R. Acost, L. Castaneda, A. L. Suarez, A. G. Santiago, Cobalt-doped zinc oxide thin solid films deposited by chemical spray techniques on silicon (100) substrates: the

effects of the [Co]/[Zn] ratio on the morphological and physical properties, *Physica B*, Volume 404, 2009, Pages 1427-1431.

- [27] M. Vagadia, A. Ravalia, U. Khachar, P. S. Solanki, R. R. Doshi, S. Rayaprol, D. G. Kuberkar, Size and grain morphology dependent magnetic behaviour of Co-doped ZnO, *Materials Research Bulletin*, Volume 46, 2011, Pages 1933-1937.
- [28] C. Xu, L. Cao, G. Su, W. Liu, X. Qu, Y. Yu, Preparation, characterization and photocatalytic activity of Co-doped ZnO powders, *Journal of Alloys and Compounds*, Volume 497, 2010, Pages 373-376.
- [29] S. C. Das, B. Tudu, N. Bhattacharya, R. Bandyopadhyay, P. Pramanik, Doped ZnO Nanostructured Sensor in Electronic Nose for Detection of Ammonia, Hydrogen and Liquefied Petroleum Gas, *Advanced Nanomaterials and Nanotechnology : Springer-Verlag Berlin Heidelberg*, Chapter 47, 2013, Pages 473-482, DOI: 10.1007/978-3-642-34216-5(47).
- [30] S. C. Das, R. Bandyopadhyay, P. Pramanik, Development of W doped ZnO nanostructure chemoresistor pellet sensors for black tea aroma monitoring, *International Journal of Innovative Science, Engineering and Technology*, Volume 2, Issue 3, 2015, Pages 107-113.
- [31] S. C. Das, K. Sadani, R. Bandyopadhyay, P. Pramanik, Sensing characteristics of Molybdenum doped Zinc Oxide nanoparticles chemoresistor pellets towards black tea-biochemicals, *International Journal of Advances in Engineering Science and Technology*, Volume 3, Issue 3, 2014, Pages 120-131.
- [32] R. Y. Hong, S. Z. Zhang, G. Q. Di, H. Z. Li, Y. Zheng, J. Ding, D. G. Wei, Synthesis of Fe<sub>3</sub>O<sub>4</sub> Nanoparticles and their Magnetic Properties, *Materials Research Bulletin*, Volume 43, 2008, Pages 2457-2468.

## Chapter 4

# Optical, Electrical and Magnetic properties of pure and metal doped ZnO nanostructures

This chapter describes the optical, electrical and magnetic properties of the synthesized material. The optical properties are carried out using optical microscopy, UV-Vis spectrometry, Photoluminescence (PL) emission spectrometer and Cathodoluminescence (CL). The electrical (current-voltage I-V and switching) measurement is carried out using semiconductor characterisation system (SCS). Superconducting quantum interferences device (SQUID), Vibrating sample magnetometer (VSM) is used for magnetic properties M-H curve, coercivity, saturation magnetisation and remanence magnetization measurement at room temperature. Inside domain structures and configuration by magnetic force microscopy (MFM) have also been carried out and the results are presented here.

### *List of sections*

- 4.1. Introduction
- 4.2. Optical properties of ZnO nanostructures
  - 4.2.1. UV-Visible spectroscopy studies
  - 4.2.2. Photoluminescence (PL) studies
- 4.3. Optical properties of doped ZnO nanostructures
  - 4.3.1. UV-Visible spectroscopy analysis
  - 4.3.2. Photoluminescence (PL) analysis
  - 4.3.3. Cathodoluminescence (CL) analysis
- 4.4. Study of Electrical properties
  - 4.4.1. Current-voltage (I–V) characteristics
  - 4.4.2. Switching characteristics
  - 4.4.3. X-ray photoelectron spectroscopy (XPS) analysis
- 4.5. Study of Magnetic properties
  - 4.5.1. Vibrating sample magnetometer (VSM) analysis
  - 4.5.2. Magnetic force microscope (MFM) analysis
- 4.6. Conclusion
- References

*Contents of this chapter are based on following publication:*

1. S. C. Das, K. Sadani, R. Bandyopadhyay, P. Pramanik, Structural, Optical and Electrical properties of pure and transition metal doped zinc oxide nanostructures through chemical synthesis route, International Journal of Development Research, (accepted).



# Chapter 4

## Optical, Electrical and Magnetic properties of pure and metal doped ZnO nanostructures

### 4.1. Introduction

Zinc oxide nanomaterials have, of late, attracted a lot of attention to the scientists, particularly for their excellent optical, catalytic, and nontoxic properties. Solution-based synthetic schemes offer inherent advantages in terms of homogeneous systems, low temperatures, and low costs compared to other methods, in addition to ecological benefits [1-2]. Although various ZnO nanostructures, including nanoneedle arrays, nanotube arrays, nanosheets, and nanoporous structures, have been obtained by chemical synthesis methods, studies on morphology of ZnO nanostructures is scarce in literature. Transitional-metal-doped ZnO ( $Zn_{1-x}M_xO$ ) is one of the most promising dilute magnetic semiconductors (DMSs), which are envisioned as being promising building blocks for spintronic devices [3]. Nevertheless, the chemical synthesis of ( $Zn_{1-x}M_xO$ ) nanostructures is rather difficult as compared to that of pure ZnO. The properties of nanostructure are strongly dependent on their shapes and sizes. Therefore, the morphology-controlled synthesis of ( $Zn_{1-x}M_xO$ ) is very important for exploring the applications of these materials in spintronics, optics, catalysis, and so on [4]. In this thesis, we report a chemical synthesis route (combustion method) to synthesize (M= Co, Ni, Mn, Pt, Pd, Mo, W, Cd)-doped ZnO ( $Zn_{1-x}M_xO$ ) where (x = 1, 3, 5 wt %). We describe of the properties of the synthesized material i.e, optical microscopy, UV-Vis spectrometry, Photoluminecence (PL) emission, Cathodoluminescence (CL). The electrical (current-voltage I-V and switching) measurement is carried out by using semiconductor characterisation system (SCS). Characterization results with Superconducting quantum interferences device (SQUID) Vibrating sample magnetometer (VSM) for magnetic properties (M-H curve, coercivity, saturation magnetisation and remanence magnetization measurement at room temperature) inside the domain structures and configuration by magnetic force microscopy (MFM) have been described in this chapter.

## 4.2. Optical properties of ZnO nanostructures

### 4.2.1. UV-Visible spectroscopy studies

Absorption of visible and ultraviolet (UV) radiation is associated with the excitation of electrons, in both atoms and molecules, from lower to higher energy levels. Since the energy levels of matter are quantized, only light with the precise amount of energy can cause transitions from one level to another. In each possible case, an electron is excited from a full (low energy, ground state) orbital into an empty (higher energy, excited state) anti-bonding orbital. Each wavelength of light has a particular energy associated with it. If that particular amount of energy is just right for making one of these electronic transitions, then that wavelength will be absorbed [5]. Fig. 4.1(a) and (b) shows the electromagnetic spectrum and absorption of ultraviolet and visible radiation, respectively. The larger the gap between the energy levels, the greater the energy required to promote the electron to the higher energy level; resulting in light of higher frequency, and therefore shorter wavelength, being absorbed. The transmittance and the reflectance of the doped ZnO nanostructure powder sample soluble in millipore / di-ionised water deposited on transparent sapphire substrate are measured by a double beam spectrophotometer (Perkin Elmer, Lamda-1050, in Fig. 4.2(b). For liquid, the sample is held in an optically flat, transparent container called a cell or cuvette. The reference cell or cuvette contains the solvent in which the sample is dissolved and this is commonly referred to as the blank. The transmittance ( $I_T/I_0$ ) and the reflectance ( $I_R/I_0$ ) of the sample is measured as a function of wavelength ( $\lambda$ ) in the wavelength range 200 nm to 800 nm at a sampling interval of 1nm. The technique can be used both quantitatively and qualitatively. The light source (a combination of tungsten/halogen and deuterium lamps) provides the visible and near ultraviolet radiation covering 200 - 800 nm.

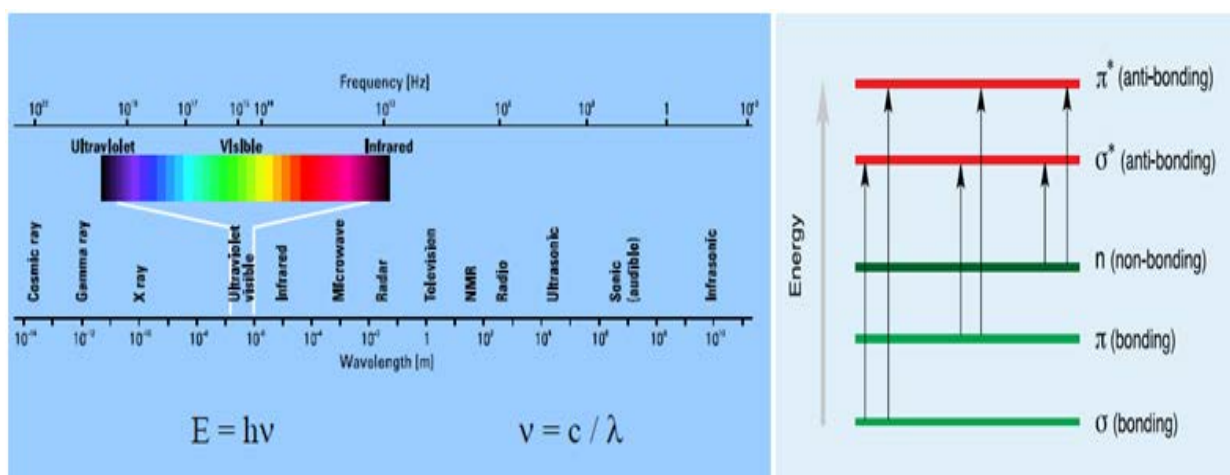


**Fig.4.1.**(a) The Electromagnetic spectrum, (b) Absorption of ultraviolet and visible radiation

The UV visible spectra of synthesized nanostructure in aqueous media showed excitonic absorption peak at 365 nm which is shown in Fig. 4.2 (a). The band-gap calculated from the UV cut-off is found to be 3.39 eV in ZnO nano-particle, which is nearly equal to that of ZnO semiconductor. This band gap value has blue shifted relative to the bulk zinc oxide having band gap of 3.37 eV.

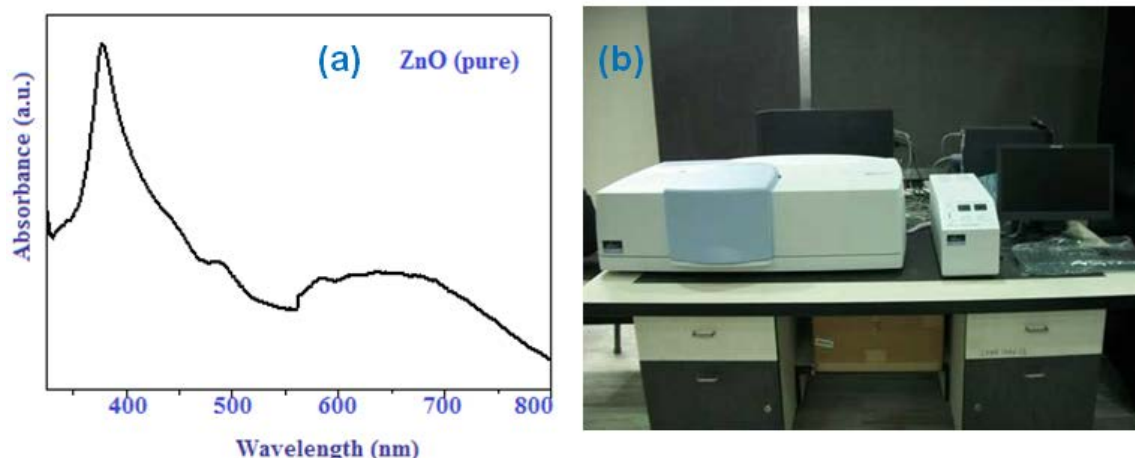


**Fig.4.2.** (a) UV absorption spectrum for pure nanostructured ZnO calcined at 500°C for 4 hours, (b) UV-vis spectrophotometer (Perkin Elmer, Lamda-1050 UV/Vis/NIR) at CRNN,CU

#### 4.2.2. Photoluminescence (PL) studies

Fig. 4.3(a) shows the room-temperature PL spectra of the ZnO nanostructure powder after annealing at 500°C for 5hrs. The ZnO nanostructure exhibited a weak peak at approximately 387 nm corresponding to near-band edge emissions (NBE) [6]. Broad emissions in the green-yellow band are also observed in the PL spectra. The visible emission located (centered) at 583 nm corresponds to oxygen vacancy and surface defect [7], which is formed due to high density surface trap states.

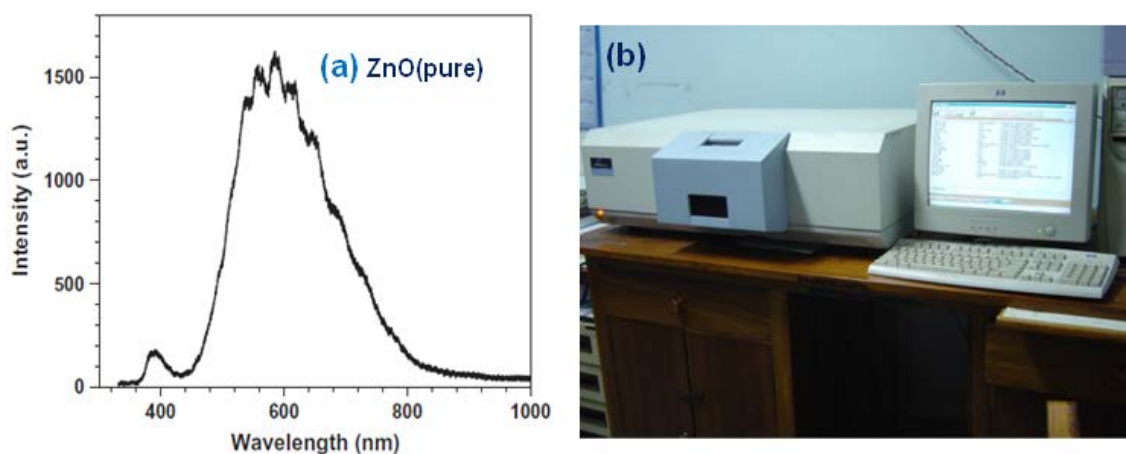


**Fig.4.3.**(a) Room temperature PL spectra of nanostructured ZnO calcined at 500°C for 4 hours, (b) Photoluminescence (PL) spectrometer (Perkin Elmer LS-55 ) at IUC, UGC, Salt Lake

The visible-to-UV intensity ratio ( $I_{VS}/I_{UV}$ ) of the PL peak is 9.78. This value indicates that the ZnO nanostructure lacked oxygen atoms, which is consistent with the EDX spectra. The mechanism of visible emission is explained by the transition of a photo generated electron from a shallow level (close to the conduction band edge) to a deeply trapped hole (a  $V_0^{**}$  center), resulting in the visible emission. The surface trapped hole can tunnel in to the particle, creating a  $V^{**}$  center (recombination center for visible emission) attributed to its recombination with an electron in an oxygen vacancy ( $V_0^*$ ) [8]. Fig. 4.3 (b) shows the Photoluminescence (PL) spectroscopy (Perkin Elmer LS-55) at IUC, UGC, Salt Lake.

### 4.3. Optical properties of doped ZnO nanostructures

#### 4.3.1. UV-Visible spectroscopy analysis

The UV-vis spectroscopy data and band-gap energy of our pure and metal doped nanostructured ZnO 3 wt % ( $Zn_{1-x}M_xO$ ), where ( $M= Ni, Co, Pt, Pd, W$  and  $Cd$ ) are shown in Fig. 4.4 (a) and (b).

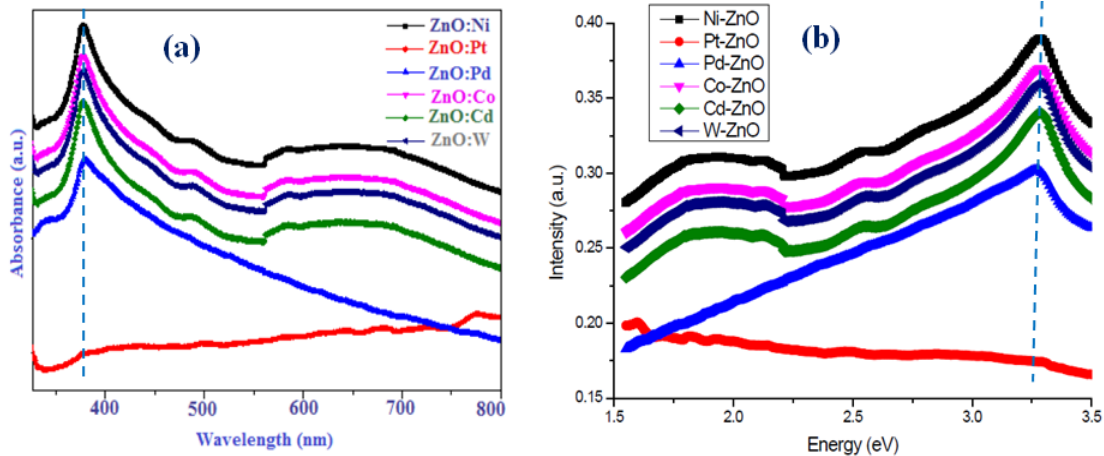


**Fig.4.4.** UV-vis spectra (a) Absorbance vs. wavelength (b) Intensity vs. energy of 3 wt % ( $Zn_{1-x}M_xO$ ), where  $M = Ni, Pt, Pd, Co, Cd$  and  $W$

Fig. 4.4 (a,b) shows UV-vis absorption spectra of the samples recorded at room temperature. Band-gap energies are calculated from the equation:

$$E_{BG}(eV) = hv = hc/\lambda \quad (4.1)$$

where  $E_{BG}$  is band-gap energy in eV,  $h=6.626 \times 10^{-34}$  J.S. is Planck's constant,  $c=3.00 \times 10^8$  m/s is the velocity of light and  $\lambda$  is the wavelength in ( $nm=10^{-9}$ m). The absorption peaks for the samples of metal doped 3 wt % ( $Zn_{1-x}M_xO$ ) nanostructures and pure ZnO are tabulated in Table 4.1. No optical absorption is observed for ( $Zn_{0.97}Pt_{0.3}O$ ) nanostructures due to the band gap being indirect. An absorption peak at about 370 nm (3.36 eV) is observed in pure



ZnO and its position gradually shifts towards higher wavelength as concentration of the magnetite increases in the nanostructure. This indicates that the band gap of ZnO is modified due to the formation of the nanostructure, where pure and Pt doped ZnO particles are bound by an adhesive force. In the nanoparticles, the 4s orbital of Pt may be mixed with the 4s orbital of Zn that results in formation of conduction band of ZnO at lower energy [9]. This fact explains the red-shift of the absorption peak in the nanostructure with increase in (Zn<sub>0.97</sub>Pt<sub>0.3</sub>O) nanostructure content. Basically transition metal (like Co, Ni, etc.) complexes are highly coloured, which is due to the splitting of the d-orbital's when the ligands approach and bond to the central metal ion. Some of the d-orbital's gain energy and some lose energy. The amount of splitting depends on the central metal ion and ligands. The transmittance is expected to decrease due to the three factors: oxygen deficiency, surface roughness and impurity centres. The optical transmittance spectrum of the samples gradually decreases in the visible region. Transmittance in the pure ZnO powder is almost 98% for the visible region [10].

**Table 4.1.** Absorption peaks and band-gap for the pure and doped ZnO nanostructure

Samples	Wavelength (nm)	Band-gap (eV)
ZnO (pure)	370 nm	3.36 eV
Zn <sub>0.97</sub> Ni <sub>0.3</sub> O	372 nm	3.34 eV
Zn <sub>0.97</sub> Co <sub>0.3</sub> O	374 nm	3.32 eV
Zn <sub>0.97</sub> W <sub>0.3</sub> O	374 nm	3.32 eV
Zn <sub>0.97</sub> Cd <sub>0.3</sub> O	374 nm	3.32 eV
Zn <sub>0.97</sub> Pd <sub>0.3</sub> O	376 nm	3.30 eV
Zn <sub>0.97</sub> Pt <sub>0.3</sub> O	-	Indirect band-gap

The band gap energy of the semiconductors can be estimated either from the UV-vis light absorbance or PL, spectra [11], both strategies revealed good results. The calculation on PL spectra is given below.

$$E_{BG}(\text{eV}) = \frac{1240}{\lambda_g} \quad (4.2)$$

where,  $\lambda_g$  is the absorption edge of the photocatalyst in nm. According to equation (4.2) the band gap  $E$  (eV) could be determined as about 2.33 eV which matches the reported value in the literature. It is well known that lower band gap suggests lower recombination rate of the electrons and holes. This finding proposes stable and efficient photocatalytic activity of both of pure and metal doped ZnO nanostructures due to the high separation and transferring of electrons and holes.

### 4.3.2. Photoluminescence (PL) analysis

PL spectroscopy is an important tool for investigating the electronic and optical properties of semiconducting materials. PL intensity may be directly correlated with the defect density in a fluorescent material. For nanostructured materials, PL spectra are very sensitive to the stoichiometry and surface states [12]. The PL spectra of the pure and 3 wt % (Co, Ni, W)-doped ZnO nanostructures recorded at room temperature are shown in Fig. 4.5.

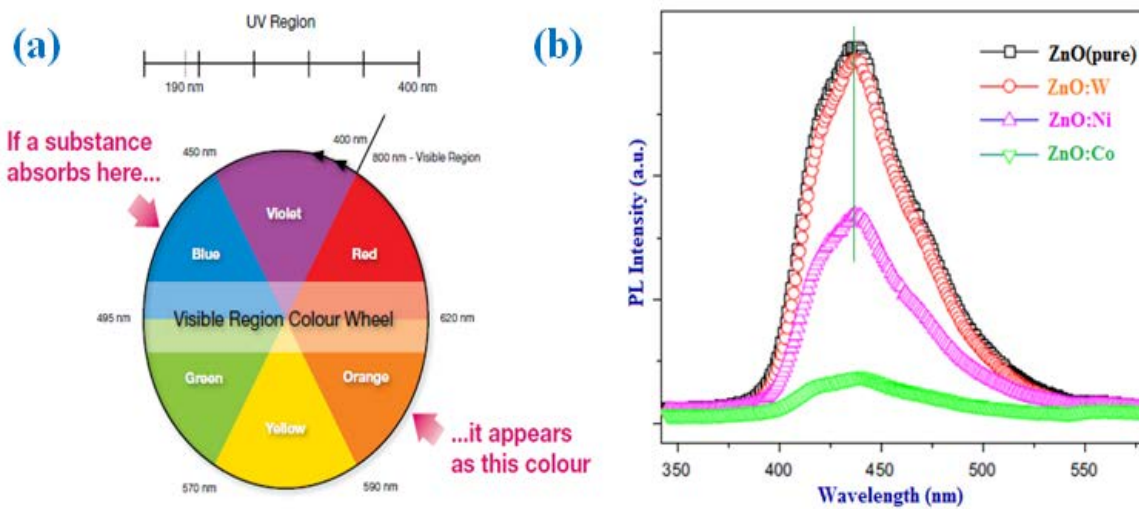


**Fig.4.5.(a)** Visible region colour wheel, **(b)** PL spectra of ZnO,  $(Zn_{0.97}Co_{0.3}O)$ ,  $(Zn_{0.97}Ni_{0.3}O)$  and  $(Zn_{0.97}W_{0.3}O)$  calcined at 600°C for 5 hours (Indicating luminescence emission in visible range)

In Fig. 4.5, the PL spectra of the nanostructures show a strong visible emission band around 400–560 nm, when the samples are excited by a light of wavelength 325 nm. The PL spectra of pure and metal (Co, Ni, W)-doped ZnO are analyzed by a Gaussian curve fitting as shown in Fig. 4.6 (a-d). The results of the peak fit show that the spectral band consisting of violet, blue and green regions. The peak positions obtained from fitting the spectra are given in Table 4.2.

**Table 4.2.** The peak positions of individual emission bands obtained from multiple Gaussian curve fitting of the PL data for ZnO,  $(Zn_{0.97}Co_{0.3}O)$ ,  $(Zn_{0.97}Ni_{0.3}O)$  and  $(Zn_{0.97}W_{0.3}O)$  nanostructures

Samples	Violet band (nm)		Avg. violet band (nm)	Blue band (nm)	Green band (nm)
<i>ZnO</i> (pure)	414.8	433.2	424.0	454.8	556.2
<i>Zn</i> <sub>0.97</sub> <i>Co</i> <sub>0.3</sub> <i>O</i>	416	435.4	425.7	453.0	566.0
<i>Zn</i> <sub>0.97</sub> <i>Ni</i> <sub>0.3</sub> <i>O</i>	415.4	434.2	424.8	456.4	556.4
<i>Zn</i> <sub>0.97</sub> <i>W</i> <sub>0.3</sub> <i>O</i>	415.2	433.4	424.3	456.3	556.4

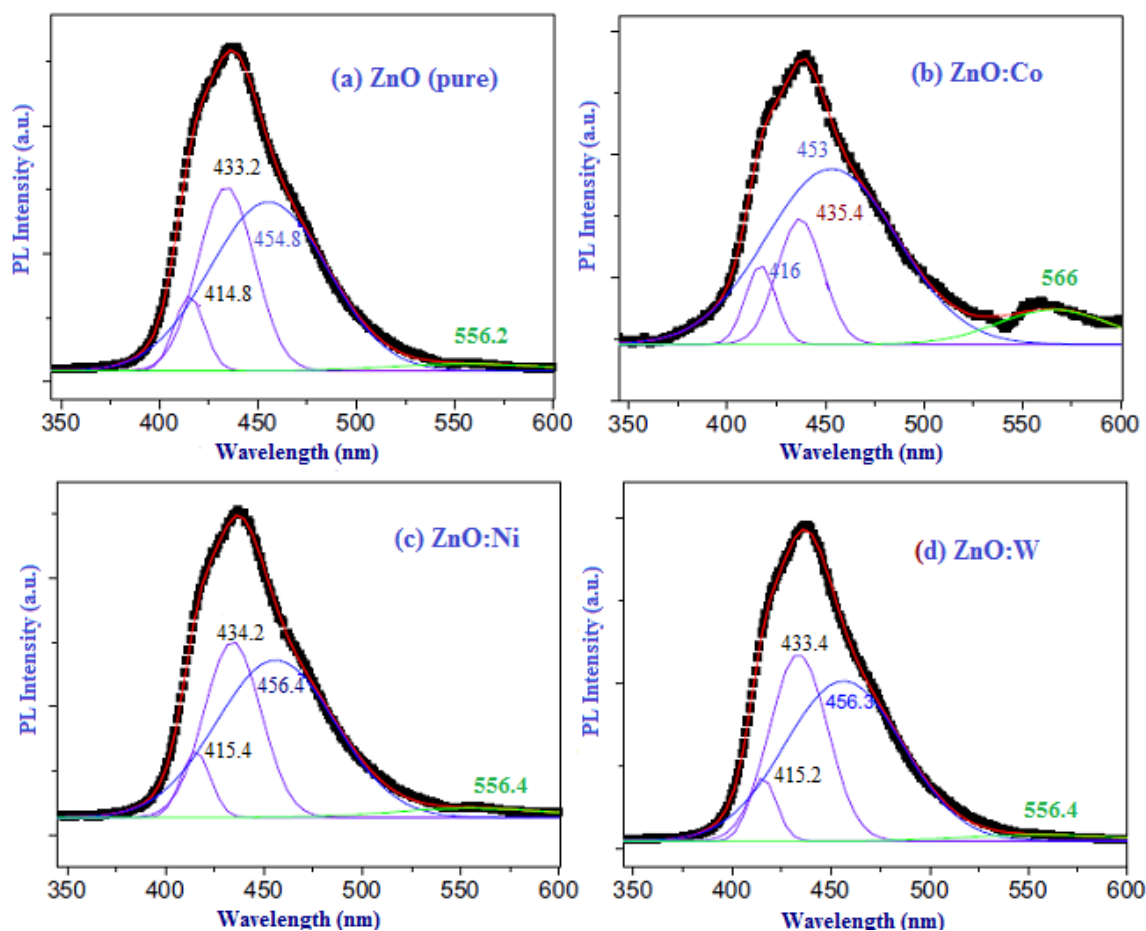


**Fig.4.6.** PL spectra fitted to multiple Gaussian curves for (a) ZnO, (b)  $(Zn_{0.97}Co_{0.3}O)$ , (c)  $(Zn_{0.97}Ni_{0.3}O)$  and (d)  $(Zn_{0.97}W_{0.3}O)$  sintered at  $600^{\circ}C$  for 5 hours

Notably, no appreciable shift in PL peaks is observed due to the metal doping in ZnO nanostructures. While the violet (424 nm) and blue (454 nm) emission peaks are strong, the green (556 nm) emission is very weak in all our samples. The violet emission band is convoluted into two peaks. However it could be a limitation of our curve fitting programme. We would consider the average violet emission peak positioned at  $\sim 424$  nm for the discussion. To our knowledge, there are no reports on the observation of only visible emission in pure and doped ZnO nanostructures. Nevertheless, there are reports showing very strong visible light emission in pure and doped ZnO nanostructures. For instance, the amorphous ZnO granular nanostructures show PL emission band due to oxygen vacancies ( $V_O$ ) and oxygen interstitials ( $O_i$ ) arising at 525 and 600 nm, respectively [13]. The violet emission peak at  $\sim 421$  nm is assigned to the recombination of an electron at zinc interstitial ( $Zn_i$ ) and a hole in the valance band (VB). The green emission at 527 nm results from the recombination of a hole with a oxygen vacancy state. Similarly, in ZnO-SiO<sub>2</sub> nanostructures, green-yellow emission transition arises from the conduction to deep trap

oxygen vacancy and the blue emission transition comes from the conduction band to zinc vacancies [14]. Recently, a strong visible light emission in ZnO quantum dots has been observed, where the green emission is attributed to the transition of electrons from the conduction band to a deep trap related mainly to defects on the surface, while the violet emission results from the transition of electrons from the shallow donor levels due to zinc interstitial ( $Zn_i$ ) of the valence band. We describe the observed visible emission in our ZnO nanostructures. Fig. 4.7 (a-b) shows the schematic energy levels of defects in ZnO [15]. The weak emission bands observed in the visible range are assigned to electronic transitions between different kinds of defect-related energy levels e.g.  $V_{Zn}$  (zinc vacancy),  $Zn_i$  (zinc interstitial) and  $V_O$  (oxygen vacancy) in ZnO nanostructures as shown in Fig. 4.7 (a). The violet emission band in the visible region ( $424 \text{ nm} = 2.92 \text{ eV}$ ) is attributed to electronic transition from  $Zn_i$  level to the top of the valence band, whereas the blue emission band in the visible region ( $454 \text{ nm} = 2.73 \text{ eV}$ ) is due to electronic transition from the  $Zn_i$  level to the  $V_{Zn}$  level [16]. The green emission ( $556 \text{ nm} = 2.23 \text{ eV}$ ) band is assigned to electronic transition from the bottom of the conduction band to the  $V_O$  level [17] though there is no consensus on the cause of the green emission [18]. In Fig. 4.7(b) the oxygen vacancy states,  $V_o^{\cdot}$  and  $V_o^{\cdot\cdot}$  are located at  $\sim 2.0$  and  $\sim 2.2 \text{ eV}$  respectively below the conduction band (CB). The shallow acceptor levels corresponds to zinc vacancies ( $V'_{Zn} / V''_{Zn}$ ) and oxygen interstitials ( $O_i$ ) (not shown here) are positioned above the valence band (VB). The zinc vacancies,  $V'_{Zn}$  and  $V''_{Zn}$  are situated at  $\sim 0.7$  and  $\sim 2.8 \text{ eV}$  respectively above the VB.

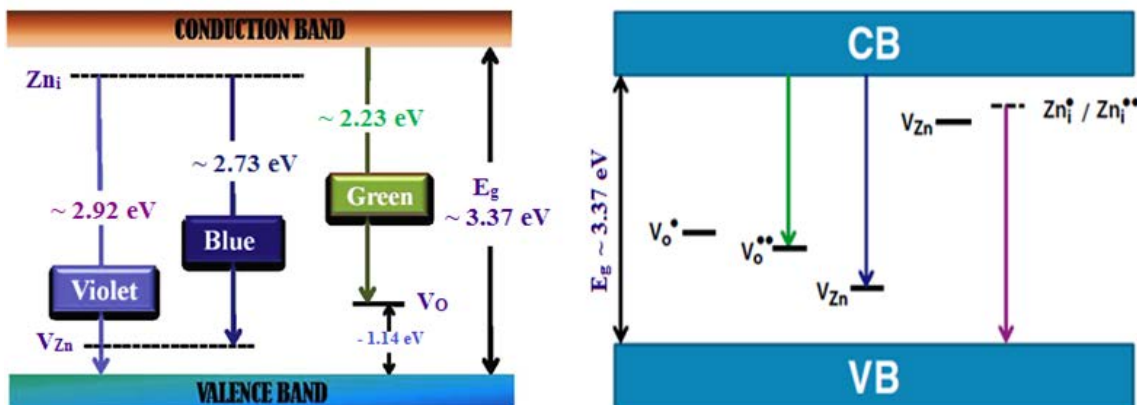


**Fig.4.7.**(a) Schematic band diagram of the defect levels of ZnO obtained from PL spectra and (b) Schematic energy levels of defects in ZnO

The zinc interstitial ( $Zn_i^{\cdot} / Zn_i^{\cdot\cdot}$ ) possesses a shallow donor level at 0.22–0.53 eV below the CB. Using this schematic diagram, we could explain the observed violet, blue and green emissions in the wavelength range 400–560 nm in our pure and metal doped ZnO

nanostructures samples. First of all, the violet emission ( $\sim 2.92$  eV) arises from the recombination of an electron from zinc interstitial ( $Zn_i^\bullet / Zn_i^{**}$ ) and a hole in the valence band. Secondly, the blue emission ( $\sim 2.73$  eV) is the result of recombination of photo generated hole with the singly ionized zinc vacancy ( $V_{Zn}^\bullet$ ). Finally, the green emission ( $\sim 2.23$  eV) could result from the recombination of photo generated hole with the doubly ionized oxygen vacancy,  $V_o^{**}$ . Incidentally, the near band edge (NBE) emission is not observed at 380 nm in the PL data of any of our ZnO nanostructures. Similar observations are reported, where the absence of band edge peak with emission band in visible region is observed in ZnO, due to the defect states in ZnO [19]. We also believe that the possible defects in our chemically synthesized pure and metal doped ZnO nanostructures could play the major role in suppressing the NBE emission. The 3d states of the metal ion doped ZnO have the bonding states, corresponding to localized electrons lie within VB, whereas the antibonding states, corresponding to traveling electrons, lie close to the bottom of the CB [20].

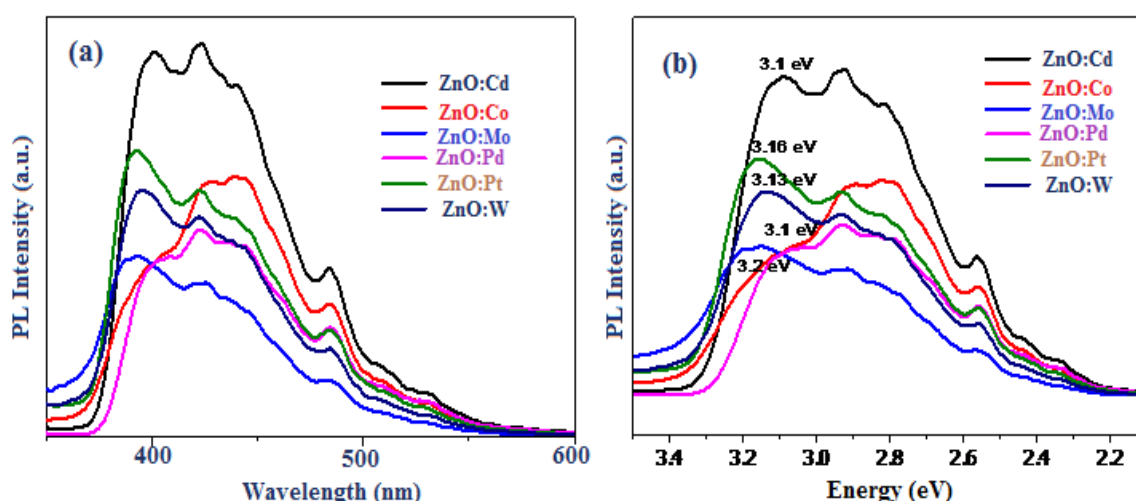


**Fig.4.8.**(a) PL intensity vs. wavelength, (b) PL intensity vs. energy of doped ZnO nanostructures sintered at 400°C for 3 hours

The dopant states are playing a role in reducing the NBE emission by non-radiative recombination. The free electrons recombine via metal ion states rather than populating donor–acceptor pairs. However the effectiveness of non-radiative recombination process depends on the metal-dopant concentration, carrier-trapping rates and ionization cross section of metal ions and host. We found that the defect states are not affected much by the metal doping in ZnO. On the other hand, a decrease in luminescence intensity is observed in our metal doped ZnO nanostructures compared to the pure one. Possibly, the non-radiative recombinations takes places due to the metal dopant states and are playing a role in

reducing the intensity of the visible emission due to defect states in our metal doped ZnO nanostructures. Suppression in PL intensity is reported in the case of Ni doped ZnO samples, where it is attributed to similar processes [21].

### 4.3.3. Cathodoluminescence (CL) analysis

CL is an effective technique for studying the optical properties of nanostructures. Fig. 4.9 shows the CL spectra measured at room temperature of the  $(\text{Zn}_{0.97}\text{Ni}_{0.3}\text{O})$  and  $(\text{Zn}_{0.97}\text{Co}_{0.3}\text{O})$  samples. Two emission bands, UV emission and visible emission, can be seen in the spectra. For  $(\text{Zn}_{0.97}\text{Ni}_{0.3}\text{O})$ , the UV emission is stronger than the visible emission, whereas for  $(\text{Zn}_{0.97}\text{Co}_{0.3}\text{O})$ , the UV emission is weakened, and the visible emission is stronger. The UV emissions of the two samples are almost centered at about 382 nm, which comes from the combinations of the excitons [22]. Compared to the band edge of pure ZnO [23], the UV emissions of  $(\text{Zn}_{0.97}\text{Ni}_{0.3}\text{O})$  and  $(\text{Zn}_{0.97}\text{Co}_{0.3}\text{O})$  are red-shifted by about 54 meV, and similar results are observed in Ni-doped ZnO films and nanowires [24]. Within this range of dopant concentration, the band edge of ZnO:Ni and ZnO:Co changed slightly and is red-shifted by about 64 meV compared to that of pure ZnO according to optical adsorption results, which is in agreement with our results. This red shift is caused by the sp-d exchange interaction [25].

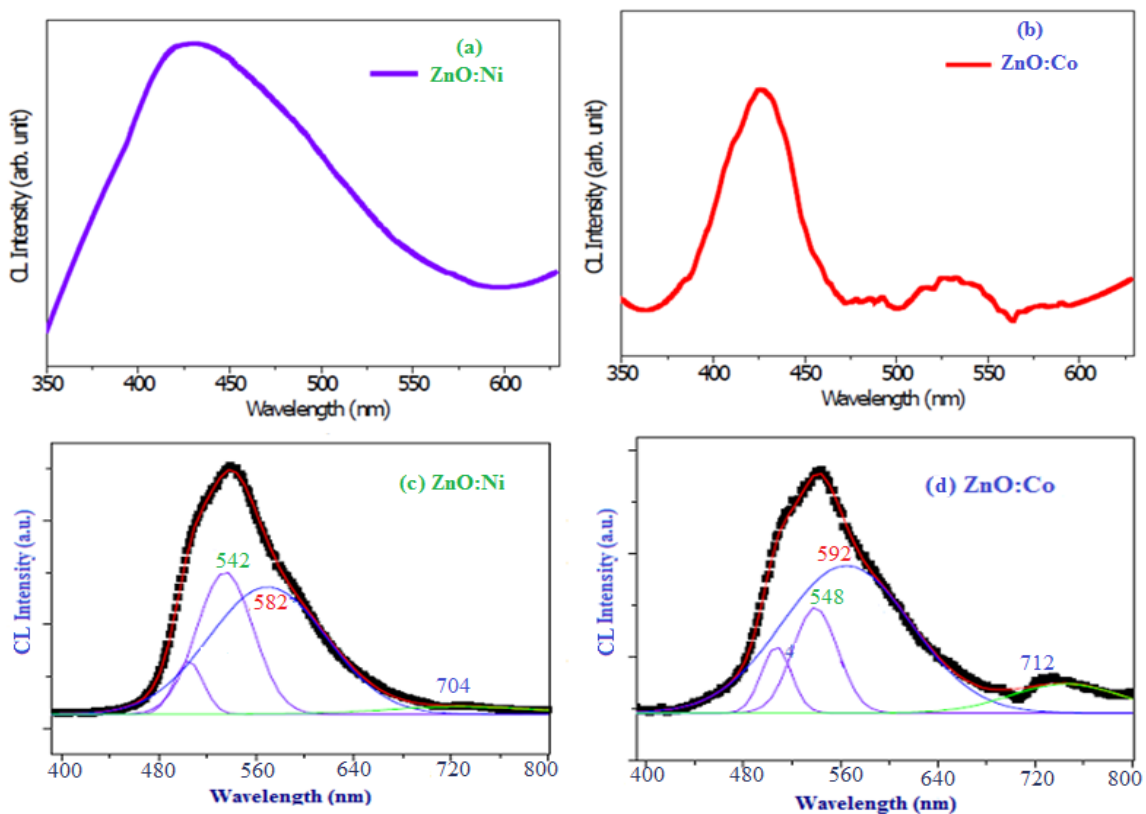


**Fig.4.9.** CL spectra of (a, c)  $(\text{Zn}_{0.97}\text{Ni}_{0.3}\text{O})$  and (b, d)  $(\text{Zn}_{0.97}\text{Co}_{0.3}\text{O})$  nanostructures, (c, d) visible emission parts of spectra (a) and (b)

The visible emissions can be divided into three emission bands (emission 1, emission 2, and emission 3) by Gauss fitting, as shown in Fig. 4.9 (c, d) and the results are listed in Table 4.3. According to literature studies, these visible emissions, especially emission 1 and emission 2, are usually ascribed to deep-level defects, such as oxygen vacancies, zinc interstitial atoms, and so on [22-25]. The variations in the relative intensities of the UV emission and the visible emission in the CL spectra are related to the different defect concentrations in  $(\text{Zn}_{0.97}\text{Ni}_{0.3}\text{O})$  and  $(\text{Zn}_{0.97}\text{Co}_{0.3}\text{O})$  [26, 27].

**Table 4.3.** UV and visible emission peaks in the CL spectra of the  $(\text{Zn}_{0.97}\text{Ni}_{0.3}\text{O})$  and  $(\text{Zn}_{0.97}\text{Co}_{0.3}\text{O})$  at room temperatures

Emission peaks	Wavelength (nm)		Energy (eV)	
	$(\text{Zn}_{0.97}\text{Ni}_{0.3}\text{O})$	$(\text{Zn}_{0.97}\text{Co}_{0.3}\text{O})$	$(\text{Zn}_{0.97}\text{Ni}_{0.3}\text{O})$	$(\text{Zn}_{0.97}\text{Co}_{0.3}\text{O})$
<i>UV emission</i>	386	390	3.21	3.18
<i>emission 1</i>	542	548	2.29	2.26
<i>emission 2</i>	582	592	2.13	2.09
<i>emission 3</i>	704	712	1.76	1.74

Emission 3 in the visible range is located at about 704 nm (1.76 eV in energy) and 712 nm (1.74 eV in energy) for  $(\text{Zn}_{0.97}\text{Ni}_{0.3}\text{O})$  and  $(\text{Zn}_{0.97}\text{Co}_{0.3}\text{O})$ , respectively. The emission at ~640-650 nm in ZnO is due to the presence of oxygen-rich in samples [28, 29]. The samples are oxygen-poor in our experiments, and there are fewer oxygen vacancies in  $(\text{Zn}_{0.97}\text{Ni}_{0.3}\text{O})$  than in  $(\text{Zn}_{0.97}\text{Co}_{0.3}\text{O})$ . However, emission 3 is weaker for  $(\text{Zn}_{0.97}\text{Ni}_{0.3}\text{O})$  than for  $(\text{Zn}_{0.97}\text{Co}_{0.3}\text{O})$ , as shown in Fig.4.9 (c) and (d).

## 4.4. Study of Electrical properties

### 4.4.1. Current-voltage (I-V) characteristics

ZnO is exploited in other niche applications such as transparent electrodes, diodes, light emitting diodes, photodiodes and transistors [30]. Response is an important aspect of ZnO, which has attracted unique attention. Many ZnO-based photodiodes with high performance, consisting of *p-n*, *p-i-n*, schottky junction, metal-insulator-metal (MIM) and metal-semiconductor-metal (MSM) structures are reported [31]. For instance, ZnO photodiodes with MSM junctions are studied with Au, Ag, Ni, Pd, etc., contacts fabricated by molecular beam epitaxy, radio frequency magnetron sputtering and atomic-layer deposition [32-34]. The slow response time ranging from a few minutes to hours is reported for ZnO films [35, 36]. Nevertheless, there are reports on ZnO nanostructures showing fast response time, which is due to high conductance in its reduced dimensionality [37]. The current-voltage (I-

V) characteristics and switching measurements of the doped ZnO nanostructures are measured using Model 4200 semiconductor characterization system (SCS) from Keithley Instruments, USA at CRNN, C.U. The photoresponse of our films is studied by illuminating the samples with a 60 W incandescent lamp.

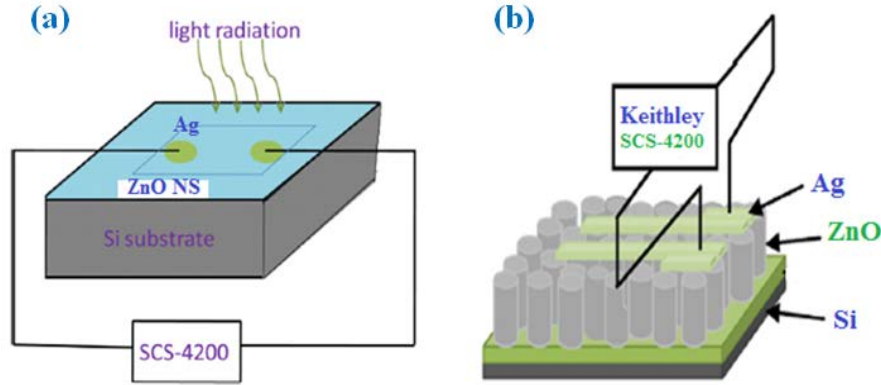


**Fig. 4.10.(a,b)** Schematic diagram of the fabricated MSM (Ag/ZnO/Ag) or (Ag/doped ZnO/Ag) Schottky diode

The schematic diagram of the planar [Ag/ZnO/Ag] or [Ag/ZnO:(Co,Ni,W)/Ag] devices fabricated in (metal-semiconductor-metal) MSM geometry for photo response measurement is shown in Fig.4.10.(a,b). On the ZnO nanostructures, top Ag contacts form schottky junctions in MSM configuration [38]. The light is illuminated through the exposed square area of 2.8 mm × 2.8 mm. The current-voltage (I–V) characteristics of the [Ag/ZnO/Ag] and [Ag/ZnO:(Co, Ni, W)/Ag] devices are shown in Fig.4.11(a–d). The I–V plots are measured in the voltage range ±10 V, showing a nonlinear and nearly symmetric behaviour under forward and reverse bias conditions. Similar I–V behaviour is reported for ZnO nanostructures pellet sensor with schottky contacts [39]. The intensity of the incandescent lamp (60 W) is calculated using a Lux meter, which is found to be ~6 mW/cm<sup>2</sup>, for the illumination distance of 25 cm as considered in our experiments. The direct heating of the sample due to the lamp is avoided at such a large illumination distance. In order to clarify that the observed photo-response is solely arising from ZnO or doped ZnO nanostructures, we have investigated the photo-response of bare Si substrate with Ag top contacts. We have found that nearly symmetric non-linear I–V curves for both dark and light illumination. Notably, the photo-response of Si is found to be nearly zero. It is observed from the plot that when the sample is illuminated with the incandescent light, photo induced current is greatly enhanced in the nanostructure due to the photo-generated carriers, which is observed for all our ZnO, ZnO:Co, ZnO:Ni and ZnO:W nanostructured devices. When the sample is illuminated, the photo-carriers generated in the nanostructure drift from one junction to other metallic junction and hence an enhancement in the



photocurrent is observed. It is also noted that ZnO and 3 wt % (Co, Ni, W)-doped ZnO samples exhibit an enhanced hysteresis behaviour on light illumination, showing switching to different resistant states. Such hysteresis could be due to the hopping of electrons in neighbouring oxygen vacancies under illumination [40]. As we have observed this hysteresis behaviour under all conditions without any forming process and due to the large dimension of our devices, we do not describe it as resistive switching, seen in other doped ZnO nanostructure chemo-resistive devices.

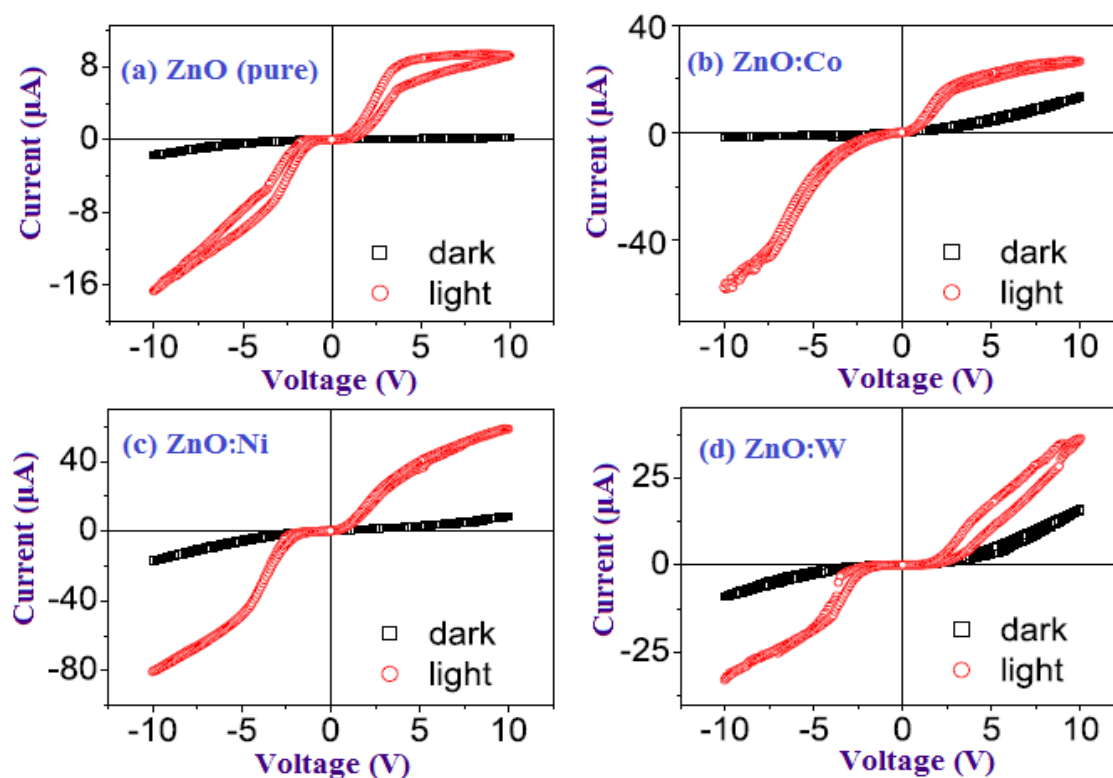


**Fig.4.11.** *I-V characteristics of (a) ZnO, (b) ZnO:Co, (c) ZnO:Ni, (d) ZnO:W nanostructures with and without light illumination*

There are many reports available on *I-V* characteristics of ZnO and metal doped ZnO using metal/ZnO/metal like MSM type heterostructures. Particularly in pursuit of photodiode and photodetector applications, the *I-V* behaviour of n-ZnO/p-Si heterojunction and n-ZnO/p-ZnO homojunction are studied under ultra-violet and visible light illumination [41, 42], showing an enhanced photo-response. In case of metal doped ZnO like ( $\text{Zn}_{0.97}\text{Ni}_{0.03}\text{O}$ ) an enhancement in electrical conductivity upon doping is reported [43, 44], while the *I-V* characteristics of ZnO:W showed an ohmic behavior [45]. Thus the study of photo-response of our doped ZnO nanostructures proves that these devices can independently be used as photo-sensors.

#### 4.4.2. Switching characteristics

Fig. 4.12 shows a typical ON/OFF light switching behaviour of our devices. The device is periodically (20 sec cycle) exposed to the light radiation under a fixed bias of 1 V and

corresponding current flow in the circuit is measured. The current is found to be nearly constant for 20 sec in ON or OFF states except for ZnO:Co nanostructures. Response times for transition between ON and OFF states (or vice versa) for all our samples are  $\leq 0.5$  sec. The ON/OFF ratios and response time for each of our devices are given in Table 4.4. The ON/OFF ratios for pure and 3 wt % (Co, Ni, W)-doped ZnO nanostructures are 8.64, 1.62, 8.04 and 4.22, respectively. A high ON/OFF ratio of 8.04 is observed for ZnO:Ni nanostructures among the doped samples. Remarkably, the ZnO nanostructures are reportedly possessing high ON/OFF ratio of 1500–10<sup>4</sup>, due to very small dimensions [39,45].

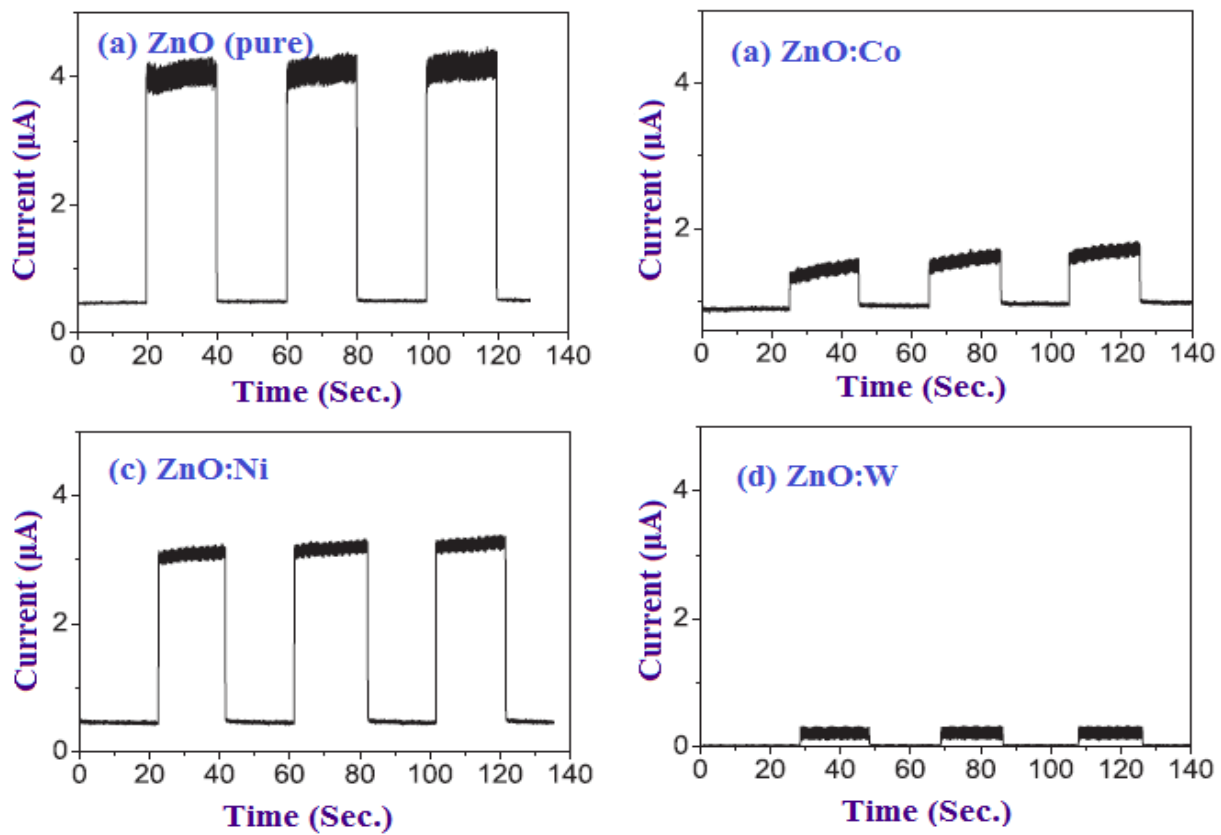


**Fig.4.12.** ON/OFF light switching behaviour at a bias of 1V for (a) ZnO, (b)  $(Zn_{0.97}Co_{0.03}O)$ , (c)  $(Zn_{0.97}Ni_{0.03}O)$  and (d)  $(Zn_{0.97}W_{0.03}O)$  nanostructures device

**Table 4.4.** ON/OFF ratios and response times for ZnO,  $(Zn_{0.97}Co_{0.03}O)$ ,  $(Zn_{0.97}Ni_{0.03}O)$  and  $(Zn_{0.97}W_{0.03}O)$  nanostructured device

Sample	$I_{light}$ ( $\mu A$ )	$I_{dark}$ ( $\mu A$ )	ON/OFF	Response
ZnO(pure)	4.32	0.52	8.64	0.22
$(Zn_{0.97}Co_{0.03}O)$	1.51	0.91	1.62	0.51
$(Zn_{0.97}Ni_{0.03}O)$	3.22	0.42	8.04	0.22
$(Zn_{0.97}W_{0.03}O)$	0.34	0.07	4.22	0.51

### 4.4.3. X-ray photoelectron spectroscopy (XPS) analysis

Using XPS data for Ni  $2p_{3/2}$  line arising at 853.4 eV, we have confirmed that Ni ions are in  $Ni^{2+}$  state in our  $(Zn_{0.97}Ni_{0.03}O)$  (Fig. 4.13). The antibonding states having higher energy lies very close to the conduction band in case of  $(Zn_{0.97}Ni_{0.03}O)$ , which gives rise to increase in conductivity [46,47]. Nevertheless, the amount of splitting leading to the proximity or overlapping of antibonding states with the conduction band may differ for each dopant ion [48]. The resistivity of ZnO is increased by Co and W doping, due to the effect of their antibonding and bonding states on shallow donor and acceptor states of ZnO [49, 50]. We believe that upon light illumination, transition of photo generated carriers to the conduction band is more probable because of the closer proximity of Ni impurity states below the conduction band in  $(Zn_{0.97}Ni_{0.03}O)$  nanostructures. Hence, in our  $(Zn_{0.97}Ni_{0.03}O)$  nanostructures, high photoconduction is observed and hence high ON/OFF ratio.

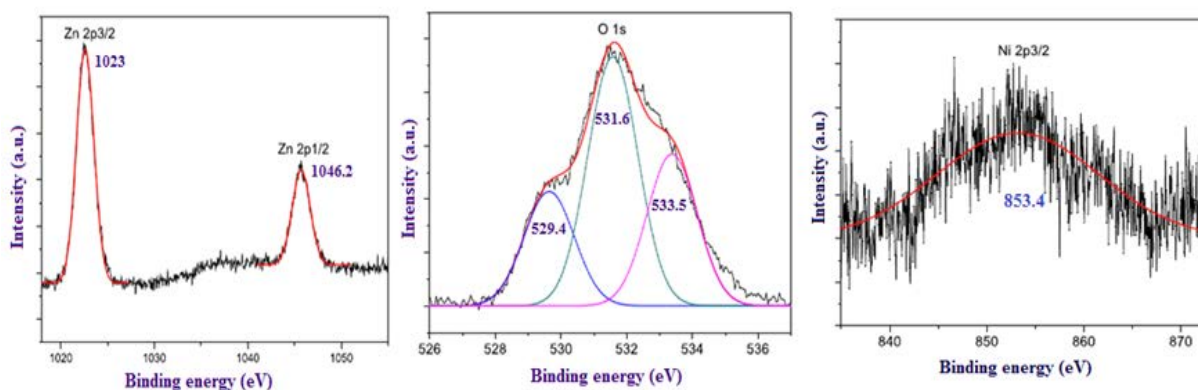


**Fig.4.13.** XPS data for Ni doped ZnO nanostructures showing peaks corresponding to Zn  $2p_{3/2}$ , Zn  $2p_{1/2}$ , O1s and Ni  $2p_{3/2}$  lines

**Table 4.5.** Dark current and photocurrent densities of ZnO,  $(Zn_{0.97}Co_{0.03}O)$ ,  $(Zn_{0.97}Ni_{0.03}O)$  and  $(Zn_{0.97}W_{0.03}O)$  nanostructured devices along with the values obtained from the literature

Device type	Dark current density (mA/cm <sup>2</sup> )	Photocurrent density (mA/cm <sup>2</sup> )
ZnO(pure)	0.0022	0.12
$(Zn_{0.97}Co_{0.03}O)$	0.15	0.31
$(Zn_{0.97}Ni_{0.03}O)$	0.13	0.72
$(Zn_{0.97}W_{0.03}O)$	0.19	0.42
<i>n</i> -ZnO/ <i>p</i> -Si [33]	>1	6.5
ITO/ <i>i</i> -ZnO/CuPc/Au [34]	0.1–0.5	3–19
<i>n</i> -ITO/ <i>i</i> -ZnO/ <i>p</i> -NiO [32]	>10 <sup>-8</sup>	<10 <sup>-6</sup>

Table 4.5 compares the dark current and photocurrent densities of ZnO, (Zn<sub>0.97</sub>Co<sub>0.03</sub>O), (Zn<sub>0.97</sub>Ni<sub>0.03</sub>O) and (Zn<sub>0.97</sub>W<sub>0.03</sub>O) nanostructured devices with the reported work. In our measurement, dark current density is observed to be 0.0022 mA/cm<sup>2</sup> for pure ZnO and further increases to ~0.19 mA/cm<sup>2</sup> for (Co, Ni, W)-doped ZnO. The photocurrent density of the order of 0.12 mA/cm<sup>2</sup> is obtained for ZnO and 0.31–0.72 mA/cm<sup>2</sup>, for our (Co, Ni, W)-doped ZnO nanostructures. A high photocurrent density of 0.72 mA/cm<sup>2</sup> is obtained for our Ni doped ZnO nanostructures. There is a spread in dark and photo current densities observed in the literature [51, 52]. Our results shows large photocurrent for the metal doped ZnO nanostructures without any heterostructure fabrication. The observed large photo response, simple, cost effective synthesis of metal doped ZnO nanostructures makes them a potential candidate for large scale fabrication of photosensing devices.

## 4.5. Study of Magnetic properties

### 4.5.1. Vibrating sample magnetometer (VSM) analysis

The magnetic measurements are done by VSM at the room temperature. The specific magnetization curves (M–H curve) obtained from VSM measurements as shown in Fig.4.14 indicate clear hysteresis ferromagnetism in the field range of 10,000 Oe. The hysteresis loops show the features of ferromagnetism at room temperature. At present there are two possible origins of the ferromagnetism in (Zn<sub>1-x</sub>M<sub>x</sub>O) system, where (M=Ni, Co, W; x =3 wt % ). One origin is due to the doped metal cluster [53-55], the other one is the metal ion substitution on Zn sites [56, 57]. The (Zn<sub>1-x</sub>Co<sub>x</sub>O) nanoparticles with 15 wt % Co have the largest saturation magnetization at room temperature because Co<sup>2+</sup> ions systematically substitute Zn<sup>2+</sup> ions. The saturation magnetization decreases to 33% of Co because doped Co<sup>2+</sup> ions have more thermal equilibrium limit in the nanostructures powders, which corresponds with the crystal orientation, resistivity and coercivity. The further increase of doping concentration results in the annihilation of Vicente's, thereby reducing the overall free charge carrier density. Hence, to achieve the best ferromagnetic character in these materials, the concentration of metal doping has to be properly optimized. At room temperature single-phase wurtzite structure (Zn<sub>0.97</sub>Ni<sub>0.03</sub>O), (Zn<sub>0.97</sub>Co<sub>0.03</sub>O) and (Zn<sub>0.97</sub>W<sub>0.03</sub>O) nanostructures show the paramagnetic behavior with no indication of ferromagnetism behavior and are presented in Fig.4.14.

As no other secondary phase is detected in the XRD pattern, the paramagnetic is the result of incorporation of Ni<sup>2+</sup>, Co<sup>2+</sup>, W<sup>2+</sup> ions into the ZnO lattice. (Zn<sub>0.97</sub>Ni<sub>0.03</sub>O) exhibited the largest saturation moments ( $M_s \approx 2.02 \times 10^{-4}$  emu/g) and the order of magnetism of the

samples is  $(\text{Zn}_{0.97}\text{Ni}_{0.03}\text{O}) > (\text{Zn}_{0.97}\text{Co}_{0.03}\text{O}) > (\text{Zn}_{0.97}\text{W}_{0.03}\text{O})$ . Coercive Field ( $H_C$ ), Saturation Magnetization ( $M_S$ ) for  $(\text{Zn}_{1-x}\text{M}_x\text{O})$  where ( $M = \text{Ni}, \text{Co}, \text{W}; x = 3 \text{ wt } \%$ ) nanostructures are given in Table 4.6.

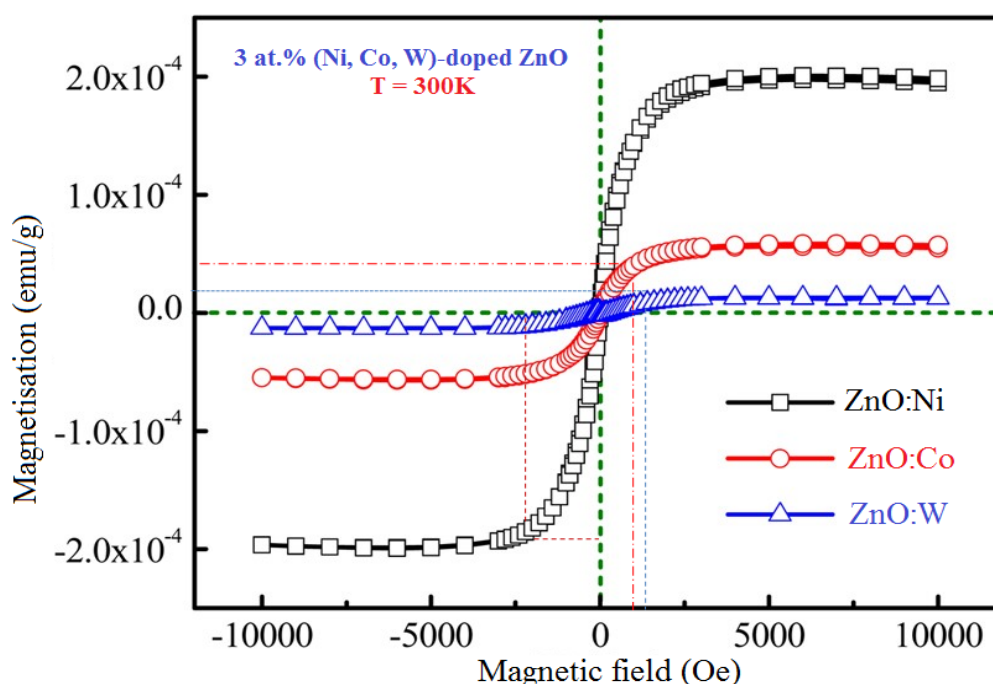


**Fig.4.14.** *M-H curves of (a)  $(\text{Zn}_{0.97}\text{Ni}_{0.03}\text{O})$ , (b)  $(\text{Zn}_{0.97}\text{Co}_{0.03}\text{O})$  and (c)  $(\text{Zn}_{0.97}\text{W}_{0.03}\text{O})$  at room temperature ( $T=300\text{K}$ ) [55]*

**Table 4.6.** *Coercive Field and Saturation Magnetization of nanostructures doped ZnO [56]*

Sample	Coercive field $H_C(\text{Oe})\pm 5.00$	Saturation magnetization ( $M_S$ ) ( $\text{emu/g})\pm 0.06$	Remanence magnetization ( $M_R$ ) ( $\text{emu/g})\pm 0.01$
$(\text{Zn}_{0.97}\text{Ni}_{0.03}\text{O})$	2350	$2.02 \times 10^{-4}$	$8.78 \times 10^{-4}$
$(\text{Zn}_{0.97}\text{Co}_{0.03}\text{O})$	1150	$0.60 \times 10^{-4}$	$2.55 \times 10^{-4}$
$(\text{Zn}_{0.97}\text{W}_{0.03}\text{O})$	1400	$0.15 \times 10^{-4}$	$1.45 \times 10^{-4}$

Fig. 4.15 (a-b) shows clear hysteresis ferromagnetism for  $(\text{Zn}_{1-x}\text{M}_x\text{O})$ , where ( $M = \text{Ni}, \text{Co}, \text{W}, \text{Mo}; x = 5 \text{ wt } \%$ ) in the field range of 10,000 Oe. Here also, the hysteresis loops shows the features of ferromagnetism at room temperature. At present there are two possible origins of the ferromagnetism. One origin is due to the doped metal cluster [55, 57], the other one is the metal ion substitution on Zn sites. Hence, to achieve the best ferromagnetic character in these materials, the concentration of metal doping has to be properly optimized [58].

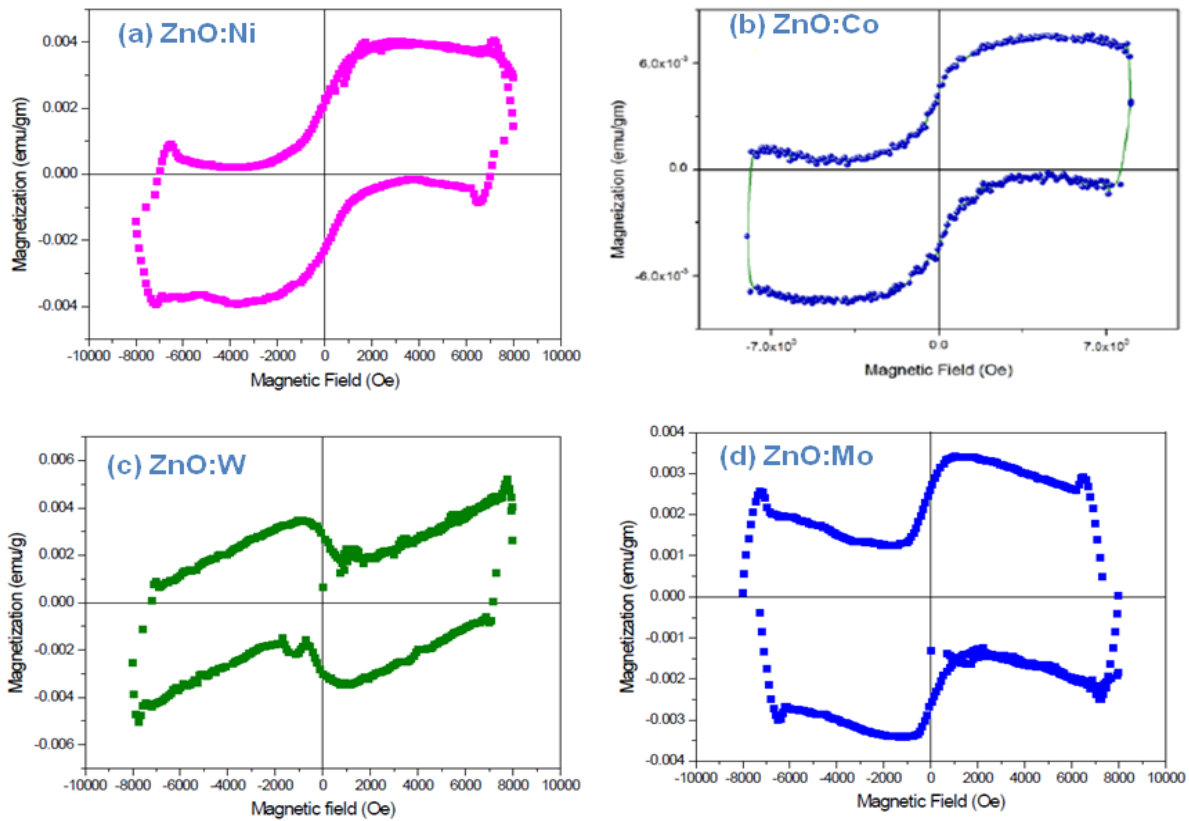


**Fig. 4.15.** *M-H curves of (a)  $(Zn_{0.95}Ni_{0.05}O)$ , (b)  $(Zn_{0.95}Co_{0.05}O)$ , (c)  $(Zn_{0.95}W_{0.05}O)$ , and (d)  $(Zn_{0.95}Mo_{0.05}O)$  at room temperature ( $T=300K$ )*

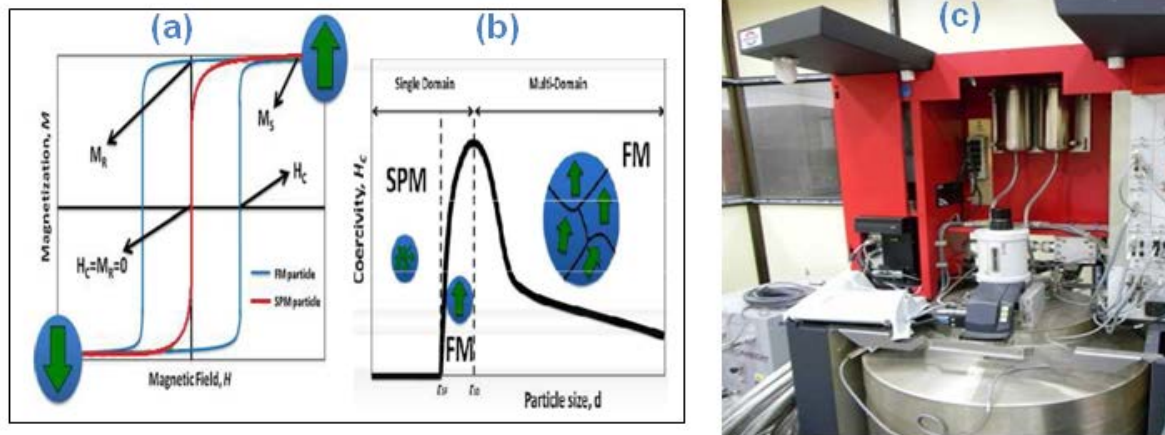


**Fig.4.16.** (a) *Theoretical M-H curve (b) Variation of the coercivity ( $H_c$ ) of magnetic nanoparticles with size, (c) View of the MPMS SQUID VSM, at CRNN, CU*

Fig. 4.16 (a-b) shows the theoretical M-H and variation of coercivity, and (c) show a picture of a modern SQUID-magnetometer from Quantum Design which allows measurements of a very high sensitivity ( $10^{-8}$  emu) in external fields up to 7 T. Due to its extremely high sensitivity a SQUID system is generally used in scientific laboratories but not in industry. The MPMS SQUID VSM dc magnetometer has been installed in CRNN, University of Calcutta. It offers  $\leq 10^{-8}$  emu sensitivity with only 4 second data averaging.

### 4.5.2. Magnetic force microscope (MFM) analysis

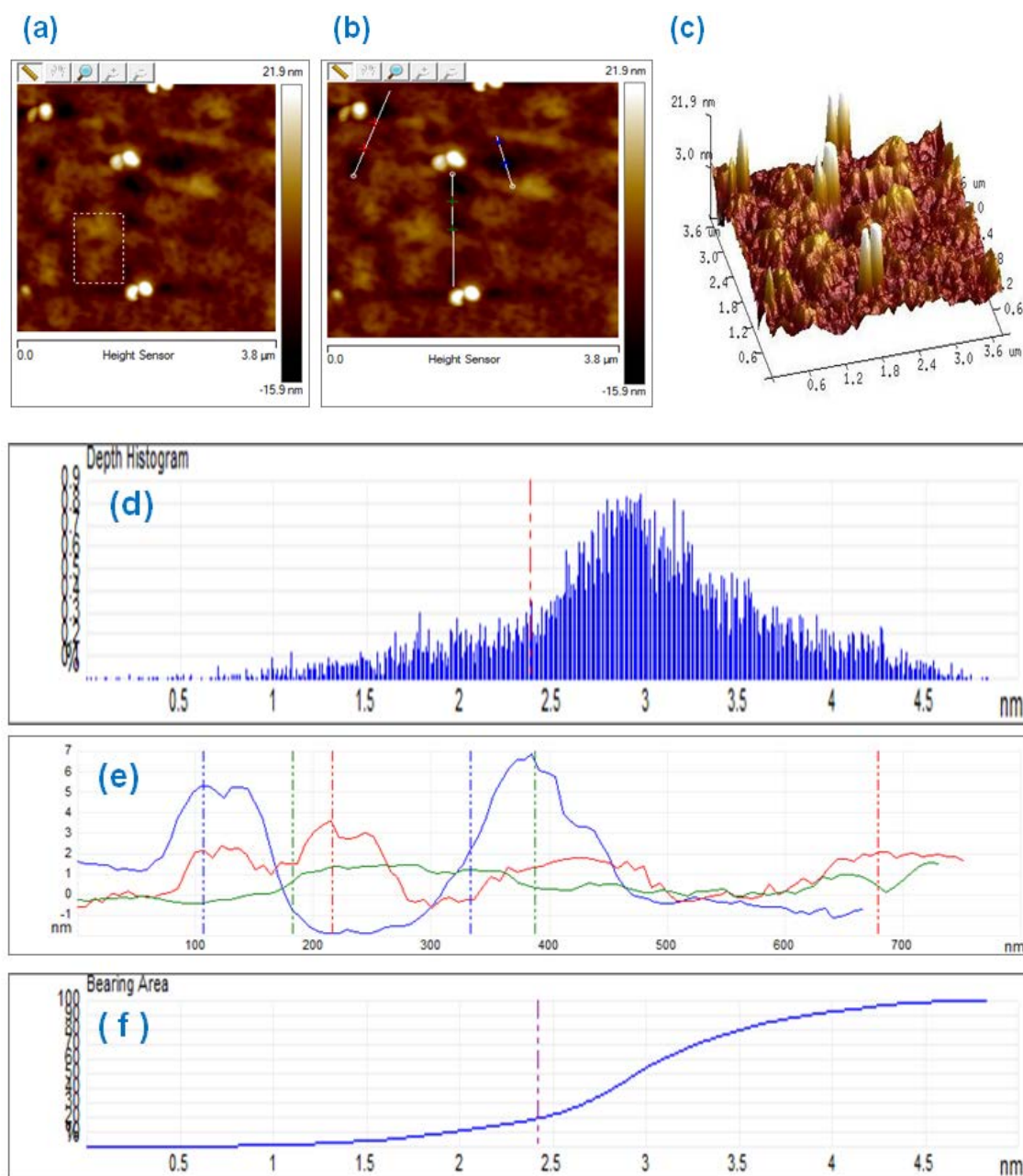


**Fig. 4.17.** MFM images of  $(\text{Zn}_{0.97}\text{Ni}_{0.03}\text{O})$  nanostructures, 2D ( $10\ \mu\text{m} \times 12.8\ \mu\text{m}$ ) for depth histogram (a, d), 3 section (b, e) and 3D ( $10\ \mu\text{m} \times 10\ \mu\text{m}$ ) for bearing area (c, f)[55]

In order to visualize the domain structures and domain configuration inside the nanostructure the MFM is used and the probe had a lift height of  $\sim 300\ \text{nm}$  over a scan size of  $2.0 \times 2.0\ \mu\text{m}$  on the nanostructure surface. The MFM images are shown in Fig.(4.17) to (4.19), where the bright and dark contrasts of the domains correspond to the high concentrations of positive and negative poles, respectively [59]. It is worth noticed that the magnetic domains are most prominent and quite regularly distributed in the  $(\text{Zn}_{0.97}\text{Ni}_{0.03}\text{O})$  nanostructures compared to the  $(\text{Zn}_{0.97}\text{Co}_{0.03}\text{O})$  and  $(\text{Zn}_{0.97}\text{W}_{0.03}\text{O})$  nanostructures. This

indicates that at room temperature ferromagnetism (RTFM) signature in the  $(\text{Zn}_{0.97}\text{Ni}_{0.03}\text{O})$  nanostructure is strongest. In the  $(\text{Zn}_{0.97}\text{W}_{0.03}\text{O})$  nanostructures, the grains are very much defused, irregular and also widely apart. For  $(\text{Zn}_{0.97}\text{W}_{0.03}\text{O})$  nanostructures although the large number of grains are present, the corresponding magnetic domains are found to be very small in size [60], which results in a lowering of the  $M_s$  compared to the  $(\text{Zn}_{0.97}\text{Ni}_{0.03}\text{O})$  nanostructures.

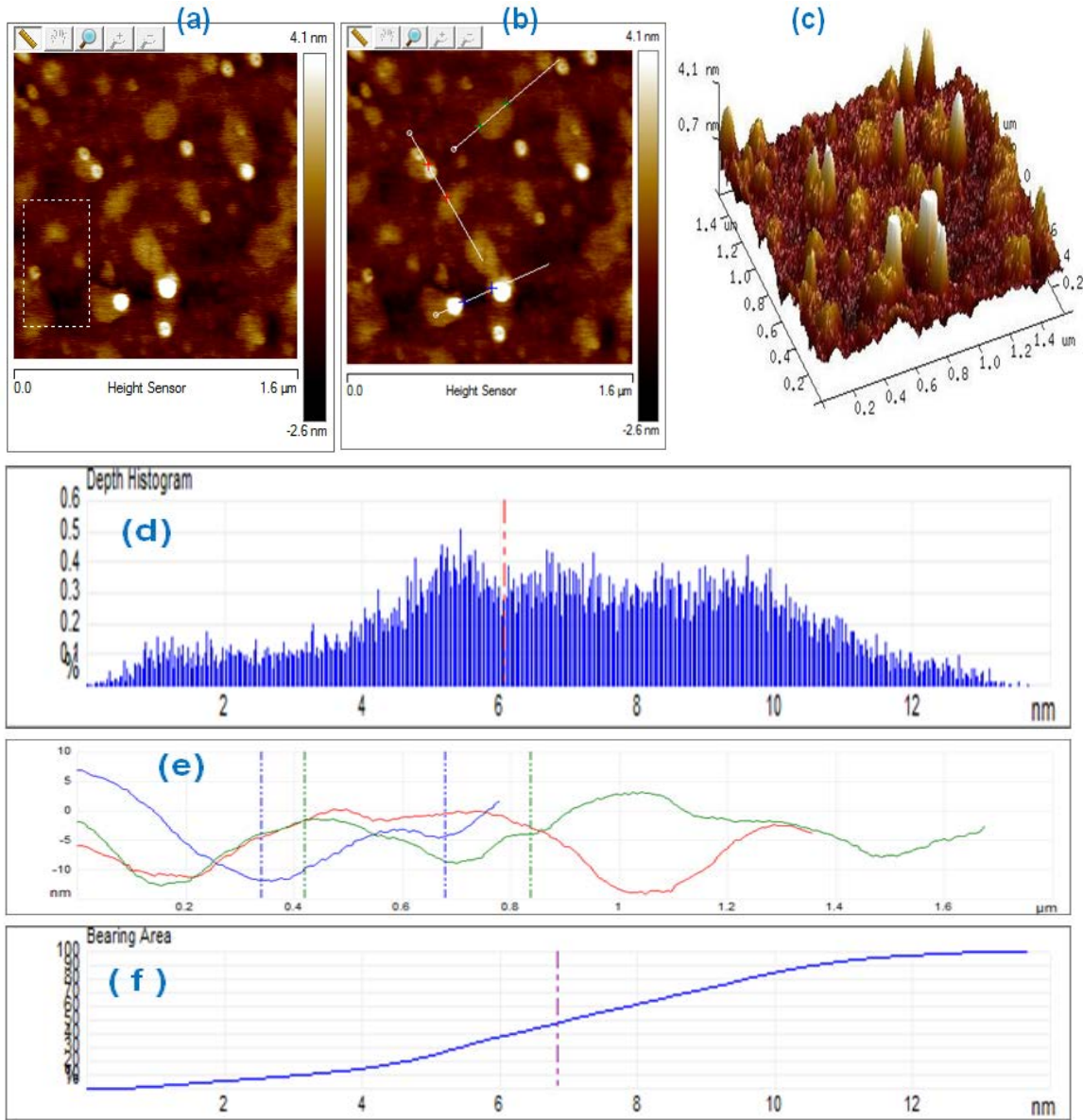


**Fig. 4.18.** MFM images of  $(\text{Zn}_{0.97}\text{Co}_{0.03}\text{O})$  nanostructures, 2D ( $10\ \mu\text{m} \times 12.8\ \mu\text{m}$ ) for depth histogram (a, d), 3 section (b, e) and 3D ( $10\ \mu\text{m} \times 10\ \mu\text{m}$ ) for bearing area (c, f)

Fig. (4.17) to (4.19) MFM images show the respective domain configurations of  $(\text{Zn}_{0.97}\text{Ni}_{0.03}\text{O})$ ,  $(\text{Zn}_{0.97}\text{Co}_{0.03}\text{O})$  and  $(\text{Zn}_{0.97}\text{W}_{0.03}\text{O})$  nanostructured powders. The particle analysis and surface roughness are summarized in Table 4.7.



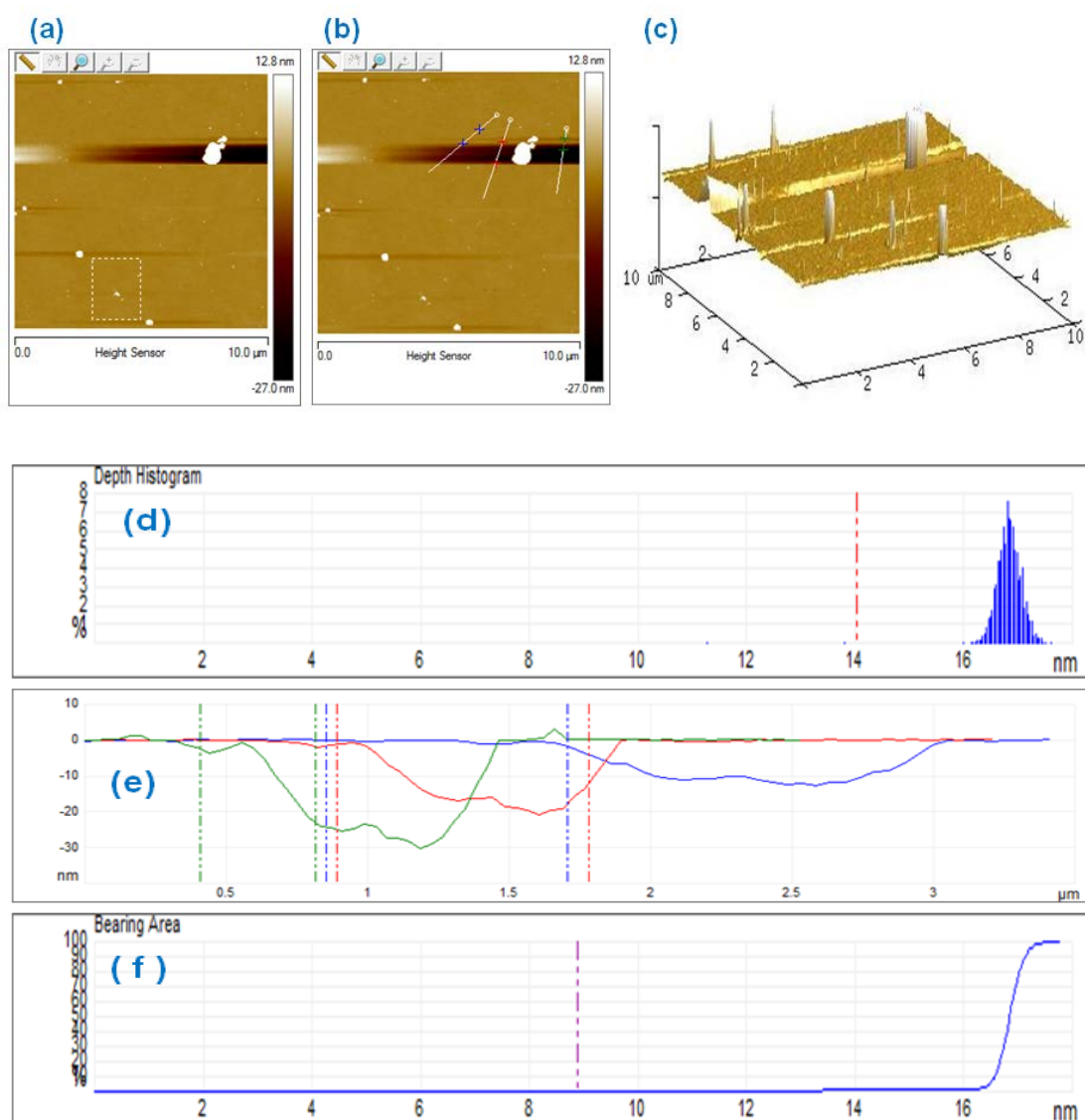


**Fig. 4.19.** MFM images of  $(\text{Zn}_{0.97}\text{W}_{0.03}\text{O})$  nanostructures, 2D ( $10\ \mu\text{m} \times 12.8\ \mu\text{m}$ ) for depth histogram (a, d), 3 section (b, e) and 3D ( $10\ \mu\text{m} \times 10\ \mu\text{m}$ ) for bearing area (c, f)

**Table 4.7:** Particle analysis and surface roughness of 3 wt % (Ni, Co, W)-doped nanostructured materials

Particle analysis			
	$(\text{Zn}_{0.97}\text{Ni}_{0.03}\text{O})$	$(\text{Zn}_{0.97}\text{Co}_{0.03}\text{O})$	$(\text{Zn}_{0.97}\text{W}_{0.03}\text{O})$
<b>Histogram depth</b>	2.38075 nm	4.83233 nm	14.0335 nm
<b>Bearing depth</b>	2.42334 nm	5.28666 nm	8.90352 nm
<b>Image projected surface area</b>	$2.41\ \mu\text{m}^2$	$14.3\ \mu\text{m}^2$	$89\ \mu\text{m}^2$
Surface roughness			
	$(\text{Zn}_{0.97}\text{Ni}_{0.03}\text{O})$	$(\text{Zn}_{0.97}\text{Co}_{0.03}\text{O})$	$(\text{Zn}_{0.97}\text{W}_{0.03}\text{O})$
<b>Image (<math>R_q</math>)</b>	0.866 nm	1.34 nm	1.82 nm
<b>Image (<math>R_a</math>)</b>	0.610 nm	1.88 nm	2.39 nm
<b>Image <math>R_{max}</math> (Image Z Range)</b>	7.82 nm	9.38 nm	10.36 nm

## 4.6. Conclusion

In summary, we have successfully prepared single phase, well crystallized pure and metal doped ZnO nanostructures by combustion synthesis route. UV-vis and PL spectra of pure and metal doped ZnO nanostructures showed a blue shift of the absorption peak with respect to the pure ZnO spectrum, indicating band gap modification of ZnO due to close proximity with doping elements in the nanostructure samples. PL spectra of the nanostructures revealed near band edge emission as well as defect-related (zinc interstitials, zinc vacancies and oxygen vacancies in the ZnO structure) emission bands. It is also clear from intensity patterns of the PL emission peaks that concentration of defects is reduced in the nanostructures with an increase in doping elements. For electrical properties, photo-response effect, studied on devices of our pure and doped ZnO nanostructures configured in metal-semiconductor-metal (MSM) junctions, reveals higher photocurrent density of our metal doped ZnO nanostructures compared to pure ZnO. Particularly, ZnO:Ni shows a high ON/OFF ratio of 8.04 and highest photocurrent density of  $0.72 \text{ mA/cm}^2$ . Moreover, a less response time of  $\sim 200 \text{ ms}$  are observed for our ZnO:Ni nanostructures. Nevertheless, these nanostructures would be a potential candidate for visible-IR photodetector and light sensor applications. The substitution of  $\text{Ni}^{2+}$  at Zn site within the ZnO matrix is confirmed by XPS study, whereas the PL spectroscopic measurements have shown the presence of large amount of  $V_{\text{Zn}}$  defects, responsible for the origin of room temperature ferromagnetic (RTFM) in  $(\text{Zn}_{0.97}\text{Ni}_{0.03}\text{O})$  nanostructures. The  $V_{\text{Zn}}$  concentration is also found to vary significantly with the nanostructure thickness and oxygen pressure and so the ferromagnetic response of  $(\text{Zn}_{0.97}\text{Ni}_{0.03}\text{O})$  nanostructures. Therefore, this chapter demonstrates that transition metal-elements could be the prime candidates to stabilize the high ferromagnetism in ZnO for potential applications in spintronics and opto-spintronics. The possibility of tuning the inherent optical, electrical and magnetic properties in the noble and transition metal doped ZnO should open up new opportunities and challenges for high-performance spintronic and optoelectronics materials based on ZnO semiconductors through proper crystal defect engineering.

## References

- [1] N. V. Hieu, D. T. T. Le, N. D. Khoang, N. V. Quy, N. D. Hoa, P. D. Tam, A. T. Le, T. Trung, Silver nanoparticles: synthesis, properties, toxicology, applications and perspectives, *International Journal of Nanotechnology*, Volume 8, 2011, Pages 174-187.

- [2] C. Klingshirn, Luminescence of ZnO under high one-and two-quantum excitation, *Journal of Physica Status Solidi B*, Volume 71, Issue 2, 1975, Pages 547-556.
- [3] H. J. Fan, F. Bertram, A. Dadgar, J. Christen, A. Krost, M. Zacharias, A low-temperature evaporation route for ZnO nanoneedles and nanosaws, *Journal of Nanotechnology*, Volume 15, 2004, pages 1401-1404
- [4] M. H. Huang, S. Mao, H. Feick, H. Yan, Y. Wu, H. Kind, E. Weber, R. Russo, P. Yang, Room-temperature ultraviolet nanowire nanolasers, *Science*, Volume 292, Issue 5523, 2001, Pages 1897-1899.
- [5] M. Law, L. E. Greene, J. C. Johnson, R. Saykally, P. D. Yang, Nanowire dye-sensitized solar cells, *Nature Materials*, Volume 4, Issue 6, 2005, Pages 455-459.
- [6] H. S. A. Salman, M. J. Abdullah, RF sputtering enhanced the morphology and photoluminescence of multi-oriented ZnO nanostructure produced by chemical vapor deposition, *Journal of Alloys and Compounds*, Volume 547, 2013, Pages 132-137.
- [7] S. Ren, G. Fan, S. Qu, Q. Wang, Enhanced H<sub>2</sub> sensitivity at room temperature of ZnO nanowires functionalized by Pd nanoparticles, *Journal of Applied Physics*, Volume 110, Issue 8, 2011, Pages 084312-6 .
- [8] Y. Kumar, J. E. Garcia, F. Singh, S. F. Olive-Méndez, V. V. Sivakumar, D. Kanjilal, V. Agarwal, Influence of mesoporous substrate morphology on the structural, optical and electrical properties of RF sputtered ZnO layer deposited over porous silicon nanostructure, *Applied Surface Science*, Volume 258, Issue 7, 2012, Pages 2283-2288.
- [9] R. Bhargavaa, K. S. Prashant, K. D. Ranu, K. Sanjeev, C. P. Avinash, K. Naresh, Systematic approach on the fabrication of Co doped ZnO semiconducting nanoparticles by mixture of fuel approach for Antibacterial applications, *Materials Chemistry and Physics*, Volume 120, 2010, Pages 393-398.
- [10] J. V. Behren, M. W. Vakrat, J. Jorne, P. M. Fauchet, Correlation of photoluminescence and band gap energies with nanocrystal sizes in porous silicon, *Journal of Porous Materials*, Volume 56, 2000, Pages 20-25.
- [11] Y. Lei, L. D. Zhang, G. W. Meng, G. H. Li, X. Y. Zhang, C. H. Liang, W. Chen, S. X. Wang, Nanotubes and Nanowires, *Applied Physical Letters*, Volume 78, 2001, Pages 1125-1127.

- [12] X. Wei, B. Man, C. Xue, C. Chen, M. Liu, Structural and Optical Properties of a bi-Structured ZnO Film Prepared Via Electrodeposition, *Japanese Journal of Applied Physics*, Volume 45, Issue 1, 2006, Pages 8581-8586.
- [13] W. C. Zhang, X. L. Wu, H. T. Chen, J. Zhu, G. S. Huang, Excitation wavelength dependence of the visible photoluminescence, *Journal of Applied Physics*, Volume 103, 2008, Pages 1661-1670.
- [14] Y. Y. Peng, T. E. Hsieh, C. H. Hsu, ZnO Nanocrystals and Allied Materials, *Journal of Nanotechnology*, Volume 17, 2006, Pages 174-180.
- [15] X. Y. Xu, C. X. Xu, Z. L. Shi, C. Yang, B. Yu, J. G. Hu, Luminescence Properties of Cobalt-Doped ZnO Films Prepared by sol-gel spin coating, *Journal of Applied Physics* Volume 111, 2012, Pages 171-178.
- [16] H. Zeng, W. Cai, J. Hu, G. Duan, P. Liu, Y. Li, Nanostructured Materials and Their Applications, *Applied Physics Letters*, Volume 88, 2006, Pages 1234-1243.
- [17] Y. Gong, T. Andelman, G. F. Neumark, S. O'Brien, I. L. Kuskovsky, Nanoscience: Nanostructures through Chemistry, *Nanoscale Research Letters*, Volume 2, 2007, Pages 297-302.
- [18] H. Zhuang, J. Wang, H. Liu, J. Li, P. Xu, Structural and Optical Properties of ZnO Nanowires Doped with Magnesium, *Journal of Acta Physica Polonica A*, Volume 119, Issue 6, Pages 819-823.
- [19] D. Li, Y. H. Leung, A. B. Djuris'ic', Z. T. Liu, M. H. Xie, S. L. Shi, S. J. Xu, W. K. Chan, Size Effects in Nanostructures: Basics and Applications, *Applied Physics Letters*, Volume 85, Issue 9, 2004, Pages 1601-1603.
- [20] Y. S. Choi, J. Y. Lee, H. S. Im, S. J. Lee, Ion Energy and Annealing Formation of Tin Oxide Thin Films, *Japanese Journal of Applied Physics*, Volume 42, 2003, Pages 1560-1562.
- [21] J. H. He, C. S. Lao, L. J. Chen, D. Davidovic, Z. L. Wang, Large-Scale Ni-Doped ZnO Nanowire Arrays and Electrical and Optical Properties, *Journal of the American Chemical Society*, Volume 127, 2005, Pages 16376-16377.

- [22] Y. C. Chang, L. J. Chen, Near UV LEDs Made with in Sn Doped p-n Homojunction ZnO Nanowire Arrays, *The Journal of Physical Chemistry C*, Volume 111, 2007, Pages 1261-1268.
- [23] H. B. Zeng, W. P. Cai, P. S. Liu, X. X. Xu, H. J. Zhou, C. Klingshirn, H. Kalt, *Nanomaterials: Processing and Characterization with Lasers*, *Journal of the American Chemical Society Nano*, Volume 2, 2008, Pages 1661-1670.
- [24] S. V. Bhat, F. L. Deepak, Magnetic and optical properties of manganese doped ZnO Semiconductor, *Journal of Solid State Communications*, Volume 30, Issue 12, 2005, Pages 767-819.
- [25] D. J. Qiu, H. Z. Wu, A. M. Feng, Y. F. Lao, N. B. Chen, T. N. Xu, Annealing effect on the microstructure and photoluminescence of ZnO thin films, *Journal of Applied Surface Science*, Volume 222, Issue 1, Pages 263-268.
- [26] D. P. Norton, M. E. Overberg, S. J. Pearton, K. Pruessner, J. D. Budai, L. A. Boatner, M. F. Chisholm, S. J. Lee, Z. G. Khim, Y. D. Park, R. G. Wilson, Ferromagnetism in cobalt-implanted ZnO, *Journal of Applied Physics Letters*, Volume 83, 2003, Pages 5488-5490.
- [27] A. B. Djuris'ic', Y. H. Leung, Optical properties of ZnO nanostructures, *Small*, Volume 2, 2006, Pages 944-961.
- [28] S. A. Studenikin, N. Golego, M. Cocivera, ZnO Bulk, Thin Films and Nanostructures: Processing Properties and Applications, *Journal of Applied Physics*, Volume 84, Issue 4, 1998, Pages 2287-2295.
- [29] H. C. Onga, G. T. Du, Optical and microhardness of ZnO nanostructures, *Journal of Crystal Growth*, Volume 262, Issue 1, 2004, Pages 261-566.
- [30] C. F. Klingshirn, A. Waag, A. Hoffmann, J. Geurts, *Zinc Oxide: From Fundamental Properties Towards Novel Applications*, Berlin, Heidelberg: Springer-Verlag, 2010.
- [31] K. Liu, M. Sakurai, M. Aono, ZnO-based ultraviolet photodetectors, *Journal of Nanoscale Sensors*, Volume 10, 2010, Pages 8604-8634.
- [32] S. J. Young, L. W. Ji, R. W. Chuang, S. J. Chang, X. L. Du, Characterizations of n-type Semiconductor with large exciton binding energy, *Journal of Science Technology*,

Volume 21, 2006, Pages 1507-1511.

- [33] D. Y. Jiang, J. Y. Zhang, Y. M. Lu, K. W. Liu, D. X. Zhao, Z. Z. Zhang, D. Z. Shen, X. W. Fan, ZnO-Based Ultraviolet Photodetectors, *Journal of Solid State Electron*, Volume 52, 2008, Pages 679-682.
- [34] C. X. Shan, J. Y. Zhang, B. Yao, D. Z. Shen, X. W. Fan, K. L. Choy, Ultraviolet photodetector fabricated from atomic-layer-deposited ZnO nanostructures, *Journal of Vacuum Science & Technology B*, Volume 27, 2009, Pages 1765-1768.
- [35] P. Sharma, K. Sreenivas, K. V. Rao, Analysis of ultraviolet photoconductivity in ZnO films, *Journal of Applied Physics*, Volume 93, Issue 7, 2003, Pages 3963-3970.
- [36] Y. Jin, J. Wang, B. Sun, J. C. Blakesley, N. C. Greenham, ZnO nanowire UV photodetectors with high internal gain, *Journal of Nano Letters*, Volume 8, Issue 6, 2008, Pages 1649-1653.
- [37] H. Kind, H. Yan, B. Messer, M. Law, P. Yang, Nanowire ultraviolet photodetectors and optical switches, *Journal of Advance Materials*, Volume 14, 2002, Pages 158-160.
- [38] S. Liang, H. Sheng, Y. Liu, Z. Huo, Y. Lu, H. Shen, Structural, optical and surface properties of ZnO nanostructures, *Journal of Crystal Growth*, Volume 225, Issue 2, 2001, Pages 110-113.
- [39] J. Zhou, Y. Gu, Y. Hu, W. Mai, P. H. Yeh, G. Bao, A. K. Sood, D. L. Polla, Z. L. Wang, UV response of ZnO nanowire and Surface Functionalization, *Journal of Applied Physics Letters*, Volume 94, 2009, Pages 1728-1735.
- [40] W. Y. Chang, Y. C. Lai, T. B. Wu, S. F. Wang, F. Chen, M. J. Tsai, Unipolar resistive switching characteristics of ZnO thin films, *Journal of Applied Physics Letters*, Volume 92, 2008, Pages 1636-1642.
- [41] J. Huang, L. Wang, R. Xu, K. Tang, W. Shi, Y. Xia, Synthesis, Characterization, and Applications of ZnO Nanowires, *Journal of Semiconductor Science and Technology*, Volume 24, 2009, Pages 21-34.
- [42] S. Mridha, D. Basak, Ultraviolet and visible photoresponse properties of heterojunction, *Journal of Applied Physics*, Volume 101, Issue 8, 2007, Pages 1063-1071.

- [43] X. Zhang, Y. Zhang, Z. L. Wang, W. Mai, Y. Gu, W. Chu, Z. Wu, Synthesis and characterization of  $(\text{Zn}_{1-x}\text{Mn}_x\text{O})$  nanowires, *Journal of Applied Physics Letters*, Volume 92, 2008, Pages 162102-3.
- [44] H. K. Yoshida, K. Sato, Bandgap Engineering in ZnO By Doping with 3d Transition Metal Ions, *Journal of Physica B*, Volume 327, 2003, Pages 337-343.
- [45] A. B. Djuris'ic', Y. H. Leung, W. C. H. Choy, K. W. Cheah, W. K. Chan, Nanomaterials: Processing and Characterization with Lasers, *Applied Physics Letters*, Volume 84, 2004, Pages 2635-2637.
- [46] S. Singh, N. Rama, M. S. Ramachandra Rao, Synthesis and study of electrical and magnetic properties of ZnO nanostructures, *Journal of Applied Physics Letters*, Volume 88, 2006, Pages 222111-3.
- [47] S. Ghosh, P. Srivastava, B. Pandey, M. Saurav, P. Bharadwaj, D. K. Avasthi, D. Kabiraj, S. M. Shivaprasad, Fabrication and characterization of NiO/ZnO p-n junctions by sol-gel method, *Journal of Applied Physics A*, Volume 90, 2008, Pages 765-769.
- [48] S. Singh, M. S. Ramachandra Rao, Optical and electrical resistivity studies of ZnO nanostructures, *Journal of Physical Review B*, Volume 80, 2009, Pages 127-133.
- [49] R. Kumar, N. Khare, Temperature dependence of conduction mechanism of ZnO and Co-doped ZnO thin films, *Journal of Thin Solid Films*, Volume 516, 2008, Pages 1302-1307.
- [50] J. Han, M. Shen, W. Cao, A. M. R. Senos, P. Q. Mantas, Hopping conduction in Mn-doped ZnO thin films, *Journal of Applied Physics Letters*, Volume 82, 2003, Pages 67-69.
- [51] K. Wang, Y. Vygranenko, A. Nathan, Stable indium oxide thin-film transistors with fast threshold voltage recovery, *Journal of Thin Solid Films*, Volume 515, Issue 17, 2007, Pages 6981-6985.
- [52] S. Karan, B. Mallik, Nanostructured organic-inorganic photodiodes with high rectification ratio, *Journal of Nanotechnology*, Volume 19, 2008, Pages 495202-10.

- [53] H. Li, C. Fan, G. Wu, H. Chen, M. Wang, Observation of ZnO nanostructures morphological variation, *Journal of Physics D: Applied Physics*, Volume 43, 2010, Pages 191-196.
- [54] J. H. Park, M. G. Kim, H. M. Jang, S. Ryu, Y. M. Kim, Co-metal clustering as the origin of ferromagnetism in Co-doped ZnO, *Journal of Applied Physics Letters*, Volume 84, 2004, Pages 1338-1340.
- [55] S. C. Das, R. Bandhyopadhyay, P. Pramanik, Structural, Optical and Electrical properties of pure and transition metal doped ZnO nanostructures through chemical synthesis route, *International Journal of Development Research*, (accepted).
- [56] D. P. Norton, M. E. Overberg, S. J. Pearton, K. Pruessner, J. D. Budai, L. A. Boatner, M. F. Chisholm, J. S. Lee, Z. G. Khim, Y. D. Park, R. G. Wilson, Ferromagnetism in cobalt-implanted ZnO, *Journal of Applied Physics Letters*, Volume 83, Issue 26, 2003, Pages 5488-5490.
- [57] K. C. Kim, E. K. Kim, Y. S. Kim, Growth and Physical Properties of Sol-gel derived Co doped ZnO thin film, *Journal of Superlattices and Microstructures*, Volume 42, 2007, Pages 246-250.
- [58] K. Ueda, H. Tabata, T. Kawai, Magnetic and electric properties of transition metal doped ZnO films, *Journal of Applied Physics Letters*, Volume 79, 2001, Pages 988-990.
- [59] S. Ghosh, G. G. Khan, K. Mandal, Defect-driven magnetism in luminescent n/p-type pristine and Gd substituted SnO<sub>2</sub> nanocrystalline thin films, *Journal of ACS Applied Materials & Interfaces*, Volume 4, Issue 4, 2012, Pages 2048-2056.
- [60] K. Sato, H. K. Yoshida, Ferromagnetism in a transition metal atom doped ZnO, *Journal of Physica E*, Volume 10, 2001, Pages 251-255.



## Chapter 5

# Experimental setup and related instrumentation

---

**This chapter provides an outline of the instrumentation setup in our laboratory used for conducting measurements with the sensors that we prepared for this experimental research work, the sensor interfacing and some responses.**

---

### *List of sections*

- 5.1. Introduction
- 5.2. Preparation of chemo-resistive pellet
  - 5.2.1. Porosity of the pellet
- 5.3. Measurement procedure with nanostructured ZnO pellet sensors
  - 5.3.1. Fabricated measurement set-up
  - 5.3.2. Heating assembly and sensor measurement circuit
  - 5.3.3. Purging assembly
  - 5.3.4. Lab-View based data acquisition system (DAS)
  - 5.3.5. Interface circuits
  - 5.3.6. Measurement procedure with volatile gases
- 5.4. Experimental studies of developed sensors
- 5.5. Conclusion
- References

### *Contents of this chapter are based on following publications:*

1. S. C. Das, K. Sadani, R. Bandyopadhyay, P. Pramanik, Sensing characteristics of Molybdenum doped Zinc Oxide nanoparticles chemoresistor pellets towards black tea-biochemicals, International Journal of Advances in Engineering Science and Technology, Volume 3, Issue 3, 2014, Pages 120-131.
2. S. C. Das, B. Tudu, N. Bhattacharyya, R. Bandyopadhyay, P. Pramanik, Nanostructured ZnO sensor in Electronic Nose for Environmental Monitoring on Industrial Premises, Book proceedings, ICLMSC-2011, Pages 165-167, ISBN: 978-93-80813-14-1.
3. S. C. Das, B. Tudu, N. Bhattacharya, R. Bandyopadhyay, P. Pramanik, Doped ZnO Nanostructured Sensor in Electronic Nose for Detection of Ammonia, Hydrogen and Liquefied Petroleum Gas, Advanced Nanomaterials and Nanotechnology, Springer-Verlag Berlin Heidelberg, Chapter 47, 2013, DOI: 10.1007/978-3-642-34216-5(47) (online).



# Chapter 5

## Experimental setup and related instrumentation

### 5.1. Introduction

This chapter describes the details of the experimental setup of pure and doped ZnO nanostructured powder and chemo-resistive pellet sensors prepared by chemical synthesis route (combustion method). The details of the chemical synthesis procedure and morphological characterization of pure and doped nanostructured ZnO samples procedure have been elaborated in chapters 2-4 of the thesis. This chapter provides an outline of the instrumentation setup in our laboratory used for conducting measurements with the sensors that we prepared for this experimental research work, the sensor interfacing and some responses [1].

### 5.2. Preparation of chemo-resistive pellet

In the pellet formation stage, 0.7gm of the nanostructured calcined ZnO powder and a drop of poly-vinyl alcohol (PVA) solution are thoroughly mixed in a crucible. The synthesized pure and metal (M = Ni, Co, Pd, Pt, Mo, W, Cd)-doped ZnO nanostructured material is shaped into pellet form of diameter 13 mm and thickness 2 mm with the help of a pellet making instrument shown in Fig. 5.1(a-c) for studying their sensing characteristics. The mass is then pressed with 8 tons of pressure using KBr pelletiser for approximately 5 minutes to obtain the sensor pellets [2-3].

#### 5.2.1. Porosity of the pellet

The porosity (%) of the prepared pellet is obtained by using the relation in equation (5.1).

$$Porosity (\%) = \left[ \frac{(T_D - A_D)}{T_D} \right] \times 100 \quad (5.1)$$

where,  $T_D$  = theoretical density of ZnO,  $A_D$  = apparent density of ZnO pellet; The apparent density of ZnO pellet is obtained using equation (5.2).

$$\text{Apparent density } (A_D) = \left[ \frac{\text{mass of the pellet}}{\text{volume of the pellet}} \right] \quad (5.2)$$

Typically, the mass of the pellet ( $m$ ) is 0.7g and the diameter of the pellet ( $d$ ) is 1.3cm, and hence the apparent density of the pellet is  $0.7 / \{4/3 \cdot \pi (1.3/2)^3\} = 0.6085 \text{ g.cc}^{-1}$ ; this gives the porosity of the pellet as 89.15 %, the theoretical density of ZnO being  $5.606 \text{ g.cc}^{-1}$ .



*Fig. 5.1. Pellet making instrument (a) Pellet press (b) Dies and (c) Pressure gauge*

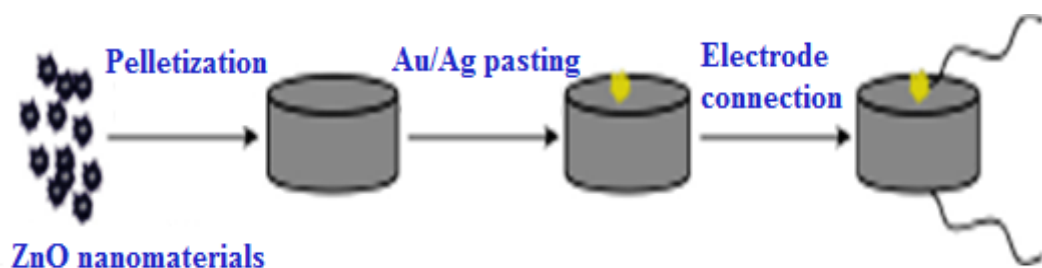


*Fig. 5.2. Schematic representation of the various steps involved for fabrication of pelletized nanostructured ZnO sensors*

**Sintering:** The pellets are sintered at  $500^\circ\text{C}$  for 5 hours. By this process the PVA volatilizes off lending some porosity to the pellet. The sintered pellet has been used for the experiments as described below.

### 5.3. Measurement procedure with nanostructured ZnO pellet sensors

The contact in each chemo-resistive pellet is made with silver paste and is used to complete the circuit as shown in Fig. 5.3 [4]. The sensors are clamped to a fabricated brass holder inside the quartz tube along with allied fittings viz. thermocouple, silica gel tube, inlets for vapours and connecting leads as anode and cathode for measurements as shown in Fig. 5.3 (b).

### 5.3.1. Fabricated measurement set-up

There are two main types of odour handling and delivery systems, the sample flow system and the static system. In the sample flow system the sensors are placed in the vapour flow, which allows the rapid exchange of vapour and hence many samples can be measured within a short time. In the static system there is no vapour flow around the sensor and measurement are usually made on the steady-state response of the sensors exposed to a vapour at a constant concentration. Our instrumentation setup is primarily a static system. The setup has different assemblies as discussed below. Though bulky, the system is extremely rugged. An ON-OFF type auto heating assembly is used to heat the sensors to 200-500°C. The sensor to be tested is contacted with silver and put in to a spring system made of brass which holds the sensor firmly on a ceramic base [5].



*Fig. 5.3. Sensor assembly inside the quartz tube along with allied fittings viz. thermocouple, silica gel tube, inlets for vapours and connecting leads: (a) Customized sensing measurement set-up*

This enables the transmission of potential change across the sensor resistance in presence of injected gas to the data acquisition system through connecting wires. The ceramic base with the sensor is placed in a temperature resistant airtight quartz tube which is placed in the tube-furnace to be operated up to a maximum of 500°C as shown in Fig.5.3 (a) [6]. Fig. 5.3(c) shows the setup for in-situ resistance measurements: 1) pellet sensor; 2) two probe sensor holder; 3) quartz test chamber; 4) furnace; 5) gas inlet; 6) gas outlet; 7) gas injection port; 8) thermocouple; 9) platinum wires; 10) flange; 11) digital multimeter; 12) personal computer; 13) temperature controller (PID controller) [4,6].

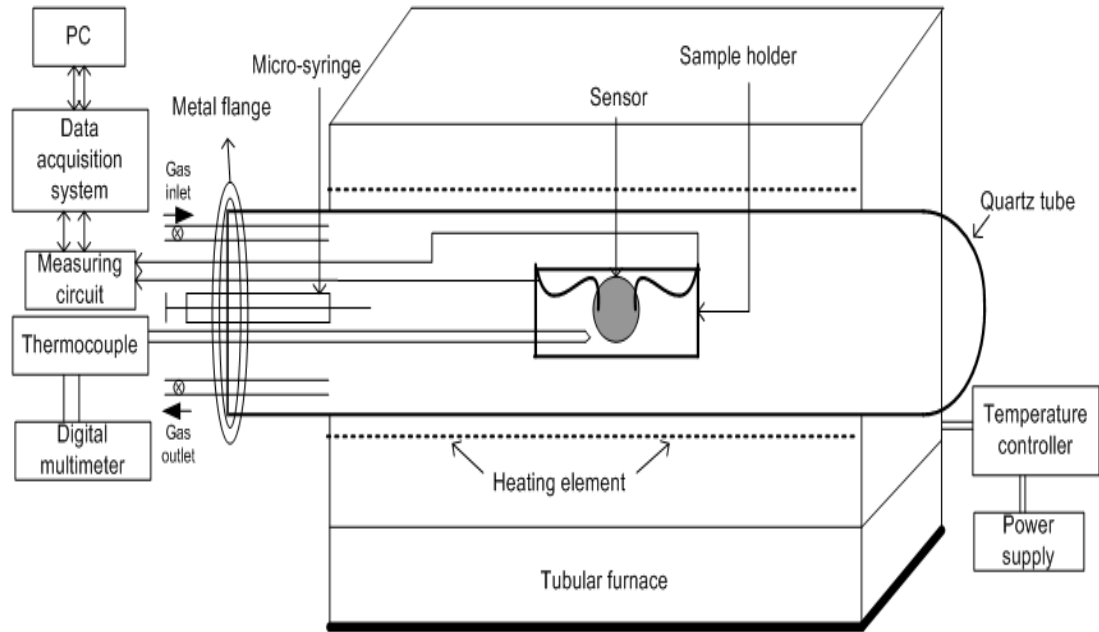


*Fig. 5.3. (b) Schematic diagram of instrument setup*

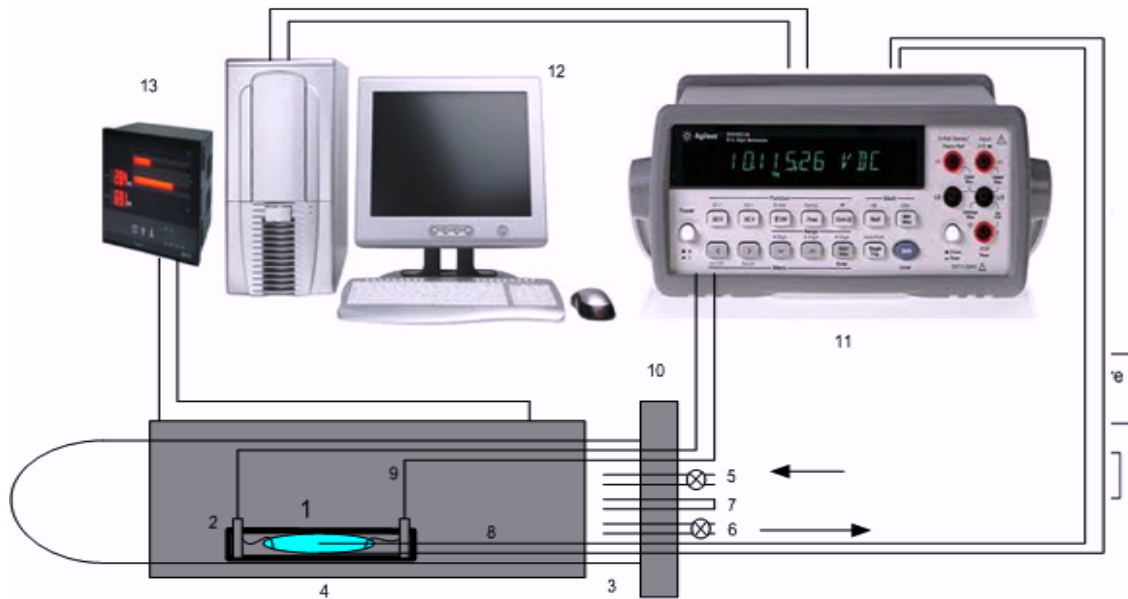


*Fig. 5.3. (c) Equipment setup of in-situ resistance measurements*

### 5.3.2. Heating assembly and sensor measurement circuit

From a 16 amp Miniature Circuit Breaker (MCB), power goes via a relay through an autotransformer to a tube furnace. The relay is controlled with a temperature controller which receives feedback from a J-type thermocouple (TC) in a quartz tube. The sensor holding in ceramic base of brass holder and the silver plates (anode and cathode) are shown

in Fig. 5.4(a) and (b). The ON-OFF temperature control loop is used for heating the quartz tube inside which the sensor is placed. The sensor is connected as a resistor in a simple voltage divider circuit fed by a DC power supply of 5V.

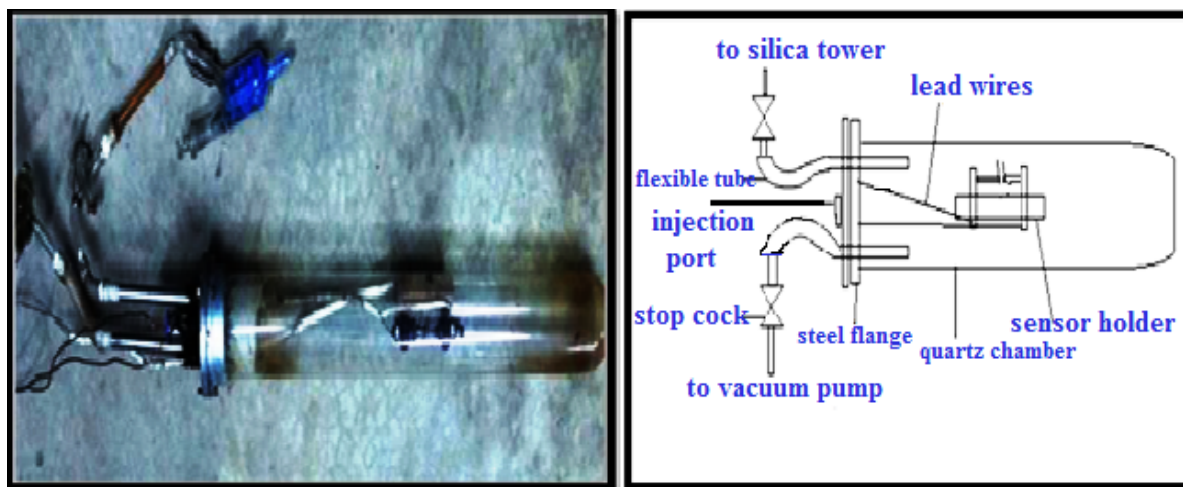


*Fig. 5.4. (a) Pellet sensor in a quartz tube (left) and schematic diagram (right)*

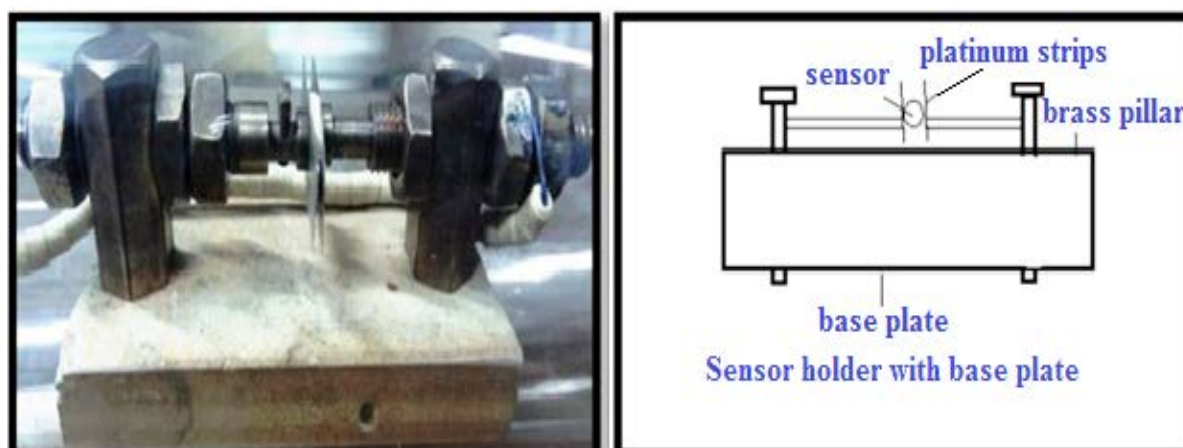


*Fig.5.4.(b) Sensor holding in ceramic base of brass holder (left) and schematic diagram of silver plate use as anode and cathode (right)*

### 5.3.3. Purging assembly

A vacuum pump is used to remove all test vapours after a sniffing cycle is completed; the sensor in the quartz tube is thereby purged with atmospheric dust and moisture free air (as the end open to atmosphere is via a tube filled with silica gel and cotton) and the sensor returns to its baseline.

### 5.3.4. Labview based data acquisition system (DAS)

The data acquisition system typically converts analog waveforms into digital values for processing and the detailed diagrams are shown in Fig. 5.5(a-f). The components of the data acquisition system are:

- i. Signal conditioning circuitry to convert sensor signals into a form that can be applied to the analog to digital converter (amplifier, buffer, attenuator),

- ii. Analog to digital converter,
- iii. Recording and processing of conditioned sensor signals to extract information,

The data acquisition system in our setup includes a simple voltage divider network, power line filter, a National Instruments NI-USB 6009 data card and Lab-view software. The NI USB-6008/6009 provides connection to eight single-ended analog input (AI) channels, two analog output (AO) channels, 12 digital input/output (DIO) channels, and a 32-bit counter with a full-speed USB interface as shown in Fig. 5.5(a).

### 5.3.5. Interface circuits

The voltage divider circuit is used to convert the resistance change of the sensor in presence of reducing gases to equivalent voltage. It consists of a 100 K $\Omega$  resistance in series with the sensor resistance with a supply voltage of +5V, as shown in Fig.5.5 (d) and (f). The output is taken across the sensor resistance which serves as the input of the instrumentation amplifier (AD 620) which provides necessary gain and removes loading due to its very high input impedance. The AD 620 is a low cost, high accuracy instrumentation amplifier that requires only one external resistor to set gains of 1 to 1000. Fig.5.5 (b) shows the connection diagram of AD 620 instrumentation amplifier. The output of AD 620 serves as the input to the PC through NI USB 6009 data acquisition card and Labview software. Fig.5.5 (c) shows the temperature control loop and in Fig.5.5 (e), the DAS block diagram is depicted.

### 5.3.6. Measurement procedure with volatile gases

A Ni-Cr heating wire is used as a resistor. This resistor ( $R_H$ ), controlled by a heating voltage ( $V_H$ , DC), ensures both substrate heating and operating temperature controls. Fig. 5.4 (a) and (b) show the photograph of the fabricated sensor and the photograph of the sensor on the socket.

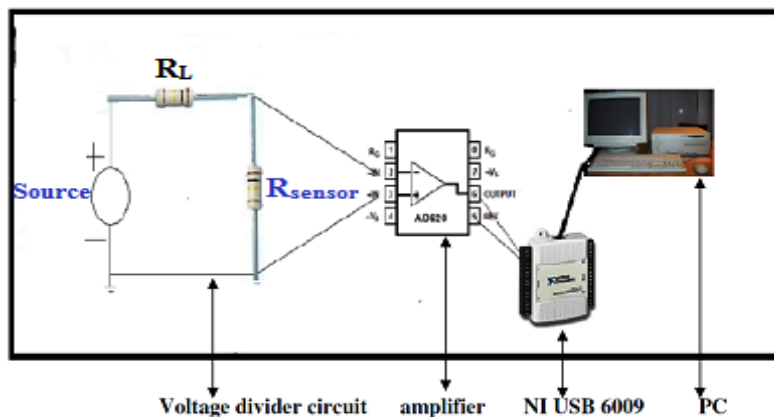


Fig. 5.5. (a) Schematic diagram of data acquisition system (DAS)



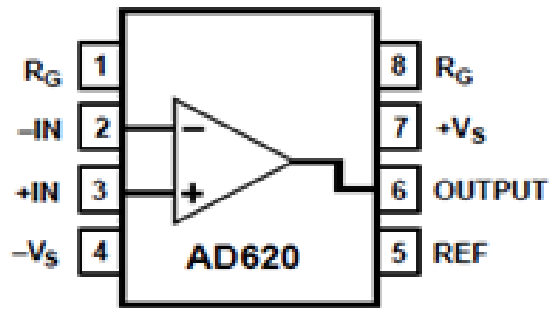


Fig. 5.5. (b) Connection of analog to digital converter (amplifier, buffer, attenuator) AD 620

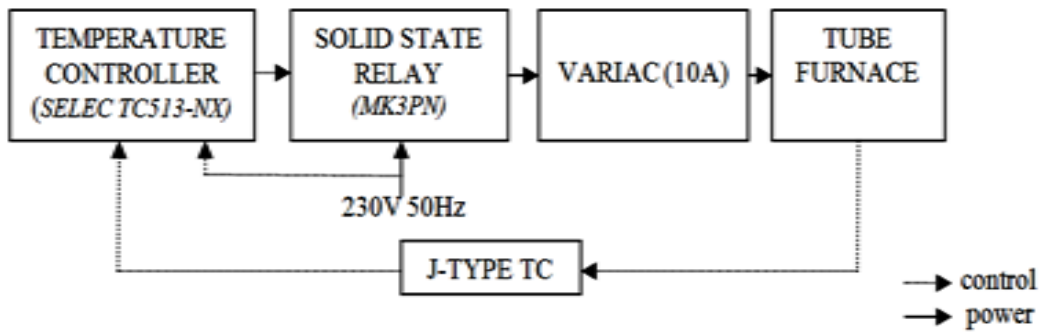


Fig. 5.5. (c) Temperature control loop

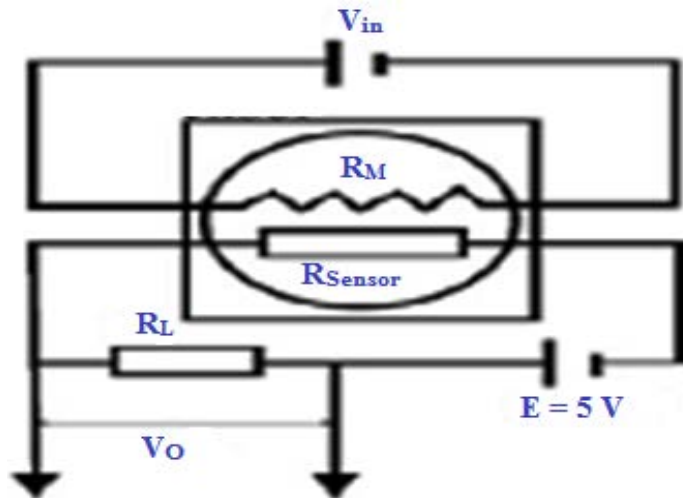


Fig. 5.5. (d) Electrical circuit for measuring the chemo-resistive pellet gas sensor

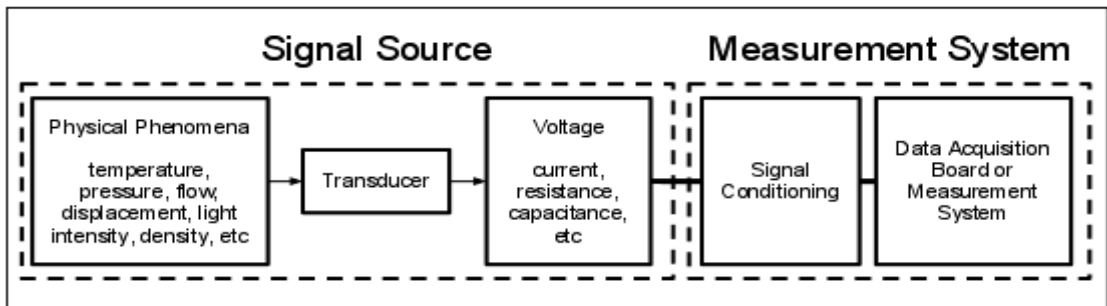
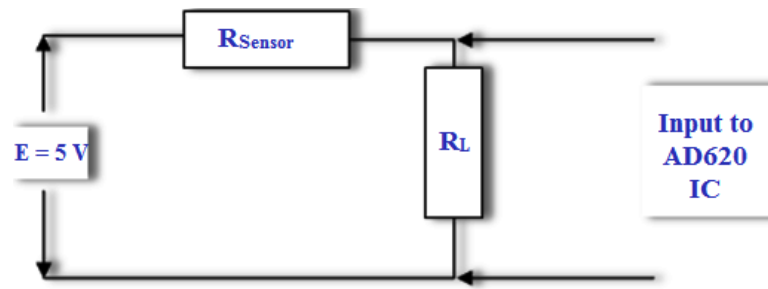


Fig. 5.5. (e) Data acquisition system block diagram



**Fig. 5.5. (f)** Voltage divider network showing connection of sensor with 100 K $\Omega$  series resistance

Gas sensing properties are measured using a static test system. Saturated target vapour is injected into a test chamber (about 1L in volume) by a syringe through a rubber plug. After fully mixing with air (relative humidity (RH) about 25%), the sensor is put into the test chamber. When the response reaches a constant value, the sensor is taken out to recover in air. The sensor response to H<sub>2</sub>O is studied by exposing the sensor to a chamber with 95% RH, which is obtained using a saturated salt solution (KNO<sub>3</sub>) as a humidity generation source. Resistance of the sensor is measured using auto ranging microvolt DMM (Model 197A, M/s Keithley Instruments, USA) for low temperatures (when the resistance is higher than 100 M $\Omega$ ) and Agilent Data Acquisition/Switch Unit (model no. 34970A) for higher temperatures. The voltage of the sensor is measured by using a conventional circuit Fig. 5.5(d) in which the element is connected with an external resistor ( $R_0$ ) in series in a circuit with an applied voltage of 5V. According to Fig. 5.5(d), the gas response value ( $R$ ) is defined as the ratio of the electrical resistance in air ( $R_a$ ) to that in target gas ( $R_g$ ):

$$R_a = \frac{5 - (V_0)_{\text{air}}}{(V_0)_{\text{air}}} R_L \quad (5.3)$$

$$R_g = \frac{5 - (V_0)_{\text{gas}}}{(V_0)_{\text{gas}}} R_L \quad (5.4)$$

$$R = \frac{R_a}{R_g} \quad (5.5)$$

where  $(V_0)_{\text{air}}$  is the voltage in air, and  $(V_0)_{\text{gas}}$  is in target gas. The time taken by the sensor to achieve 90% of the total resistance change is defined as the response time in the case of adsorption or the recovery time in the case of desorption.

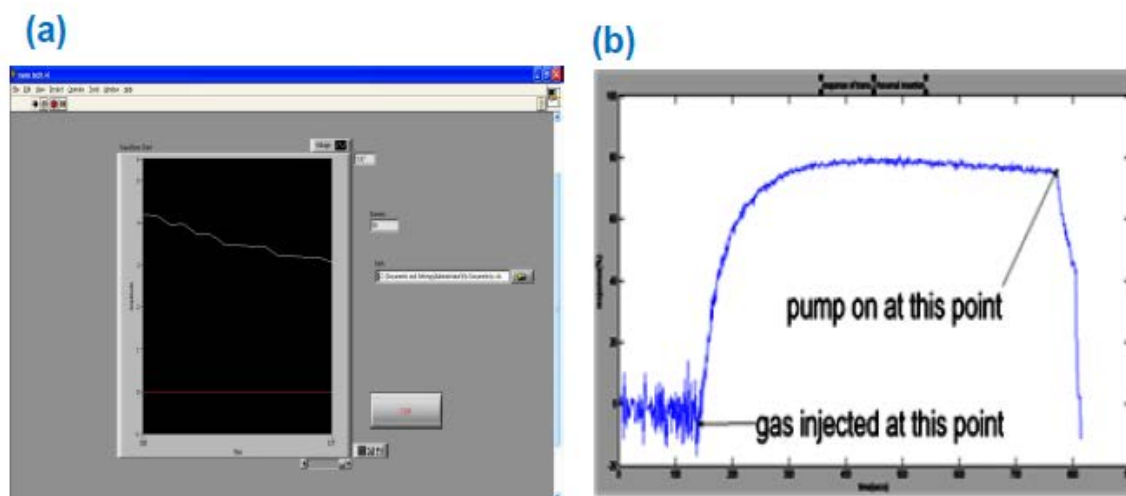
#### 5.4. Experimental studies of developed sensors

The sensor to be tested is contacted with silver and put in to a spring system made of brass which holds the sensor firmly on a ceramic base. The ceramic base with the sensor is

placed in a temperature resistant airtight quartz tube which is placed in a tube-furnace to be operated up to a maximum of 500°C as already shown in Fig. 5.4(a). The set point of the temperature controller for the tube furnace is 200°C initially and the voltage across the sensor is allowed to stabilize at its affixed value which is the potential corresponding to base resistance of sensor in dry air ( $R_a$ ). Before further measurements are carried out, we confirm the ohmic nature of sensor-silver-brass contacts. To evaluate our sensor response, we inject calculated ppm of each of the test vapours one by one and record its response. When the reducing vapours come in contact with the sensor surface [7], they are oxidized and the active sensor surface is reduced leading to release of electrons. So resistance of the sensor decreases and settles down at a steady value ( $R_g$ ). This resistance ( $R_g$ ) is measured in presence of the injected gas and its percentage response is calculated using equation (5.6).

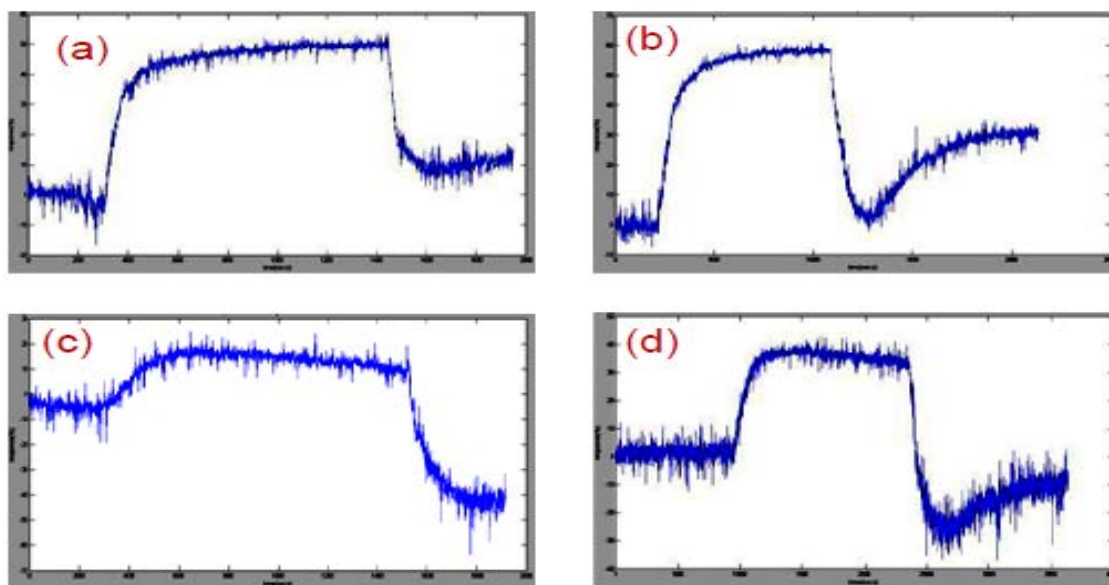
$$\text{Response}(R) = \left[ \frac{(R_a - R_g)}{R_a} \right] \times 100\% = \left[ \frac{(V_{01} - V_{02}) \times 5}{(V_{01} (5 - V_{02}))} \right] \times 100\% \quad (5.6)$$

Fig. 5.6 (a) shows screen shot of data acquisition software using Labview 8.0, and Fig. 5.6 (b) shows the sample response of the sensor to bio-chemical compounds of black tea. Now this procedure has been repeated for all the four compounds. After taking the readings for all the four compounds, the temperature of the furnace is increased to 250°C and all the compounds are tested again at this temperature [8]. This step is repeated for 300°C, 350°C and 400°C. Once the sensor has been tested against all the compounds at all the temperatures, it is taken out and replaced by another sensor and the entire process is repeated.



**Fig. 5.6.** (a) Screen shot of DAS software using Labview and (b) the sample response of nanostructured sensor to bio-chemical compounds of black tea

The plots of a  $(\text{Zn}_{0.97}\text{Ni}_{0.03}\text{O})$  nanostructured sensor with the four volatiles of tea are shown in Fig. 5.7 (a-d) [9].



**Fig.5.7.** Response of  $(\text{Zn}_{0.98}\text{Ni}_{0.02}\text{O})$  nanostructured sensors at  $350^{\circ}\text{C}$  towards (a) Geraniol (b) Trans-2-Hexenal (c) Linalool Oxide (d) Linalool

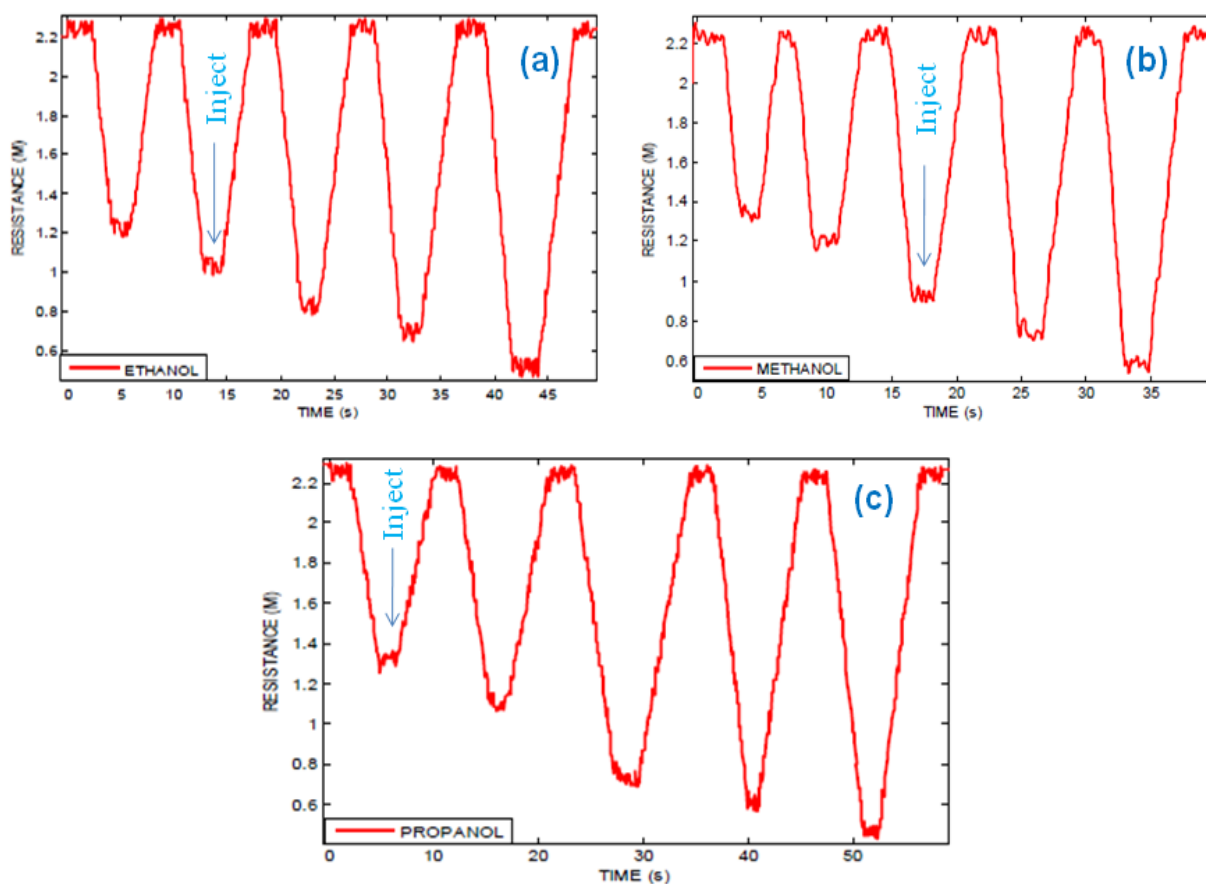


**Fig. 5.8.** Response of  $(\text{Zn}_{0.98}\text{Cd}_{0.02}\text{O})$  nanostructures sensors at  $300^{\circ}\text{C}$  towards (a) Ethanol, (b) Methanol, and (c) Propanol to increasing injected ppm [10].

## 5.5. Conclusion

In this chapter the fabricated instrumentation setup is described in details with photographs and schematics. The procedures of gas injection, measurement of change in resistance, electronic interface circuits and data acquisition systems are explained. This experimental setup has been used for studying differently doped nanostructured sensors and their responses with different volatiles and the results are presented in the next chapter. Also presented are some of the raw responses as recorded by this setup.

## References

- [1] S. C. Das, B. Tudu, N. Bhattacharyya, R. Bandyopadhyay, P. Pramanik, Nanostructured ZnO sensor in Electronic Nose for Environmental Monitoring on Industrial Premises, ICLMSC-2011, Pages 165-167, ISBN: 978-93-80813-14-1.
- [2] S. C. Das, B. Tudu, N. Bhattacharyya, R. Bandyopadhyay, P. Pramanik, Development of Nanostructured ZnO based Gas Sensors to use in Electronic Nose towards Hydrogen, Ammonia and LPG, MDCCT-2012, Pages 204-207, ISBN: 978-93-80663-36-4.
- [3] H. Wang, C. Xie, Low-dimensional Systems and Nanostructures, Physica E, Volume 44, 2008, Pages 7-8.
- [4] S. C. Das, B. Tudu, N. Bhattacharya, R. Bandyopadhyay, P. Pramanik, Doped ZnO Nanostructured Sensor in Electronic Nose for Detection of Ammonia, Hydrogen and Liquefied Petroleum Gas, Advanced Nanomaterials and Nanotechnology : Springer-Verlag Berlin Heidelberg, Chapter 47, 2013, Pages 473-482, DOI: 10.1007/978-3-642-34216-5(47) (online).
- [5] T. C. Pearce, S. S. Schiffman, H. T. Nagle, J. W. Gardner, Handbook on machine olfaction: electronic nose technology, WILEY-VCH Verlag GmbH & Co. KGaA, Weinheim, 2003.
- [6] S. C. Das, K. Sadani, R. Bandyopadhyay, P. Pramanik, Sensing characteristics of Molybdenum doped Zinc Oxide nanoparticles chemoresistor pellets towards black tea-biochemicals, International Journal of Advances in Engineering Science and Technology, Volume 3, Issue 3, 2014, Pages 120-131.

- [7] J. W. Gardner, P. N. Barlett, *Electronic Nose: Principles and Applications*, Oxford University Press, New York, 1999.
- [8] J. W. Gardner, M. Craven, C. Dow, E. L. Hines, The prediction of bacteria type and culture growth phase by an electronic nose with a multi-layer perceptron network, *Measurement Science and Technology*, Volume 9, 1998, Pages 120–127.
- [9] S. C. Das, R. Bandyopadhyay, P. Pramanik, Development of W doped ZnO nanostructure chemoresistor pellet sensors for black tea aroma monitoring, *International Journal of Innovative Science, Engineering and Technology*, Volume 2, Issue 3, 2015, Pages 107-113.
- [10] S. C. Das, R. Bandyopadhyay, P. Pramanik, Volatile Organic Compounds sensing characteristics of doped Zinc Oxide nanostructured sensors for E-nose applications, *Nanospectrum: A Current Scenario*, Allied Publishers, 2015, Pages 121-131, ISBN: 978-93-85926-06-8.

## Chapter 6

# Nanostructured ZnO for VOC and Gas-Sensor Applications

In this chapter, we present the detailed results of experimentation with the doped nanostructured ZnO sensors. The metals chosen for doping the ZnO semiconductors are Nickel, Cobalt, Platinum, Palladium, Cadmium, Molybdenum and Tungsten. The performance of the sensors with different VOCs like tea volatile compounds (linalool, linalool oxide, geraniol and trans-2-hexenal), ammonia, hydrogen, LPG, methanol, ethanol, propanol are presented in details.

### *List of sections*

- 6.1. Introduction
- 6.2. Electrical measurements and gas sensing studies
- 6.3. Results and discussions
  - 6.3.1. Performance of pure and 3 wt % (Ni, Co, Pt, Pd)-doped ZnO in black tea bio-chemicals
  - 6.3.2. Performance of pure and 3 wt % (Ni, Co, Pt)-doped ZnO at optimum temperature
  - 6.3.3. Performance of (Zn<sub>0.97</sub>Pd<sub>0.03</sub>O) sensors in ammonia, hydrogen, liquefied petroleum gas
  - 6.3.4. Performance of pure and (1, 2, 3) wt % Mo-doped ZnO in black tea bio-chemicals
  - 6.3.5. Performance of (5, 10, 15) wt % W-doped ZnO in black tea bio-chemicals and ethanol, methanol and propanol VOC gases
  - 6.3.6. Performance of (1, 2, 3) wt % Cd-doped ZnO in ethanol, methanol and propanol
- 6.4. Conclusion
- References

### *Contents of this chapter are based on following publications:*

1. S. C. Das, R. Bandyopadhyay, P. Pramanik, Nanostructured ZnO based Gas Sensors to use in Electronic Nose for Biochemical Compounds in Black Tea, International Journal of Advanced Information Science and Technology, Volume 29, Issue 29, 2014, Pages 124-128.
2. S. C. Das, B. Tudu, N. Bhattacharya, R. Bandyopadhyay, P. Pramanik, Doped ZnO Nanostructured Sensor in Electronic Nose for Detection of Ammonia, Hydrogen and Liquefied Petroleum Gas, Advanced Nanomaterials and Nanotechnology, Springer-Verlag Berlin Heidelberg, Chapter 47, 2013, Pages 473-482, DOI: 10.1007/978-3-642-34216-5(47)(online).
3. S. C. Das, R. Bandyopadhyay, P. Pramanik, Development of W doped ZnO nanostructure chemoresistor pellet sensors for black tea aroma monitoring, International Journal of Innovative Science, Engineering and Technology, Volume 2, Issue 3, 2015, Pages 107-113.





# Chapter 6

## Nanostructured ZnO for VOC and Gas-Sensor Applications

### 6.1. Introduction

Chemical sensors play a significant role for the detection and monitoring of poisonous hazardous chemicals. Scientific community and researchers around the globe thus are trying to develop novel chemical sensors with superior performances. These chemical sensors also play other important and vital roles in other areas such as gas alarms, sensors for water and soil pollutants, human health, temperature sensor, speed sensor, magnetic field sensor, and emission control [1]. A sensor is a component of an electronic circuit which senses and undergoes physical and chemical changes on its surface due to the adsorption of a chemical stimulant [2]. These adsorbed chemical species change the electrical properties of the sensor and subsequently convert these changes into measurable quantities [3-4]. It has been reported and observed that there is a remarkable change in the electrical properties at high temperatures for semiconductor materials on exposure to reducing or oxidizing gases [5-6]. It was observed that at high temperature ranges of 200-400°C, the adsorption and desorption of analytic gases result in a comprehensive change in electrical conductivity and resistivity of semiconductor materials. Basic gas sensing characteristics such as sensitivity, response time, recovery time, selectivity, detection limit, stability and recyclability, etc have been discussed in chapter 1. Here in this chapter, we present the responses of doped nanostructured ZnO with different volatiles. First, the results with the volatiles of tea are discussed followed by other gases and volatiles like methanol, ethanol, propanol, and detection of ammonia, hydrogen, liquefied petroleum gas, etc. In this context, we discuss the importance and requirement of sensors particularly for tea chemicals. Though the main aromatic ingredients in made tea are same, the quality of made black tea mainly differs on their flavour types, which rely on their trace volatile organic compounds (VOC) like linalool, linalool oxide, geraniol and trans-2-hexenal. These compounds are major aroma chemicals responsible for sweet, floral, fruity and fresh flavour [7] and are indicated in table 6.1. There are several types of tea like black tea, green tea, Oolong tea etc., and out of these, black tea is the most common beverage. Black tea has two major varieties, viz., (1) orthodox and (2) CTC (Cut-Tear-Curl). For measurement of tea quality, unfortunately no instrumental

methods are deployed on regular basis in the industry and for the assessment of quality; traditional methods of employing professional tea tasters [8] are still being practiced. Tea tasters, based on their own experience and own judgment, assess the quality of tea and the pricing of tea is made accordingly. The tea-tasters give a mark in the range of 1 to 10 each for leaf quality, infusion and liquor of the sample [9]. The mentioned method is purely subjective and error-prone in principle. Thus there is a need of some automated devices for quality evaluation of black tea which is low cost and portable. In this regard, electronic nose has been demonstrated to be an appropriate candidate [10] for the same.

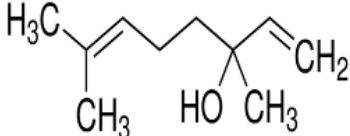
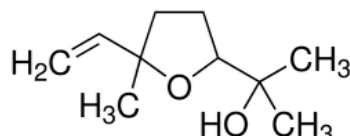
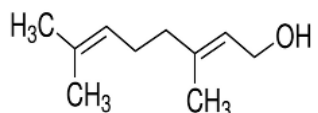
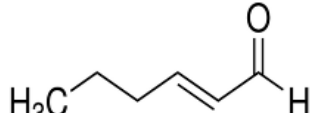
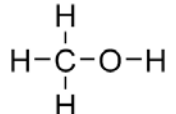
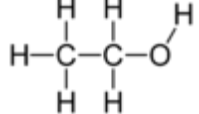
**Table 6.1.** Aroma chemicals responsible for black tea flavour

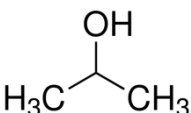
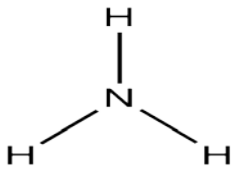
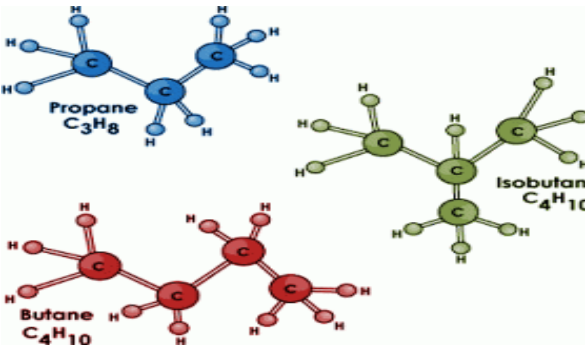
Compounds	Flavour
Linalool, Linalool oxide	Sweet
Geraniol, Phenylacetaldehyde	Floral
Nerolidol, Benzaldehyde, Methyl, Salicylate, Phenyl ethanol	Fruity
Trans-2-Hexenal, n-Hexenal, Grassy, Cis-3-Hexenal, b-Ionone	Fresh flavour

Recently, ZnO nanostructures are considered as excellent material for fabrication of highly sensitive and selective gas sensors for interesting and multifunctional properties. Thus, pure and doped ZnO nanomaterials are widely used to fabricate efficient gas sensors for the detection of various hazardous and toxic gases. As already mentioned, the most important aspect of the ZnO material is that it is completely an environment-friendly direct band gap material with wide band-gap energy of 3.37 eV and high exciton binding energy of  $\sim 60$  meV. Another attractive feature of ZnO is that its bandgap energy can be engineered by changing the dopant materials [11]. Very recently, nanostructured ZnO gas sensors have attracted more interest due to their better properties of detecting pollutants, toxic gases, alcohols and food freshness, especially fish freshness [12], or as gas-sensing films integrated on one chip to make an 'electronic nose' [13]. The sensitivities of gas sensors can be greatly improved by doping  $\text{MnO}_2$ ,  $\text{TiO}_2$  and  $\text{Co}_2\text{O}_3$ . In a recent paper, identification of flavour components through pattern recognition analysis of Chinese liquors has been carried out using doped nano ZnO gas sensor array and different statistical techniques are compared for their classification ability [14]. The volatile organic compounds (VOCs) are important areas of study for monitoring the status of pollution in environment, because these pollutants enter water, soil, atmosphere and are very much harmful for the human beings. It is due to the carcinogenic, teratogenetic or mutagenic

behavior of VOCs. The VOCs like methanol, ethanol and propanol are produced in human daily lives from home and personal care products. Methanol is highly toxic and often fatal to human health, which is a very useful organic solvent. It is widely used in the manufacturing of hair dye, perfumes, colors, formaldehyde, etc [15]. The nano-structured sensors made for this thesis work were exposed to these gases and their responses are presented in this chapter. The chemical structures of the volatile aromatic tea compounds and other gases considered for this study are presented here in Table 6.2.

**Table 6.2:** Chemical structure and properties of used volatile organic compounds and gases

 <p style="text-align: center;"><b>(a) Linalool</b></p>		 <p style="text-align: center;"><b>(b) Linalool oxide</b></p>	
<b>Properties</b>	<b>Values</b>	<b>Properties</b>	<b>Values</b>
Molecular formula	$C_{10}H_{18}O$	Molecular formula	$C_{10}H_{18}O_2$
Molar mass	$154.25 \text{ g mol}^{-1}$	Molar mass	$170.14 \text{ g mol}^{-1}$
Density	$0.858 \text{ g/cm}^3$	Density	$0.861 \text{ g/cm}^3$
Boiling point	$198-199^\circ\text{C}$	Boiling point	$190^\circ\text{C}$
Solubility in water	$1.589 \text{ g/l}$	Solubility in water	partial soluble
 <p style="text-align: center;"><b>(c) Geraniol</b></p>		 <p style="text-align: center;"><b>(d) Trans-2-hexenal</b></p>	
<b>Properties</b>	<b>Values</b>	<b>Properties</b>	<b>Values</b>
Molecular formula	$C_{10}H_{18}O$	Molecular formula	$C_6H_{10}O$
Molar mass	$154.25 \text{ g mol}^{-1}$	Molar mass	$98.14 \text{ g mol}^{-1}$
Density	$0.889 \text{ g/cm}^3$	Density	$0.851 \text{ g/cm}^3$
Boiling point	$229^\circ\text{C}$	Boiling point	$160^\circ\text{C}$
Solubility in water	Insoluble	Solubility in water	partial soluble
 <p style="text-align: center;"><b>(e) Methanol</b></p>		 <p style="text-align: center;"><b>(f) Ethanol</b></p>	
<b>Properties</b>	<b>Values</b>	<b>Properties</b>	<b>Values</b>
Molecular formula	$CH_3OH$	Molecular formula	$C_2H_5OH$
Molar mass	$32.04186 \text{ g mol}^{-1}$	Molar mass	$46.0684 \text{ g mol}^{-1}$
Density	$0.791 \text{ g/cm}^3$ at $25^\circ\text{C}$	Density	$0.789 \text{ g/cm}^3$ at $20^\circ\text{C}$

 <b>(g) Iso-propanol</b>		<b>H—H</b> <b>(h) Hydrogen</b>	
<i>Properties</i>	<i>Values</i>	<i>Properties</i>	<i>Values</i>
Molecular formula Molar mass Density	(CH <sub>3</sub> ) <sub>2</sub> CHOH 60.10 g mol <sup>-1</sup> 0.786 g/cm <sup>3</sup> at 20°C	Molecular formula Molar mass Density	H <sub>2</sub> 1.0079 g mol <sup>-1</sup> 0.08988 g/cm <sup>3</sup> at 0°C
 <b>(i) Ammonia</b>		 <b>(j) LPG = ( n-butane + iso-butane + propen)</b>	
<i>Properties</i>	<i>Values</i>	<i>Properties</i>	<i>Values</i>
Molecular formula Molar mass Density	NH <sub>3</sub> 17.03 g mol <sup>-1</sup> 0.6826g/cm <sup>3</sup> at 25°C	Molecular formula Molar mass Density	C <sub>4</sub> H <sub>10</sub> +C <sub>3</sub> H <sub>8</sub> +C <sub>4</sub> H <sub>10</sub> 44.1 g mol <sup>-1</sup> 0.525 to 0.580 at 15°C

## 6.2. Electrical measurements and gas sensing studies

Electrical as well as gas sensing properties of the synthesized material were studied by dc measurement. For the experiment, a pellet (10 mm diameter and 2.5 mm thickness) was made from the powder material using 1–2 drops of polyvinyl alcohol (PVA) (5%). The pellet was then heat-treated at 450°C for 4 hours to remove the residual polymer which helped to produce porous solid. The porous pellet with thin platinum electrodes was housed inside a quartz test-chamber, which was heated by a resistance furnace as mentioned in chapter 5 Fig. 5.3 (a-c). The temperature of the test-chamber was controlled using a temperature controller. Resistance of the sensor was measured using auto ranging microvolt DMM (Model 197A, M/s Keithley Instruments, USA) for low temperatures (when the resistance is higher than 100M) and Agilent Data Acquisition/Switch Unit (model no. 34970A) for higher temperatures. At each sensor operating temperature, the test gas was

injected into the chamber through an injection port after a steady base line resistance in air was established. Average crystallite size and particle size are observed to be between 24 and 33 nm, which were analyzed through XRD and transmission electron microscope (TEM) as shown in chapter 3. The response of the material to the test gases have been calculated using the equation:

$$\text{Response}(R) = \left[ \frac{(R_a - R_g)}{R_a} \right] \times 100\% \quad (6.1)$$

where,  $R_a$  denotes the resistance in air and  $R_g$  the resistance in the presence of a test gas. The response of the material is examined with black tea aroma (Linalool, Linalool oxide, Geraniol, Trans-2-hexenal), ammonia, hydrogen, liquefied petroleum gas, and VOC vapour (methanol, ethanol, propanol) in the temperature range of 200–400°C, and the sensitivity have been observed to be quite appreciable. The pure nanostructured ZnO has lower stability in corrosive, humid ambient due to large amount of oxygen vacancies. The properties of such ZnO nanostructures are often altered by adsorption of CO<sub>2</sub>, O<sub>2</sub>, and water. The electrical resistance decreases with doping with elements of noble and transition metals like Ni, Co, Pt, Pd, Mo, W, Cd and with rapid photothermal processing temperature up to 650°C that takes place simultaneously with the elimination of voids inside the pure and doped nanostructured ZnO. Irreversible changes in the electrical characteristics have been observed when the nanostructured ZnO after growth was rapidly photothermally processed at temperatures higher than 300°C for 20 sec duration. In the temperature range of 550-650°C, improvement of the quality and stability of the ZnO sensor samples has been observed [16].

### 6.3. Results and discussions

#### 6.3.1. Performance of pure and 3 wt % (Ni, Co, Pt, Pd)-doped ZnO in black tea bio-chemicals

Responses of the five sensors are represented in bar graphs in Fig. 6.1(a-e). Each bar-graph corresponds to the performance of a single sensor over a temperature range of 200°C-400°C towards each of the four major bio-chemical compounds of black tea aroma indicated by different colours as follows:

- (a) Geraniol - blue
- (b) Trans-2-hexenal - red
- (c) Linalool Oxide - green
- (d) Linalool - violet [13]

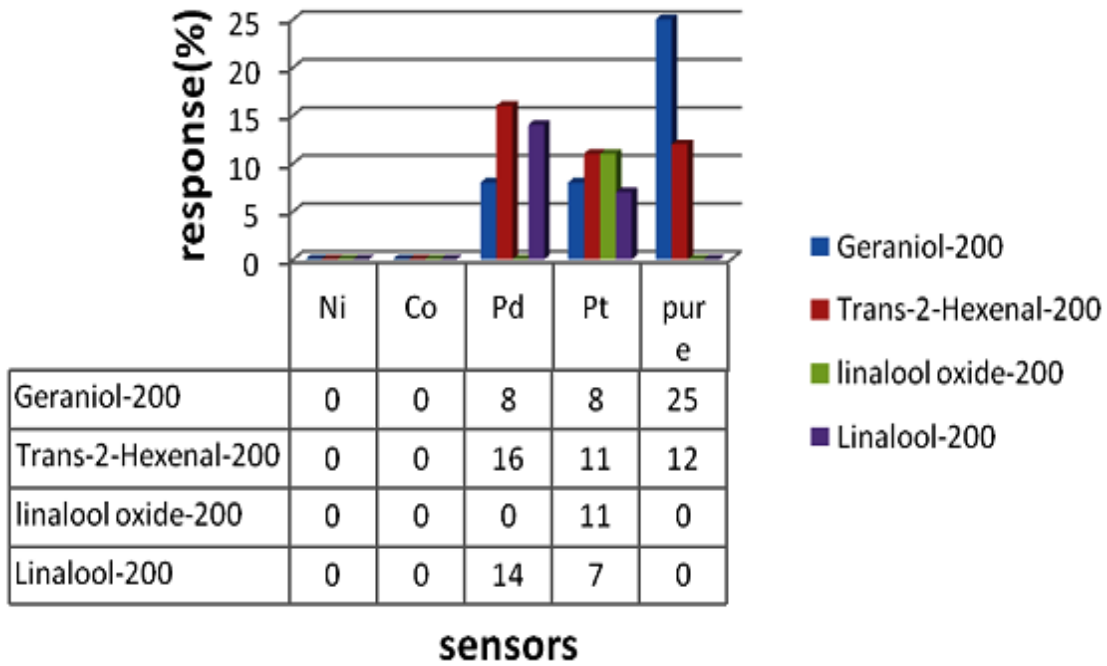


**Fig. 6.1.(a)** Performance of pure and 3 wt % (Ni, Co, Pt, Pd)-doped nanostructured ZnO sensors towards VOCs of black tea aroma (linalool, linalool oxide, geraniol, trans-2-hexenal) at 200°C

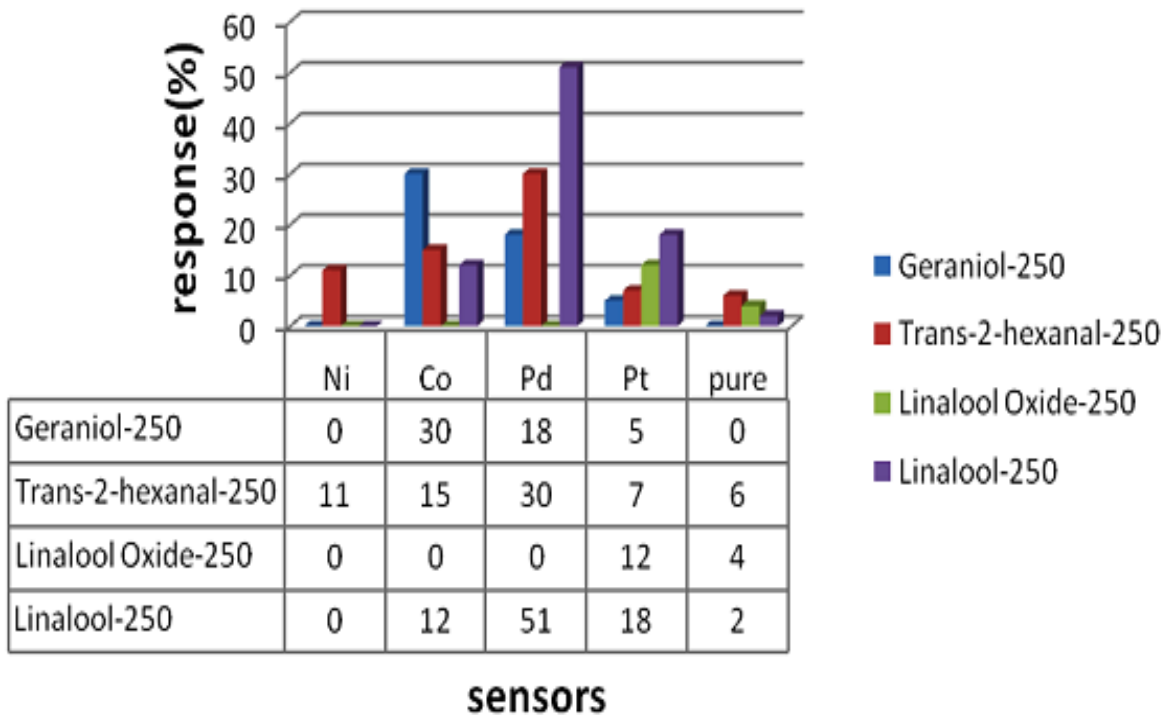


**Fig. 6.1. (b)** Performance of pure and 3 wt % (Ni, Co, Pt, Pd)-doped nanostructured ZnO sensors towards VOCs of black tea aroma (linalool, linalool oxide, geraniol, trans-2-hexenal) at 250°C

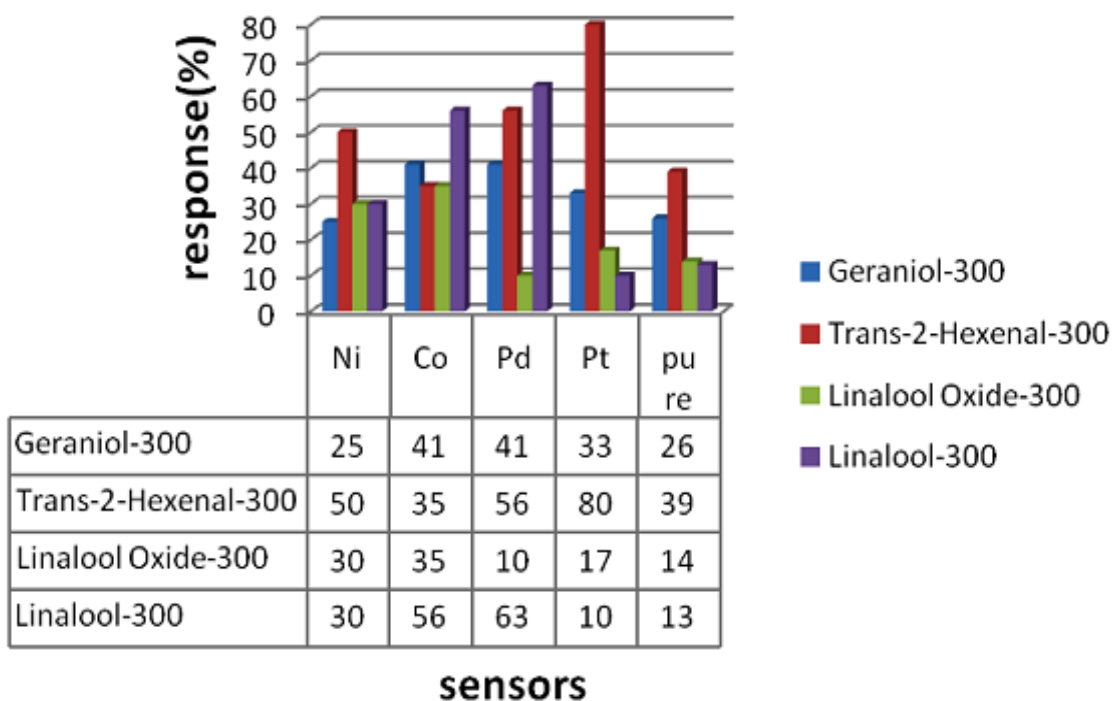


**Fig. 6.1. (c)** Performance of pure and 3 wt % (Ni, Co, Pt, Pd)-doped nanostructured ZnO sensors towards VOCs of black tea aroma (linalool, linalool oxide, geraniol, trans-2-hexenal) at 300°C

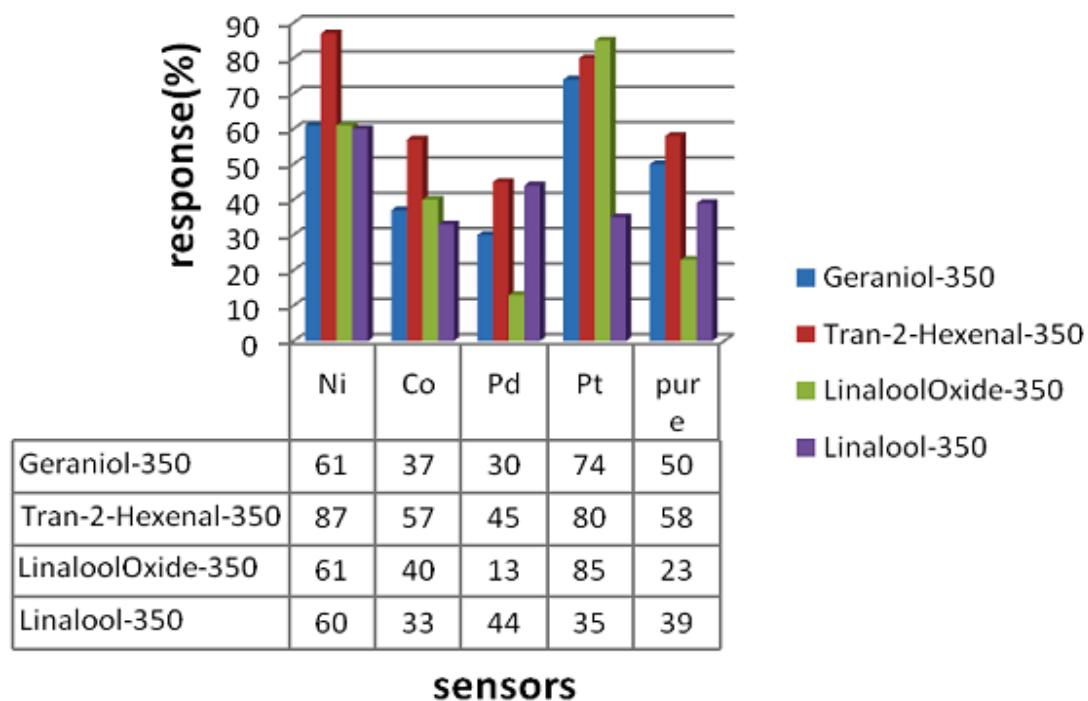


**Fig. 6.1. (d)** Performance of pure and 3 wt % (Ni, Co, Pt, Pd)-doped nanostructured ZnO sensors towards VOCs of black tea aroma (linalool, linalool oxide, geraniol, trans-2-hexenal) at 350°C

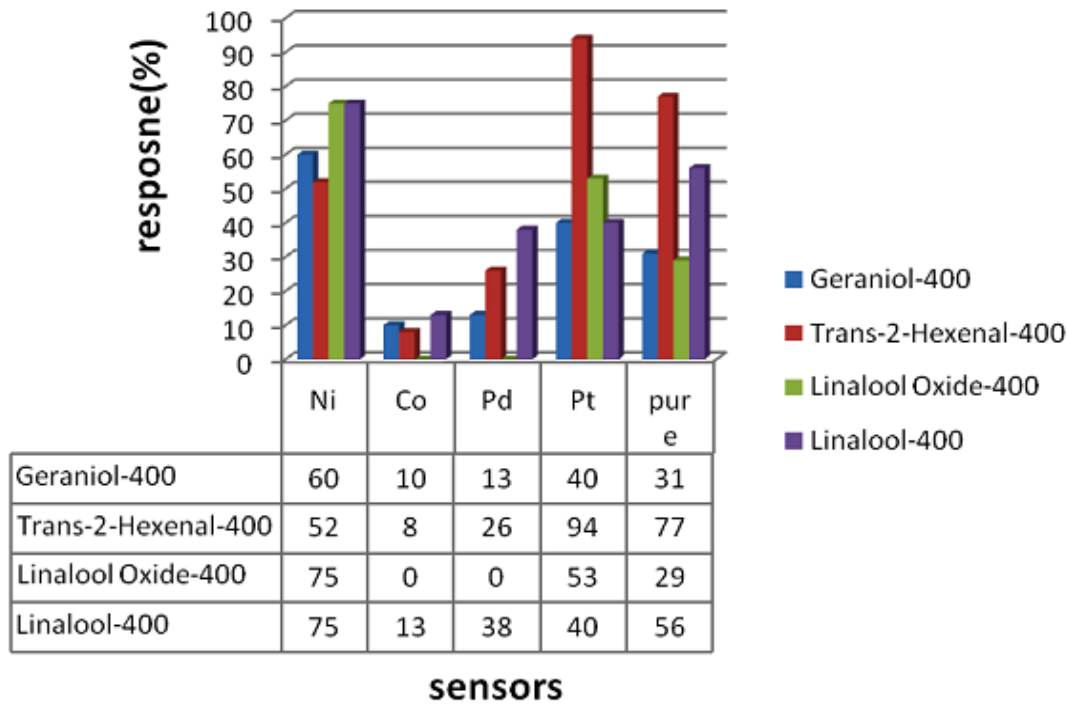


**Fig. 6.1. (e)** Performance of pure and 3 wt % (Ni, Co, Pt, Pd)-doped nanostructured ZnO sensors towards VOCs of black tea aroma (linalool, linalool oxide, geraniol, trans-2-hexenal) at 400°C

### 6.3.2. Performance of pure and 3 at % (Ni, Co, Pt, Pd)-doped ZnO at optimum temperature

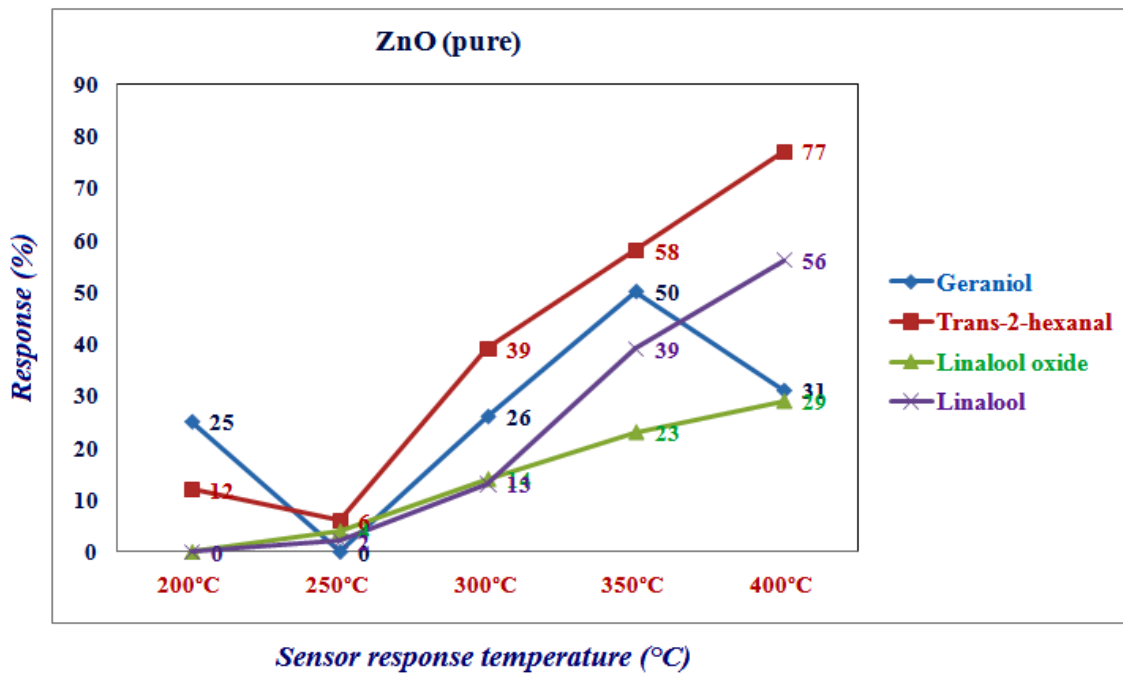


**Fig. 6.2. (a)** Performance of pure nanostructured ZnO sensors towards VOCs of black tea aroma (linalool, linalool oxide, geraniol, trans-2-hexenal) at optimum temperature 350°C



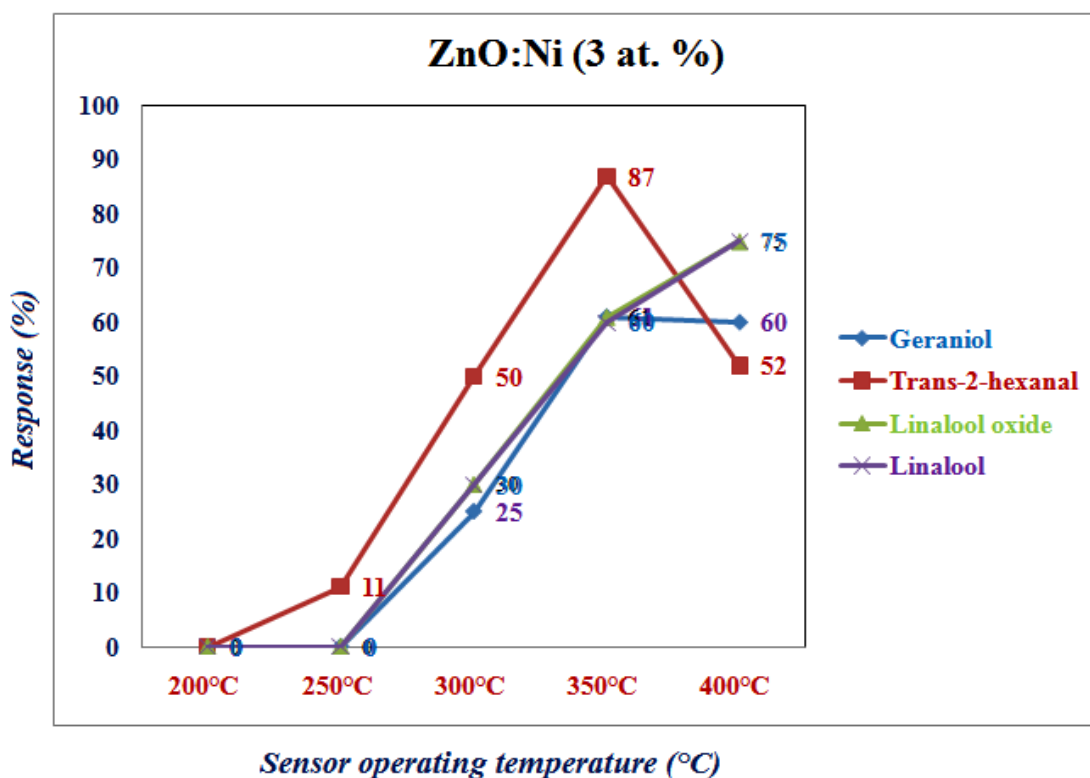


**Fig. 6.2. (b)** Performance of 3 at % Ni-doped nanostructured ZnO sensors towards VOCs of black tea aroma (linalool, linalool oxide, geraniol, trans-2-hexenal) at optimum temperature 350°C

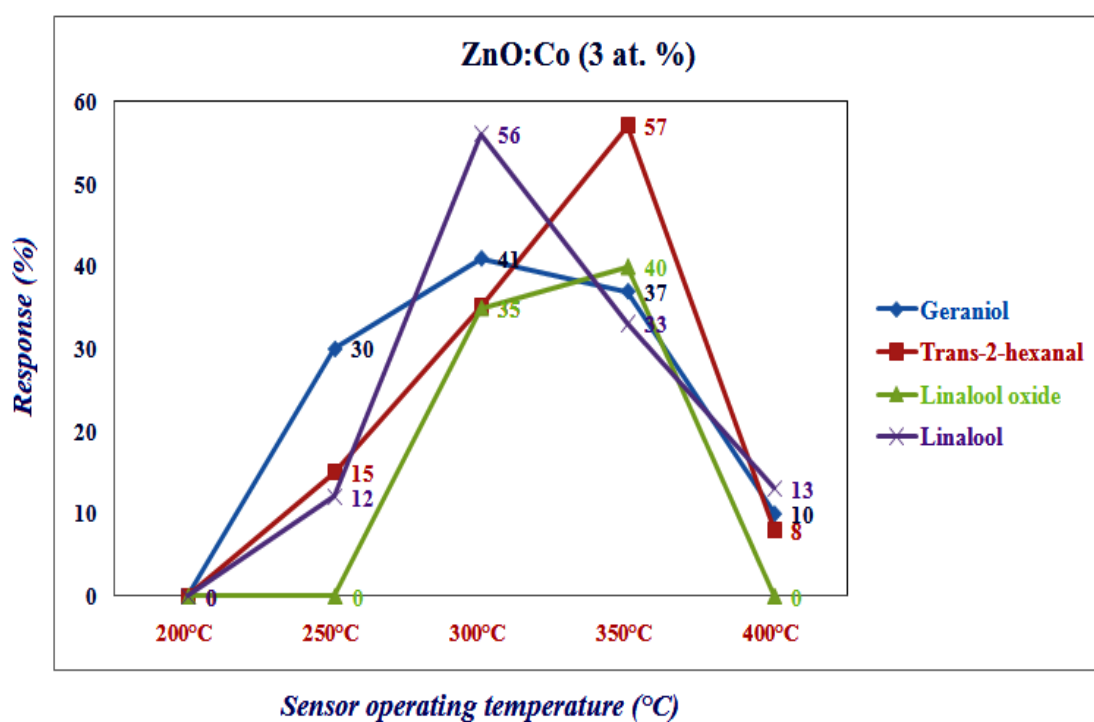


**Fig. 6.2. (c)** Performance of 3 at % Co-doped nanostructured ZnO sensors towards VOCs of black tea aroma (linalool, linalool oxide, geraniol, trans-2-hexenal) at optimum temperature 350°C

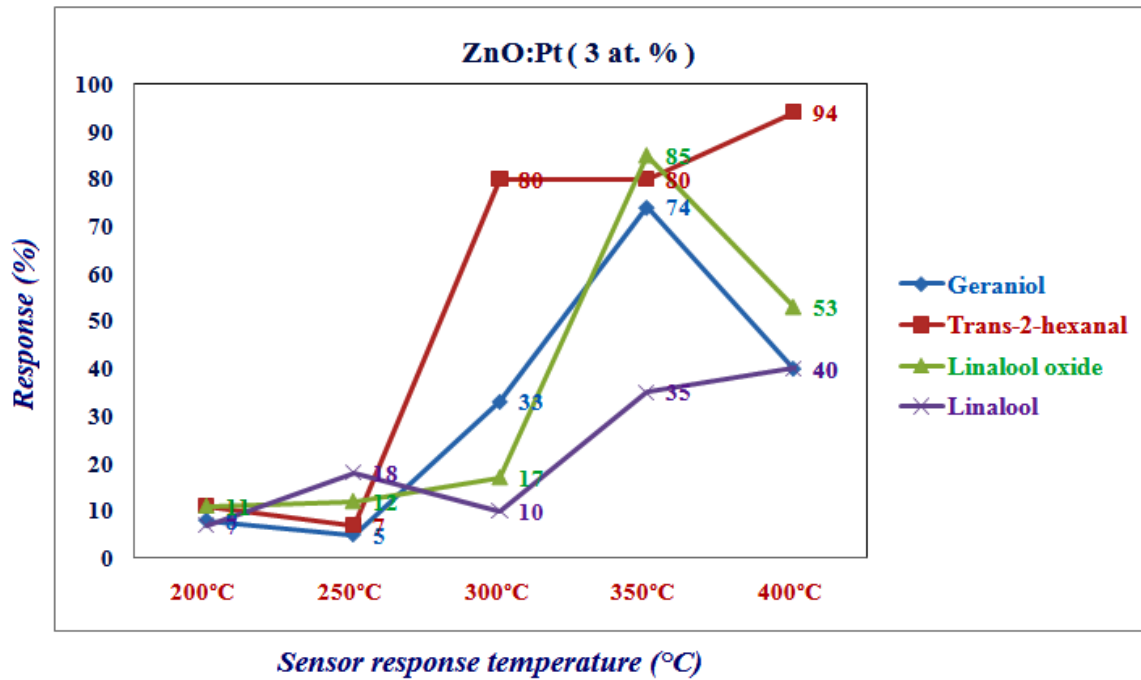


**Fig. 6.2. (d)** Performance of 3 at % Pt-doped nanostructured ZnO sensors towards VOCs of black tea aroma (linalool, linalool oxide, geraniol, trans-2-hexenal) at optimum temperature 350°C

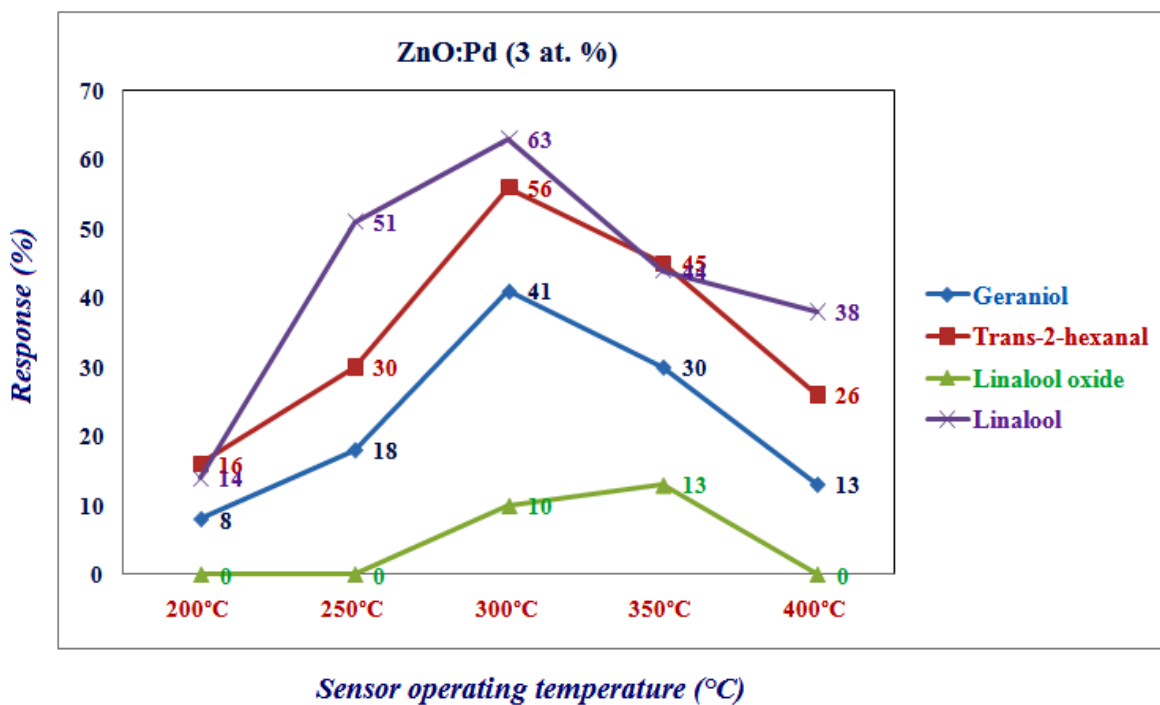


**Fig. 6.2. (e)** Performance of 3 at % Pd-doped nanostructured ZnO sensors towards VOCs of black tea aroma (linalool, linalool oxide, geraniol, trans-2-hexenal) at optimum temperature 350°C

In Figures 6.2 (a-e) the performances are shown for the developed sensors for VOCs of black tea bio-chemical compounds, pure and 3 wt % (Ni, Co, Pt, Pd)-doped nanostructured

ZnO. The obtained material is characterized and the crystallite size is calculated. It is found to be in a range of 40 nm to 52 nm. Then a suitable setup is designed to test the sensors against individual compounds of black tea like Geraniol, Trans-2-Hexenal, Linalool Oxide and Linalool in a temperature range of 200°C - 400°C. The response of all the sensors towards the compounds is studied and it is concluded that both the n-type semiconducting nanostructures ( $\text{Zn}_{0.97}\text{Ni}_{0.03}\text{O}$ ) and ( $\text{Zn}_{0.97}\text{Pt}_{0.03}\text{O}$ ) are best suited to sense VOCs of black tea aroma at an optimum temperature of 350°C.

From Figures 6.3 (a-d), none of the sensors show a good response at 200°C or 250°C. At 300°C, ( $\text{Zn}_{0.97}\text{Pt}_{0.03}\text{O}$ ) gives the maximum response as in Fig.6.3 (a), whereas ( $\text{Zn}_{0.97}\text{Ni}_{0.03}\text{O}$ ) shows the most consistent response towards all compounds. At 350°C ( $\text{Zn}_{0.97}\text{Ni}_{0.03}\text{O}$ ) and ( $\text{Zn}_{0.97}\text{Pt}_{0.03}\text{O}$ ) show an increase in response while ( $\text{Zn}_{0.97}\text{Co}_{0.03}\text{O}$ ) show a decrease in response as shown in Fig. 6.3 (b). It can be observed that the sensors show a better response at 350°C than at any other temperature for the biochemical aroma compounds of black tea.

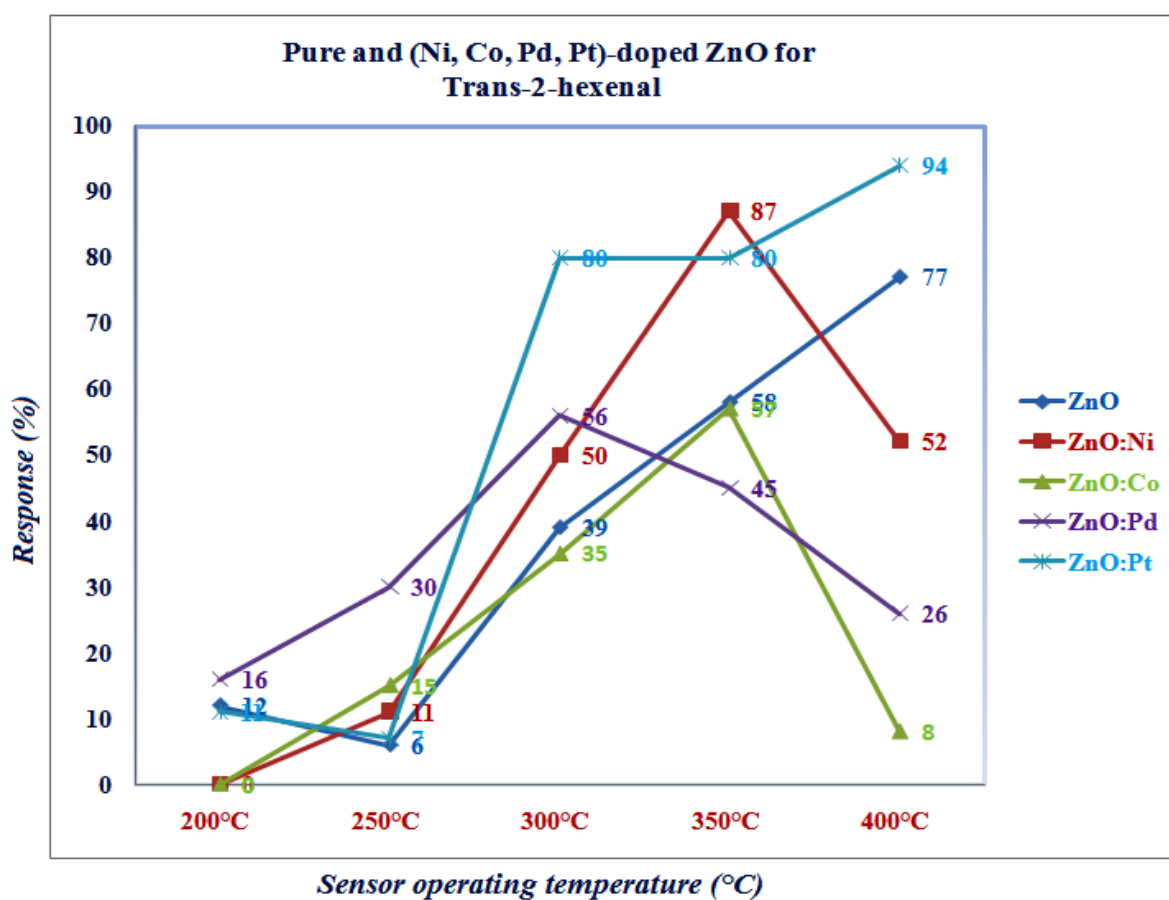


**Fig. 6.3. (a)** Performance of pure and 3 wt % (Ni, Co, Pt, Pd)-doped nanostructured ZnO sensors towards VOCs of black tea aroma for Trans-2-hexenal vapour at optimum temperature 350°C

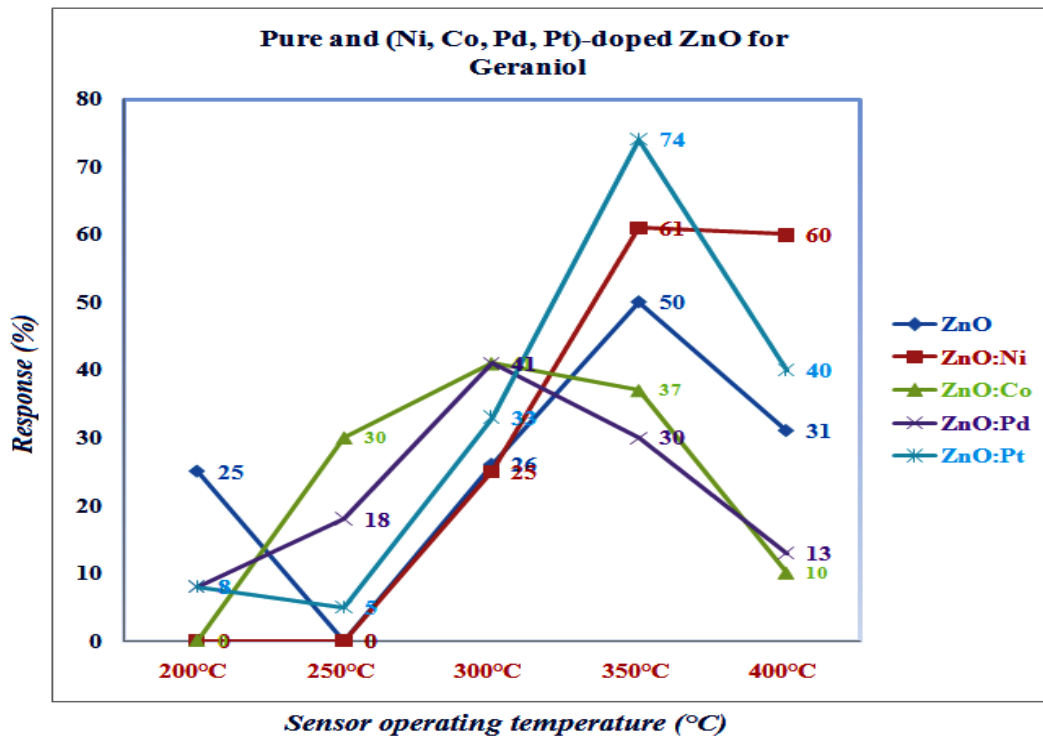


**Fig. 6.3. (b)** Performance of pure and 3 wt % (Ni, Co, Pt, Pd)-doped nanostructured ZnO sensors towards VOCs of black tea aroma for Geraniol vapour at optimum temperature 350°C

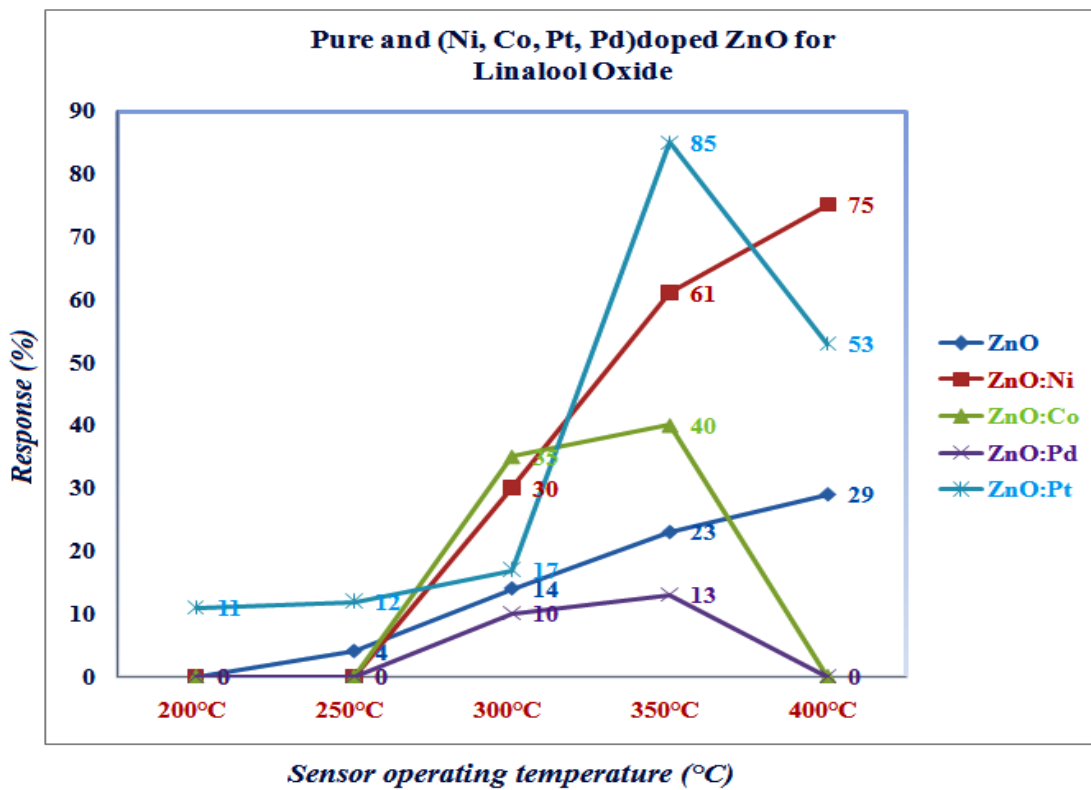


**Fig. 6.3. (c)** Performance of pure and 3 wt % (Ni, Co, Pt, Pd)-doped nanostructured ZnO sensors towards VOCs of black tea aroma for Linalool oxide vapour at optimum temperature 350°C

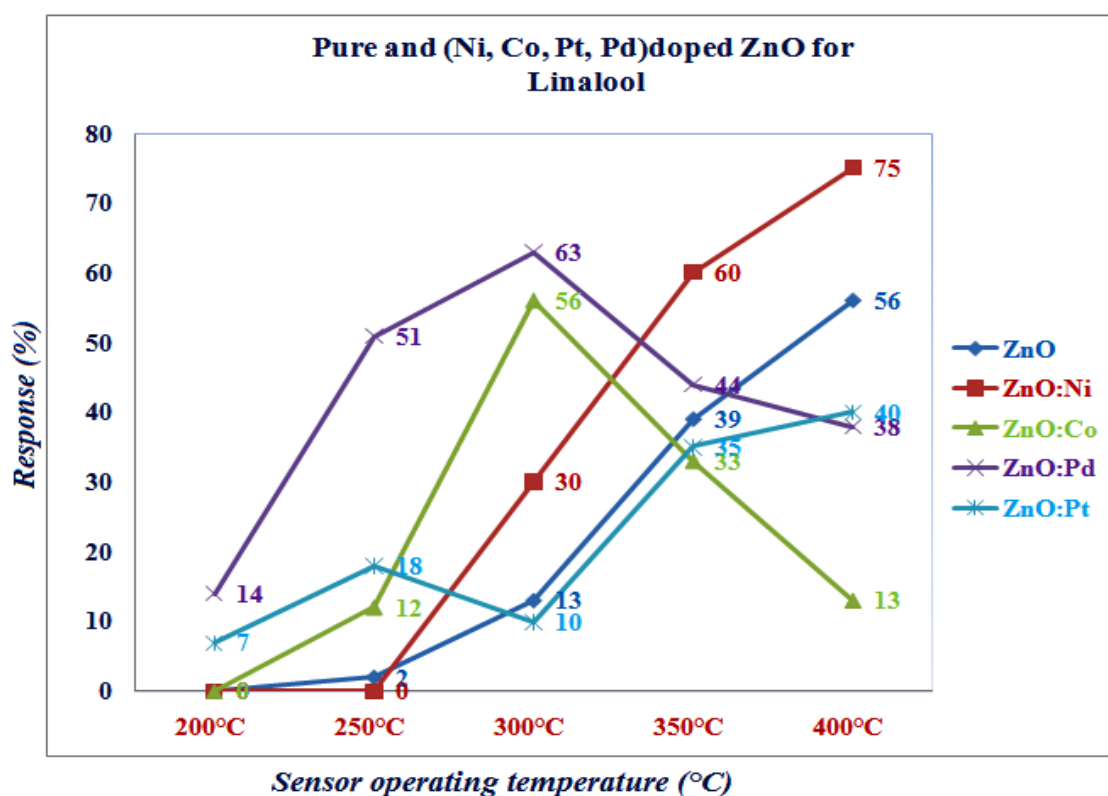


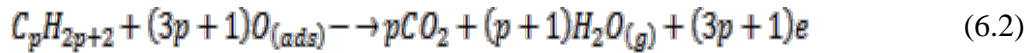
Fig. 6.3. (d) Performance of pure and 3 wt % (Ni, Co, Pt, Pd)-doped nanostructured ZnO sensors towards VOCs of black tea aroma for Linalool vapour at optimum temperature 350°C

Table 6.3. Summary of the performances of doped ZnO nanostructured sensors at optimum temperature of 350°C

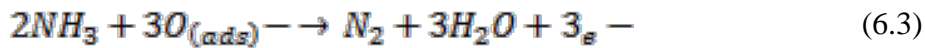
VOCs	Maximum Response (%)	Nanostructures sensors	Optimum temperature (°C)	Semi-conductor type	Crystallite size (nm)
<i>Trans-2-hexenal</i>	87	(Zn <sub>0.97</sub> Ni <sub>0.03</sub> O)	350	n-type	40-52
	80	(Zn <sub>0.97</sub> Pt <sub>0.03</sub> O)	350	intrinsic	
	59	ZnO	350		
<i>Geraniol</i>	74	(Zn <sub>0.97</sub> Pt <sub>0.03</sub> O)	350	n-type	
	61	(Zn <sub>0.97</sub> Ni <sub>0.03</sub> O)	350	intrinsic	
	50	ZnO	350		
<i>Linalool oxide</i>	85	(Zn <sub>0.97</sub> Pt <sub>0.03</sub> O)	350	n-type	
	61	(Zn <sub>0.97</sub> Ni <sub>0.03</sub> O)	350	intrinsic	
	23	ZnO	350		
<i>Linalool</i>	60	(Zn <sub>0.97</sub> Ni <sub>0.03</sub> O)	350	n-type	
	35	(Zn <sub>0.97</sub> Pt <sub>0.03</sub> O)	350	intrinsic	
	39	ZnO	350		

### 6.3.3. Performance of $(\text{Zn}_{0.97}\text{Pd}_{0.03}\text{O})$ sensors for ammonia, hydrogen, liquefied petroleum gas

The oxidation reactions of  $\text{H}_2$  and LPG could be represented as in equation [6.2]:



LPG is a mixture of hydrocarbons like n-propane and n-butane, so  $p = 3$  or  $4$ . This equation is valid for  $\text{H}_2$  when  $p = 0$ . The oxidation reactions of  $\text{NH}_3$  could be represented as follows [6.3]:



Performance of  $(\text{Zn}_{0.97}\text{Pd}_{0.03}\text{O})$  nanostructured chemo-resistive sensor in alternating environment of air at 500 ppm

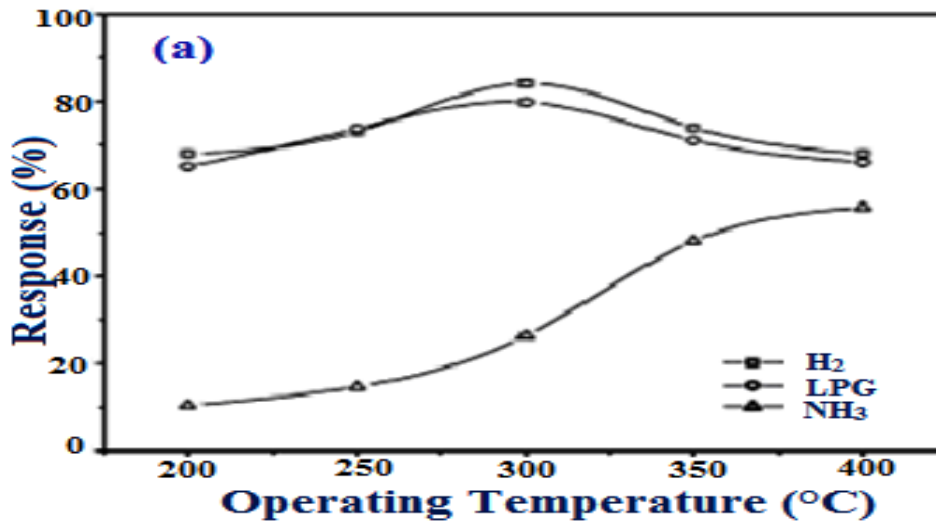


Fig.6.4. (a) Response vs. operating temperature of  $\text{H}_2$ , LPG and  $\text{NH}_3$

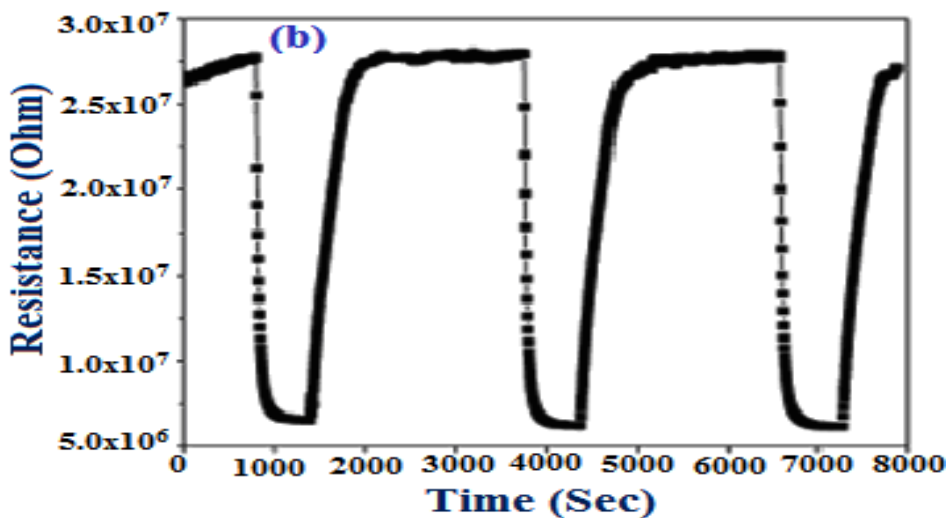


Fig.6.4.(b) Electrical resistance vs. time of at  $300^\circ\text{C}$

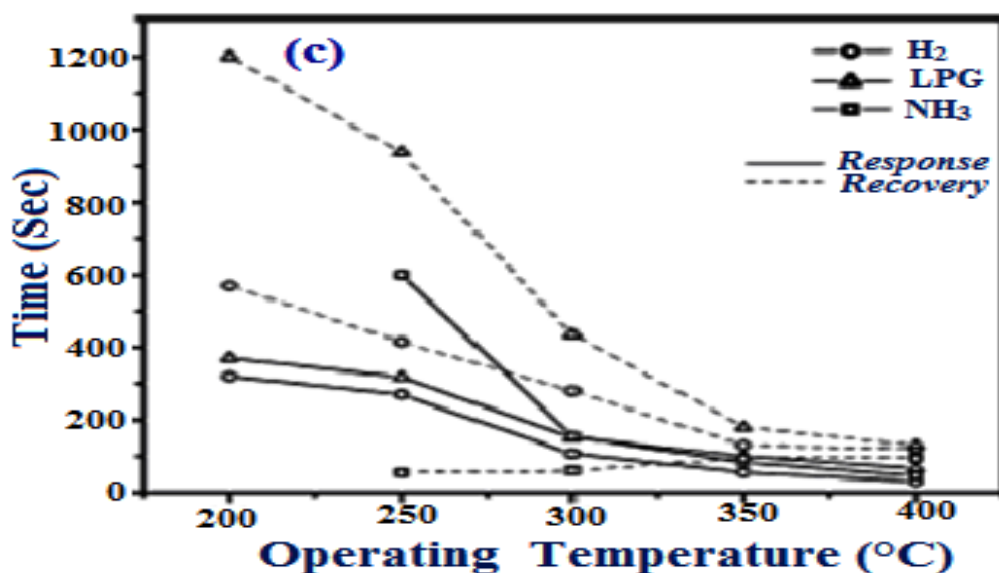


Fig.6.4.(c) Response and recovery time vs. operating temperature of H<sub>2</sub>, LPG and NH<sub>3</sub>

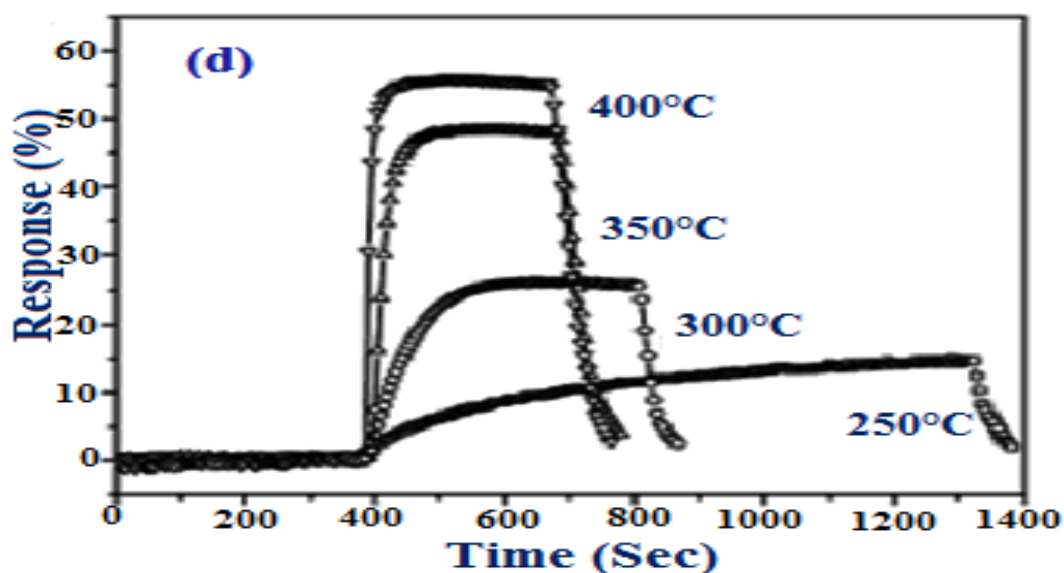


Fig.6.4.(d) Response vs. time of NH<sub>3</sub> in air at different temperatures

Sensing characteristics of nanosized ZnO (Pd) in the form of porous pellet towards 500 ppm of hydrogen, ammonia and liquefied petroleum gas [16] in air as function of temperature is shown in Fig. 6.4(a), change in electrical resistance is shown in alternating environments of air and 500 ppm LPG at 300°C in Fig. 6.4(b). Fig. 6.4(c) shows the temperature variation of response and recovery times for ZnO (Pd) for 500 ppm ammonia, hydrogen and liquefied petroleum gas. The response of nanocrystalline ZnO (Pd) towards 500 ppm of NH<sub>3</sub> in air at different temperatures is shown Fig. 6.4(d). In Fig.6.4 (Zn<sub>0.97</sub>Pd<sub>0.03</sub>O) nanostructure chemo-resistive sensor powders have been synthesized by aqueous based metal ion-ligand complex precursor route for the first time. The hexagonal-wurtzite structure of (Zn<sub>0.97</sub>Pd<sub>0.03</sub>O) and (Zn<sub>0.97</sub>Pt<sub>0.03</sub>O) was calcined at 500°C. The low processing temperature in this method prevented grain growth in the powder [16].

**Table 6.4.** Performance of noble metal doped ZnO nanostructure chemo-resistive pellet for sensor applications

Sensors	Calcined temperature (°C) and time (hrs)	Structure	Particle size (HRTEM)	% of Response and working temperature at 500 ppm		
				H <sub>2</sub>	NH <sub>3</sub>	LPG
(Zn <sub>0.97</sub> Pd <sub>0.03</sub> O)	600°C (5 hrs)	Hexagonal-wurtzite	35-60 nm	84 (300°C)	52 (350°C)	81 (300°C)
(Zn <sub>0.97</sub> Pt <sub>0.03</sub> O)	600°C (5 hrs)	Hexagonal-wurtzite	35-60 nm	80 (300°C)	54 (350°C)	78 (300°C)

The n-type semiconducting nanostructured (Zn<sub>0.97</sub>Pd<sub>0.03</sub>O) and (Zn<sub>0.97</sub>Pt<sub>0.03</sub>O) showed reasonably good sensitivities towards hydrogen, ammonia and liquefied petroleum gas. The maximum sensing responses of (Zn<sub>0.97</sub>Pd<sub>0.03</sub>O) and (Zn<sub>0.97</sub>Pt<sub>0.03</sub>O) towards H<sub>2</sub>, LPG and NH<sub>3</sub> from 200°C - 400°C in alternating environments of air are depicted in Figs. 6.4 (a-b). The details of the sensors and their observed gas sensing behaviours towards reducing gases such as, hydrogen, ammonia and liquefied petroleum gas are summarized in Table 6.4.

#### 6.3.4. Performance of pure and (1, 2, 3) wt % Mo-doped ZnO in black tea bio-chemical

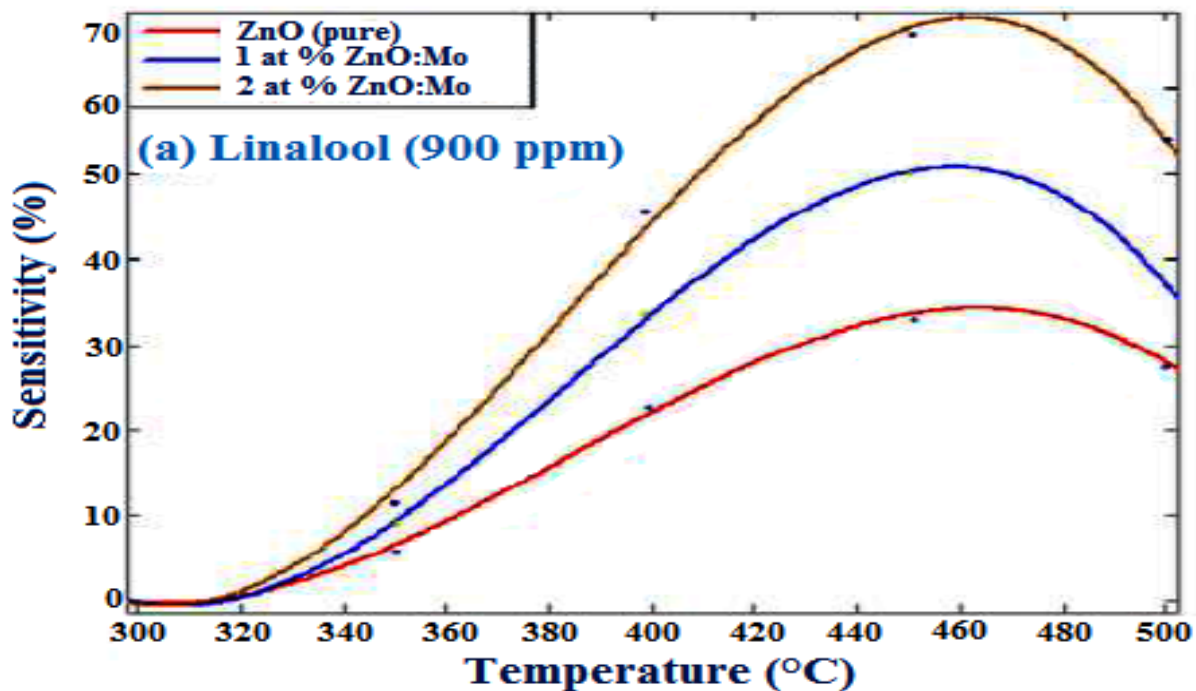


**Fig. 6.5.** (a) Sensitivity vs. Temperature to 900 ppm of pure and (1, 2) wt % Mo-doped ZnO chemo-resistive pellets sintered at 500°C for 3 hours with linalool



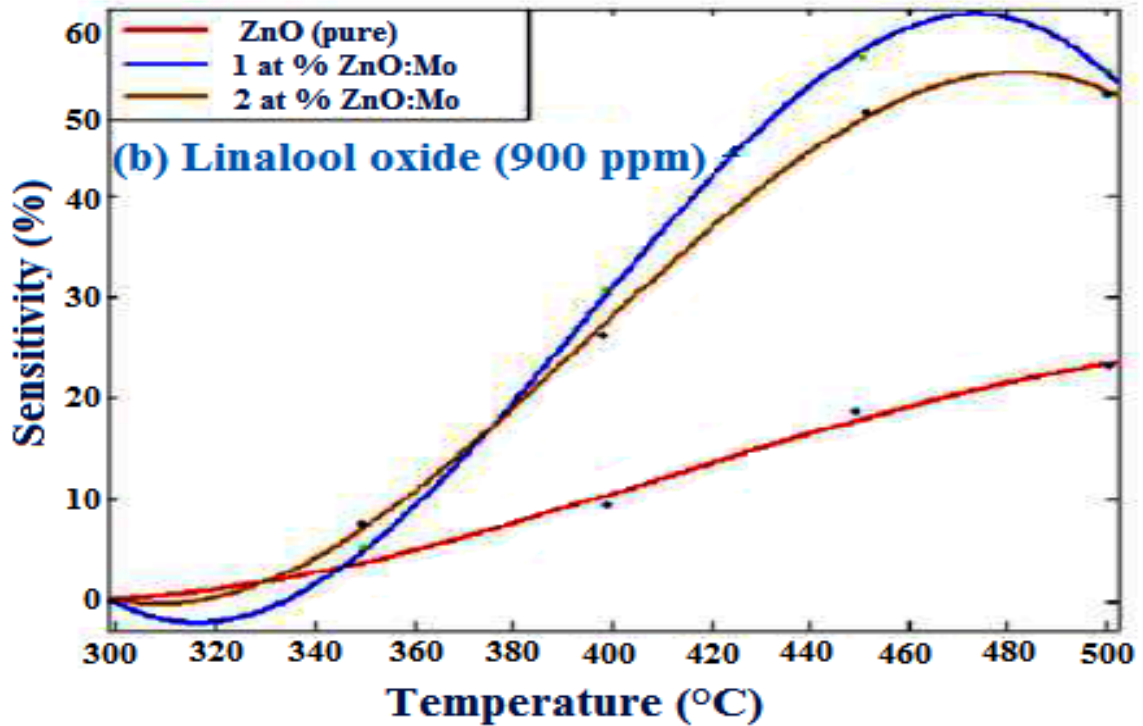


Fig. 6.5. (b) Sensitivity vs. Temperature to 900 ppm of pure and (1, 2) wt % Mo-doped ZnO chemo-resistive pellets sintered at 500°C for 3 hours with linalool oxide

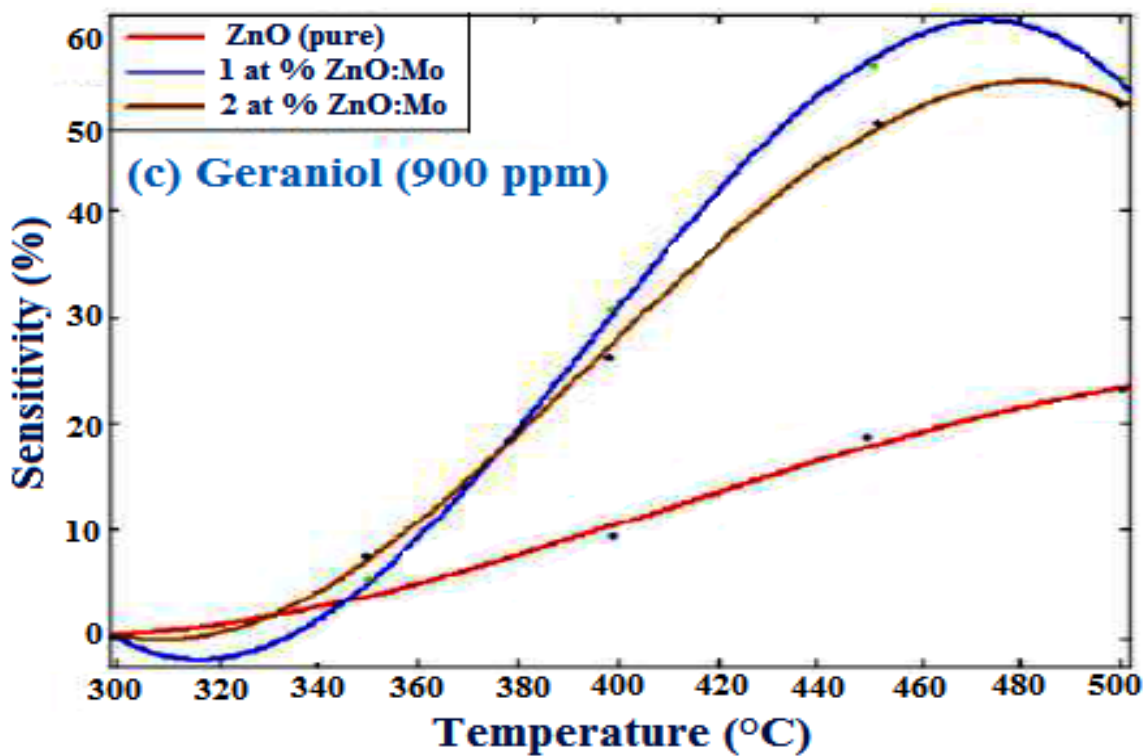
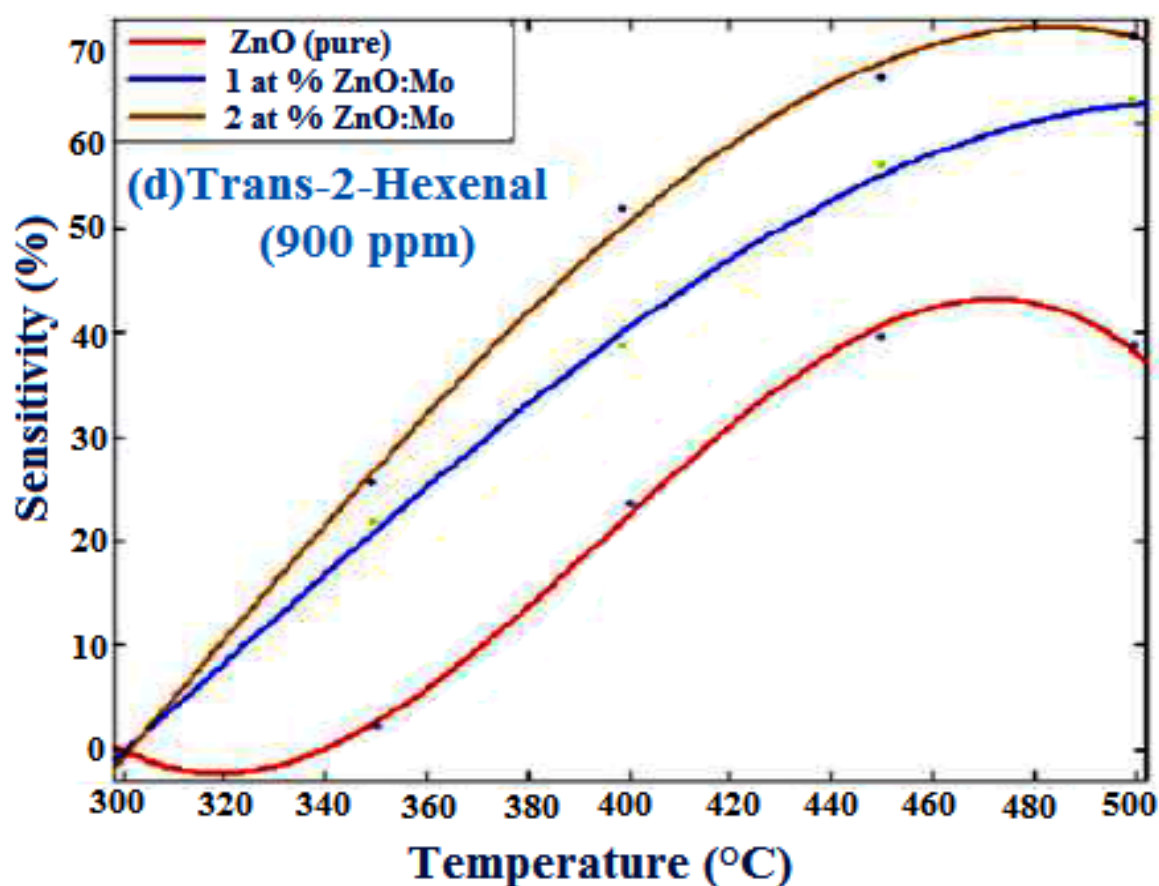
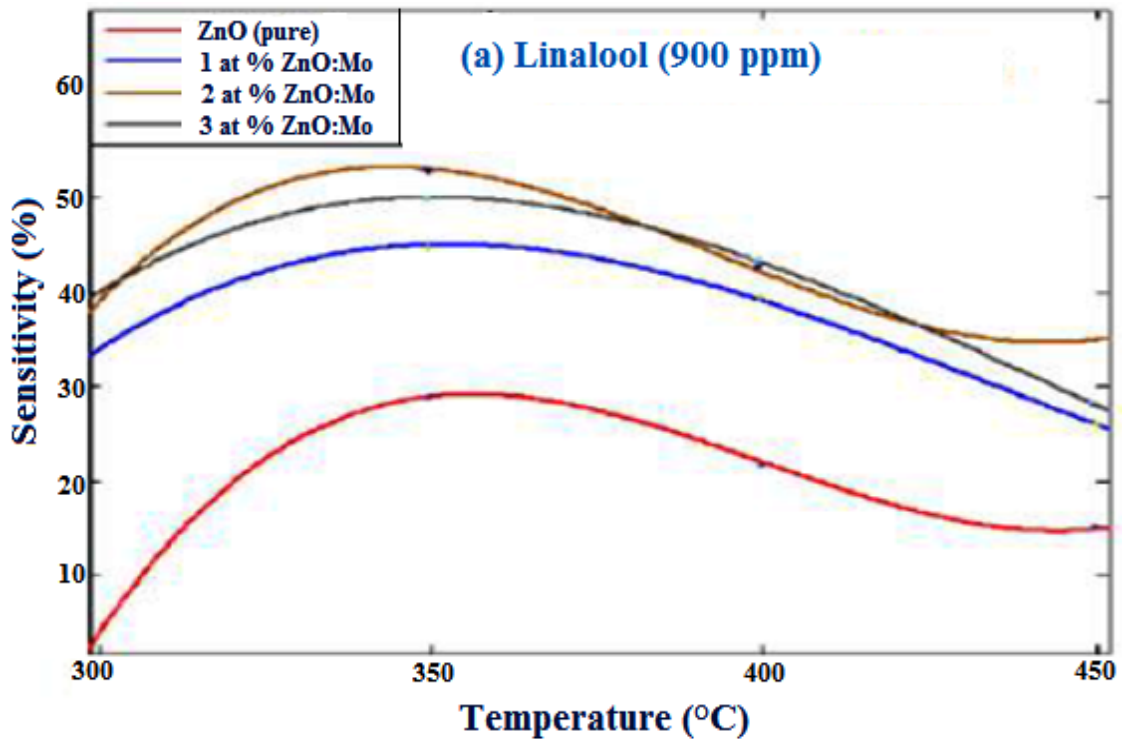


Fig. 6.5. (c) Sensitivity vs. Temperature to 900 ppm of pure and (1, 2) wt % Mo-doped ZnO chemo-resistive pellets sintered at 500°C for 3 hours with geraniol



**Fig. 6.5. (d)** Sensitivity vs. Temperature to 900 ppm of pure and (1, 2) wt % Mo-doped ZnO chemo-resistive pellets sintered at 500°C for 3 hours with trans-2-hexenal

The pure and (1,2,3) wt % Mo-doped nanostructured ZnO sensor shows a characteristic activity which causes its sensitivity to increase appreciably while the nature of change of sensitivity remains almost the same. VOCs of black tea aroma (linalool, linalool oxide, geraniol, trans-2-hexenal) vapours show a characteristic change in sensitivity with temperature which is unique as shown in Fig. 6.5 (a-d). The sensors sintered at 350°C for 6 hours show monotonic increase in sensitivity for Geraniol and Trans-2-hexenal while the response is peaked at 350°C for linalool and linalool oxide as shown in Fig. 6.6 (a-d). On increasing the sintering temperature, we obtain peaks for all but the maximum sensitivity points are obtained at temperatures greater than 400°C. Repeatability for sensors sintered at 350°C is at  $\pm 3\%$  of the mean value for all tea bio-chemicals. There is a substantial increase in sensitivity for all the sensors when sintered at 500°C but repeatability falls to  $\pm 5.5\%$  of the mean. Sintering temperatures play an important role in nanocrystal formation at the active sensor surface and this is discussed in details in [17].



*Fig. 6.6. (a) Sensitivity vs. Temperature to 900 ppm of pure and (1, 2, 3) at % Mo-doped ZnO chemo-resistive pellets sintered at 350°C for 6 hours with linalool*

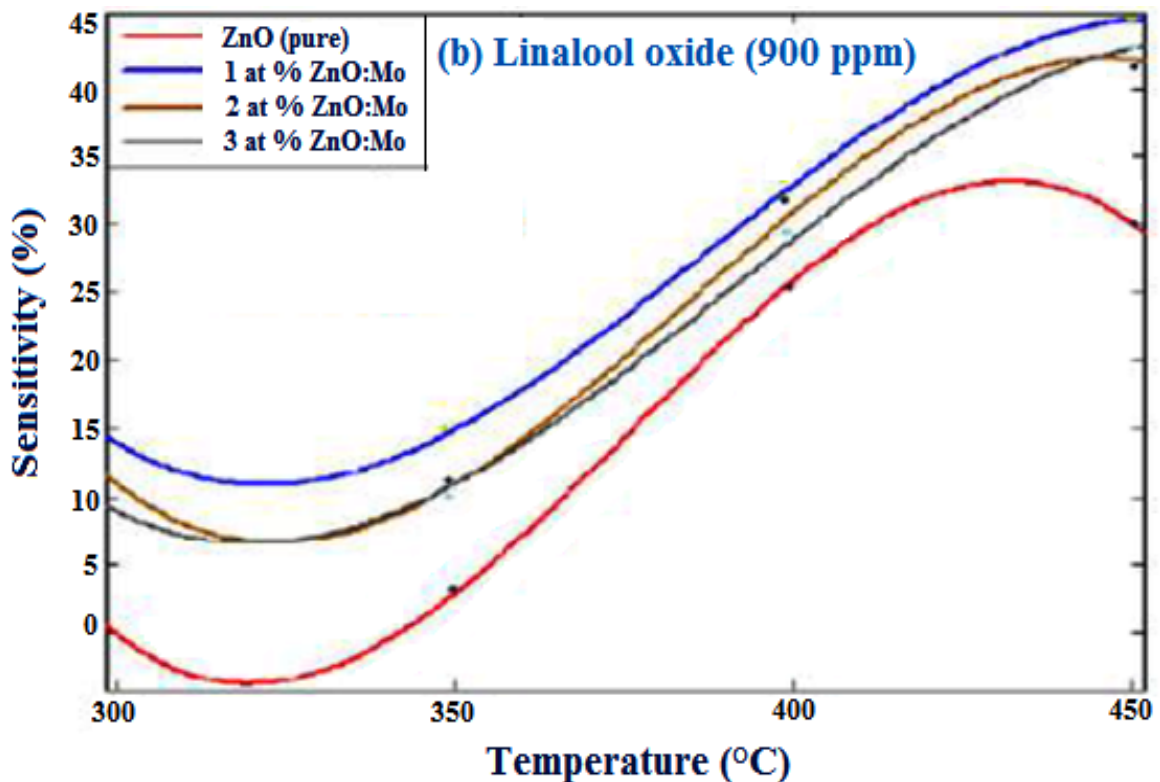


*Fig.6.6.(b) Sensitivity vs. Temperature to 900 ppm of pure and (1, 2, 3) at % Mo-doped ZnO chemo-resistive pellets sintered at 350°C for 6 hours with linalool oxide*

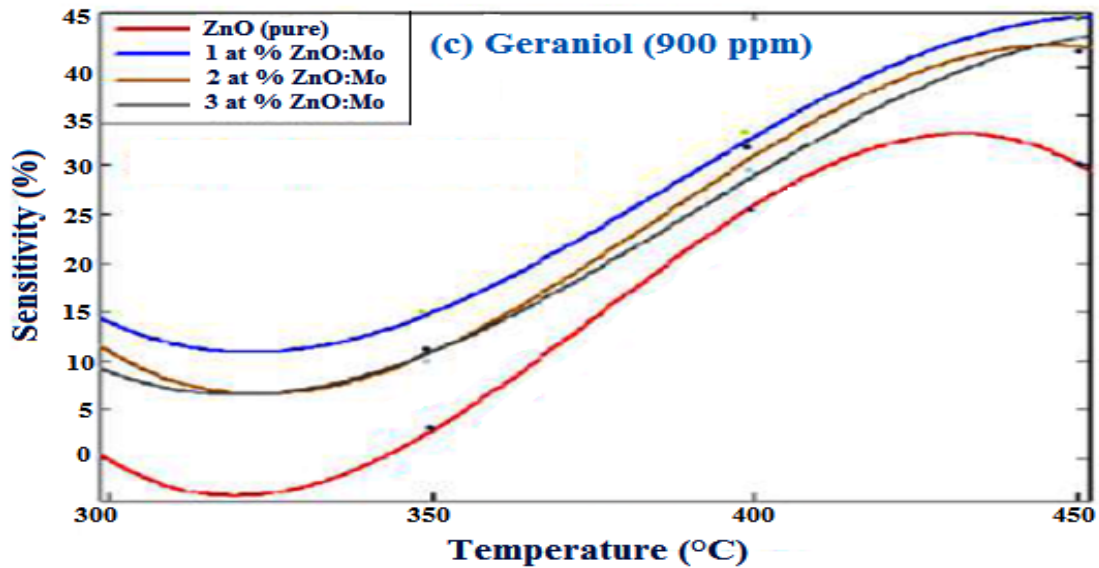


**Fig.6.6.(c)** Sensitivity vs. Temperature to 900 ppm of pure and (1, 2, 3) at % Mo-doped ZnO chemo-resistive pellets sintered at 350°C for 6 hours with geraniol

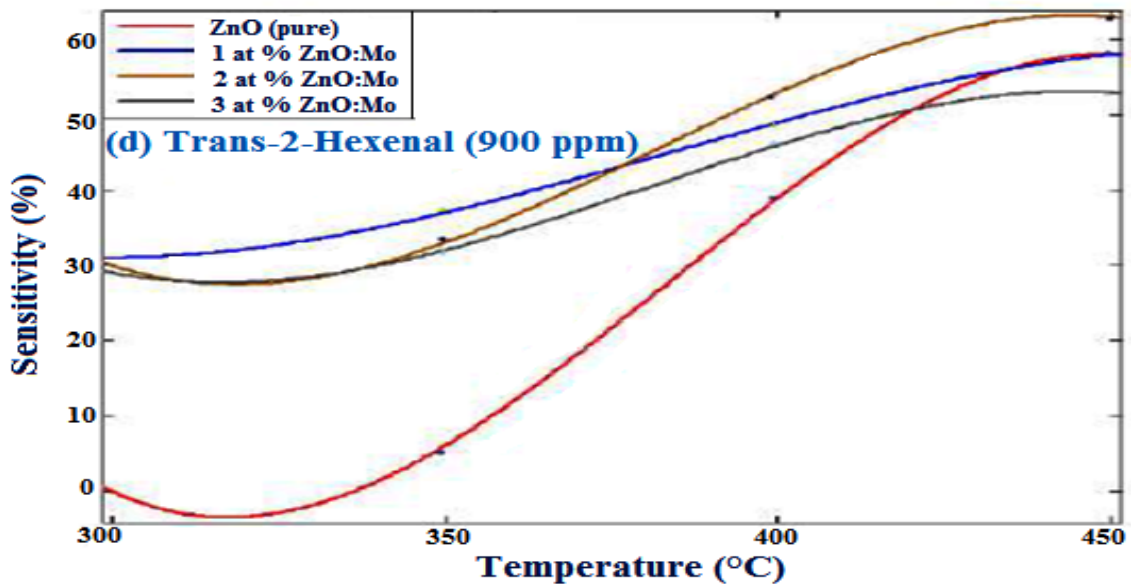


**Fig.6.6.(d)** Sensitivity vs. Temperature to 900 ppm of pure and (1, 2, 3) at % Mo-doped ZnO chemo-resistive pellets sintered at 350°C for 6 hours with trans-2-hexenal

**Table 6.5.** Performance of ZnO:Mo nanostructure sensors at optimum temperature 350°C

VOCs	Sensitivity (%)		Nanostructures sensors	optimum temperature (°C)	Sintered temperature (°C) and hours	Crystallite size(nm)
	Initial	Final				
<i>Linalool Oxide</i>	28	53	(Zn <sub>0.98</sub> Mo <sub>0.02</sub> O)	350	350°C, 6 hours	40-52
	32	62		450	500°C, 3 hours	
<i>Trans-2-hexenal</i>	40	60	(Zn <sub>0.98</sub> Mo <sub>0.02</sub> O)	350	500°C, 3 hours	

Thus, in general the ( $\text{Zn}_{0.98}\text{Mo}_{0.02}\text{O}$ ) nanostructure pellet sintered at  $350^\circ\text{C}$  for 6 hours is better as compared to other ( $\text{Zn}_{0.99}\text{Mo}_{0.01}\text{O}$ ) and ( $\text{Zn}_{0.97}\text{Mo}_{0.03}\text{O}$ ) sensors we have prepared for black tea bio-chemicals.

### 6.3.5. Performance of (5, 10, 15) wt % W-doped ZnO in black tea bio-chemicals and ethanol, methanol and propanol

The interesting feature to be observed that in all cases linalool exhibits the maximum and trans 2-hexenal the minimum sensitivity, but trans 2-hexenal exhibits the maximum rate of response. In Fig. 6.7, (a) and (b) are the responses of ( $\text{Zn}_{0.95}\text{W}_{0.05}\text{O}$ ) sensor, (c, d) are of ( $\text{Zn}_{0.90}\text{W}_{0.10}\text{O}$ ) sensor and (e) and (f) are of ( $\text{Zn}_{0.85}\text{W}_{0.15}\text{O}$ ) sensors. The trans-2-hexenal responds fastest with minimum sensitivity and is clearly justified as it is the smallest molecule. Linalool and geraniol have the same molecular weight but though linalool is a tertiary alcohol, it is evident from its structure that it is more unstable than Geraniol and hence though the rate of response of both linalool and geraniol are near about the same, sensitivity to linalool is more than geraniol [18]. Lastly linalool oxide is the most stable of all of the above compounds and hence the slowest to respond. The major achievement with tungsten doping is that saturating time which was around 40-50 seconds in case of ( $\text{Zn}_{0.98}\text{Mo}_{0.02}\text{O}$ ) nanostructured sensors is now down to 5-6 seconds. Also the sensors are very stable and repeated temperature recycling hardly affects its performance. Also the same sensor may be used for all volatiles under study which is not the case in ( $\text{Zn}_{0.98}\text{Mo}_{0.02}\text{O}$ ). However for real time applicability, speed of response is still not small [18].

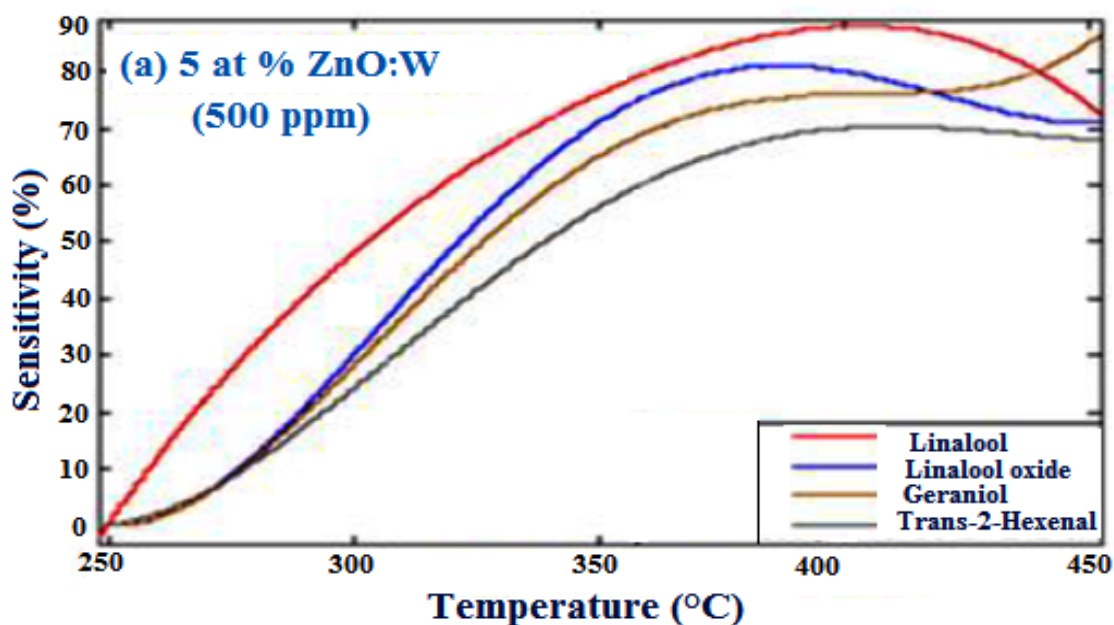


Fig.6.7.(a) Performance of 5 at % ZnO:W (500 ppm) Sensitivity vs. Temperature

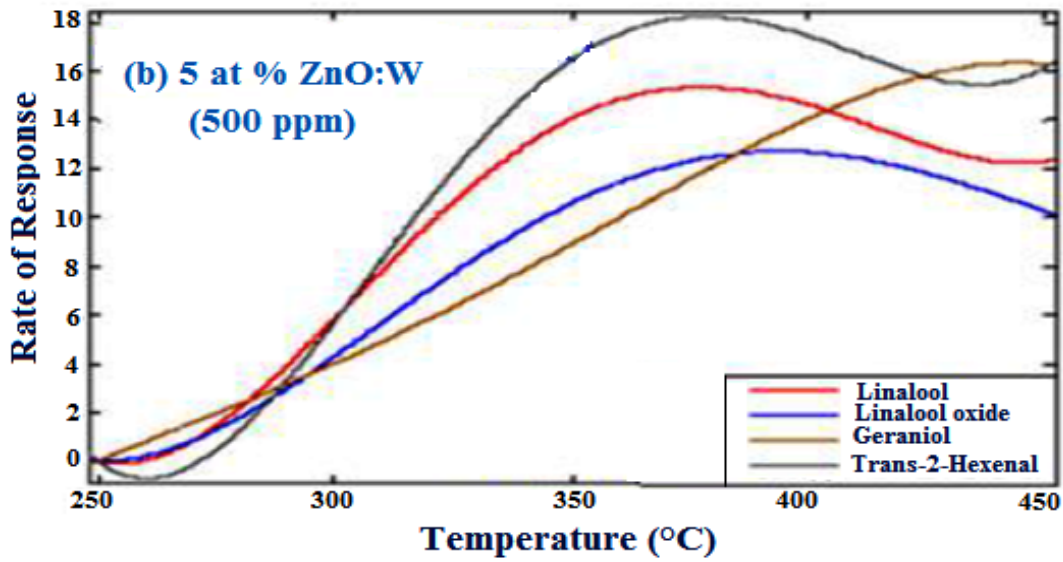


Fig.6.7.(b) Performance of 5 at % ZnO:W (500 ppm) Rate of Response vs. Temperature

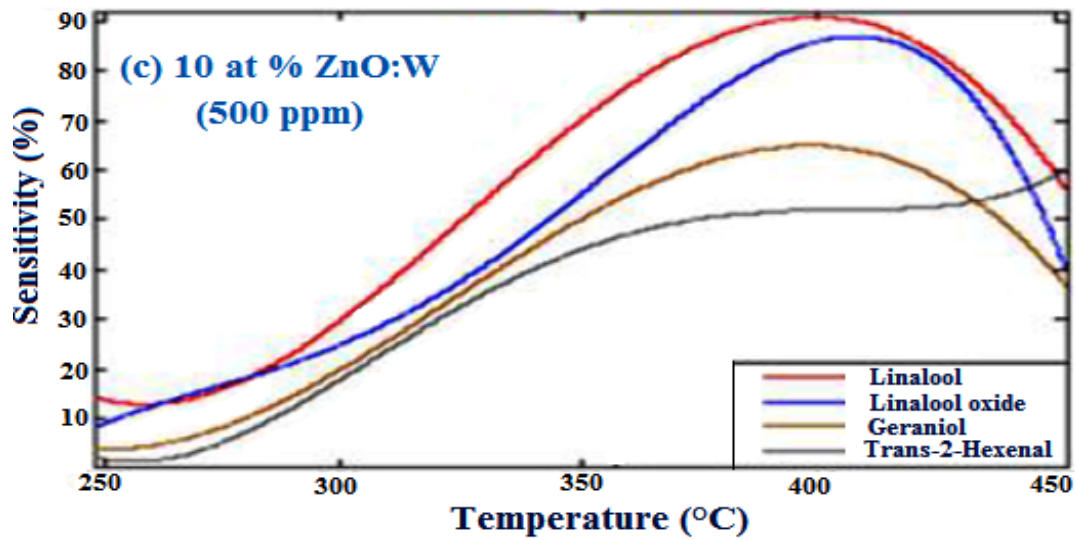


Fig.6.7.(c) Performance of 10 at % ZnO:W (500 ppm) Sensitivity vs. Temperature

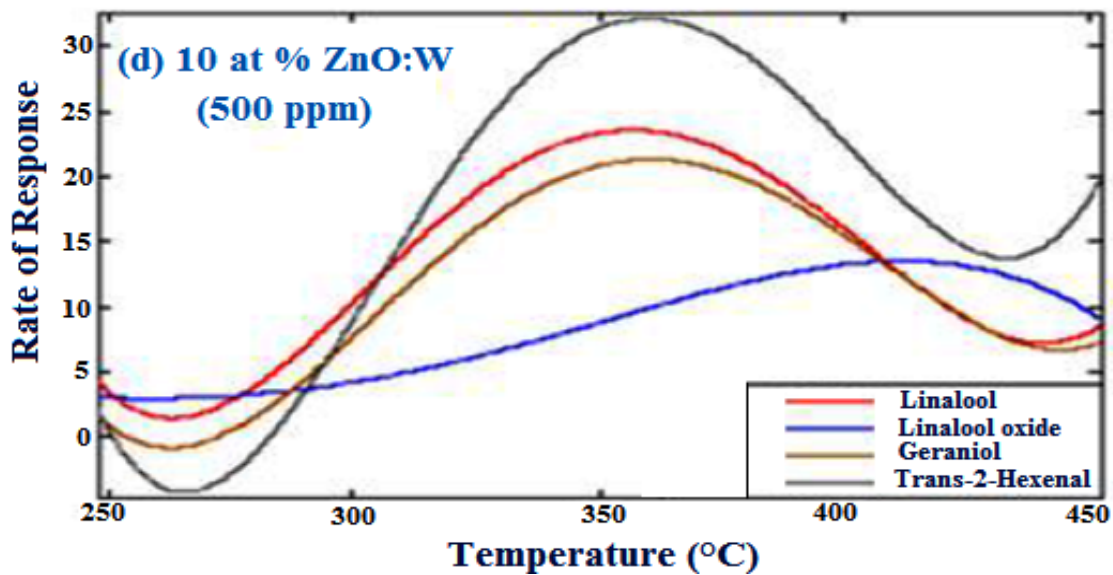


Fig.6.7.(d) Performance of 10 at % ZnO:W (500 ppm) Rate of Response vs. Temperature

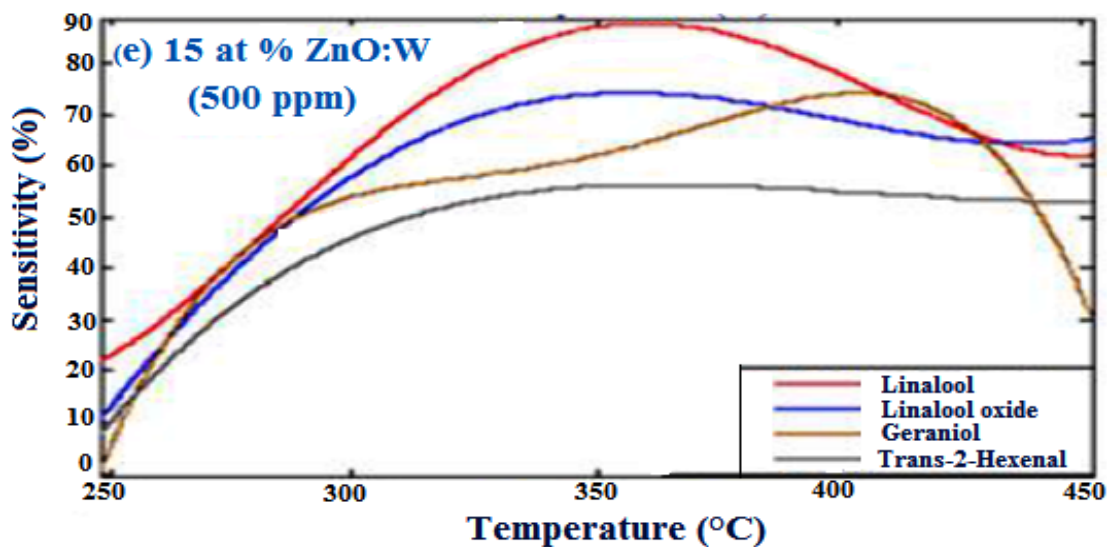


Fig.6.7.(e) Performance of 15 at % ZnO:W (500 ppm) Sensitivity vs. Temperature

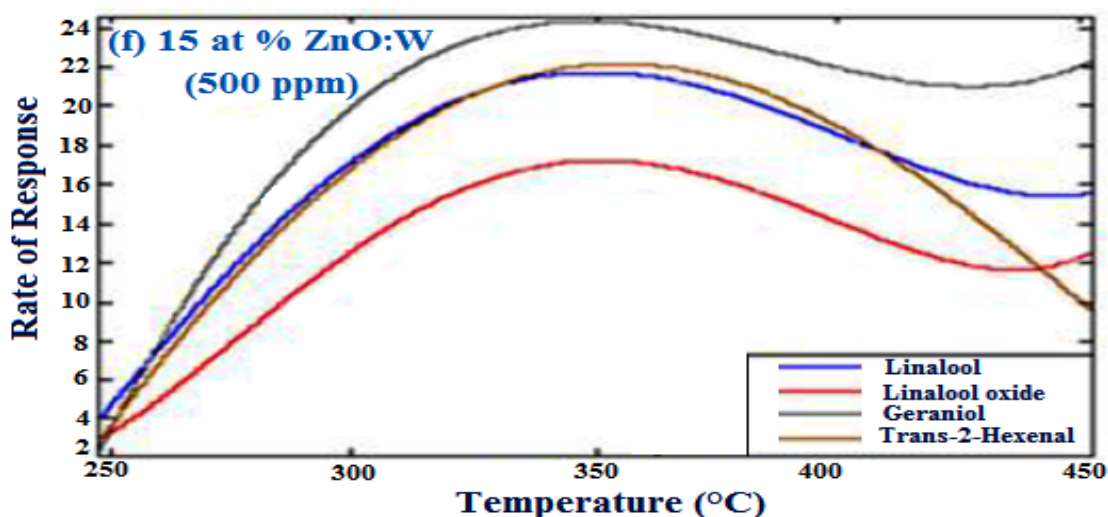


Fig.6.7.(f) Performance of 15 at % ZnO:W (500 ppm) Rate of Response vs. Temperature

In summary, Fig.6.7.(a-f) Performance of (5,10,15) at % W-doped nanostructured ZnO sensors with 500 ppm towards VOCs of black tea aroma (linalool, linalool oxide, geraniol, trans-2-hexenal) vapour, (a, c, e) Sensitivity vs. Temperature and (b, d, f) Rate of Response vs. Temperature. Figures (a, b) are 5 at %, (c, d) are 10 at % and (e, f) 15 at % at 250°C - 450°C.

Hence, Fig. 6.7 (a-f) shows the results of black tea aroma (linalool, linalool oxide, geraniol, trans-2-hexenal) vapour sensing studies, which were carried out at concentrations of 500 ppm. The selectivity study shows that nanostructured pellet sensors are most sensitive to linalool than geraniol. Lastly, linalool oxide is most stable of all of the above compounds and hence the slowest to respond. The maximum gas response of 25.3% was achieved with 87.3% stability for the nanostructured sensors upon exposure to 500 ppm linalool at

optimum temperature of 350°C. The stability study indicates that  $(\text{Zn}_{0.85}\text{W}_{0.15}\text{O})$  is a potential material to be used as an effective black tea aroma sensing.

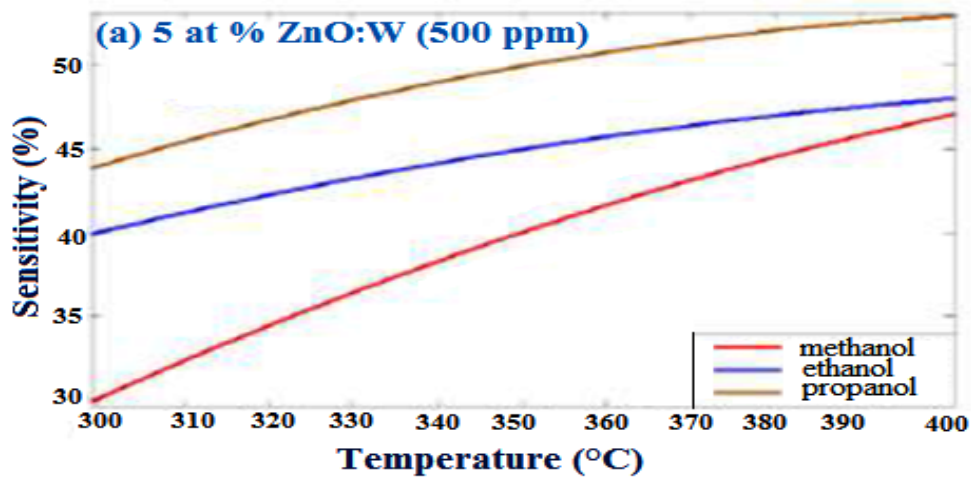


Fig. 6.8. (a) Performance of 5 at % ZnO:W (500 ppm) Sensitivity vs. Temperature

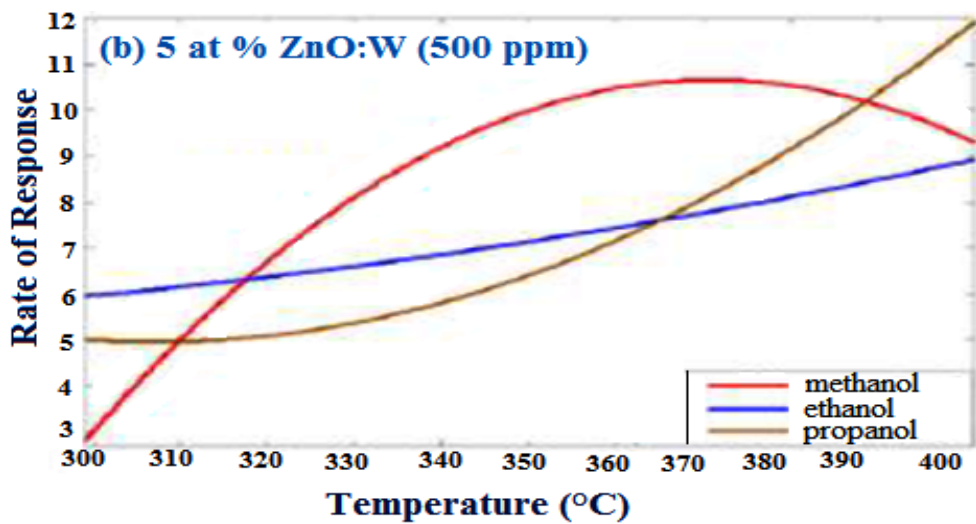


Fig. 6.8. (b) Performance of 5 at % ZnO:W (500 ppm) Rate of Response vs. Temperature

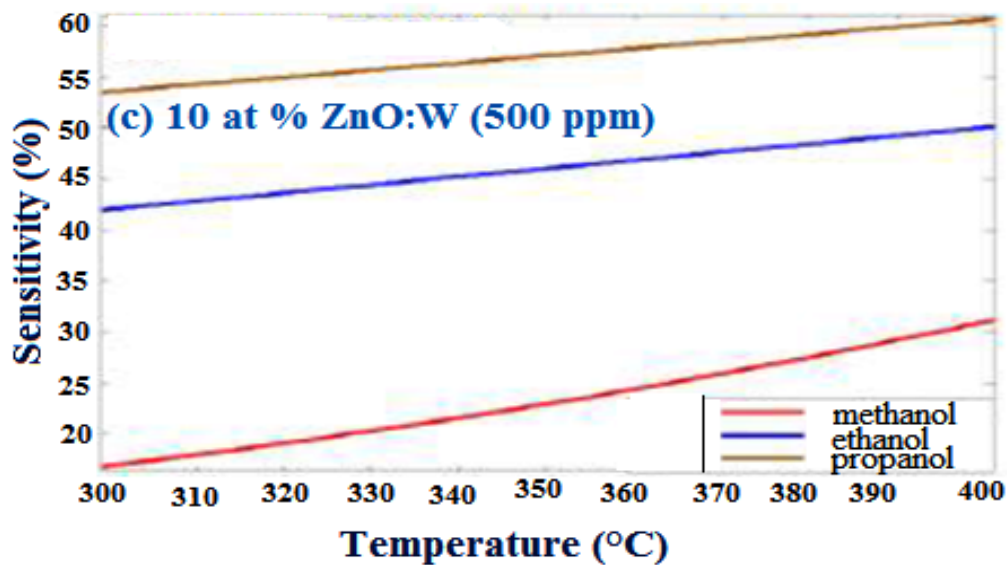


Fig. 6.8. (c) Performance of 10 at % ZnO:W (500 ppm) Sensitivity vs. Temperature



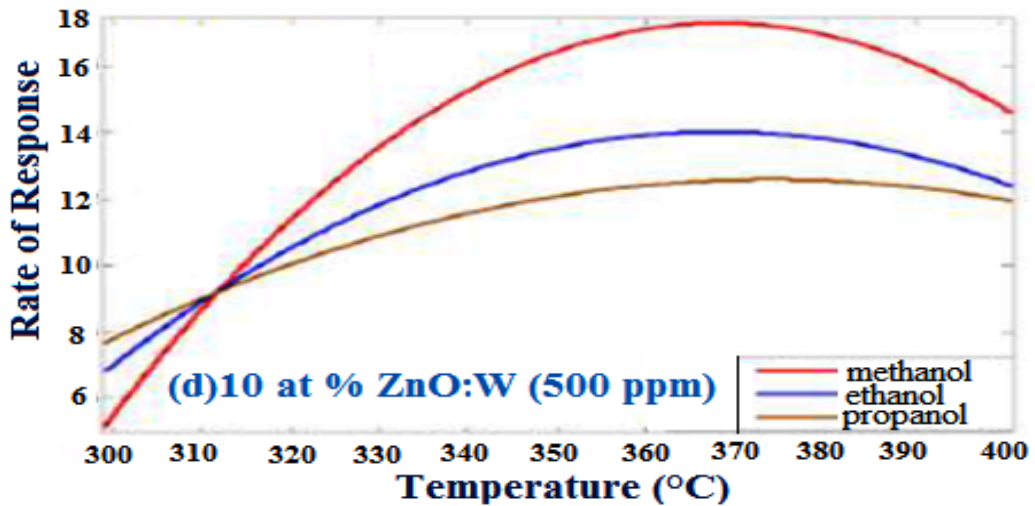


Fig. 6.8. (d) Performance of 10 at % ZnO:W (500 ppm) Rate of Response vs. Temperature

In summary, Fig. 6.8. (a-d) Performance of (5,10) at % W-doped nanostructured ZnO sensors with 500 ppm towards VOCs (methanol, ethanol, propanol) (a, c) Sensitivity vs. temperature and (b, d) Rate of Response vs. temperature. Figures (a, b) are 5 at %, (c, d) are 10 at % at 300°C - 400°C

### 6.3.6. Performance of (1, 2, 3) wt % Cd-doped ZnO in ethanol, methanol and propanol

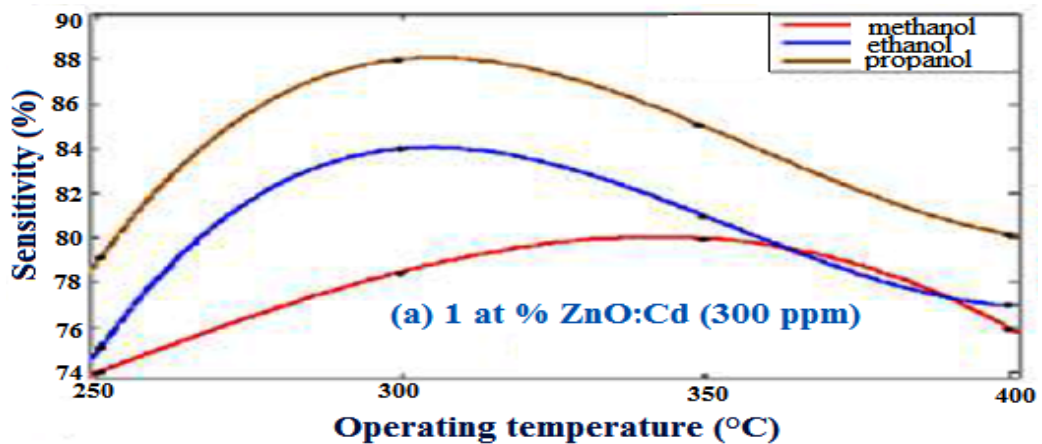


Fig.6.9.(a) Performance of 1 at % ZnO:Cd (300 ppm) Sensitivity vs. Operating temperature

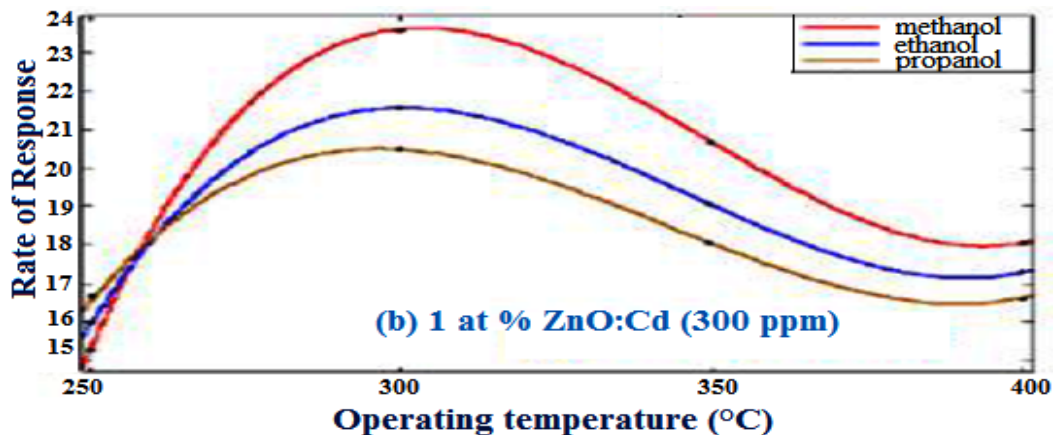


Fig.6.9.(b) Performance of 1 at % ZnO:Cd (300 ppm) Rate of Response vs. Operating temperature

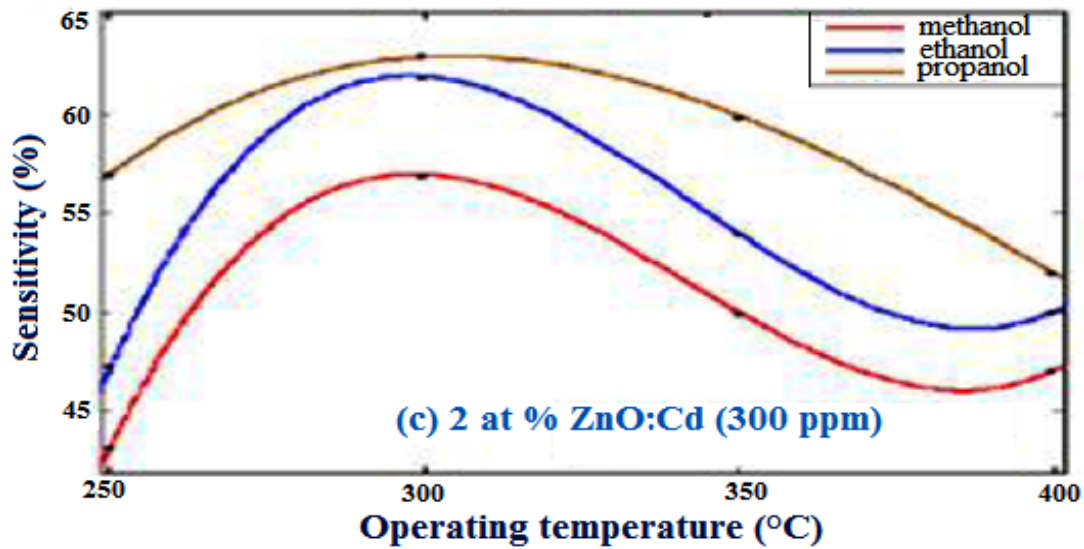


Fig. 6.9.(c) Performance of 2 at % ZnO:Cd (300 ppm) Sensitivity vs. Operating temperature

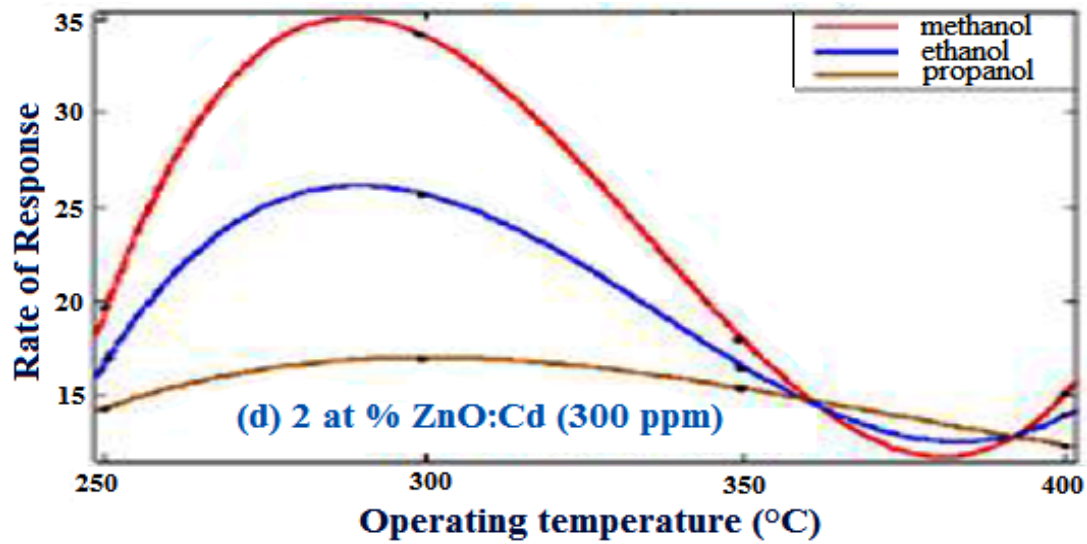


Fig. 6.9.(d) Performance of 2 at % ZnO:Cd (300 ppm) Rate of Response vs. Operating temperature

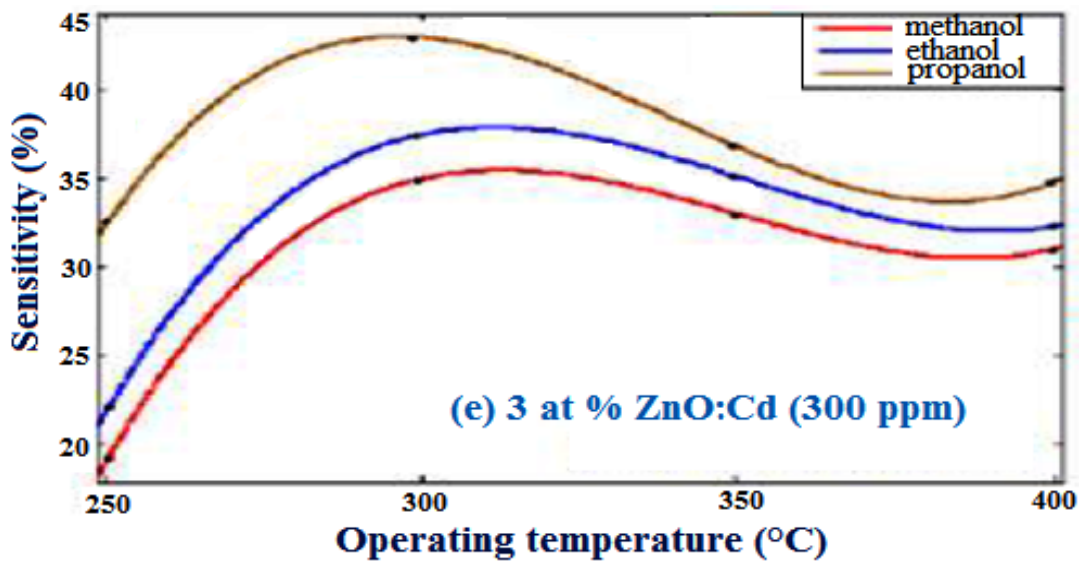
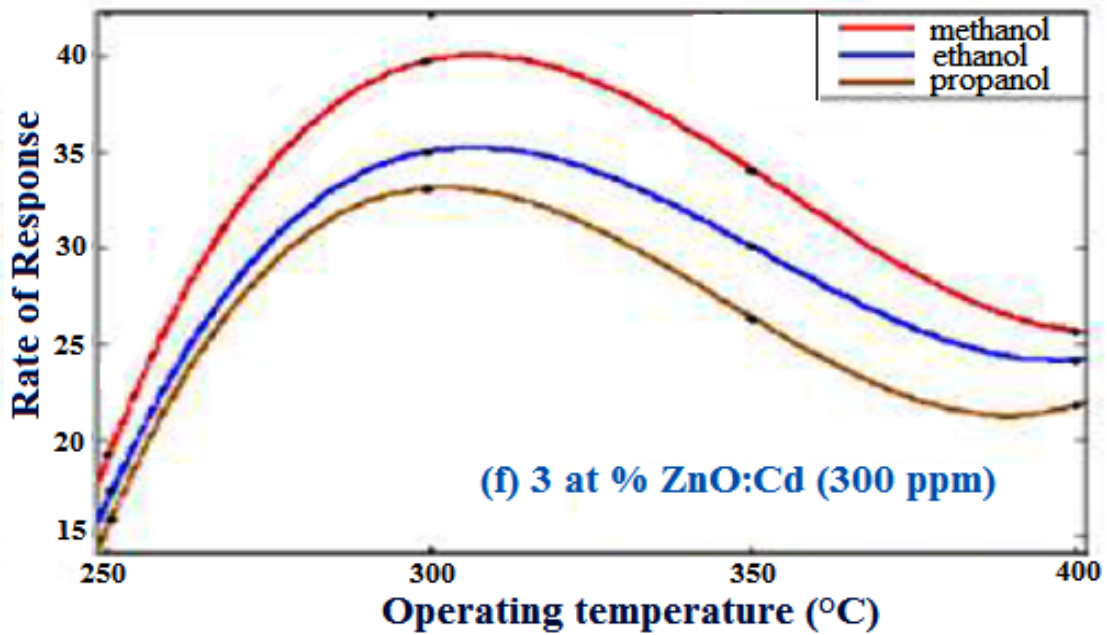
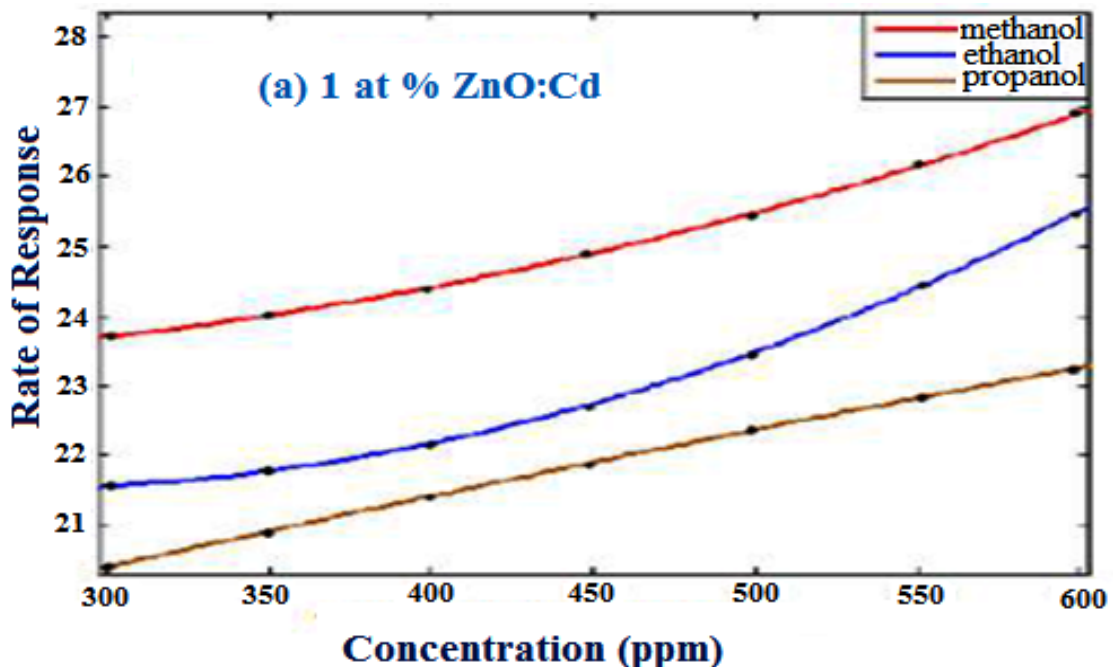


Fig. 6.9.(e) Performance of 3 at % ZnO:Cd (300 ppm) Sensitivity vs. Operating temperature



**Fig. 6.9.(f)** Performance of 3 at % ZnO: Cd (300 ppm) Rate of Response vs. Operating temperature

In summary, **Fig.6.9.(a-f)** Performance of (1, 2, 3) at % Cd-doped nanostructured ZnO sensors with 300 ppm towards VOCs (Methanol, Ethanol, Propanol) (a, c, e) Sensitivity vs. operating temperature and (b, d, f) Rate of Response vs. operating temperature. Figures (a, b) are 1 at %, (c, d) are 2 at % and (e, f) 3 at % at 250°C - 400°C



**Fig.6.10.(a)** Performance of the 1at % Cd-doped nanostructured ZnO chemo-resistive sensors Rate of response vs. concentrations (ppm) of methanol, ethanol, propanol at 350°C.

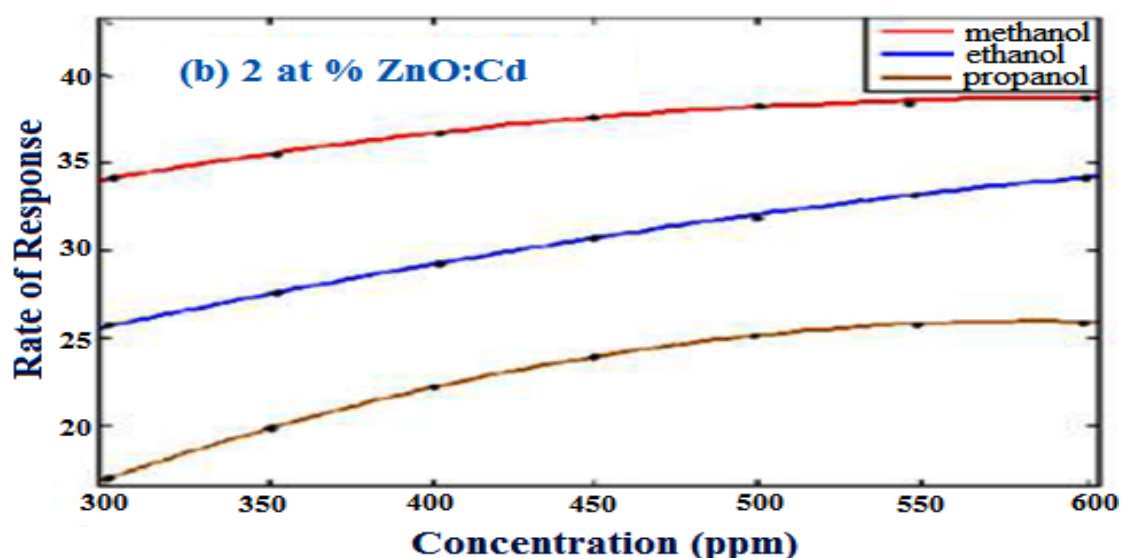


**Fig.6.10. (b)** Performance of the 2 at % Cd-doped nanostructured ZnO chemo-resistive sensors Rate of response vs. concentrations (ppm) of methanol, ethanol, propanol at 350°C

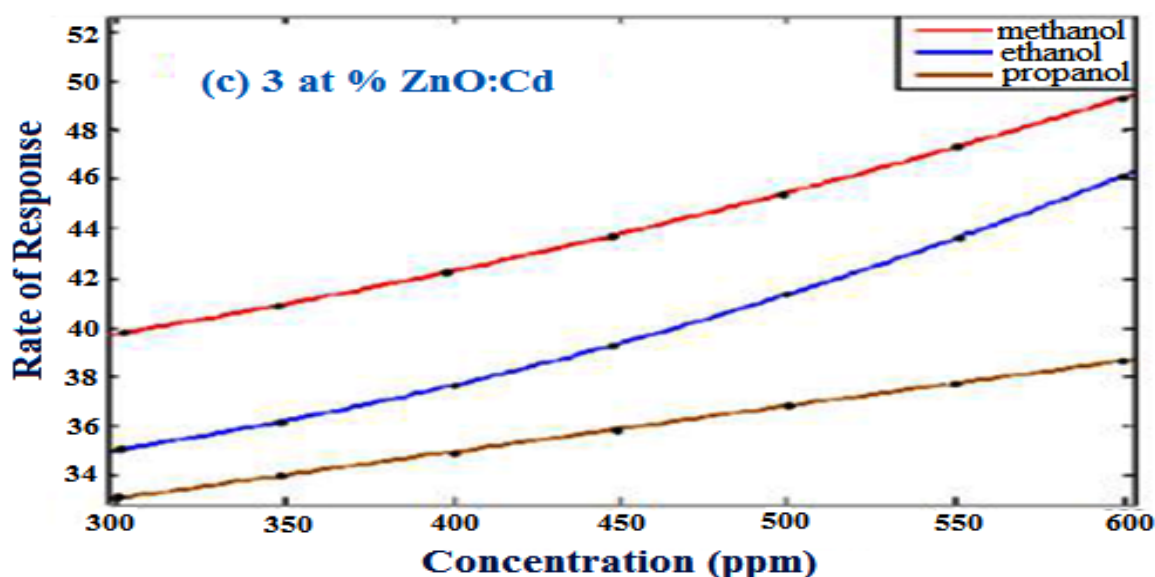


**Fig. 6.10. (c)** Performance of the 3 at % Cd-doped nanostructured ZnO chemo-resistive sensors Rate of response vs. concentrations (ppm) of methanol, ethanol, propanol at 350°C

The performance of  $\text{Zn}_{0.98}\text{Cd}_{0.02}\text{O}$  nanostructured chemo-resistive sensor to different VOC vapour (methanol, ethanol, propanol) shows excellent selectivity, sensitivity and stability in Fig. 6.9 of (1, 2, 3) at % Cd-doped ZnO at 300 ppm. Five repeatability tests were performed on each sensor and its rate of response was found to be in a range of  $\pm 1.5\% \text{ s}^{-1}$  of its mean value at all temperatures.

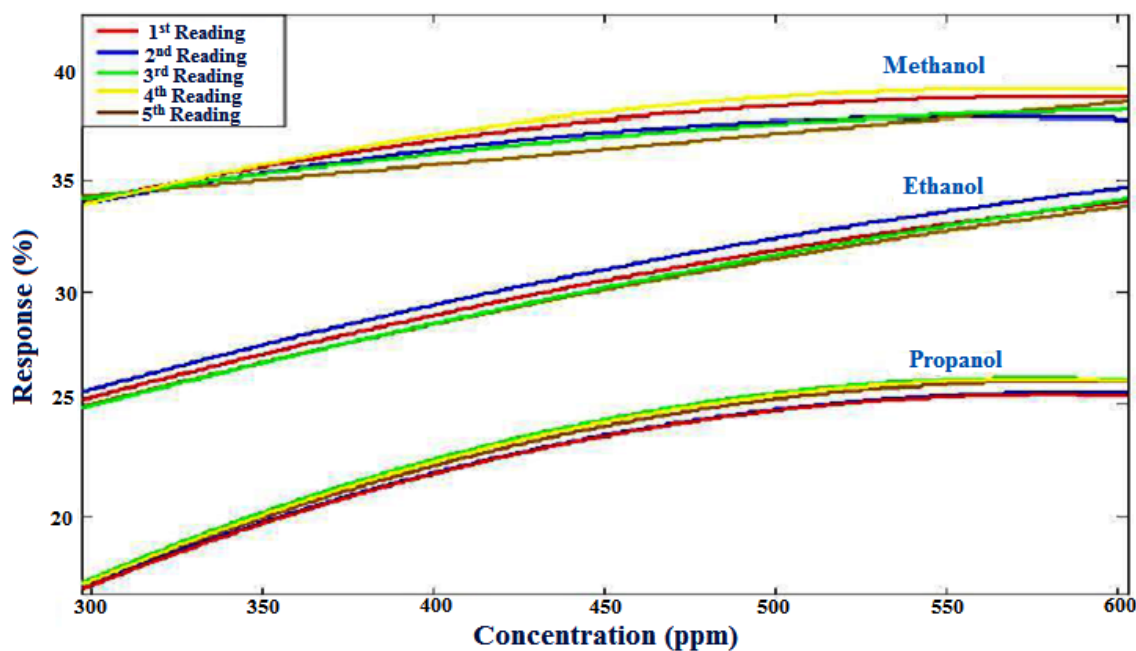


**Fig. 6.11.** Response (%) vs. concentration of  $(\text{Zn}_{0.98}\text{Cd}_{0.02}\text{O})$  nanostructured chemo-resistive sensors to methanol, ethanol, propanol for better performance analysis using sensor array at  $350^\circ\text{C}$

The repeatability of the  $(\text{Zn}_{0.98}\text{Cd}_{0.02}\text{O})$  chemo-resistive sensor array was found to be in a range of  $\pm 1\% \text{ s}^{-1}$  of its mean value at  $350^\circ\text{C}$  [19] and is shown in Fig.6.10 and Fig.6.11. The sensor array showed no temporal or permanent drift when operated and stored in a moisture free environment. Thus we can confirm that there are no structural and/or morphological degradation or any agglomeration over a period of time as shown in the XRD, TEM, FESEM and EDX images in chapter 3.

**Table 6.6.** Performance of  $(\text{Zn}_{0.98}\text{Cd}_{0.02}\text{O})$  nanostructured sensors

Properties	VOCs vapour sequence	Maximum	Minimum
<i>Sensitivity</i>	propanol > ethanol > methanol	propanol	methanol
<i>Response</i>	methanol > ethanol > propanol	methanol	propanol

From Table 6.6, we may ascertain that it is mainly catalytic surface redox reactions and not inter-grain diffusions, which determine our sensor response. Thus the  $(\text{Zn}_{0.98}\text{Cd}_{0.02}\text{O})$  nanostructure chemo-resistive sensor showed maximum response to different VOC (methanol, ethanol, propanol) with fast response, sensitivity and recovery time characteristics [19].

The response versus time curves at different concentrations of the VOCs is shown in Fig. 6.12(a). In the measurements, the period was examined at each fixed concentration at

350°C. When exposed to 200 ppm VOC (linalool, geraniol, linalool oxide, trans-2-hexenal), the response of the sensor is ~ (3-6). With increasing concentration of the VOCs, the response increases significantly. For VOC at level of 300, 400, 500, 650, 800, and 900 ppm, the response is about (6-15), (8-18), (9-24), (11-31), (12-38), and (12-38), respectively. The response time and recovery time are about 12 and 26 sec, respectively. The large surface of the doped ZnO nanostructures makes the absorption of VOC's molecules on the surface of the material easily. The 1D structures of the doped ZnO Nanostructures can facilitate fast mass transfer of the VOC's molecules to and from the interaction region as well as improve the rate for charge carriers to transverse the barriers induced by molecular recognition along the nanostructure. Additionally, comparing with 2D nanostructure, the interfacial areas between the active sensing region of the nanostructures and the underlying substrate is greatly reduced. Those advantages lead to significant gain in the fast response of the prepared sensors. Additionally, the response values are not changed in the sensing cycles in each case, indicating very good repeatability of the sensor.

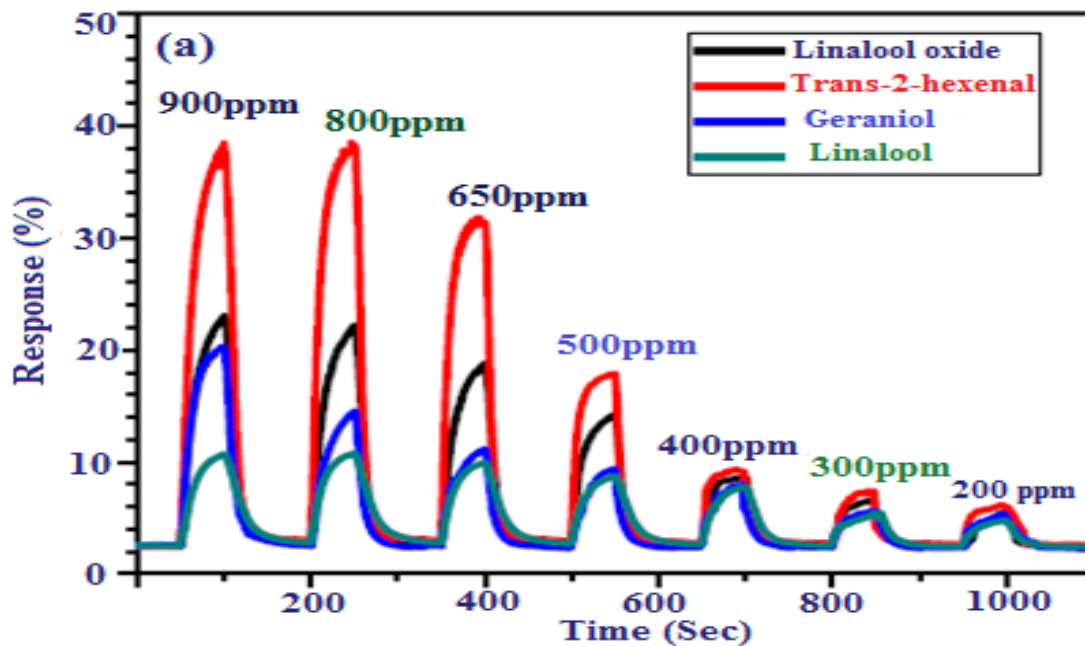


**Fig. 6.12.** (a) Response of  $(Zn_{0.85}W_{0.15}O)$  nanostructured chemo-resistive sensors as a function of time with different concentrations of VOCs at 350°C

Fig.6.12 (b) shows the sensor response versus VOC concentration at 350°C. The response rapidly increases with increasing the VOC concentration up to 650 ppm. Above 650 ppm, the response slowly increases with increasing the VOC concentration, which indicates that

the sensor becomes more or less saturated. Finally the sensor reaches saturation at about 900 ppm. At a high concentration of 900 ppm trans-2-hexenal and linalool, the response can reach about 0.38 and 0.12.

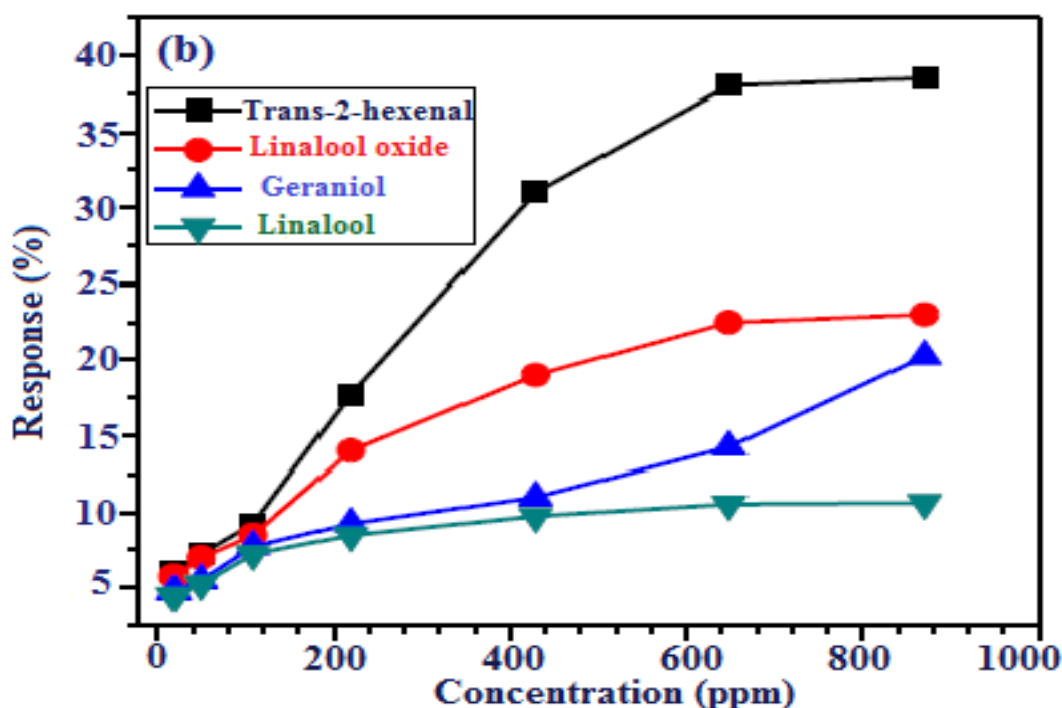


Fig. 6.12. (b) Response of  $(Zn_{0.85}W_{0.15}O)$  nanostructured sensors as a function of the operation temperature at  $350^{\circ}C$  with different ppm of VOCs

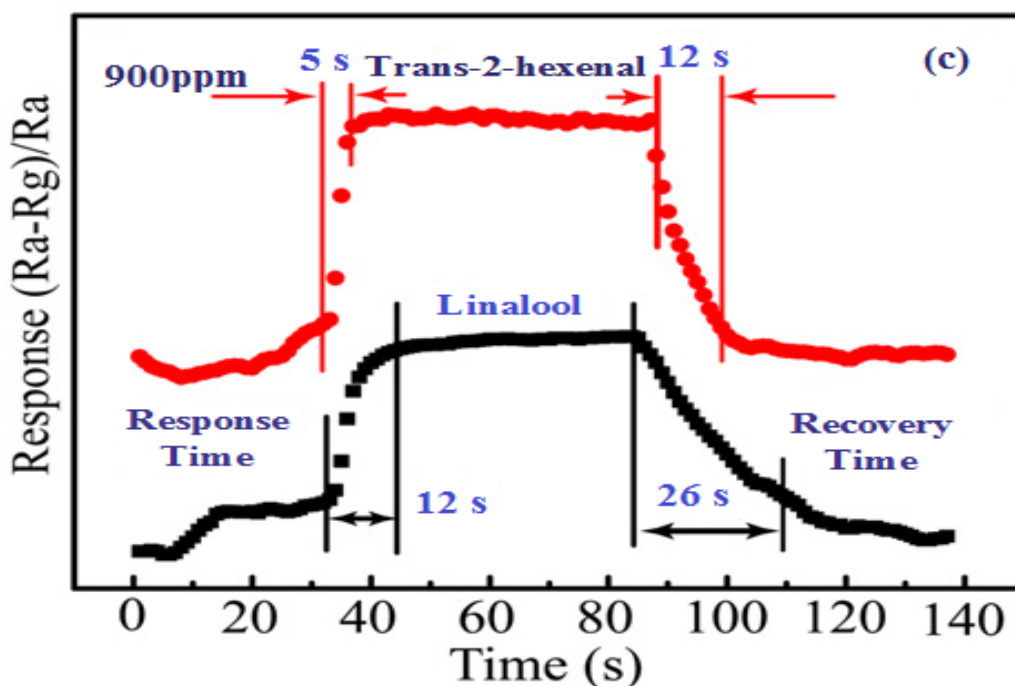
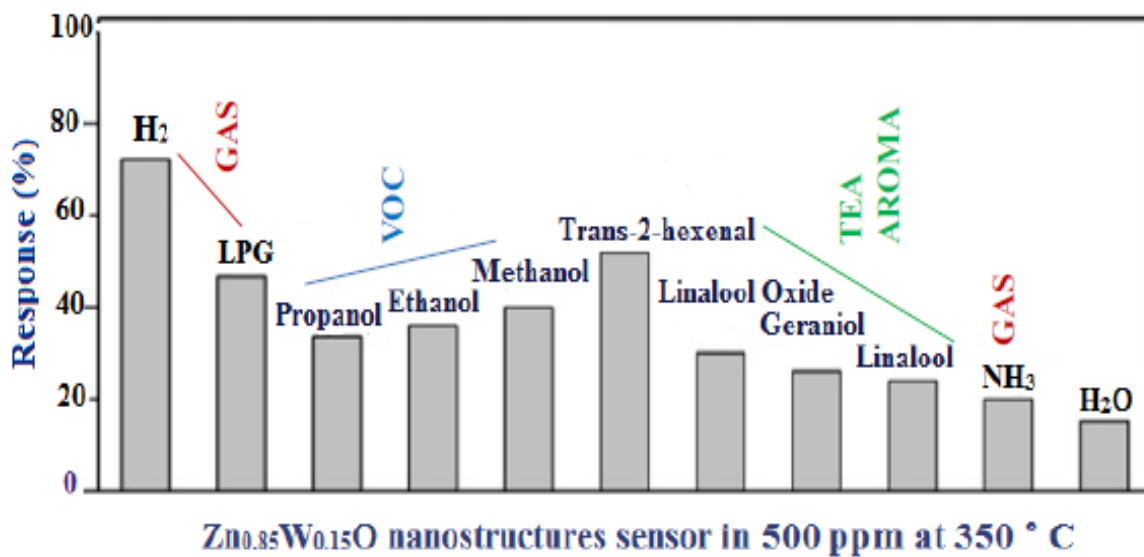


Fig. 6.12. (c) Response vs. recovery time of the gas sensors based on Co-doped nanostructured ZnO chemo-resistive pellet to 900 ppm of trans-2-hexenal and linalool

The response and recovery times to 900 ppm trans-2-hexenal and linalool are 5 sec and 12 sec, and 12 sec and 26 sec, respectively, shown in Fig. 6.12(c). In fact, the response of the semiconducting oxide gas sensitive sensor can usually be empirically represented as  $R = A[C]^N + B$ , where  $A$  and  $B$  are constants and  $[C]$  is the concentration of the target gas.  $N$  usually has a value between 0.5 and 1.0, depending on the charge of the surface species and the stoichiometry of the elementary reactions on the surface [20-21]. For the  $(\text{Zn}_{0.85}\text{W}_{0.15}\text{O})$  nanostructures,  $N$  is around 1 for VOC in the 500 ppm at  $350^\circ\text{C}$ . Such a linear dependence further shows that the doped nanostructure can be used as promising materials for VOC sensors [22].



**Fig. 6.13.** Response of  $(\text{Zn}_{0.85}\text{W}_{0.15}\text{O})$  nanostructured chemo-resistive sensors with 500 ppm different VOC (propanol, ethanol, methanol, trans-2-hexenal, linalool oxide, geraniol, linalool), gases ( $\text{NH}_3$ ,  $\text{H}_2$ , LPG) and  $\text{H}_2\text{O}$  (95% RH) at  $350^\circ\text{C}$

The response of the  $(\text{Zn}_{0.85}\text{W}_{0.15}\text{O})$  sensor to different VOCs (propanol, ethanol, methanol, trans-2-hexenal, linalool oxide, geraniol, linalool), gases ( $\text{NH}_3$ ,  $\text{H}_2$ , LPG) and  $\text{H}_2\text{O}$  (95% RH) at  $350^\circ\text{C}$  are shown in Fig.6.13. The sensor exhibits excellent selectivity to these common interference gases, which may be due to the higher operating temperature than many ZnO sensors reported before [23-25]. For most semiconducting oxide gas sensors, the change in resistance is primarily caused by the adsorption and desorption of the gas molecules on the surface of the sensing structure [26].

In ambient air, metal doped ZnO nanostructures adsorb the oxygen molecule on the surface to generate chemisorbed oxygen species ( $\text{O}_2^-$ ,  $\text{O}^{2-}$ ,  $\text{O}^-$ ), and depletion region is formed on the surface area of metal doped ZnO nanostructures, resulting in a decrease of carrier concentration and electron mobility [27-28]. When the doped ZnO nanostructures are



exposed to a reducing gas (such as LPG) at moderate temperature, the gas reacts with the surface oxygen species, decreasing the depletion width and resulting in an increase of the carrier concentration and electron mobility of the doped ZnO nanostructures, which eventually increases the conductivity of the nanostructure. In our sensor, the excellent sensing properties may be due to the high surface-to-volume ratios associated with 1D nanostructure [29-30]. In the case of the MOS particle devices, only a small fraction of the species adsorbed near the grain boundaries is active in modifying the electrical transport properties, which limited the response value and decelerated the response speed. On the other hand, there are nanostructure-nanostructure junctions on the surface of sensor [31]. Such junctions should form a depleted layer around the intersection and thus block the electron flow in a way which is more efficient than the surface depletion of single nanowires with metal contacts. Thus, the response of our sensor can be attributed to the changes in the resistance of the gas sensor due to both surface depletion region of each nanostructure and the potential barrier height in the junction [32].

## 6.4. Conclusions

In summary, pure and metal doped ZnO nanostructure chemo-resistive sensors ( $Zn_{1-x}M_xO$ ), where ( $M = Co, Ni, Pt, Pd, Mo, W, Cd$ ) are synthesized through a chemical synthesis (combustion) method. The sensor fabricated from these nanostructure chemo-resistive pellet exhibits excellent gas sensing properties at 350°C. The response of all the sensors towards the compounds is studied and it is concluded that ( $Zn_{0.97}Ni_{0.03}O$ ) and ( $Zn_{0.97}Pt_{0.03}O$ ), the two n-type semiconducting nanostructures are best suited to sense VOCs of black tea aroma at an optimum temperature of 350°C. The response and recovery times of Ni-doped ZnO samples were quick and fast compared to other doped ZnO and pure ZnO. The ( $Zn_{0.97}Ni_{0.03}O$ ) showed maximum response to black tea aroma with fast response and recovery time characteristics. The response and recovery times to 900 ppm trans-2-hexenal and linalool are 5 sec and 12 sec, and 12 sec and 26 sec, respectively. The response rapidly increases with increasing the concentration of the VOCs up to 650 ppm. Above 650 ppm, the response slowly increases with increasing the VOC concentration, which indicates that the sensor becomes more or less saturated. Finally, the sensor reaches saturation at about 900 ppm. The sensor also shows good selectivity to common interference gases. Large scale synthesis and excellent sensing properties demonstrate that the pure and metal doped ZnO nanostructures are very promising materials for fabricating gas sensors at the industrial level.

## References

- [1] L. Stolt, J. Hedström, J. Kessler, Advanced Characterization Techniques for Thin Film Solar Cells, *Journal of Applied Physics Letters*, Volume 62, 1993, Pages 597-599.
- [2] M. H. Koch, P. Y. Timbrell, R. N. Lamb, Environmental Applications of Nanomaterials: Synthesis, Sorbents and Sensors, *Semiconductors Science and Technology*, Volume 10, 1995, Pages 1523-1527.
- [3] H. Tang, M. Yan, X. Ma, H. Zhang, M. Wang, D. Yang, Temperature and thickness dependence of the sensitivity of nitrogen, *Sensors and Actuators B*, Volume 113, 2006, Pages 324-328.
- [4] W. Shen, Y. Zhao, C. Zhang, Sol gel porous ZnO thin films for gas sensing applications, *Journal of Thin Solid Films*, Volume 483, 2005, Pages 382-387.
- [5] D. Wang, X. Chu, M. Gong, Single-Crystalline LaFeO<sub>3</sub> Nanotubes with Rough Tube Walls: Synthesis and Gas-Sensing Properties, *Journal of Nanotechnology*, Volume 17, 2006, Pages 5501-5505.
- [6] T. Seiyama, A. Kato, K. Fujiishi, M. Nagatani, A New Detector for Gaseous Components Using Semiconductive Thin Films, *Analytical Chemistry*, Volume 34, Issue 11, 1962, Pages 1502-1523.
- [7] B. Tudu, B. Kow, N. Bhattacharyya, R. Bandyopadhyay, Normalization techniques for gas sensor array as applied to classification for black tea, *IJSSIS*, Volume 2, 2009, Pages 176-189.
- [8] N. Bhattacharyya, R. Bandyopadhyay, M. Bhuyan, B. Tudu, D. Ghosh, A. Jana, E-nose for black tea classification and correlation of measurements with 'Tea Taster' marks, *IEEE Transactions on Instrumentation and Measurement*, Volume 57, Issue 7, 2008, Pages 1313-1321.
- [9] R. Dutta, E. L. Hines, J. W. Gardner, K. R. Kashwan, M. Bhuyan, Tea quality prediction using a tin oxide-based electronic nose: An artificial intelligence approach, *Sensors and Actuators B: Chemical*, Volume 94, Issue 2, 2003, Pages 228-237.
- [10] S. C. Das, R. Bandyopadhyay, S. Ghosh, P. Pramanik, Fabrication of doped zinc oxide nanostructured sensor array in electronic nose for aroma estimation of CTC black tea

- and PCA clustering, *International Journal of Innovative Science and Applied Engineering Research*, Volume 13, Issue 40, 2014, Pages 8-18.
- [11] I. B. Karki, J. J. Nakarmi, P. K. Mandal, S. Chatterjee, Study of Tea Aroma Based on ZnO Nanorod Sensing Element, *The Himalayan Physics*, Volume 3, 2012, Pages 1-5.
- [12] Ü. Özgür, A comprehensive review of ZnO materials and devices, *Journal of Applied Physics*, Volume 98, 2005, Pages 1-103.
- [13] S.C. Das, R. Bandyopadhyay, P. Pramanik, Nanostructured ZnO based Gas Sensors to use in Electronic Nose for Biochemical Compounds in Black Tea, *IJAIST*, Volume 29, Issue 29, 2014, Pages 124-128.
- [14] R. Srivastava, Investigation on Temperature Sensing of Nanostructured Zinc Oxide Synthesized via Oxalate Route, *Sensors and Actuators B*, Volume 2, 2012, Pages 8-12.
- [15] R. Das, S. Biswas, R. Bandyopadhyay, P. Pramanik, Polymerised linseed oil coated quartz crystal microbalance for the detection of volatile organic vapours, *Sensors and Actuators B: Chemical*, Volume 185, 2013, Pages 293-300.
- [16] S. C. Das, B. Tudu, N. Bhattacharya, R. Bandyopadhyay, P. Pramanik, Doped ZnO Nanostructured Sensor in Electronic Nose for Detection of Ammonia, Hydrogen and Liquefied Petroleum Gas, *Advanced Nanomaterials and Nanotechnology*, Springer-Verlag Berlin Heidelberg, Chapter 47, 2013, Pages 473-482, DOI: 10.1007/978-3-642-34216-5(47)(online).
- [17] S. C. Das, K. Sadani, R. Bandyopadhyay, P. Pramanik, Sensing characteristics of Molybdenum doped Zinc Oxide nanoparticles chemoresistor pellets towards black tea-biochemicals, *International Journal of Advances in Engineering Science and Technology*, Volume 3, Issue 3, 2014, Pages 120-131.
- [18] S. C. Das, R. Bandyopadhyay, P. Pramanik, Development of W doped ZnO nanostructure chemoresistor pellet sensors for black tea aroma monitoring, *International Journal of Innovative Science, Engineering and Technology*, Volume 2, Issue 3, 2015, Pages 107-113.
- [19] S. C. Das, R. Bandyopadhyay, P. Pramanik, Volatile Organic Compounds sensing characteristics of doped Zinc Oxide nanostructured sensors for E-nose applications,

- Nanospectrum: A Current Scenario, Allied Publishers, 2015, Pages 121-131, ISBN: 978-93-85926-06-8.
- [20] G. Nam, M. S. Kim, D. Y. Kim, K. G. Yim, S. Kim, S. O. Kim, D. Y. Lee, J. Y. Leem, Oxygen plasma power dependence on ZnO grown on porous silicon substrates by plasma-assisted molecular beam epitaxy, *Materials Research Bulletin*, Volume 47, 2012, Pages 2879-2883.
- [21] S. Li, X. Zhang, X. Jiao, H. Lin, One-step large-scale synthesis of porous ZnO nanofibers and their application in dye-sensitized solar cells, *Journal of Material Letters*, Volume 65, 2011, Pages 2975-2978.
- [22] K. A. Salman, K. Omar, Z. Hassan, Nanocrystalline ZnO film grown on porous silicon layer by radio frequency sputtering system, *Journal of Material Letters*, Volume 68, 2012, Pages 51-53.
- [23] E. Kayahan, White light luminescence from annealed thin ZnO deposited porous silicon, *Journal of Luminescence*, Volume 130, 2010, Pages 1295-1299.
- [24] H. I. Abdulgafour, F. K. Yam, Z. Hassan, K. A. Heuseen, M. J. Jawad, ZnO nanocoral reef grown on porous silicon substrates without catalyst, *Journal of Alloys and Compounds*, Volume 509, 2011, Pages 5627-5630.
- [25] M. Rajabi, R. S. Dariani, A. I. Zad, Comparative study of ZnO nanostructures grown on silicon (100) and oxidized porous silicon substrates with and without Au catalyst by chemical vapor transport and condensation, *Journal of Alloys and Compounds*, Volume 509, 2011, Pages 4295-4299.
- [26] X. Li, Y. Chang, Y. Long, Influence of Sn doping on ZnO sensing properties for ethanol and acetone, *Materials Science and Engineering: C*, Volume 32, 2012, Pages 817-821.
- [27] M. S. Kim, S. Kim, G. Nam, D. Y. Lee, J. Y. Leem, Effects of growth temperature for buffer layers on properties of ZnO thin films grown on porous silicon by plasma-assisted molecular beam epitaxy, *Optical Materials*, Volume 34, 2012, Pages 1543-1548.

- [28] S. Ren, G. Fan, S. Qu, Q. Wang, Enhanced H<sub>2</sub> sensitivity at room temperature of ZnO nanowires functionalized by Pd nanoparticles, *Journal of Applied Physics*, Volume 110, Issue 8, 2011, Pages 084312-6.
- [29] Y. Kumar, J. E. Garcia, F. Singh, S. F. Olive-Méndez, V. V. Sivakumar, D. Kanjilal, V. Agarwal, Influence of mesoporous substrate morphology on the structural, optical and electrical properties of RF sputtered ZnO layer deposited over porous silicon nanostructure, *Applied Surface Science*, Volume 258, 2012, Pages 2283-2288.
- [30] T. T. Trinh, N. H. Tu, H. H. Le, K. Y. Ryu, K. B. Le, K. Pillai, J. Yi, Improving the ethanol sensing of ZnO nano-particle thin films-The correlation between the grain size and the sensing mechanism, *Sensors and Actuators B*, Volume 152, 2011, pages 73-81.
- [28] H. Yang, S. Nie, Preparation and characterization of Co-doped ZnO nanomaterials, *Materials Chemistry and Physics*, Volume 114, 2009, Pages 279-282.
- [29] T. Ghosh, M. Dutta, D. Basak, Effect of substrate-induced strain on the morphological, electrical, optical and photoconductive properties of RF magnetron sputtered ZnO thin films, *Materials Research Bulletin*, Volume 46, 2011, Pages 1039-1044.
- [30] P. Prepelita, R. Medianu, B. Sbarcea, F. Garoi, M. Filipescu, The influence of using different substrates on the structural and optical characteristics of ZnO thin films, *Applied Surface Science*, Volume 256, 2010, Pages 1807-1811.
- [31] S. Y. Seo, C. H. Kwak, S. H. Kim, S. H. Park, I. J. Lee, S. W. Han, Synthesis and characterization of ferromagnetic (Zn<sub>1-x</sub>Co<sub>x</sub>O) films, *Journal of Crystal Growth*, Volume 346, 2012, Pages 56-60.
- [32] J. Spadavecchia, G. Ciccarella, R. Rella, S. Capone, P. Siciliano, Metallophthalocyanines thin films in array configuration for electronic optical nose applications, *Sensors Actuators B: Chemical*, Volume 96, 2003, Pages 489-497.



# Chapter 7

## Conclusion and Future scope

---

This chapter presents the main conclusions or findings of the entire research work in brief. Nanotechnology is a very broad area of research and development which has several applications in the fields of optoelectronic devices, biosensors and devices, medical instruments, nano-optics and many others. Considerable progress has been made in this frontier area of research, but a lot of issues are still unresolved for the nano-science researchers in the context of synthesis, characterization and applications of different nanostructures. The future scope of the present research work is also discussed in this chapter.

---

### *List of sections*

- 7.1. Summary of work
- 7.2. Concluding remarks
- 7.3. Future scope





# Chapter 7

## Conclusion and Future scope

Nanotechnology is a very broad area of research and development which has several applications in the fields of optoelectronic devices, biosensors and devices, medical instruments, nano-optics and many others. Considerable progress has been made in this frontier area of research, but a lot of issues are still unresolved for the nano-science researchers in the context of synthesis, characterization and applications of different nanostructures. In this thesis work, development of new sensors which are specifically selective for tea volatiles and other gases like hydrogen, ammonia, liquefied petroleum gas was taken up. The base material was chosen as nanostructured zinc oxide and in order to change the selectivity towards various volatiles, different additives were added. Extensive experimentation was carried out and as a result a few gas sensors with reasonably good performance have been obtained. This chapter presents the summary of the work and main conclusions or findings of the entire research work in brief. The future scope of the present research work is also discussed in this chapter.

### 7.1. Summary of the work

As already mentioned, in this thesis work, synthesis, characterization and analysis of responses (sensitivity, selectivity, speed of response etc.) of pure zinc oxide and metal doped ( $Zn_{1-x}M_xO$ ) nanostructures [where,  $M = Ni, Co, Pd, Pt, Mo, W, Cd$ , and  $x = 0.1, 0.2, 0.3$ , etc.] have been carried out. The present research work establishes a versatile and technically simple chemical synthesis methodology through successful preparation of variety of noble and transition metal doped ZnO nanostructure powders. The synthesis method involves pyrolysis of aqueous-based precursor solutions that comprises of water-soluble, metal ion-ligand complexes of the desired metal ions and diethanolamine (DEA), in the requisite molar ratios. We have prepared pure and metal doped ZnO nanomaterials by chemical synthesis route particularly in combustion method. A homogeneous aqueous solution of water soluble zinc acetate dihydrate and other chemicals are used to prepare the doped oxides. DEA and sucrose are used as fuel for combustion in addition to 70% concentrated nitric acid as oxidizer and calcined  $600^\circ C$  for 5h. PVA is used as a binder to prepare the pellets. The prepared powders have been used for gas sensing of volatile organic compounds (VOC) like ethanol, methanol, propanol and volatile bio-chemicals

present in black tea like linalool, linalool oxide, geraniol, trans-2-hexenal and reducing gases such as hydrogen, ammonia, liquefied petroleum gas. The work carried out in the present investigation can be summarized in a tabular form as follows:

**Table 7.1. Prepared ZnO nanostructures and their properties**

Prepared ZnO nanostructures	Properties studied
<ul style="list-style-type: none"> <li>▪ Pure ZnO nanostructures calcined at 400°C and 600°C in 3 and 5 hours, respectively.</li> <li>▪ Transition metals doped to obtain <math>(\text{Zn}_{0.97}\text{Ni}_{0.03}\text{O})</math> and <math>(\text{Zn}_{0.97}\text{Co}_{0.03}\text{O})</math> nanostructures powders.</li> <li>▪ Noble metals doped to obtain <math>(\text{Zn}_{0.97}\text{Pt}_{0.03}\text{O})</math>, <math>(\text{Zn}_{0.97}\text{Pd}_{0.03}\text{O})</math>, <math>(\text{Zn}_{1-x}\text{Mo}_x\text{O})</math>, <math>x=0.01,0.02,0.03</math>, <math>(\text{Zn}_{1-x}\text{W}_x\text{O})</math>, <math>x=0.5,0.10,0.15</math>, <math>(\text{Zn}_{1-x}\text{Cd}_x\text{O})</math>, <math>x=0.01,0.02,0.03</math> nanostructures powders</li> <li>▪ Preparation of chemo-resistive pellets of all samples with the help of pellet making instrument to study their sensing characteristics</li> </ul>	<ul style="list-style-type: none"> <li>▪ X-ray diffractometer (XRD), particle size analyzer (PSA), field emission scanning electron microscopy (FESEM), energy dispersive X-ray spectroscopy (EDAX), high resolution transmission electron microscopy (HRTEM), fourier transform infrared (FTIR) spectroscopy and atomic force microscopy (AFM) for crystal structure, average particle size, shape, elemental compositions and morphology.</li> <li>▪ UV-Vis spectrometry, photoluminescence (PL) emission, cathodoluminescence (CL), for optical properties. The characterization details of their electrical (current-voltage I-V and switching measurement) using semiconductor characterization system (SCS), superconducting quantum interferences device (SQUID), vibrating sample magnetometer (VSM) for magnetic (M-H curve, coercivity, saturation magnetization and remanence magnetization measurement at room temperature), magnetic force microscopy (MFM) for inside domain structures and configuration.</li> <li>▪ Gas sensing property through electrical conductivity measurement in dry air.</li> <li>▪ Gas sensing property towards 500 and 900 ppm of black tea bio-chemicals (Linalool, Linalool oxide, Geraniol, Trans-2-hexenal) at 200°C - 400°C.</li> <li>▪ Gas sensing property towards 500 ppm of reducing gases such as, hydrogen, ammonia, liquefied petroleum gas at 200°C - 400°C.</li> <li>▪ Gas sensing property towards of 300 and 500 ppm of VOC gases (methanol, ethanol, propanol) at 200°C - 400°C.</li> </ul>

## 7.2. Concluding remarks

- The synthesis method developed in this present study is versatile and can be extended to the preparation of nanostructure powders of a variety of metal doped ZnO nanostructures. Particularly, doping with metals like nickel, cobalt, tungsten are difficult to process otherwise and may be attempted with this method.
- The developed method results in polycrystalline and single phase final powders of the desired doped ZnO nanostructures at processing temperatures (i.e.,  $\leq 850^\circ\text{C}$ ) that are comparatively lower than those reported in literature so far, with grain sizes in the nano-scale range (i.e.,  $< 60\text{ nm}$ ) and the specific surface from  $40\text{-}120\text{ m}^2/\text{g}$ .
- The present investigation establishes the gas-sensing behaviour of pure and metal doped ( $\text{Zn}_{1-x}\text{M}_x\text{O}$ ) nanostructures, where ( $\text{M} = \text{Ni, Co, Pd, Pt, Mo, W, Cd}$ ) and ( $x = 0.1, 0.2, 0.3, \text{etc.}$ ) systems for the first time in literature. The synthesized nanostructure powders exhibit n-type semiconducting behaviour and excellent gas sensing characteristics towards black tea biochemical compounds like linalool, linalool oxide, geraniol and, trans-2-hexenal as well as volatile organic compounds like methanol, ethanol, propanol, and gases like ammonia, hydrogen, liquefied petroleum gas.
- The prepared pure and doped ZnO nanostructure sensors show response towards hydrogen, ammonia, and liquefied petroleum gas at operating temperatures ranging between  $200^\circ\text{C} - 400^\circ\text{C}$ . Incorporation of noble metal palladium and platinum to make ZnO nanostructures i.e. ( $\text{Zn}_{0.97}\text{Pd}_{0.03}\text{O}$ ) and ( $\text{Zn}_{0.97}\text{Pt}_{0.03}\text{O}$ ) improves the system's gas sensing properties through reduction in the sensor operating temperature, sensor response time and recovery time. The details of the sensors and their observed gas sensing behaviours towards reducing gases such as, hydrogen, ammonia and liquefied petroleum gas are summarized as follows:

**Table 7.2.** Noble metal 3 wt % (Pd, Pt)-doped ZnO nanostructures chemo-resistive pellet for sensor applications

Sensors	Calcined temperature ( $^\circ\text{C}$ ) and time (hrs)	Structure	Particle size (HRTEM)	% of Response and working temperature at 500 ppm		
				H <sub>2</sub>	NH <sub>3</sub>	LPG
( $\text{Zn}_{0.97}\text{Pd}_{0.03}\text{O}$ )	600 $^\circ\text{C}$ (5 hrs)	Hexagonal wurtzite	35-60 nm	84 (300 $^\circ\text{C}$ )	52 (350 $^\circ\text{C}$ )	81 (300 $^\circ\text{C}$ )
( $\text{Zn}_{0.97}\text{Pt}_{0.03}\text{O}$ )	600 $^\circ\text{C}$ (5 hrs)	Hexagonal wurtzite	35-60 nm	80 (300 $^\circ\text{C}$ )	54 (350 $^\circ\text{C}$ )	78 (300 $^\circ\text{C}$ )

- Optical characteristics are found to be an excellent tool in determining the quality of the prepared doped ZnO nanostructures powders. By analysing UV, PL and CL of these nanostructures as a function of wavelength in the range of 200-900 nm we have estimated visible band, emission band and band gap energy of these nanostructures as a function of  $(\text{Zn}_{1-x}\text{M}_x\text{O})$  volume constants.
- Non-toxic, chemically inert, thermally stable nanostructure powders of transition metal doped i.e.  $(\text{Zn}_{0.97}\text{Ni}_{0.03}\text{O})$  and  $(\text{Zn}_{0.97}\text{Co}_{0.03}\text{O})$  have been prepared, characterized and tested for their sensing properties.  $\text{Ni}^{2+}$  and  $\text{Co}^{2+}$  doped ZnO nanostructures powders show interesting colour shades in different colour ranges due to d-d transition of the d-electrons of  $\text{Ni}^{2+}$  and  $\text{Co}^{2+}$  ions. The details of the doped nanostructures and their structural, morphological and optical properties are summarized as follows:

**Table 7.3.** Transition metal 3 at. % (Ni, Co)-doped ZnO nanostructure powders for absorption band colour

Nanostructures	Calcined temperature (°C) and time (hrs)	Phase	Particle size (HRTEM)	Absorption band for the d-d transitions(nm)		
				Violet colour	Blue colour	Green colour
$(\text{Zn}_{0.97}\text{Ni}_{0.03}\text{O})$	600°C ( 5 hrs)	wurtzite	25-60 nm	424.8	456.4	556.4
$(\text{Zn}_{0.97}\text{Co}_{0.03}\text{O})$	600°C ( 5 hrs)	wurtzite	25-60 nm	425.7	453.0	566.0

- There are many reports available on  $I-V$  characteristics of ZnO and metal doped ZnO using metal/ZnO/metal like MSM type heterostructures. Particularly in pursuit of photodiode and photodetector applications, the  $I-V$  behaviour of n-ZnO/p-Si heterojunction and n-ZnO/p-ZnO homojunction were studied under ultra-violet and visible light illumination, showing an enhanced photo-response. In case of metal doped ZnO like  $(\text{Zn}_{0.97}\text{Ni}_{0.03}\text{O})$  was reported to show an enhancement in electrical conductivity upon doping, while the  $I-V$  characteristics of ZnO:W showed an ohmic behavior. Thus the study of photo-response of our doped ZnO nanostructures proves that these devices can independently be used as photo-sensors. The ON/OFF ratios for pure and 3 at.% (Co, Ni, W)-doped ZnO nanostructures are 8.64, 1.62, 8.04 and 4.22, respectively. A high ON/OFF ratio of 8.04 was observed for ZnO:Ni nanostructures among the doped samples and the results are summarized as follows.

**Table 7.4.** ON/OFF ratios and response times for ZnO, (Zn<sub>0.97</sub>Co<sub>0.03</sub>O), (Zn<sub>0.97</sub>Ni<sub>0.03</sub>O) and (Zn<sub>0.97</sub>W<sub>0.03</sub>O) nanostructure device

Sample	I <sub>light</sub> (μA)	I <sub>dark</sub> (μA)	ON/OFF	Response
ZnO(pure)	4.32	0.52	8.64	0.22
(Zn <sub>0.97</sub> Co <sub>0.03</sub> O)	1.51	0.91	1.62	0.51
(Zn <sub>0.97</sub> Ni <sub>0.03</sub> O)	3.22	0.42	8.04	0.22
(Zn <sub>0.97</sub> W <sub>0.03</sub> O)	0.34	0.07	4.22	0.51

Remarkably, the ZnO nanostructures are reportedly possessing high ON/OFF ratio of 1500–10<sup>4</sup>, due to very small dimensions.

- At room temperature single-phase wurtzite structure (Zn<sub>0.97</sub>Ni<sub>0.03</sub>O), (Zn<sub>0.97</sub>Co<sub>0.03</sub>O) and (Zn<sub>0.97</sub>W<sub>0.03</sub>O) nanostructures show the paramagnetic behavior with no indication of ferromagnetism behavior. As no other secondary phase is detected in the XRD pattern, the paramagnetic is the result of incorporation of Ni<sup>2+</sup>, Co<sup>2+</sup>, W<sup>2+</sup> ions into the ZnO lattice. (Zn<sub>0.97</sub>Ni<sub>0.03</sub>O) exhibited the largest saturation moments ( $M_S \approx 2.02 \times 10^{-4}$  emu/g) and the magnetism order of the samples was (Zn<sub>0.97</sub>Ni<sub>0.03</sub>O) > (Zn<sub>0.97</sub>Co<sub>0.03</sub>O) > (Zn<sub>0.97</sub>W<sub>0.03</sub>O). Coercive field ( $H_C$ ), Saturation magnetization ( $M_S$ ) and Remanence magnetization ( $M_R$ ) for (Zn<sub>1-x</sub>M<sub>x</sub>O) where (M=Ni, Co, W; x =3at.%) are summarized as below.

**Table 7.5.** Coercive field ( $H_C$ ), Saturation magnetization ( $M_S$ ), and Remanence-magnetization ( $M_R$ ) of doped ZnO nanostructures

Sample	Coercive field $H_C(\text{Oe}) \pm 5.00$	Saturation magnetization $(M_S) (\text{emu/g}) \pm 0.06$	Remanence magnetization $(M_R)(\text{emu/g}) \pm 0.01$
(Zn <sub>0.97</sub> Ni <sub>0.03</sub> O)	2350	$2.02 \times 10^{-4}$	$8.78 \times 10^{-4}$
(Zn <sub>0.97</sub> Co <sub>0.03</sub> O)	1150	$0.60 \times 10^{-4}$	$2.55 \times 10^{-4}$
(Zn <sub>0.97</sub> W <sub>0.03</sub> O)	1400	$0.15 \times 10^{-4}$	$1.45 \times 10^{-4}$

- Molybdenum doping has indeed enhanced the sensitivity (saturation time ~30 sec.) of pure ZnO significantly, but the saturating time was found to be high. Moreover the materials did not possess the degree of stability which is required for commercial viability. In pursuit of a material on which absorptions and deabsorption could proceed real fast, we found tungsten doped materials exhibited quick enough responses when doping concentrations were 5 wt % or more. The sensors possessed fairly good stability to repeat temperature recycling even when subject to sensing VOC and gases. Sensitivities of the sensors was similar to the molybdenum doped sensors but since sensor saturating times came down within 4-7 sec. with excellent repeatable response dynamics, these sensors did have the applicability in real time sensing. Finally by

sensor resistance saturated in less than 4 seconds in all cases at all temperatures and hence the mission of developing materials for real fast sensor was accomplished.

- The doped sensors could be used to make up an electronic-nose for black tea monitoring where by co-relating the sensitivity and speed of response the concentrations of the biochemicals vapour in a particular black tea sample could be estimated. However, this would require prior training and extensive use of artificial intelligence.
- The cadmium doped sensors may be fabricated in a taguchi form to make an off-line VOC and gas sensor for breath inspection. Also these sensors could be directly sputtered on to the inner walls of pipelines. Molecular sieves could then be coated on them to make them rugged. This could find extensive applications in brewing industry.
- Among the Mo, W and Cd doped ZnO sensors, the W and Cd doping exhibit much faster responses than Mo and ( $Zn_{0.98}Cd_{0.02}O$ ) is the best one of three materials developed, which make a new indicator further research.

### 7.3. Future scopes

- Further studies on the sensitivity of all the synthesized pure and metal doped ZnO nanostructures can be carried out using their chemo-resistive pellet sensors.
- The effect of doping of the different noble metal and transition metals in the prepared ZnO nanostructures chemo-resistive pellet sensors can be studied for improving the sensitivity of these materials.
- The developed synthesis method can be applied for the preparation of different group of metal doped nanostructured ZnO sensor materials.
- Cadmium with another bivalent element could be incorporated as co-doped ZnO nanostructures to enhance the sensing characteristics and for fast response and low saturation time. For real time usage the materials must be micro-machined with inbuilt micro heaters. The selectivity of the sensors could be further optimised by nanostructures fabrication and use of molecular sieves for continuous assessment of VOC and gas composition.

In summary, it is evident that the research on ZnO nanostructures for VOC and gas sensing is highly significant for the quality assessment of tea and has implications for human health and safety, and environmental change. While this area has seen a recent flourish, there remains a lot of research, that needs to be performed, and it will be interesting to follow the progress and direction of this exciting field into the future.

*Francis Chandra Das*

*Rajy Bandhyopadhyay*  
 Professor  
 Dept. of Inst. & Electronics Engg.  
 Jadavpur University  
 Salt Lake Campus  
 Kolkata-98

*P. P. Choudhary*  
 Former Professor  
 Department of Chemistry  
 Indian Institute of Technology, Kharagpur